International Journal of Optics

Nanoplasmonics and Metamaterials

Guest Editors: Zhaolin Lu, Xiaoyue Huang, Mark Mirotznik, Georgios Veronis, and Qiwen Zhan

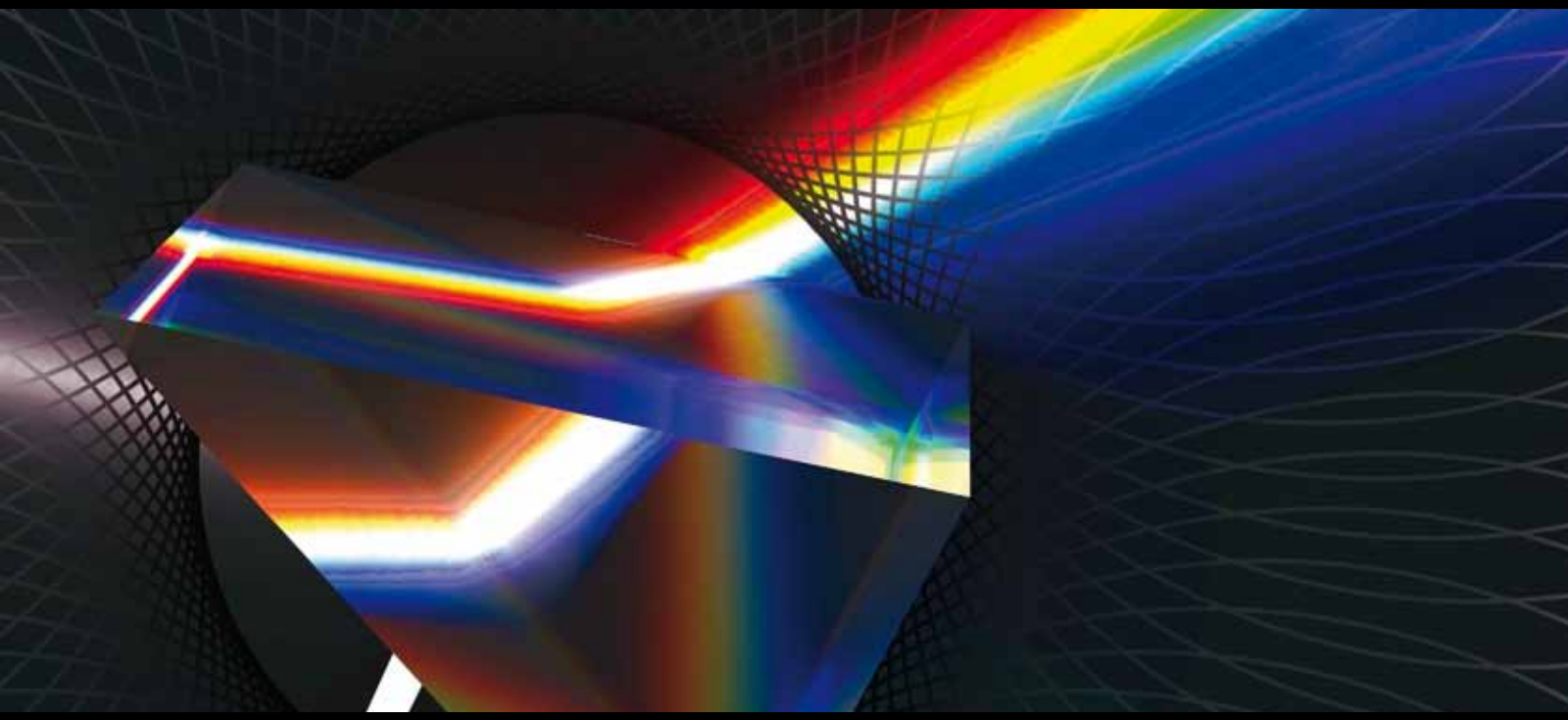

Nanoplasmonics and Metamaterials

International Journal of Optics

Nanoplasmonics and Metamaterials

Guest Editors: Zhaolin Lu, Xiaoyue Huang, Mark Mirotznik, Georgios Veronis, and Qiwen Zhan

Copyright © 2012 Hindawi Publishing Corporation. All rights reserved.

This is a special issue published in "International Journal of Optics." All articles are open access articles distributed under the Creative Commons Attribution License, which permits unrestricted use, distribution, and reproduction in any medium, provided the original work is properly cited.

Editorial Board

Alejandro Aceves, USA
Fortunato Tito Arecchi, Italy
Victor Arrizon, Mexico
Gaetano Assanto, Italy
Jose Azana, Canada
Ole Bang, Denmark
Randy A. Bartels, USA
Augusto Belendez, Spain
E. Bernabeu, Spain
Le Nguyen Binh, Germany
Keith J. Blow, UK
A. D. Boardman, UK
Wojtek J. Bock, Canada
Neil Broderick, UK
Hrvoje Buljan, Croatia
A. Cartaxo, Portugal
Giulio Cerullo, Italy
K. S. Chiang, Hong Kong
W. C. H. Choy, Hong Kong
David Coutts, Australia
Ilaria Cristiani, Italy
Michael J. Damzen, UK
Vittorio Degiorgio, Italy
Cornelia Denz, Germany
Ivan Djordjevic, USA
Niloy K. Dutta, USA
Robert G. Elliman, Australia
Charles M. Falco, USA
Mahmoud Fallahi, USA
Pietro Ferraro, Italy
Mário F. Ferreira, Portugal
Rashid A. Ganeev, Uzbekistan
Hooshang Ghafouri-Shiraz, UK
Ivan Glesk, UK
Qihuang Gong, China
N. A. Halliwell, UK
Sang-Kook Han, Republic of Korea
Sulaiman Wadi Harun, Malaysia
W. F. Hsieh, Taiwan
Mark Humphrey, Australia
Nicusor Iftimia, USA
Mohammed N. Islam, USA
Chennupati Jagadish, Australia
Wonho Jhe, Korea
Mirosław A. Karpierz, Poland
Yu S. Kivshar, Australia
Wieslaw Krolikowski, Australia
Nayot Kurukitkoson, Thailand
R. Leitgeb, Switzerland
Gong Ru Lin, Taiwan
Michael E. Marhic, UK
Lorenzo Marrucci, Italy
John McInerney, Ireland
Andrea Melloni, Italy
Adam Miranowicz, Poland
Roberto Morandotti, Canada
Uwe Morgner, Germany
Dragomir Neshev, Australia
Jean-Michel Nunzi, Canada
Takashige Omatsu, Japan
Wolfgang Osten, Germany
Ben Ovryn, USA
Nicolae C. Panoiu, UK
Vittorio M. N. Passaro, Italy
Gang-Ding Peng, Australia
Reji Philip, India
Armando Nolasco Pinto, Portugal
Adrian Podoleanu, UK
Jianan Qu, Hong Kong
Chenggen Quan, Singapore
Marek Samoc, Poland
John T. Sheridan, Ireland
Ping Shum, Singapore
Mohammad Taghizadeh, UK
R. P. Tatam, UK
Markus E. Testorf, USA
Mustapha Tlidi, Belgium
Stefano Trillo, Italy
Stefan Wabnitz, Italy
Boris Y. Zeldovich, USA

Contents

Nanoplasmonics and Metamaterials, Zhaolin Lu, Xiaoyue Huang, Mark Mirotznik, Georgios Veronis, and Qiwen Zhan
Volume 2012, Article ID 740487, 2 pages

Anomalous Propagation in Low Index Contrast Metamaterials: Assessment of the Beam Collimation Condition, Jun Tan, Weiwei Song, and Wei Jiang
Volume 2012, Article ID 120731, 6 pages

Deep Subwavelength Power Concentration-Based Hyperbolic Metamaterials, Amanpreet Kaur, Saptarshi Banerjee, Wangshi Zhao, Jayanti Venkataraman, and Zhaolin Lu
Volume 2012, Article ID 879392, 6 pages

Tuning Metamaterials for Applications at DUV Wavelengths, Andrew Estroff and Bruce W. Smith
Volume 2012, Article ID 603083, 7 pages

Green Function Formulism for Electromagnetic Wave Generated in Nanostructured Metamaterial of Finite Thickness: Isotropy and Anisotropy, Shunbo Li, Xiao Xiao, Bo Hou, and Weijia Wen
Volume 2012, Article ID 532316, 19 pages

Nanoscale Plasmonic Devices Based on Metal-Dielectric-Metal Stub Resonators, Yin Huang, Changjun Min, Liu Yang, and Georgios Veronis
Volume 2012, Article ID 372048, 13 pages

Passive Infrared Sensing Using Plasmonic Resonant Dust Particles, Mark Mirotznik, William Beck, Kimberly Olver, John Little, and Peter Pa
Volume 2012, Article ID 651563, 8 pages

Subwavelength Plasmonic Waveguides and Plasmonic Materials, Ruoxi Yang and Zhaolin Lu
Volume 2012, Article ID 258013, 12 pages

Surface Plasmon Singularities, Gabriel Martínez-Niconoff, P. Martinez-Vara, G. Diaz-Gonzalez, J. Silva-Barranco, and A. Carbajal-Domínguez
Volume 2012, Article ID 152937, 7 pages

Plasmonic Bandgaps in 1D Arrays of Slits on Metal Layers Excited by Out-of-Plane Sources, Roberto Marani, Marco Grande, Vincenzo Petruzzelli, and Antonella D'Orazio
Volume 2012, Article ID 146396, 12 pages

Coupling Schemes in Terahertz Planar Metamaterials, Dibakar Roy Chowdhury, Ranjan Singh, Antoinette J. Taylor, Hou-Tong Chen, Weili Zhang, and Abul K. Azad
Volume 2012, Article ID 148985, 12 pages

Hindawi Publishing Corporation
International Journal of Optics
Volume 2012, Article ID 740487, 2 pages
doi:10.1155/2012/740487

Editorial
Nanoplasmonics and Metamaterials

Zhaolin Lu,[1] Xiaoyue Huang,[2] Mark Mirotznik,[3] Georgios Veronis,[4] and Qiwen Zhan[5]

[1] *Microsystems Engineering PhD Program, Rochester Institute of Technology, Rochester, NY 14623, USA*
[2] *Advance Material and Process Group, ATD, Recording Head Operation, Seagate Technology, 7801 Computer Avenue South, Bloomington, MN 55435, USA*
[3] *Department of Electrical and Computer Engineering, University of Delaware, Newark, DE 19710, USA*
[4] *Department of Electrical and Computer Engineering, Center for Computation and Technology, Louisiana State University, Baton Rouge, LA 70803, USA*
[5] *Electro-Optics Graduate Program, University of Dayton, Dayton, OH 45469, USA*

Correspondence should be addressed to Zhaolin Lu, zhaolin.lu@rit.edu

Received 9 December 2012; Accepted 9 December 2012

Copyright © 2012 Zhaolin Lu et al. This is an open access article distributed under the Creative Commons Attribution License, which permits unrestricted use, distribution, and reproduction in any medium, provided the original work is properly cited.

Nanoplasmonics and metamaterials have been two interplayed and heated topics for over a decade. This issue on nanoplasmonics and metamaterials compiles 10 well-prepared manuscripts, most of which are meticulously performed reviews of the available current literature.

This issue contains two review articles. R. Yang and Z. Lu review the progress of subwavelength or deep subwavelength plasmonic waveguides and fabrication techniques of plasmonic materials, including the theory of plasmonic waveguides, the mode size defined by plasmonic waveguides, spoof plasmonic waveguides, and various media for plasmonic waveguide. D. R. Chowdhury et al. present a review of different coupling schemes in a planar array of terahertz metamaterials. The different coupling mechanisms in planar metamaterials could be exploited for the development of terahertz devices with various functionalities.

Three papers address the theory and applications of metamaterials with abnormal electromagnetic properties. S. Li et al. developed a Green function formulism to calculate the electromagnetic fields generated by sources embedded in nanostructured medium which could be represented by an effective permittivity tensor with finite thicknesses. An extreme case is material with indefinite permittivity tensor, which contains both positive and negative elements. One result is its unique hyperbolic dispersion. A. Kaur et al. studied the electromagnetic properties of wired media and explored their hyperbolic dispersion when used in imaging systems. Based on hyperbolic dispersion, deep subwavelength focusing (or power concentration) is demonstrated both numerically and experimentally. The results verify that hyperbolic metamaterials can focus a broad collimated beam on a subwavelength scale. G. Martínez-Niconoff et al. describe the synthesis of optical singularities propagating in free space and on a metallic surface, where a slit-shaped curve as a boundary condition is applied. They show that singularities in free space may generate bifurcation effects.

Three articles discuss the applications of novel metallic gratings or periodic structures. M. Mirotznik et al. describe a novel infrared sensing technique using plasmonic resonant dust particles. They present computational and experimental results of dust particles that can be tuned to preferentially reflect or emit IR radiation within the LWIR (8–14 μm) band. This technique creates distinct IR absorption resonances by combining the plasmonic resonance of the grating with the natural resonance of the cavity. R. Marani et al. analyze plasmonic bandgaps in a one-dimensional array of slits on metal layers excited by out-of-plane sources. They demonstrate through finite-element simulation that a nonzero angle of incidence induces the formation of an effective finite bandgap. J. Tan et al. analyze the anomalous beam propagation in low-index-contrast metamaterials, which is formed by patterning periodic arrays of air holes in polymer with a low refractive index. The requirements for achieving well-collimated beams in a metamaterial are established.

Two papers deal with the applications of surface plasmons in nanophotonic circuits and nanolithography. Y. Huang et al. present novel plasmonic devices based on metal-dielectric-metal (MDM) stub resonators for manipulating

light at the nanoscale. In particular, they demonstrate slow-light effect, a plasmonic analog of electromagnetically induced transparency, and absorption switches based on subwavelength MDM waveguide side coupled to one or more MDM stub resonators. A. Estroff and B. W. Smith explore the applications of surface plasmons based on tuning metamaterials in DUV lithography and propose a method for performing plasmonic interference lithography, with calculations showing the potential for half-pitch imaging resolution of 25 nm.

By compiling these papers, we hope to enrich our readers and researchers with respect to nanoplasmonics and metamaterials.

Zhaolin Lu
Xiaoyue Huang
Mark Mirotznik
Georgios Veronis
Qiwen Zhan

Hindawi Publishing Corporation
International Journal of Optics
Volume 2012, Article ID 120731, 6 pages
doi:10.1155/2012/120731

Research Article

Anomalous Propagation in Low Index Contrast Metamaterials: Assessment of the Beam Collimation Condition

Jun Tan,[1] Weiwei Song,[1] and Wei Jiang[1,2]

[1] *Department of Electrical and Computer Engineering, Rutgers University, Piscataway, NJ 08854, USA*
[2] *Institute for Advanced Materials, Devices, and Nanotechnology, Rutgers University, Piscataway, NJ 08854, USA*

Correspondence should be addressed to Wei Jiang, wjiangnj@rci.rutgers.edu

Received 1 June 2012; Accepted 10 August 2012

Academic Editor: Georgios Veronis

Copyright © 2012 Jun Tan et al. This is an open access article distributed under the Creative Commons Attribution License, which permits unrestricted use, distribution, and reproduction in any medium, provided the original work is properly cited.

Anomalous beam propagation in low index-contrast metamaterials has been analyzed. The condition for a well-collimated beam is found to be depending on the beam width and the pertinent Fourier component of the dielectric function. Guided by this condition, an ultra-compact metamaterial structure is designed to deflect a light beam at a wide angle. The structure is tolerant to structural parameter deviation and has a wide bandwidth.

1. Introduction

Metamaterials have aroused wide spread interest in recent years [1–12]. Many metamaterial structures involve metallic and dielectric components with a large refractive index-contrast between two material components. Such a large index-contrast results in the capability of confining and maneuvering light path in a very small scale. On the other hand, it is possible to construct metamaterials with relatively low index-contrast. It would be helpful to understand the capability and limit of metamaterials in the low index-contrast case. In this work, we will study a low index-contrast metamaterial system composed of polymer and air components in such a context. Negative refraction is a topic of wide interest in metamaterials research [1]. Negative refraction can be considered as one aspect of the anomalous characteristics of an optical beam in metamaterials. We will analyze low index-contrast metamaterials that can produce certain anomalous propagation characteristics. This can be utilized to maneuver light beams of sufficiently large widths with potential applications in polymer photonic integrated circuits [13]. Note that the low index-contrast metamaterials discussed here differ from the low-index (or epsilon-near-zero) metamaterials, whose constitutive components have relatively large indices.

Anomalous beam propagation in metamaterials can be traced back to early studies of photonic crystals in 1998 [14]. Note that photonic crystals can be considered as one category of metamaterials whose refractive indices are usually real. The abnormalities include negative refraction, unusually large refraction/deflection angle, and unusual wavelength sensitivity [14]. The proposed applications of these effects include beam deflectors [15], wavelength-division multiplexers [14, 15]. To utilize such anomalous propagation in compact devices, it is generally preferred to use a narrow beam at the entrance so that the device lateral width can be minimized. However, the anomalous propagation is usually accompanied by greater angular dispersion, which significantly exacerbates the angular divergence of a narrow beam in a metamaterial. For high index-contrast systems such as silicon-air photonic crystals, this problem can be solved through engineering the dispersion surface [16]. However, this angular divergence problem has not been analyzed in a general manner, especially for metamaterials of small index-contrasts. Note that many low-index materials such as polymers are attractive in a wide range of photonics applications because of their low fabrication/processing cost and flexible form [13]. In this work, we will start from analyzing the beam collimation condition in low index-contrast metamaterials in Section 2. Then Section 3 will present a

design of a beam deflection device and address some other practical issues of low index-contrast metamaterials. Lastly, conclusions will be presented in Section 4.

2. Beam Collimation Condition in Low Index-Contrast Metamaterials

The anomalous propagation characteristics observed in these metamaterials originate from the underlying subwavelength structures. Related problems have been studied in various scenarios in other fields. Particularly, in X-ray diffraction study, a "dynamic theory" has been developed [17] to understand the beam divergence related issue for X-ray propagation in a crystal. Of particular value is the spherical wave part of the dynamic theory of X-ray diffraction. In the limit of zero beam width, the entering beam becomes a completely diverging spherical wave (a cylindrical wave in two dimensional problems), which represents the worst beam divergence scenario. This spherical wave formulation can be easily adapted to help understand the beam divergence issue in a low index-contrast metamaterial. Considering an entering beam with center wavevector $\mathbf{k}_0$ diffracted by a Fourier component $\varepsilon_{\mathbf{G}}$ of the dielectric function, the first order diffraction has a wave vector $\mathbf{k}_g = \mathbf{k}_0 + \mathbf{G}$, where $\mathbf{G}$ is a reciprocal lattice vector. The dynamic X-ray diffraction theory gives the wave in the crystal as [17]:

$$E_g(x,y) = A(x,y) \sum_{\sigma=\pm 1} \int_{-\infty}^{+\infty} B(s) \left[\frac{\beta}{\sigma\sqrt{s^2+\beta^2}} \right] \times \exp\left[i\sigma\xi_1\sqrt{s^2+\beta^2} - i\xi_2 s \right] ds, \quad (1)$$

where $A(x,y)$ is a fast oscillating field with the ensuing integral being its envelope, ξ_1 and ξ_2 represent the local coordinates of an oblique two-dimensional (2D) coordinate system (hence, ξ_1 and ξ_2 are two linear functions of x and y) induced by the dispersion surface; $\sigma = 1$ and -1 for two branches of dispersion surface, respectively; $s = \Delta k + C_1 k_0$, with Δk being the wavevector deviation from k_0; $\beta = C_2 k_0 \varepsilon_{\mathbf{G}}$. The geometric constants C_1, C_2 are of order unity. Here the dispersion surface refers to the constant frequency surface in the reciprocal space. The function $B(s)$ is introduced by us in this work to describe the wavevector distribution (note that s is a function of Δk). The usage of $B(s)$ will be discussed shortly. Equation (1) was obtained through lengthy and complicated derivations, where the physical meaning of the quantities s, β, and ξ_i became obscure. However, it is sufficient to note that the phase factor $\exp\lfloor i\sigma\xi_1\sqrt{s^2+\beta^2} - i\xi_2 s\rfloor$ in (1) is equivalent to $\exp[i(\mathbf{k} - \mathbf{k_0}) \cdot \mathbf{r}]$, where $\mathbf{k_0}$ is constant. Thus, s and $\sqrt{s^2+\beta^2}$ are the projections of wavevector deviation $\Delta\mathbf{k} = \mathbf{k} - \mathbf{k_c}$ on the ξ_1 and ξ_2 axes, respectively. Note that as s varies, β varies accordingly, so that $\mathbf{k}$ remains on the dispersion surface. Therefore, β is a function of s. In the spherical-wave dynamic X-ray theory [17], due to the limitation of analytic study, only the case $B(s) \equiv 1$ is investigated. It was analytically shown that the wave pattern $E_g(x,y)$ spreads within a triangle spanned by $\mathbf{k}_0$ and $\mathbf{k}_g$ and have hook-shaped interference patterns. For polymer photonic integrated circuits applications, such a triangular spread leads to significant beam divergence, which may increase device lateral dimensions and optical loss. In addition, an additional beam focuser or waveguide taper becomes necessary to couple light into an output waveguide. This increases the device complexity and size.

To overcome these issues originated from beam divergence, it is necessary to quantitatively study the beam divergence with varying structure parameters and seek approaches to minimize the beam divergence under the constraints of small index-contrast. To start, we note that in the X-ray theory, the beam is assumed to originate from a point source with a uniform angular intensity spectrum. Such an ideal simplification is not applicable to integrated optics applications where the input beam has a finite width. We have introduced a wavevector distribution function $B(s)$ in (1) to deal with arbitrary beam profiles. Note that for any given lateral beam profile $b(x_\perp)$ in space ($x_\perp$ being the coordinate transverse to the beam propagation direction), the corresponding wavevector distribution function $\widetilde{B}(\Delta k_\perp)$ can be obtained from the Fourier transform of $b(x_\perp)$. Note that for a monochromatic beam in 2D space, the wavevector deviation has only one degree of freedom. Therefore, one can easily link $\widetilde{B}(\Delta k_\perp)$ to $B(s)$, noting that s is a linear function of Δk. Here we address the case where the wavevector is limited to a small angular range such that $\Delta k_{\max} \ll |\beta|$. Assuming a Gaussian beam profile $B(s)$ and expanding (1) in $\Delta s/\beta$ (or equivalently $\Delta k/\beta$), one can readily show that for a sufficiently small $\Delta k/\beta \ll 1$, the beam is well collimated without obvious divergence. This case is of our interest here. Introduce the wavevector angle θ_k, with respect to the beam axis, we find $\Delta k = k_0 \sin\theta_k$. Also, note $\beta = C_2 k_0 \varepsilon_{\mathbf{G}}$, where C_2 is a constant on the order of unity. Hence, the condition ($\Delta k_{\max} \ll |\beta|$) for a well-collimated beam can also be formulated as

$$\theta_{\mathrm{km}} \ll \varepsilon_G, \quad (2)$$

where θ_{km} is the characteristic angular spread of the wavevector (roughly speaking, the beam divergence angle) for a finite beam. Consider a Gaussian beam with a width w propagating in a 2D square lattice of air holes in a medium of relative dielectric constant ε_1. It is well known that the beam angular divergence is related to the beam width as $\theta_{\mathrm{km}} \propto \lambda/w$. One can also readily show that the Fourier coefficient ε_G generally has the form of Bessel functions for a photonic crystal composed of circular holes [18]. Thus, based on (2), we can readily show that the condition for a well-collimated beam is given by

$$w \gg w_c = \frac{2\lambda}{\pi\sqrt{\varepsilon_1}(\varepsilon_1 - 1)} \frac{a}{r J_1(2\pi r/a)}, \quad (3)$$

where r is the hole radius, a is the lattices constant, λ is the wavelength, $J_1(x)$ is a Bessel function of the first kind, and w_c can be regarded a characteristic beam width pertinent to the divergence issue. Assume a metamaterial is composed of air holes in a polymer matrix with typical polymer index $n_{\mathrm{polymer}} = 1.5$, we plot w_c as a function

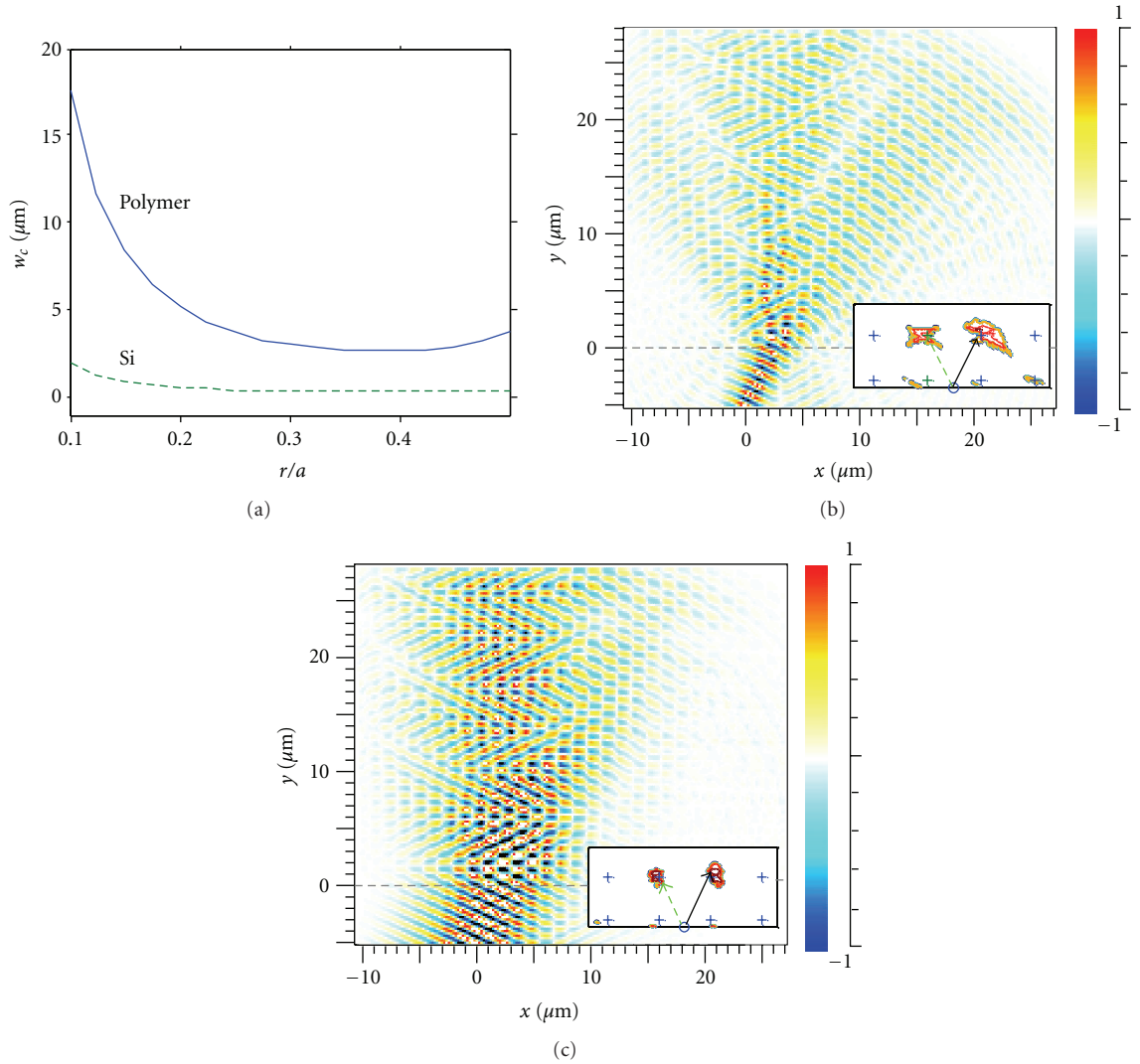

FIGURE 1: (a) w_c versus r/a curve given by (3) for polymer-based and silicon-based metamaterials. (b) Beam propagation in a polymer metamaterial for a Gaussian beam with a width $w = 3\,\mu$m. The metamaterial region starts at $5\,\mu$m from the bottom of the figure (the interface is indicated by a dashed line) and extends upwards. Inset: 2D Fourier transform of the spatial field in the photonic crystal. The wavevector $\mathbf{k}_0$ and $\mathbf{k}_g$ are indicated by a black arrow and a green dash arrow. The wavevector of various diffraction orders (on a square lattice in the reciprocal space) are marked by crosses. (c) Same as in (b) except $w = 10\,\mu$m.

of r/a in Figure 1(a) for $\lambda = 1.55\,\mu$m. For comparison, the w_c for a high index-contrast metamaterial composed of air holes in a silicon matrix is also shown. Evidently, the polymer-based metamaterial system requires substantially wider beams than the silicon-based metamaterial system. In this work, the low index-contrast regime pertaining to metamaterial beam collimation refers to $|\Delta n|$ substantially less than unity (e.g., $|\Delta n| \sim 0.5$), which is in contrast to high index-contrast metamaterial systems such as silicon-air or silver-air. Note that w should usually be at least 3 to 10 times larger than w_c in order to satisfy (3). For the polymer-based metamaterial, the minimal $w_c \sim 2.7\,\mu$m appears at $r/a \sim 0.37$. For $r/a \geq 0.3$, the curve is relatively flat, indicating w_c is insensitive to hole radius change in this range. Overall, Figure 1(a) shows that the beam width must be much larger than $3\,\mu$m for a polymer-based metamaterial at $\lambda = 1.55\,\mu$m. Figures 1(b) and 1(c) compare two beams of $3\,\mu$m and $10\,\mu$m wide, propagating in a $r/a = 0.3$ lattice as simulated by the Finite Difference Time-Domain (FDTD) method for polarization normal to the plane. The metamaterial region starts at $5\,\mu$m from the bottom (each division on the axis is a micron) and extends upward. For the $10\,\mu$m wide beam case in Figure 1(c), the optical wave inside the metamaterial has the majority of its power propagating in a collimated beam (vertically upwards and slightly tilting to the left), whereas the 3-μm wide beam in Figure 1(b) results in a diverging field spreading over a triangle whose left and right edges are roughly parallel to $\mathbf{k_0}$ and $\mathbf{k_g}$. Note that in Figure 1(c), the incident beam points towards the right hand side whereas the beam propagation direction inside the metamaterial slightly tilts towards the left side. This indicates that the beam experiences negative refraction

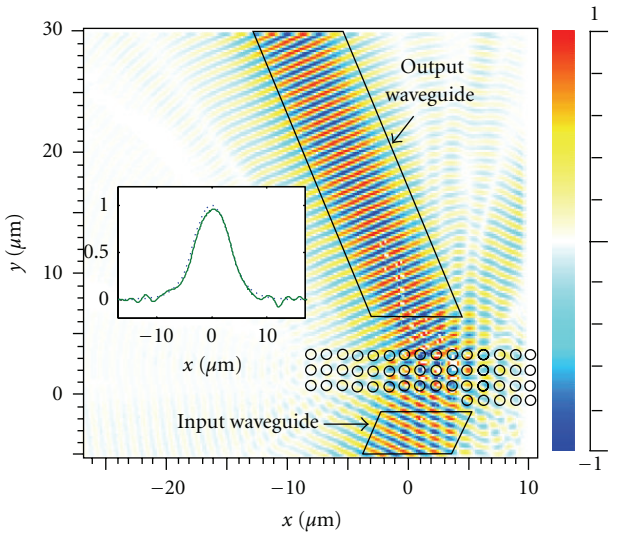

FIGURE 2: An ultra-compact 47.3° beam deflector (effectively a wide-angle waveguide bend). Inset indicates the output beam profile (solid curve) is well matched to the waveguide mode profile (dotted line).

at the metamaterial surface, which is anomalous compared to ordinary refraction. For Figure 1(b), the diverging beam wipes out the signature of negative refraction. These FDTD simulation results confirm that the beam width w must be sufficiently larger than the characteristic beam width w_c in order to form a well-collimated beam and observe negative refraction in a low index-contrast metamaterial. The insets in Figures 1(b) and 1(c) show the power spectrum of the 2D spatial Fourier transforms of the respective spatial fields. The un-diffracted wavevector $\mathbf{k}_0$ is shown by an arrow with the origin $\mathbf{k} = 0$ noted by a circle. Because the lower half of the Fourier spectrum is symmetric to the upper half, only the upper half the 2D Fourier spectrum is shown. The wavevectors of various diffraction orders (on a square lattice in the reciprocal space) are marked by crosses. Their spatial Fourier spectra are dominated by two Fourier components (centered around $\mathbf{k}_0$ and $\mathbf{k}_g$).

3. Potential Device Application: A Beam Deflector

A closer look of Figure 1(c) reveals an alternation of two different wave components, whose (center) wavevectors are different from the beam direction. When the beam is collimated as Figure 1(c), this can be utilized to realize low-loss wide angle beam deflection. Figure 2 presents the 2D FDTD simulation result of a wide-angle (47.3°) deflector, which essentially has the functionality of a wide-angle waveguide bend. The incident beam is a waveguide mode matched to a typical fiber mode, which has a mode width around 10 μm. The 2D square lattice metamaterial has a lattice constant $a = 1.3\,\mu$m, and a hole radius $r = 0.3a$. The lattice constant and hole radius are relatively large to facilitate fabrication. More discussion on practical implementation and fabrication will be presented at the end of this section. High transmission and excellent mode match (see the inset of Figure 2) are achieved at the output end, giving an insertion loss less than 0.5 dB. Note that for the noncollimated case shown in Figure 1(b), because of widely spread beam (whose profile quickly deviates from Gaussian after a short propagation length) inside the metamaterial, it is very difficult to achieve a collimated deflected beam at the output and the loss is usually significantly higher. Note that for the case shown in Figure 2, the beam profile quickly stabilizes after exiting the metamaterial region. The bottom layer of the structure is intentionally designed to be incomplete. Our simulation indicates that such an incomplete layer enhances the transmission. One possible explanation is that when the beam is making a left turn, the right portion of the beam is on the "outer track" and travels a longer distance. Thus, the right portion of the beam also needs a longer interaction length in the metamaterial to complete the turn on the "outer track." Therefore, the right portion of the metamaterial shall be relatively thicker. It is worth noting that at the output surface of the metamaterial region in Figure 2, the beam experiences a second negative refraction. The negative refractions at the front and back surfaces both contribute substantially to producing a large total beam deflection angle.

Figure 3 shows the transmission loss variation with respect to two essential parameters (λ and n). For simulation results in Figure 3, the baseline structure has all parameters same as the optimized structure in Figure 2 except that we have used a generic polymer refractive index $n_{\text{polymer}} = 1.5$ (the structure in Figure 2 is optimized to have $n_{\text{polymer}} = 1.42$). This baseline structure has an insertion of 0.7 dB. Additionally, the loss variation with 50 nm hole radius deviation is less than 0.1 dB. These results show that this device is wide band (whole C-Band) and relatively insensitive to slight deviation of polymer index and fabrication tolerance of the hole radius. Note that a hole radius tolerance of 50 nm is readily achievable using electron beam lithography. Also, the relative insensitivity to polymer index allows a wide range of polymers to choose from. Note that we have intentionally designed our structure with a relatively large a, and an intermediate r/a to facilitate the fabrication. Note the traditional waveguide bends for polymer integrated photonic devices are usually several millimeters long due to the small index-contrast of polymers [13]. The metamaterial structures obviously have advantages in device miniaturization.

For practical implementation of this structure, each waveguide will be a channel waveguide composed of higher index polymer core and lower index polymer cladding, as shown in Figure 4. In the metamaterial region, the core layer will be etched away; thus, the conformal nature of the top polymer cladding will likely lower the top cladding surface to the same height as the top surface of the core layer. To ensure the functionality of the metamaterial, the metamaterial region will be etched to a depth that is greater than the depth the polymer core. Note that polymer waveguides generally have fairly small refractive index-contrasts ($\Delta n \sim 0.01$) between core and cladding,

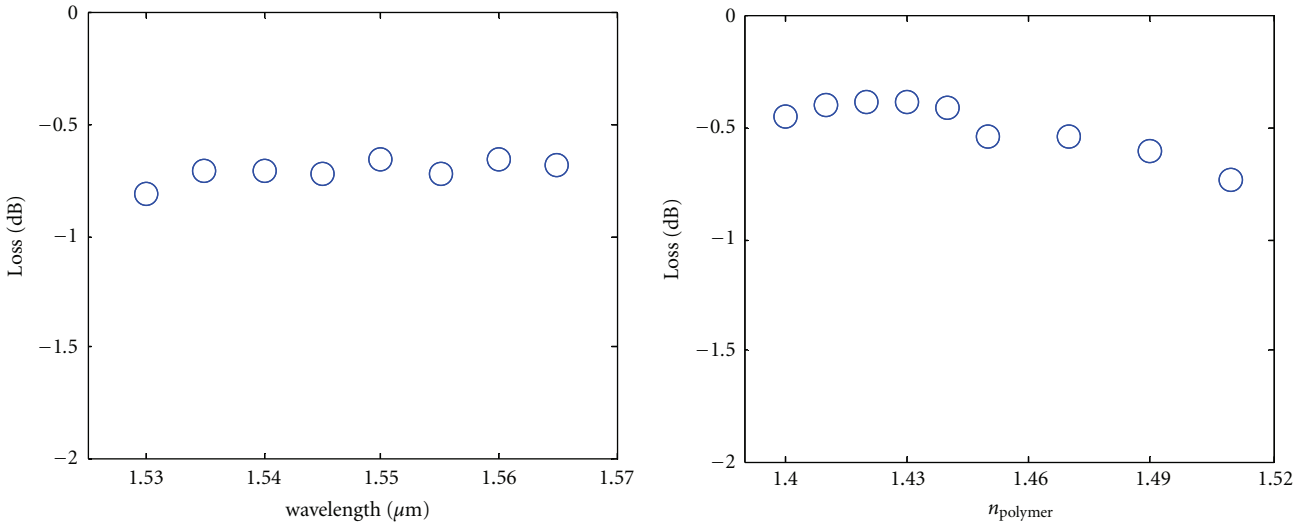

Figure 3: Loss variation with (a) wavelength and (b) polymer index.

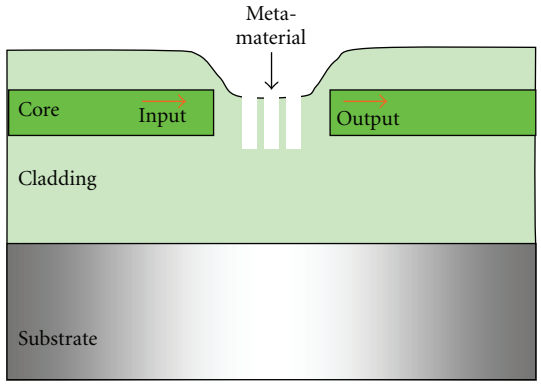

Figure 4: Schematic of an example device structure (side view, not drawn to scale).

and relatively large cross-sections. Here we assume a core thickness of 3 μm and a top cladding thickness of 2 μm. As such, it is estimated that we need to etch ~3 μm deep into the polymer in the metamaterial region. Although there is no vertical confinement mechanism in the metamaterial region, optical loss due to beam divergence in the vertical direction is expected to be insignificant due to the short length of the metamaterial region (~5 μm long) through which the beam travels.

4. Conclusions

In summary, the condition for achieving well-collimated beams in a metamaterial has been analyzed. Guided by this analysis, we have designed ultra-compact, wide-angle beam deflection devices that are significantly smaller than conventional polymer integrated photonic devices. The simulations also show that these devices have a wide bandwidth and are insensitive to fabrication tolerances. A wide range of polymers can be chosen to fabricate these structures. Such polymer photonic devices are attractive for their compact size, low cost and flexible form.

Acknowledgment

This work is supported in part by AFOSR Grant No. FA9550-08-1-0394.

References

[1] D. R. Smith, J. B. Pendry, and M. C. K. Wiltshire, "Metamaterials and negative refractive index," *Science*, vol. 305, no. 5685, pp. 788–792, 2004.

[2] V. M. Shalaev, W. Cai, U. K. Chettiar et al., "Negative index of refraction in optical metamaterials," *Optics Letters*, vol. 30, no. 24, pp. 3356–3358, 2005.

[3] S. Zhang, W. Fan, N. C. Panoiu, K. J. Malloy, R. M. Osgood, and S. R. J. Brueck, "Experimental demonstration of near-infrared negative-index metamaterials," *Physical Review Letters*, vol. 95, no. 13, Article ID 137404, 4 pages, 2005.

[4] S. Linden, C. Enkrich, M. Wegener, J. Zhou, T. Koschny, and C. M. Soukoulis, "Magnetic response of metamaterials at 100 terahertz," *Science*, vol. 306, no. 5700, pp. 1351–1353, 2004.

[5] D. Schurig, J. J. Mock, B. J. Justice et al., "Metamaterial electromagnetic cloak at microwave frequencies," *Science*, vol. 314, no. 5801, pp. 977–980, 2006.

[6] H. J. Lezec, J. A. Dionne, and H. A. Atwater, "Negative refraction at visible frequencies," *Science*, vol. 316, no. 5823, pp. 430–432, 2007.

[7] N. Engheta, "Circuits with light at nanoscales: optical nanocircuits inspired by metamaterials," *Science*, vol. 317, no. 5845, pp. 1698–1702, 2007.

[8] J. A. Schuller, R. Zia, T. Taubner, and M. L. Brongersma, "Dielectric metamaterials based on electric and magnetic resonances of silicon carbide particles," *Physical Review Letters*, vol. 99, no. 10, Article ID 107401, 4 pages, 2007.

[9] J. Valentine, S. Zhang, T. Zentgraf et al., "Three-dimensional optical metamaterial with a negative refractive index," *Nature*, vol. 455, no. 7211, pp. 376–379, 2008.

[10] S. E. Kocabaş, G. Veronis, D. A. B. Miller, and S. H. Fan, "Transmission line and equivalent circuit models for plasmonic waveguide components," *IEEE Journal on Selected Topics in Quantum Electronics*, vol. 14, no. 6, pp. 1462–1472, 2008.

[11] W. Zhao, X. Huang, and Z. Lu, "Super Talbot effect in indefinite metamaterial," *Optics Express*, vol. 19, no. 16, pp. 15297–15303, 2011.

[12] J. X. Chen, P. Wang, C. C. Chen, Y. H. Lu, H. Ming, and Q. W. Zhan, "Plasmonic EIT-like switching in bright-dark-bright plasmon resonators," *Optics Express*, vol. 19, no. 7, pp. 5970–5978, 2011.

[13] R. T. Chen, "Polymer-based photonic integrated circuits," *Optics and Laser Technology*, vol. 25, no. 6, pp. 347–365, 1993.

[14] H. Kosaka, T. Kawashima, A. Tomita et al., "Superprism phenomena in photonic crystals," *Physical Review B*, vol. 58, no. 16, pp. 10096–10099, 1998.

[15] T. Baba and M. Nakamura, "Photonic crystal light deflection devices using the superprism effect," *IEEE Journal of Quantum Electronics*, vol. 38, no. 7, pp. 909–914, 2002.

[16] B. Momeni, J. Huang, M. Soltani et al., "Compact wavelength demultiplexing using focusing negative index photonic crystal superprisms," *Optics Express*, vol. 14, no. 6, pp. 2413–2422, 2006.

[17] L. V. Azaroff, R. Kaplow, N. Kato, R. J. Weiss, A. J. C. Wilson, and R. A. Young, *X-Ray Diffraction*, McGraw-Hill, New York, NY, USA, 1974.

[18] W. Jiang and R. T. Chen, "Symmetry-induced singularities of the dispersion surface curvature and high sensitivities of a photonic crystal," *Physical Review B*, vol. 77, no. 7, Article ID 075104, 8 pages, 2008.

Hindawi Publishing Corporation
International Journal of Optics
Volume 2012, Article ID 879392, 6 pages
doi:10.1155/2012/879392

Research Article

Deep Subwavelength Power Concentration-Based Hyperbolic Metamaterials

Amanpreet Kaur,[1] Saptarshi Banerjee,[1] Wangshi Zhao,[1] Jayanti Venkataraman,[2] and Zhaolin Lu[1,2]

[1] *Microsystems Engineering, Kate Gleason College of Engineering, Rochester Institute of Technology, Rochester, NY 14623, USA*
[2] *Department of Electrical and Microelectronic Engineering, Kate Gleason College of Engineering, Rochester Institute of Technology, Rochester, NY 14623, USA*

Correspondence should be addressed to Amanpreet Kaur, axk6400@rit.edu

Received 31 May 2012; Revised 6 August 2012; Accepted 27 August 2012

Academic Editor: Xiaoyue Huang

Copyright © 2012 Amanpreet Kaur et al. This is an open access article distributed under the Creative Commons Attribution License, which permits unrestricted use, distribution, and reproduction in any medium, provided the original work is properly cited.

Hyperbolic metamaterials can manipulate electromagnetic waves by converting evanescent waves into propagating waves and thus support light propagation without diffraction limit. In this paper, deep subwavelength focusing (or power concentration) is demonstrated both numerically and experimentally using hyperbolic metamaterials. The results verify that hyperbolic metamaterials can focus a broad collimated beam to spot size of $\sim \lambda_0/6$ using wired medium design for both normal and oblique incidence. The nonmagnetic design, no-cut-off operation, and preferred direction of propagation in these materials significantly reduce the attenuation in electromagnetic waves.

In conventional materials, focusing is diffraction limited due to the loss of evanescent waves which carry subwavelength information. Therefore, projecting a subdiffraction-limited image would require the recovery of the evanescent waves. The negative index material (NIM), which simultaneously has negative permittivity and negative permeability, was first theoretically studied by Veselago in 1968 [1]. Many years later, Pendry theoretically investigated that a slab of NIM can be used to make a "perfect lens" [2]. Since then, various designs have been explored, and negative refraction has been demonstrated from microwave to optical frequencies [3–9]. The realization of a lens using NIM in practice is rather difficult as negative values of ε and μ are very sensitive to frequency, and ideal condition can only be satisfied at carefully selected frequencies. Some properties of the NIM are based on the resonance of the magnetic component of electromagnetic (EM) wave and thus suffer from energy loss due to the dissipation at the resonances, which reduces the resolution of an imaging system significantly [10–12]. Recently, negative refraction effect and imaging by negative refraction were proposed and demonstrated in indefinite metamaterials [13–22]. Indefinite metamaterials are anisotropic material, in which one or more components of the permittivity tensor have negative sign while others are positive, which results in hyperbolic dispersion relation. These materials are therefore also called hyperbolic metamaterials (HMMs). In a two-dimensional imaging system (assuming that the material is nonmagnetic), the dispersion relation can be expressed as

$$\frac{k_z^2}{\varepsilon_x} + \frac{k_x^2}{\varepsilon_z} = k_0^2 = \frac{\omega^2}{c^2}, \quad (\varepsilon_x > 0,\ \varepsilon_z < 0), \tag{1}$$

where ω is angular frequency, and c is the speed of light in free space while k_x, k_z, and k_0 are the wavenumbers (or spatial frequencies) in the transverse direction x, propagation direction z, and free space, respectively. Compared with the circular dispersion relation in a conventional isotropic material (Figure 1(a)) and elliptical relation (Figure 1(b)) in anisotropic material with finite permittivity (ε_x, $\varepsilon_z > 0$), the dispersion curve for an indefinite metamaterial ($\varepsilon_x > 0$, $\varepsilon_z < 0$) is hyperbolic as shown in Figure 1(c). From (1), we have

$$k_z = \sqrt{\varepsilon_x \left(k_0^2 - \frac{k_x^2}{\varepsilon_z} \right)}. \tag{2}$$

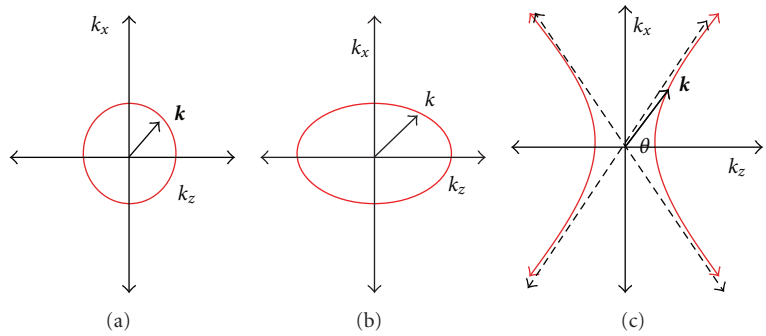

FIGURE 1: (a) Equifrequency surface diagram for an isotropic medium ($\varepsilon_z = \varepsilon_x$). (b) Equifrequency surface diagram for an anisotropic medium ($\varepsilon_z \neq \varepsilon_x$). (c) Equifrequency surface diagram for an indefinite medium (hyperbolic) with ($\varepsilon_z < 0$, $\varepsilon_x > 0$).

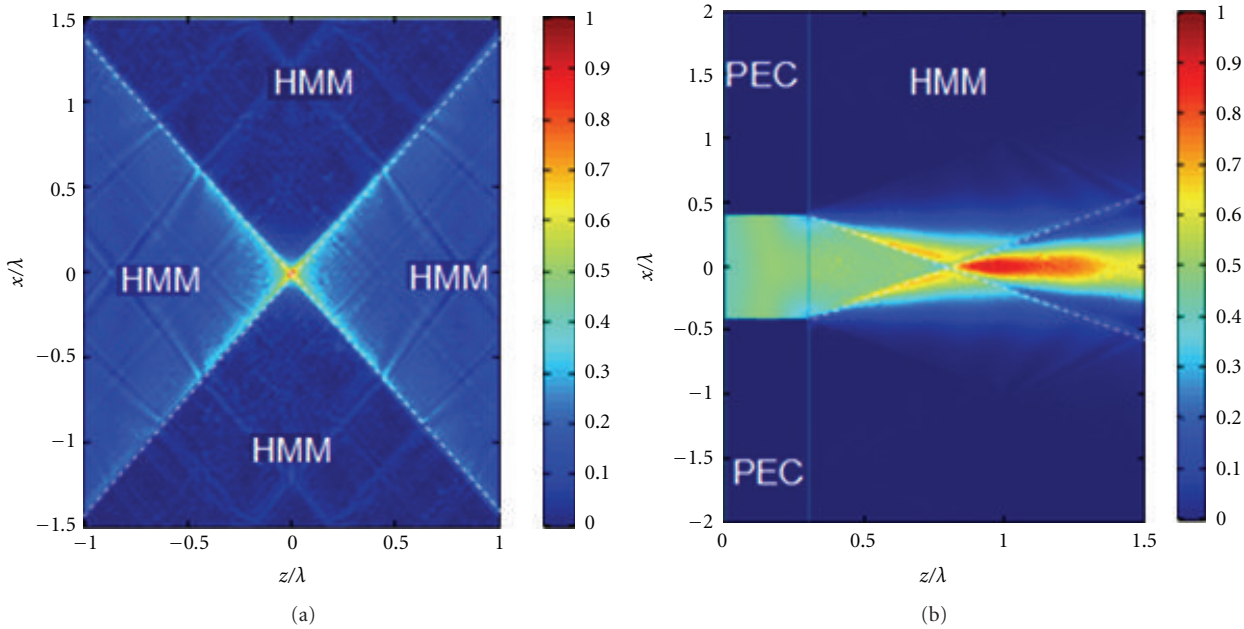

FIGURE 2: (a) Radiation of a point source inside a HMM ($\varepsilon_z = -4$ and $\varepsilon_x = 1$). (b) Light propagation through a sharp edge aperture in HMM and the cross of preferred directions resulting in focusing.

For an elliptically dispersive material there is a theoretical cutoff on the spatial frequency vector while on the other hand there is no limit in dispersion relation of a hyperbolically dispersive material. Assuming that the optical axis is along the z direction, the transfer function for such a system is given by

$$H(k_x) = \exp(jk_z z) = \exp\left(jz\sqrt{\varepsilon_x}\sqrt{k_0^2 - \frac{k_x^2}{\varepsilon_z}}\right). \quad (3)$$

When $\varepsilon_z < 0$ and $\varepsilon_x > 0$, there is no cutoff for any high spatial frequency k_x varying from $-\infty$ to $+\infty$. This means that the HMM can convert the evanescent waves in conventional media into propagating waves. The losses in the HMM also play an important role in the performance as different k components may have different propagation lengths in a HMM; thus the k vectors attenuate differently.

Furthermore, light inside a HMM propagates along some preferred directions [13]. From the dispersion diagram of a HMM (Figure 1(c)), the angle of propagation to z-axis can be calculated as $\theta = \tan^{-1}(k_x/k_z)$ which depends on the ratio of the components of the permittivity tensor in x and z directions. Note that the higher spatial frequency components tend to propagate more towards the asymptotes of hyperbola than the lower spatial frequency vector as θ varies very slowly with k_x as shown by $d\theta/dk_x = k_z/(k_x^2 + k_z^2)$. Thus, the hyperbolic dispersion curves give rise to the two preferred propagation directions which are along the asymptotes of the hyperbola. To verify this, we simulated the radiation pattern of a point source in a HMM with $\varepsilon_x = 1$ and $\varepsilon_z = -4$. As shown in Figure 2(a), the asymptotes define the angular spectrum boundaries and preferred propagation directions.

This effect can be used to make a lens which focuses a broad beam into an ultrasmall spot, where a sharp aperture is

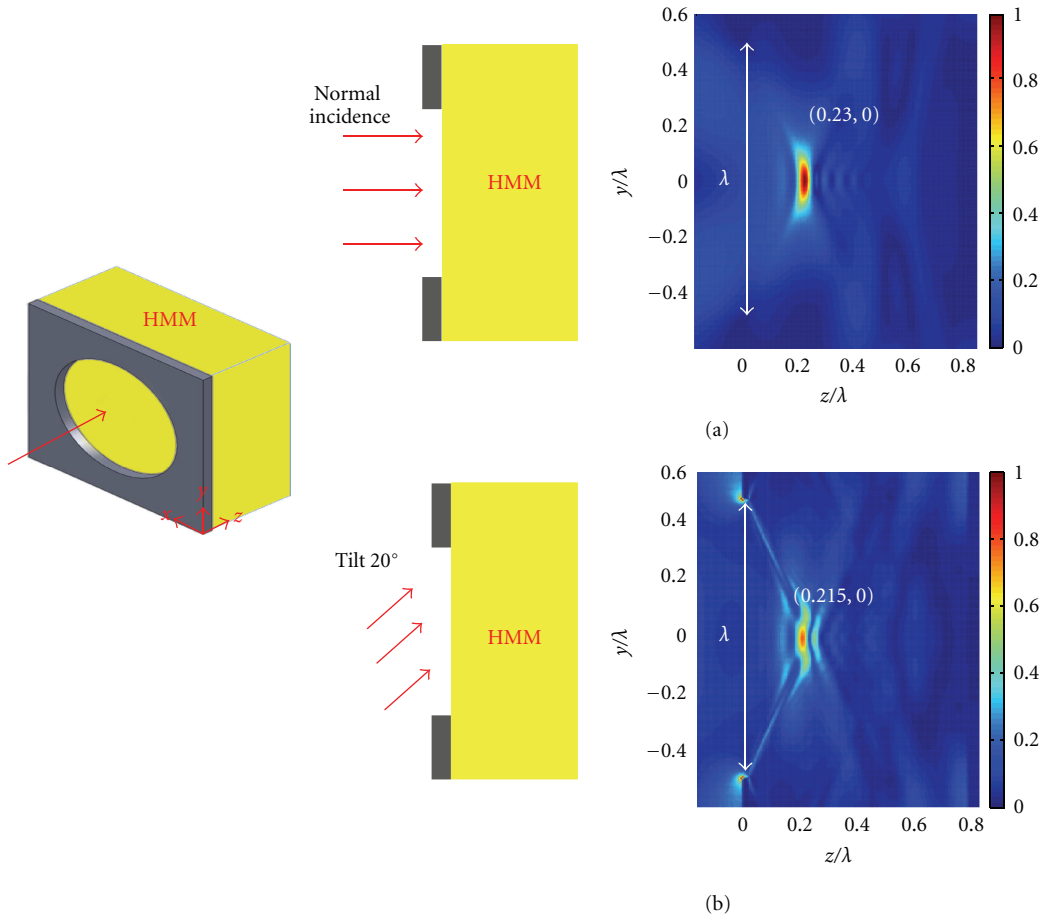

Figure 3: Numerical simulation results for focusing using HMM (a) at normal incidence (b) with tilt angle of 20°.

used to excite high spatial frequency components. As shown in Figure 2(b), the light from such an aperture propagates in the direction of asymptotes and is focused at the intersection of them. Note that all focused waves in the HMM are propagating waves. This effect can also be extended into three-dimensional (3D) configurations. Thus, the propagation of high spatial frequency components and preferred direction gives us confidence to achieve subwavelength focusing using a slab of a HMM. In contrast, negative refractive index material can make flat lenses, but focusing a broad collimated beam into deep subwavelength spot size may require curved surface area of the lens [23].

Another feature of the lens is that the location of the focused spot is not sensitive to the incident angle. To verify the subwavelength focusing at different incidence angles in a HMM slab, some 3D FDTD simulations were performed using the Lumerical FDTD solution software. In simulations, a HMM medium with the effective permittivity ($\varepsilon_z = -1$, and $\varepsilon_x = 1$) was assumed. The simulations were performed for normal incidence as well as oblique incidence of 20°, and the resulting field distribution is shown in Figures 3(b) and 3(c), respectively. It clearly verifies focusing using the HMM structure at two different incident angles. In addition, the incident angle of the 20° focus spot is shifted only by a small distance. The reason is that the location of the focused spot depends on the material properties, or more specifically the ratio of ε_x (ε_y) and ε_z.

In comparison to NIM, HMMs are easier to fabricate as only permittivity in one direction is required to be negative, and it does not rely on magnetic resonance. In addition, most metamaterials are inherently anisotropic [21, 22, 24]. In this paper, we also present experimental demonstration of deep subwavelength focusing using a HMM. A HMM structure can be realized using wired medium design in which an array of parallel conducting wires are embedded in a matrix of a dielectric material as illustrated in Figure 4(a). The wire medium structure exhibits novel electromagnetic properties in the GHz region. In the wired medium, parallel wires are separated from each other by a certain lattice constant, and, due to this periodic arrangement, the effective plasma frequency (ω_p) can be derived for the collective oscillation of electrons [7, 25] and is given as

$$\omega_p^2 = \frac{2\pi c^2}{a^2 \ln(a/r)}, \tag{4}$$

where a is lattice constant and r is radius of the metal wire. For incident waves with parallel polarization, the wired

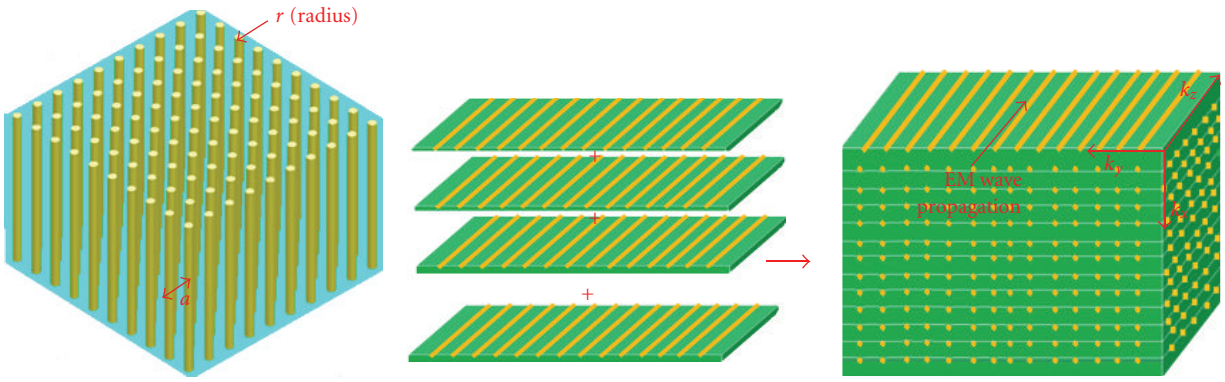

Figure 4: (a) Schematic illustration of a wired medium design. (b) Illustration of the HMM slab structure (yellow-metal wires), green (PCB slab).

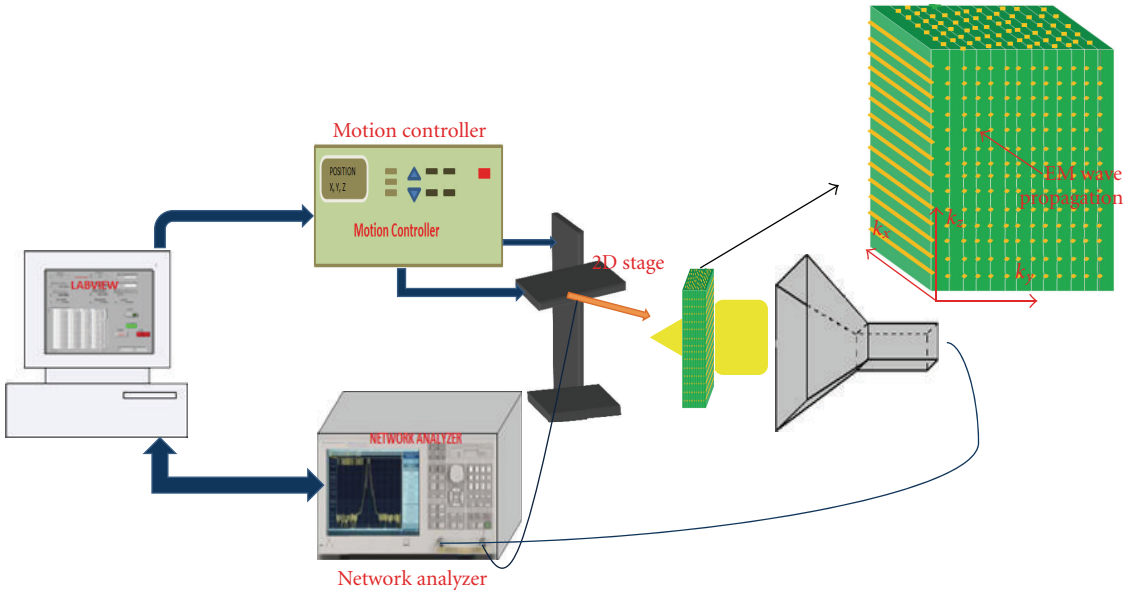

Figure 5: Schematic diagram of the experimental setup for superfocusing in the HMM.

medium can be characterized by an effective permittivity $\varepsilon_z = 1 - (\omega_p^2/\omega^2)$ in the direction of propagation. Below the plasma frequency, dielectric constant (ε_z) becomes negative, and above the plasma frequency the ε_z becomes positive. However, when the electric field is no longer parallel to the wires, the wire medium exhibits spatial dispersion [25]. The geometric parameters used in the HMM design, that is, the wire radius and lattice constant, are much smaller than the free-space wavelength (λ_0) of the incident EM wave. Thus, this medium can be considered as a homogenous effective medium [26]. Printed circuit boards (PCBs) were used as dielectric, and copper was used as metal wires which behave as perfect electric conductor (PEC) at microwave frequencies. Very thin metal wires are embedded periodically on top of a PCB slab of thickness a. These copper wires were etched on the top surface of the PCB and run parallel to the breadth of the board. The radius of copper wire used was approximately 0.1 mm, and the resulting lattice constant of the structure was $a = 2$ mm. The dimensions of a single PCB plate are 12 cm × 2.5 cm × 0.2 cm. Then 65 such slabs were stacked on top of each other to act equivalently to a wired medium structure as shown in Figure 4(b). The permittivity along the direction of propagation ε_z is −37.49 for a plasma frequency of 34.58 GHz which is calculated using (4). In the experimental setup (Figure 5), a collimated beam from a horn antenna is incident on the HMM slab along the direction of metal wires. The antenna was directly fed by a coaxial cable from a vector network analyzer with frequency ranging from 4.0 to 5.8 GHz. A circular aperture mask of diameter 80 mm was made out of aluminum so as to define the input beam and excite high spatial frequency components at the aperture edge. The center position of the slab and the transmitted beam is aligned up to act as the reference under the normal incidence.

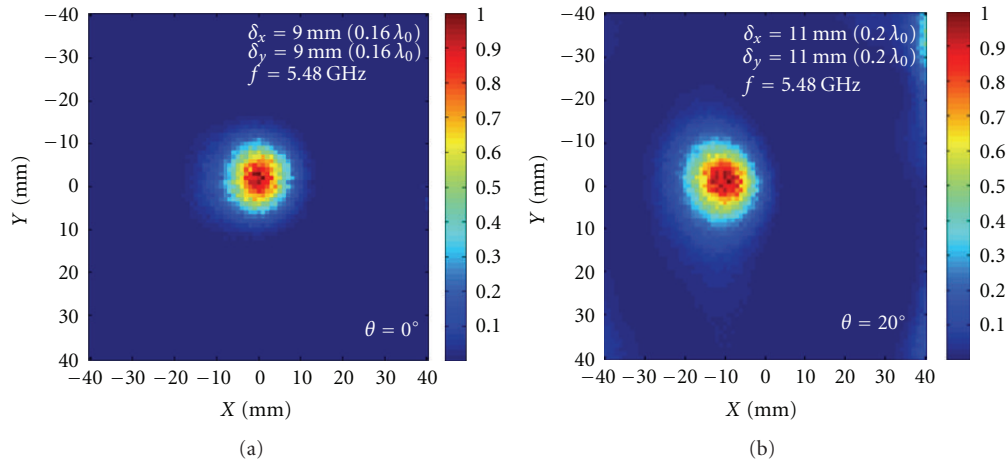

FIGURE 6: (a) Experimental verification of focusing a broad collimated (Φ80 mm) beam to a spot size of 9 mm × 9 mm ($\lambda_0/6$) at normal incidence. (b) Focusing to 11 mm × 11 mm ($\lambda_0/5$) at oblique incidence.

The electromagnetic waves transmitted through the slab are mapped by a near-field scanning probe which was controlled by a motion controller via LabVIEW programming. The measurements were done in x and y directions, and the best quality of focusing was observed at 5.48 GHz. It was verified that light from a larger apperture size (Φ80 mm) can be focused to deep-subwavelength image size of 9 × 9 mm which is approximately $\lambda_0/6$ at normal incidence and 11 × 11 mm ($\lambda_0/5$) at incidence angle of 20°. The experimental results are shown in Figures 6(a) and 6(b). However, we had done experiments at different incident angles that is at 20°, 30°, and 40° and found that focusing is achieved at all the angles, and the focus will be shifted accordingly. The greater the tilt angle, the greater the shift in focus. If the size of aperture is further reduced, focusing was still observed but with a different focal length. Thus, the wire medium supports the transmission of propagating modes for any angle of incidence.

In conclusion, we reported super focusing (power concentration) using a HMM based on a wired medium design. This focusing was verified both numerically and experimentally at gigahertz frequencies with different angles of incidence. It is experimentally verified that higher spatial frequency components can be excited using a sharp apperture for a broad collimated beam. The subwavelength focusing of $\lambda_0/6$ has been demonstrated. This is possible due to coupling of higher spatial frequency components into the preferred directions of propagation inside a HMM. The present realization of the HMM using wire medium is advantageous at microwave frequencies. This phenomenon can be further explored for applications in nanolithography, optical tweezers, solar cells, nanowaveguide coupler, and optical storage.

Acknowledgments

Acknowledgment is made to the Donors of the American Chemical Society Petroleum Research Fund for partial support of this research and RIT Research Computing for technical support. The numerical simulation was based on FDTD solutions from Lumerical Solution, Inc. (http://www.lumerical.com/).

References

[1] V. G. Veselago, "The electrodynamics of substances with simultaneously negative values of ε and μ," *Soviet Physics Uspekhi*, vol. 10, pp. 509–514, 1968.

[2] J. B. Pendry, "Negative refraction makes a perfect lens," *Physical Review Letters*, vol. 85, no. 18, pp. 3966–3969, 2000.

[3] R. A. Shelby, D. R. Smith, and S. Schultz, "Experimental verification of a negative index of refraction," *Science*, vol. 292, no. 5514, pp. 77–79, 2001.

[4] A. A. Houck, J. B. Brock, and I. L. Chuang, "Experimental observations of a left-handed material that obeys Snell's law," *Physical Review Letters*, vol. 90, no. 13, Article ID 137401, 4 pages, 2003.

[5] X. Zhang and Z. Liu, "Superlenses to overcome the diffraction limit," *Nature Materials*, vol. 7, no. 6, pp. 435–441, 2008.

[6] N. Fang, H. Lee, C. Sun, and X. Zhang, "Sub-diffraction-limited optical imaging with a silver superlens," *Science*, vol. 308, no. 5721, pp. 534–537, 2005.

[7] J. B. Pendry, A. J. Holden, W. J. Stewart, and I. Youngs, "Extremely low frequency plasmons in metallic mesostructures," *Physical Review Letters*, vol. 76, no. 25, pp. 4773–4776, 1996.

[8] A. Berrier, M. Mulot, M. Swillo et al., "Negative refraction at infrared wavelengths in a two-dimensional photonic crystal," *Physical Review Letters*, vol. 93, no. 7, Article ID 073902, 4 pages, 2004.

[9] C. Luo, S. G. Johnson, J. D. Joannopoulos, and J. B. Pendry, "Negative refraction without negative index in metallic photonic crystals," *Optics Express*, vol. 11, no. 7, pp. 746–754, 2003.

[10] M. Born and E. Wolf, *Principles of Optics: Electromagnetic Theory of Propagation, Interference and Diffraction of Light*, Cambridge University Press, 7th edition, 1999.

[11] J. O. Dimmock, "Losses in left-handed materials," *Optics Express*, vol. 11, no. 19, pp. 2397–2402, 2003.

[12] I. A. Larkin and M. I. Stockman, "Imperfect perfect lens," *Nano Letters*, vol. 5, no. 2, pp. 339–343, 2005.

[13] D. R. Smith and D. Schurig, "Electromagnetic wave propagation in media with indefinite permittivity and permeability tensors," *Physical Review Letters*, vol. 90, no. 7, Article ID 077405, 4 pages, 2003.

[14] D. R. Smith, P. Kolinko, and D. Schurig, "Negative refraction in indefinite media," *Journal of the Optical Society of America B*, vol. 21, no. 5, pp. 1032–1043, 2004.

[15] M. Cheng and R. Chen, "Large positive and negative lateral shifts from an anisotropic metamaterial slab backed by a metal," *Chinese Physics Letters*, vol. 26, no. 1, Article ID 014101, 2009.

[16] W. Yan, L. Shen, L. Ran, and J. A. Kong, "Surface modes at the interfaces between isotropic media and indefinite media," *Journal of the Optical Society of America A*, vol. 24, no. 2, pp. 530–535, 2007.

[17] L. Zhang, Q. Wang, Y. Zhao, W. Qiao, and J. Zhao, "Surface modes of the sandwhich structure containing indefinite metamaterials," in *Proceedings of the International Conference on Microwave and Millimeter Wave Technology (ICMMT '10)*, pp. 1669–1672, May 2010.

[18] D. R. Smith, D. Schurig, J. J. Mock, P. Kolinko, and P. Rye, "Partial focusing of radiation by a slab of indefinite media," *Applied Physics Letters*, vol. 84, no. 13, pp. 2244–2246, 2004.

[19] R. Wangberg, J. Elser, E. E. Narimanov, and V. A. Podolskiy, "Nonmagnetic nanocomposites for optical and infrared negative-refractive-index media," *Journal of the Optical Society of America B*, vol. 23, no. 3, pp. 498–505, 2006.

[20] Z. Jacob, L. V. Alekseyev, and E. Narimanov, "Optical hyperlens: far-field imaging beyond the diffraction limit," *Optics Express*, vol. 14, no. 18, pp. 8247–8256, 2006.

[21] B. Wood, J. B. Pendry, and D. P. Tsai, "Directed subwavelength imaging using a layered metal-dielectric system," *Physical Review B*, vol. 74, no. 11, Article ID 115116, 8 pages, 2006.

[22] Y. Liu, G. Bartal, and X. Zhang, "All-angle negative refraction and imaging in a bulk medium made of metallic nanowires in the visible region," *Optics Express*, vol. 16, no. 20, pp. 15439–15448, 2008.

[23] J. B. Pendry, "Perfect cylindrical lenses," *Optics Express*, vol. 11, no. 7, pp. 755–760, 2003.

[24] W. Cai, D. A. Genov, and V. M. Shalaev, "Superlens based on metal-dielectric composites," *Physical Review B*, vol. 72, no. 19, Article ID 193101, 4 pages, 2005.

[25] P. A. Belov, R. Marqués, S. I. Maslovski et al., "Strong spatial dispersion in wire media in the very large wavelength limit," *Physical Review B*, vol. 67, no. 11, Article ID 113103, 4 pages, 2003.

[26] J. Elser, R. Wangberg, V. A. Podolskiy, and E. E. Narimanov, "Nanowire metamaterials with extreme optical anisotropy," *Applied Physics Letters*, vol. 89, no. 26, Article ID 261102, 3 pages, 2006.

Hindawi Publishing Corporation
International Journal of Optics
Volume 2012, Article ID 603083, 7 pages
doi:10.1155/2012/603083

Research Article

Tuning Metamaterials for Applications at DUV Wavelengths

Andrew Estroff and Bruce W. Smith

Microsystems Engineering, Rochester Institute of Technology, 77 Lomb Memorial Drive, Rochester, NY 14623, USA

Correspondence should be addressed to Andrew Estroff, ace9411@rit.edu

Received 9 April 2012; Accepted 23 July 2012

Academic Editor: Xiaoyue Huang

Copyright © 2012 A. Estroff and B. W. Smith. This is an open access article distributed under the Creative Commons Attribution License, which permits unrestricted use, distribution, and reproduction in any medium, provided the original work is properly cited.

The unique properties of metamaterials, namely, their negative refractive index, permittivity, or permeability, have gained much recent attention. Research into these materials has led to the realization of a host of applications that may be useful to enhance optical nanolithography. A selection of materials has been examined both experimentally and theoretically to verify their support of surface plasmons, or lack thereof, in the DUV spectrum via the attenuated total reflection (ATR) method using the Kretschmann configuration. At DUV wavelengths, materials that were previously useful at mid-UV and longer wavelengths no longer act as metamaterials. Structured materials comprised of alternating layers of aluminum and aluminum oxide (Al_2O_3), as well as some other absorption-free dielectrics, exhibit metamaterial behavior, as do some elemental materials such as aluminum. These elemental and structured materials exhibit the best properties for use in plasmonic nanolithographic applications. Therefore, a simulator was created to examine material and thickness combinations to generate a tunable metamaterial for use in the DUV. A method for performing plasmonic interference lithography with this metamaterial has been proposed, with calculations showing the potential for half-pitch imaging resolution of 25 nm.

1. Introduction

A surface plasmon (SP) is an electromagnetic wave carried by free electrons that travels along the boundary between a conductor and a dielectric. Surface plasmons were first noticed experimentally in the early 1900s by Wood [1] as anomalous drops in the reflected intensity from metal-backed gratings, but it was not until the 1940s that Fano [2] linked this to earlier theory developed by Sommerfeld [3]. In the late 1950s, Ritchie [4] performed experiments on electron energy losses in thin foils, and Pines and Bohm [5–7] discovered that these losses were due to the excitation of conducting electrons, plasma oscillations they named plasmons [8]. In the 1960s, Kretschmann and Raether [9], as well as Otto [10], developed techniques to optically excite surface plasmons via attenuated total reflection (ATR). It was not until the early 1990s that exponential growth in plasmon research began [11].

In 2000, Pendry [12] showed that Veselago's [13] theoretical negative refractive index slab lens was realizable using a negative permittivity material instead, and that this near field imaging system was enabled by surface plasmons. This discovery encouraged research into plasmonic lithography [14–17].

While the idea of Pendry's perfect lens is of importance and allows deep subwavelength imaging of arbitrary shapes, it requires a complex mask with feature sizes on the same order as those to be imaged. More recently, others have proposed the idea of maskless plasmonic interference lithography, in which two beams are input at opposite sides of a Kretschmann configured prism, creating two counter propagating surface plasmons, resulting in a standing wave [18, 19]. The pitch for this setup is shown in (1) and is dependent upon the permittivity of the prism, incident angle (resonance angle), and the incident wavelength [20]:

$$p = \frac{\lambda_0}{2\sqrt{\varepsilon_d}\sin\theta}. \quad (1)$$

Much of this research has been performed at mid-UV wavelengths, as silver is a near ideal material for use in that spectrum. However, most currently lithography is performed in the DUV spectrum, and it is our goal to examine

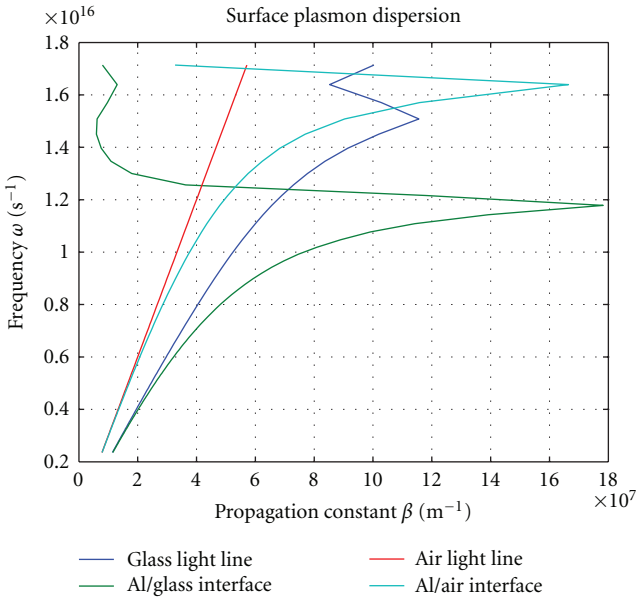

Figure 1: Surface plasmon dispersion curves for Kretschmann ATR configuration, calculated using material properties for Al and SiO_2 from RIT material database [22].

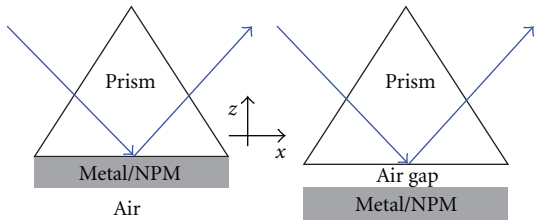

Figure 2: Kretschmann configuration (left), Otto configuration (right).

metamaterials that could be used for plasmonic imaging in this regime.

2. Approach

The dispersion relation for surface plasmons can be obtained by solving the wave equation and is described well in [21]. The resulting surface plasmon dispersion relation for a single interface is

$$\beta = \frac{\omega}{c}\sqrt{\frac{\varepsilon_m \varepsilon_d}{\varepsilon_m + \varepsilon_d}}, \tag{2}$$

where β is the propagation constant, ω is the wave vector of the incident radiation, and ε_m and ε_d are the dielectric functions of the conductor and dielectric. It should be noted that this dispersion relation is only valid for TM polarization (also known as p polarization) states; surface plasmons are not excited by TE polarization. An example of the dispersion relation for SPs is shown in Figure 1.

Equation (2) shows that the propagation constant becomes asymptotic when the dielectric functions are equal

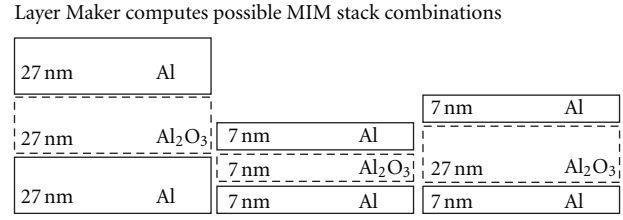

Figure 3: Diagram representing Layer Maker application output.

and opposite in sign, for example, $\varepsilon_m = -\varepsilon_d$. This condition is known as the surface plasmon resonance (SPR). In Figure 1, the red air line represents the dispersion line for radiation in free space, while the SP dispersion curve for the air-metal interface is the light blue curve that lies to the right of it (same convention for glass). At frequencies far below the SPR frequency, the SP propagation constant is relatively small, meaning that the SP wavelength, $\lambda_{sp} = 2\pi/\mathrm{Re}(\beta)$, is only slightly smaller than the incident radiation. As the frequency of the incident radiation increases to the surface plasmon resonance frequency, the propagation constant increases and approaches infinity at the SPR frequency, meaning that the SP wavelength becomes infinitesimally small. For real metals that are not perfect conductors and exhibit some absorption, the dispersion curves do not become entirely asymptotic, and the dispersion curve sharply moves back to a smaller propagation constant (longer wavelength).

It is apparent from the dispersion curves that a surface plasmon on a simple metal-dielectric interface cannot be excited by light due to the SP propagation constant always being larger than the wave vector of light in the dielectric. However, incident light can be phase matched with the SP by means of prism coupling, a technique referred to as ATR, using either the Kretschmann configuration [9], which has the prism and metal film in direct contact (Figure 2(a)), or the Otto configuration [10], in which a dielectric prism and metal are separated by an air gap (Figure 2(b)). In both configurations, phase matching is accomplished by varying the angle of incidence of the TM-polarized radiation, resulting in a sharp decrease in the reflected intensity at some angle beyond the critical angle. The phase matching occurs when the in-plane wave vector of the reflected beam along the metal surface is the same as the propagation constant; this relationship is shown in (3). The only propagation constants available are those that lie between the air and prism light lines (in Figure 1, this would be between air and glass)

$$k_x = k_0 n_p \sin\theta = \beta. \tag{3}$$

The surface plasmon dispersion equation shows that a negative permittivity material is needed in conjunction with a dielectric to support surface plasmons. We have previously shown that aluminum is one of the best candidates for use in the DUV spectrum [23]. However, while it is clear that these results demonstrate aluminum supports surface plasmons in the DUV, they need to be considered in conjunction with the plasmon dispersion equation for this ATR setup. Figure 1 shows the dispersion curves for an ATR configuration with an aluminum film and quartz prism.

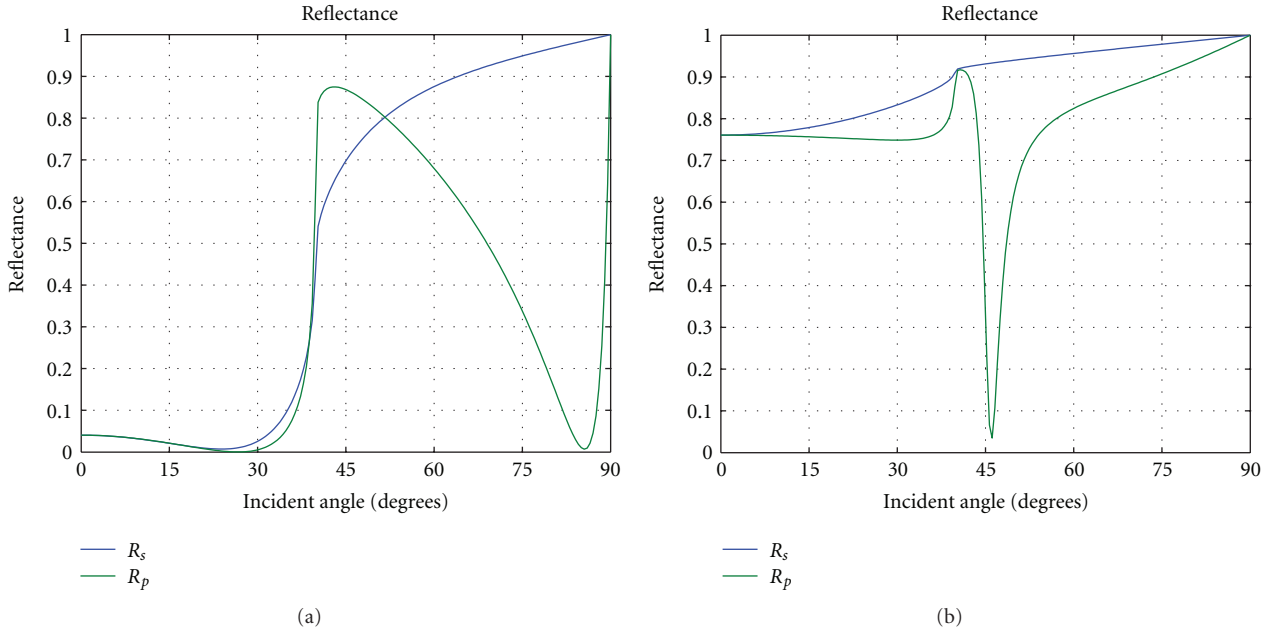

FIGURE 4: ATR results for 7 nm Al, 27 nm Al_2O_3, 7 nm Al stack (left), and single 20 nm Al layer (right).

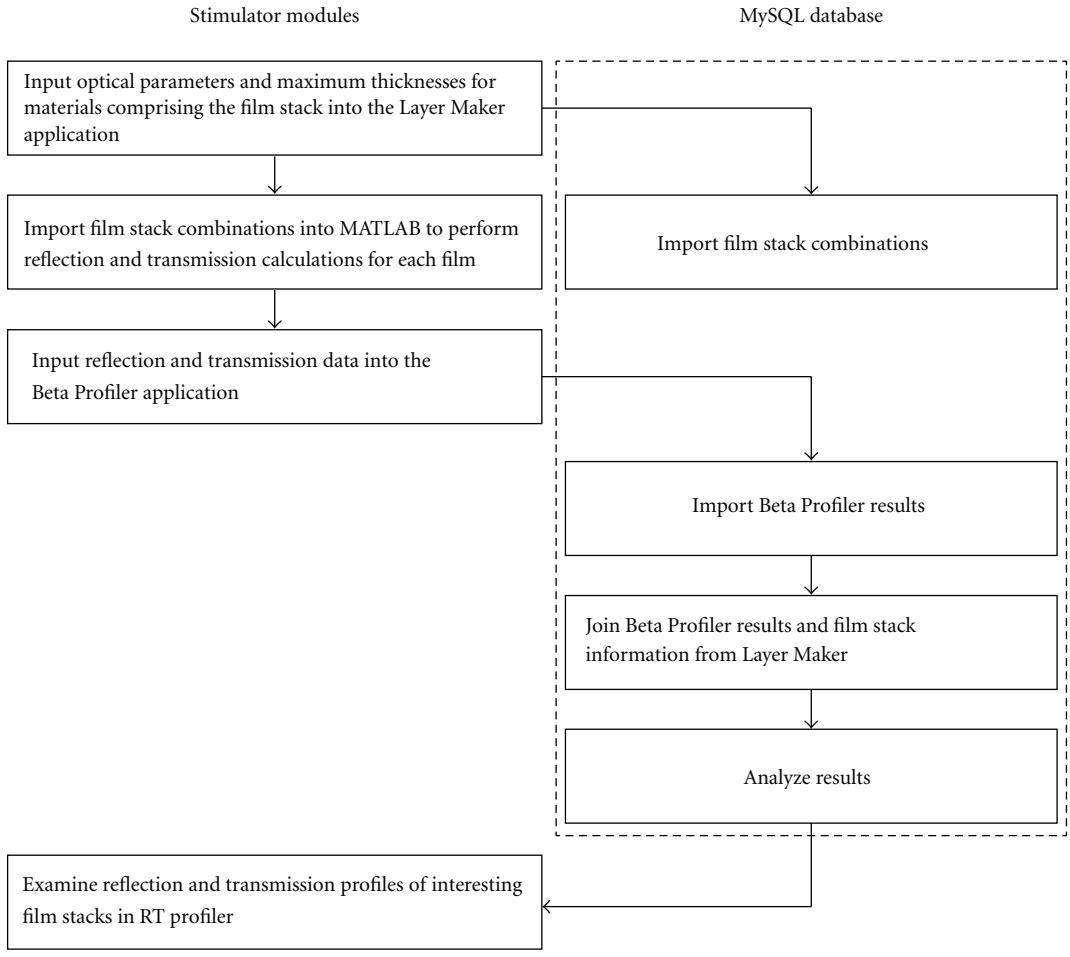

FIGURE 5: Simulator flow chart.

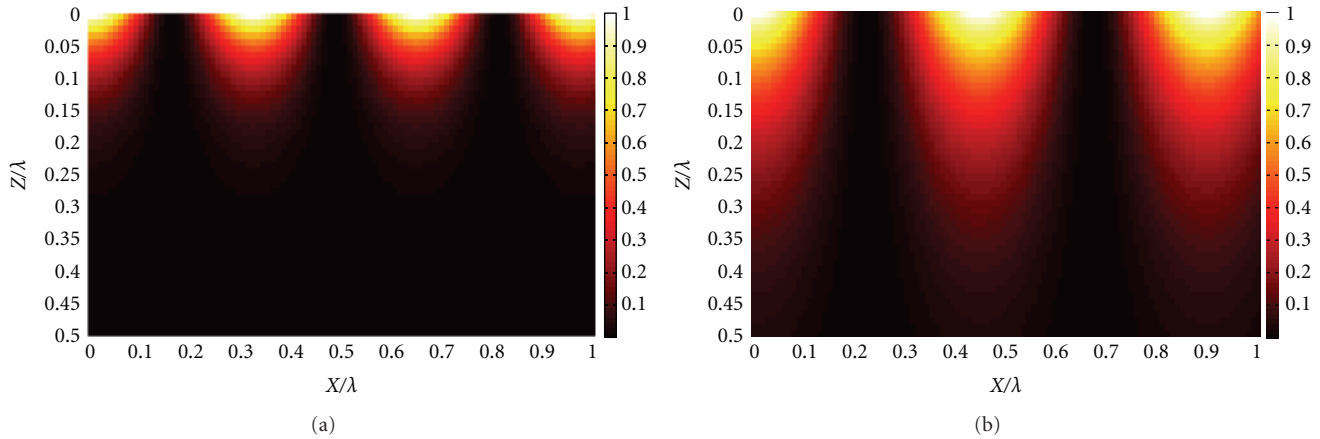

Figure 6: Electric field intensity profiles below a 7 nm-27 nm-7 nm Al-Al_2O_3-Al stack (left) and 20 nm Al film (right) deposited on a quartz prism.

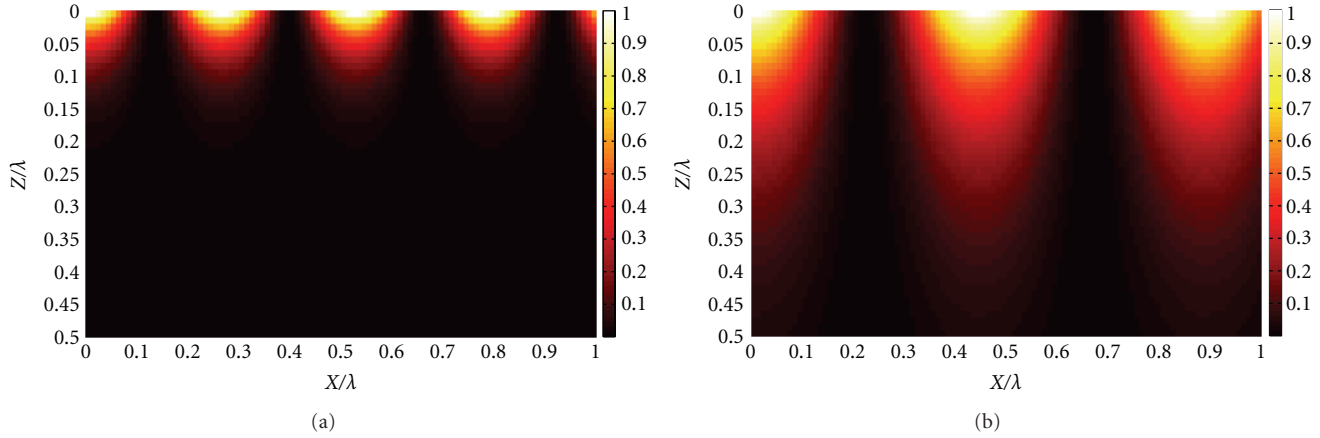

Figure 7: Electric field intensity profiles below 7 nm-34 nm-7 nm Al-Al_2O_3-Al stack (left) and 20 nm Al film (right) deposited on a sapphire prism.

Incident radiation of 193 nm corresponds to an angular frequency of $\sim 9.7 \times 10^{15}\ s^{-1}$, which means that the accessible surface plasmons are of a wavelength very similar to that of the incident radiation (λ_{sp} ~171 nm). Plasmonic interference lithography takes advantage of the fact that at the surface plasmon resonance, the SP wavelength is much smaller than the exciting wavelength. Therefore, a metamaterial needs to be designed to produce a surface plasmon resonance at the desired input frequency.

Pendry has previously demonstrated that it is possible to create a structured material that can be tuned to provide the desired plasma response [24, 25]. Pendry has more recently shown that this structure needs not to be comprised of wires, but that holes in a thin metal film can be designed to provide surface plasmons with arbitrary dispersion [26]. Others have shown that an even simpler design of a layered metal-insulator-metal (MIM) stack can be used to accomplish this [27–31]. Thus, an MIM stack should be examined to provide the desired dispersion characteristics.

Since aluminum is one of the best plasmonic materials in the DUV, and Al_2O_3 is a relatively high-index, absorption-free dielectric, a layered Al-Al_2O_3 system will be examined. A simulator was created to generate and analyze multilayer MIM stacks in order to obtain the largest propagation constants possible, resulting in the shortest plasmon wavelength.

The first module of the simulator is the Layer Maker application, which generates the multilayer stacks to be examined. The refractive index and absorption coefficients of the superstrate (prism), metal, dielectric, and substrate can be input, as well as the maximum total stack thickness to be allowed, the maximum dielectric thickness, and the maximum metal thickness allowed (this is the overall maximum metal thickness, not one individual layer thickness, as it is known in the Kretschmann configuration that if the metal is too thick, SPs cannot couple through it). This application then outputs two files containing all layer combinations within the boundary conditions specified. One file is a MySQL table that will be linked to the output of

Table 1: Joined data in MySQL.

Layer ID	Layers	Metal thick (nm)	Metal count	Dielectric thick (nm)	Dielectric count	Angle (deg)	Reflectance	Beta
15127	3	5	2	28	1	87.51	0.0042	50738563
15156	3	5	2	29	1	87.51	0.0682	50738563
15098	3	5	2	27	1	87.02	0.1021	50717534
15185	3	5	2	30	1	87.02	0.2338	50717534
17574	3	6	2	27	1	87.02	0.0072	50717534
17551	3	6	2	26	1	86.52	0.0358	50692685
17597	3	6	2	28	1	86.52	0.1171	50692685
15214	3	5	2	31	1	86.02	0.3819	50664018
15069	3	5	2	26	1	85.52	0.2362	50631535
17620	3	6	2	29	1	85.52	0.2723	50631535
19837	3	7	2	26	1	85.52	0.0034	50631535
19856	3	7	2	27	1	85.52	0.0898	50631535
15243	3	5	2	32	1	85.03	0.4932	50595239
17528	3	6	2	25	1	85.03	0.1433	50595239
19818	3	7	2	25	1	85.03	0.0348	50595239
17643	3	6	2	30	1	84.53	0.4044	50555133
19875	3	7	2	28	1	84.53	0.2368	50555133
21971	3	8	2	26	1	84.53	0.0294	50555133
15040	3	5	2	25	1	84.03	0.3425	50511218
15272	3	5	2	33	1	84.03	0.5753	50511218
21954	3	8	2	25	1	84.03	0.0040	50511218
21988	3	8	2	27	1	84.03	0.1495	50511218
15301	3	5	2	34	1	83.54	0.6369	50463500
17666	3	6	2	31	1	83.54	0.5052	50463500
19894	3	7	2	29	1	83.54	0.3722	50463500
17505	3	6	2	24	1	83.04	0.2461	50411980
22005	3	8	2	28	1	83.04	0.2939	50411980
23936	3	9	2	26	1	83.04	0.0465	50411980
15330	3	5	2	35	1	82.54	0.6840	50356665
17689	3	6	2	32	1	82.54	0.5813	50356665

the other applications via an identity string assigned to each MIM stack. The second file contains a machine readable instruction file for the second application. An example of this table is shown in Figure 3. It should be noted that this application generates stacks comprised of many layers, not simply a 3-layer MIM stack. We are only examining a 3-layer stack here as it is most likely the easiest to fabricate.

The second application is the Matrix Material Calculator (MMC) and is written in MATLAB. It reads the instruction file from the Layer Maker application and calculates reflection profiles through angle for each generated stack. These calculations are performed using matrix methods described by Macleod [32], shown in (4) through (10). The substrate is air, and the initial medium is the quartz prism. The characteristic admittance of each layer is represented as y_j and consists of the optical parameters of the layer. The oblique optical admittance is represented by η and must be calculated for each polarization state. The film phase factor is δ. The amplitude reflection coefficient ρ can be calculated from the characteristic matrix of the film stack (4), and from this result, the reflectance can be obtained (shown in (10)). With oblique incidence and absorbing materials, care must be taken to ensure that the solutions for η for TE polarization states and δ are in the fourth quadrant to obtain the correct solution (positive real, negative imaginary):

$$\begin{bmatrix} B \\ C \end{bmatrix} = \left\{ \prod_{j=1}^{q} \begin{bmatrix} \cos\delta_j & \dfrac{i\sin\delta_j}{\eta_j} \\ i\eta_j \sin\delta_j & \cos\delta_j \end{bmatrix} \right\} \begin{bmatrix} 1 \\ \eta_{\text{sub}} \end{bmatrix}, \tag{4}$$

$$y_j = n - ik, \tag{5}$$

$$\eta_{j_s} = \sqrt{n_j^2 - k_j^2 - n_0^2 \sin^2\theta_0 - 2in_jk_j}, \tag{6}$$

$$n_{j_p} = \frac{y_j^2}{n_{j_s}}, \tag{7}$$

$$\delta_j = \frac{2\pi d}{\lambda} \sqrt{n_j^2 - k_j^2 - n_0^2 \sin^2\theta_0 - 2in_jk_j}, \tag{8}$$

$$\rho = \frac{y_0 B - C}{y_0 B + C}, \tag{9}$$

$$R = \rho\rho^*. \tag{10}$$

The third application is the Beta Profiler. It analyzes the reflection profiles and calculates the angle at which the

reflection minimum occurs, the reflectance value, and the value of the propagation constant (from (3)). This data is also stored in a MySQL table. By itself, this data is not inherently useful. However, using join statements in MySQL, this data can be merged with the table from the Layer Maker application and sorted to display results that are useful.

Since outputs of the MMC and the Beta Profiler are stored in a MySQL databases it is possible to quickly sort though the data to find optimal cases and analyze the results. An example of a joined output from the Layer Maker and Beta Profiler is shown in Table 1.

The fourth application is the RT Profiler, which is uses the Layer ID to test cases that appear promising. The results shown in Figure 4 are the output of the RT Profiler application. They show that a 3-layer stack comprised of 7 nm-27 nm-7 nm of Al-Al_2O_3-Al yields a metamaterial with a shorter plasmon wavelength than is capable with just aluminum (124 nm compared to 171 nm). A summary of the simulator is shown in the flow chart in Figure 5.

Since the final layer of the tunable metamaterial proposed is Al, it is understood that it will oxidize. The Layer Maker application has been modified to allow an asymmetric stack to be simulated. This makes it possible to simulate our metamaterial stack with a surface oxide layer present, or with a capping material comprised of some other element that may offer more desirable optical properties than an aluminum oxide.

There are several benefits of this simulation approach. Firstly, this matrix method of calculation provides fast results. Simulations of 1 single-layer ATR stack in FDTD software took on the order of a minute to complete. Using this matrix method-based simulator, 50,000 different thin film stack combinations were completed in approximately 90–120 minutes. Secondly, it is quite flexible. Any optical constants desired can be input, and it has been modified further to allow for an asymmetric stack to be input. It has also been modified to allow the optical parameters and thicknesses to vary in order to help model errors that will be seen during fabrication. The joined output data allows one to see the fabrication tolerances allowed to achieve an acceptable result.

The thin film matrix calculations used throughout this document can also be used to calculate the electric field intensity below the stack, which would be representative of imaging possible for plasmonic interference nanolithography. Results for the configurations in Figure 4 are shown in Figure 6. The resulting pitches of 62 nm and 84 nm are similar to those calculated using (1).

If a higher index prism is used, an even smaller plasmon wavelength can be achieved. Figure 7 shows the electric field intensity for a 7 nm-34 nm-7 nm Al-Al_2O_3-Al stack using a sapphire prism ($n = 1.92$), resulting in a 50 nm pitch (the ATR profile is nearly identical to that for the quartz prism example shown in Figure 4). The resulting pitch for the 20 nm Al film with the sapphire prism is still nearly identical to that with the quartz prism, due to the fact that the higher index of the prism is offset by a 10° shift, from ~46° down to ~36°, in the resonance angle.

3. Conclusion

Little research in metamaterials and plasmonics has been done in the DUV spectrum. This paper demonstrates a simulator developed using thin film matrix methods to create tunable metamaterials for the DUV spectrum. It showed that a quartz prism coated with a 7 nm-27 nm-7 nm Al-Al_2O_3-Al thin film stack or a sapphire prism coated with 7 nm-34 nm-7 nm Al-Al_2O_3-Al is possible solutions, providing more desirable propagation constants, and thus shorter plasmon wavelengths for use in DUV plasmonic interferometric imaging.

References

[1] R. W. Wood, "On a remarkable case of uneven distribution of light in a diffraction grating spectrum," *Philisophical Magazine*, vol. 4, pp. 396–402, 1902.

[2] U. Fano, "The theory of anomalous diffraction gratings and of quasi-stationary waves on metallic surfaces (sommerfeld's waves)," *Journal of the Optical Society of America*, vol. 31, no. 3, pp. 213–222, 1941.

[3] A. Sommerfeld, "Ueber die fortpflanzung elektrodynamischer wellen längs eines drahtes," *Annalen der Physik*, vol. 303, no. 2, pp. 233–290, 1899.

[4] R. H. Ritchie, "Plasma losses by fast electrons in thin films," *Physical Review*, vol. 106, no. 5, pp. 874–881, 1957.

[5] D. Bohm and D. Pines, "A collective description of electron interactions. i. magnetic interactions," *Physical Review*, vol. 82, no. 5, pp. 625–634, 1951.

[6] D. Pines and D. Bohm, "A collective description of electron interactions: ii. Collective vs individual particle aspects of the interactions," *Physical Review*, vol. 85, no. 2, pp. 338–353, 1952.

[7] D. Bohm and D. Pines, "A collective description of electron interactions: III. Coulomb interactions in a degenerate electron gas," *Physical Review*, vol. 92, no. 3, pp. 609–625, 1953.

[8] C. T. Walker, "Who named the -oN's?" *American Journal of Physics*, vol. 38, p. 1380, 1970.

[9] E. Kretschmann and H. Raether, "Radiative decay of non radiative surface plasmons excited by light," *Zeitschrift Fur Naturforschung*, vol. 23A, pp. 2135–2136, 1968.

[10] A. Otto, "Excitation of nonradiative surface plasma waves in silver by the method of frustrated total reflection," *Zeitschrift für Physik*, vol. 216, no. 4, pp. 398–410, 1968.

[11] M. L. Brongersma and P. G. Kik, *Surface Plasmon Nanophotonics*, vol. 131, Springer, 2007.

[12] J. B. Pendry, "Negative refraction makes a perfect lens," *Physical Review Letters*, vol. 85, no. 18, pp. 3966–3969, 2000.

[13] V. G. Veselago, "The electrodynamics of substances with simultaneously negative values of epsilon and mu," *Soviet Physics Uspekhi*, vol. 10, no. 4, pp. 509–514, 1968.

[14] N. Fang, H. Lee, C. Sun, and X. Zhang, "Sub-diffraction-limited optical imaging with a silver superlens," *Science*, vol. 308, no. 5721, pp. 534–537, 2005.

[15] R. J. Blaikie and D. O. S. Melville, "Imaging through planar silver lenses in the optical near field," *Journal of Optics A*, vol. 7, no. 2, pp. S176–S183, 2005.

[16] D. O. S. Melville and R. J. Blaikie, "Super-resolution imaging through a planar silver layer," *Optics Express*, vol. 13, no. 6, pp. 2127–2134, 2005.

[17] D. O. S. Melville and R. J. Blaikie, "Analysis and optimization of multilayer silver superlenses for near-field optical lithography," *Physica B*, vol. 394, no. 2, pp. 197–202, 2007.

[18] X. Guo and Q. Dong, "Coupled surface plasmon interference lithography based on a metal-bounded dielectric structure," *Journal of Applied Physics*, vol. 108, no. 11, Article ID 113108, 2010.

[19] K. V. Sreekanth and V. M. Murukeshan, "Large-area maskless surface plasmon interference for one- and two-dimensional periodic nanoscale feature patterning," *Journal of the Optical Society of America A*, vol. 27, no. 1, pp. 95–99, 2010.

[20] A. Passian, A. Wig, A. L. Lereu et al., "Probing large area surface plasmon interference in thin metal films using photon scanning tunneling microscopy," *Ultramicroscopy*, vol. 100, no. 3-4, pp. 429–436, 2004.

[21] S. A. Maier, *Plasmonics: Fundamentals and Applications*, Springer, 2007.

[22] "RIT Nanolithograpy Research Labs > Optical Properties of Thin Films," http://www.rit.edu/kgcoe/microsystems/lithography/thinfilms/thinfilms/thinfilms.html.

[23] A. Estroff, N. V. Lafferty, P. Xie, B. W. Smith et al., "Metamaterials for enhancement of DUV lithography," in *Optical Microlithography XXIII*, vol. 7640 of *Proceedings of the SPIE*, pp. 76402W–76402W-10, 2010.

[24] J. B. Pendry, A. J. Holden, D. J. Robbins, and W. J. Stewart, "Low frequency plasmons in thin-wire structures," *Journal of Physics Condensed Matter*, vol. 10, no. 22, pp. 4785–4809, 1998.

[25] J. B. Pendry, A. J. Holden, W. J. Stewart, and I. Youngs, "Extremely low frequency plasmons in metallic mesostructures," *Physical Review Letters*, vol. 76, no. 25, pp. 4773–4776, 1996.

[26] J. B. Pendry, L. Martín-Moreno, and F. J. Garcia-Vidal, "Mimicking surface plasmons with structured surfaces," *Science*, vol. 305, no. 5685, pp. 847–848, 2004.

[27] E. N. Economou, "Surface plasmons in thin films," *Physical Review*, vol. 182, no. 2, pp. 539–554, 1969.

[28] K. R. Welford and J. R. Sambles, "Coupled surface plasmons in a symmetric system," *Journal of Modern Optics*, vol. 35, no. 9, pp. 1467–1483, 1988.

[29] G. J. Kovacs and G. D. Scott, "Optical excitation of surface plasma waves in layered media," *Physical Review B*, vol. 16, no. 4, pp. 1297–1311, 1977.

[30] G. J. Kovacs and G. D. Scott, "Attenuated total reflection angular spectra of a system of alternating plasma-dielectric layers," *Applied Optics*, vol. 17, no. 22, pp. 3627–3635, 1978.

[31] R. Yang, X. Huang, and Z. Lu, "Arbitrary super surface modes bounded by multilayered metametal," *Micromachines*, vol. 3, no. 1, pp. 45–54, 2012.

[32] H. A. Macleod, *Thin-Film Optical Filters*, CRC Press, 2001.

Hindawi Publishing Corporation
International Journal of Optics
Volume 2012, Article ID 532316, 19 pages
doi:10.1155/2012/532316

Research Article

Green Function Formulism for Electromagnetic Wave Generated in Nanostructured Metamaterial of Finite Thickness: Isotropy and Anisotropy

Shunbo Li,[1] Xiao Xiao,[1] Bo Hou,[2] and Weijia Wen[1]

[1] *Department of Physics, The Hong Kong University of Science and Technology, Clear Water Bay, Kowloon, Hong Kong*
[2] *School of Physical Science and Technology, Suzhou University, No. 1 Shizi Street, Jiangsu, Suzhou 215006, China*

Correspondence should be addressed to Weijia Wen, phwen@ust.hk

Received 31 May 2012; Accepted 2 July 2012

Academic Editor: Zhaolin Lu

Copyright © 2012 Shunbo Li et al. This is an open access article distributed under the Creative Commons Attribution License, which permits unrestricted use, distribution, and reproduction in any medium, provided the original work is properly cited.

A Green function formulism is developed to calculate the electromagnetic fields generated by sources embedded in nanostructured medium which could be represented by an effective electric permittivity tensor with finite thicknesses. The method begins with the decomposition of the generated mode into the eigenmodes in the medium, which have definite dispersions. To account the interface effect at boundaries, especially the mode conversion at the interface between anisotropic media, mode expansion method is combined into the theoretical framework. Thus, the electromagnetic wave in any given position can be gotten clearly. The formulism can provide conveniences of studying the novel properties of nanostructured metamaterials.

1. Introduction

Artificially constructed metamaterials [1, 2] have unique electromagnetic properties which cannot be obtained in natural materials, such as artificial magnetism, negative refraction [3], and near-field focusing [4]. Recently, active research areas related to metamaterials attracted much attention [5, 6], for instance, high/low epsilon metamaterials, designer dispersion, transformation optics metamaterials, switchable metamaterials, amplifying metamaterials, sensor metamaterials, nonlinear metamaterials, and quantum metamaterials [7]. The origin of novel property of structured metamaterial comes from the modification of effective permittivity and permeability. There are many developed methods to determine the effective permittivity and permeability [8, 9]. Nanostructured metamaterials have wide applications in real world, such as manipulation of thermal radiation [10], plasmonic biosensor [11], artificial magnetic material [12], and superlens imaging [13]. Patterned metal at the interface between two media will generate surface-plasmon polaritons which alter surface waves and subsequently change radiative heat transfer, coherence properties, and Casimir forces [14].

To obtain the electromagnetic property of a nanostructured metamaterial, one would have to calculate Green function of the given system [15, 16]. The conventional formulism [17] can handle homogeneous isotropic media very well, and the interface effects can be trivially accounted by introducing Fresnel coefficients. However, a lot of metamaterials exhibit anisotropy properties due to the special arrangement of structure [18]. Thus, the story becomes quite complex, when anisotropy of media is introduced. One distinguishing phenomenon of anisotropic media is the mode conversion [19, 20] happening at the interface between anisotropic media. Under the situation, the previous formulism is no longer suitable and convenient, since the mode conversion leads to an infinite multiplication for the Fresnel transmission and reflection coefficients. Thus, to study the coherence property of thermally radiative field from anisotropic media consisted by subwavelength structures with finite thickness, we have firstly to build up a general Green function theory working well in both isotropic media and anisotropic media. Exactly the motivation drives us to the present work. Since the development of metamaterial and nanooptics paves the way to design innovative structures, we herein proposed a Green function

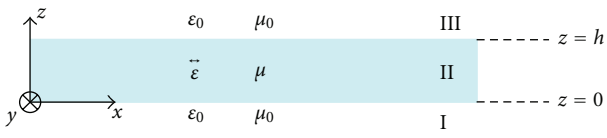

Figure 1: Schematic illustration of the geometry of the system under considering shows the thickness (h) of the anisotropic (isotropic) layer and the coordinate system.

method to calculate electromagnetic wave generated by a structured metamaterials which have definite permittivity and permeability. In the following sections, we will firstly present our formulism for an arbitrary anisotropic medium with finite thickness in Section 2. To prove the correction of the method, we apply it to an isotropic medium case to recover the results in [17] in the same section. In Section 3, the Green functions linking spatial fields and sources in uniaxial and biaxial medium of finite thickness are calculated by following the general formulism shown in Section 2. A brief conclusion remark is made in the last section.

2. Theoretical Formulism and Its Correction

To begin with, we consider a piece of anisotropic medium with a finite thickness h placed in vacuum (Figure 1), so that random sources locate only in the anisotropic medium. In the present work, it is assumed the relative permittivity tensor is anisotropic but its relative permeability is isotropic (the current formulism can be applied to the case that both permittivity and permeability are anisotropic, but we stay at the current situation to achieve a better demonstration of the formulism), and they can be written as:

$$\overleftrightarrow{\varepsilon} = \begin{pmatrix} \varepsilon_1 & 0 & 0 \\ 0 & \varepsilon_2 & 0 \\ 0 & 0 & \varepsilon_3 \end{pmatrix}, \qquad \mu = \mu. \tag{1}$$

The relative permittivity and relative permeability of vacuum are equal to 1. Once the information is given, for a given frequency the electromagnetic property is totally governed by Maxwell equations [17]:

$$\begin{aligned} \nabla \cdot \left(\overleftrightarrow{\varepsilon}_r \cdot \vec{E}\left(\vec{r}\right)\right) &= -4\pi \nabla \cdot \vec{P}\left(\vec{r}\right), \\ \nabla \times \vec{B}\left(\vec{r}\right) + i\tilde{\omega}\mu_r \overleftrightarrow{\varepsilon}_r \cdot \vec{E}\left(\vec{r}\right) &= -i4\pi\tilde{\omega}\mu_r \vec{P}\left(\vec{r}\right) \\ &\quad + 4\pi\mu_r \nabla \times \vec{M}\left(\vec{r}\right) \\ \nabla \cdot \vec{B}\left(\vec{r}\right) &= 0 \\ \nabla \times \vec{E}\left(\vec{r}\right) - i\tilde{\omega}\vec{B}\left(\vec{r}\right) &= 0, \end{aligned} \tag{2}$$

where $\overleftrightarrow{\varepsilon}_r$ represents the relative permittivity tensor in different regions shown in Figure 1, μ_r means the permeability in different regions, $\tilde{\omega}$ represents ω/c (angular frequency over velocity of light in vacuum), $\vec{P}\ (\vec{r})$ denotes the random electric dipole source distribution in space, and $\vec{M}\ (\vec{r})$ is for random magnetic dipole source distribution.

2.1. Propagation Property in Homogeneous Medium. One can extract the information about the eigen-plane-wave modes and their corresponding dispersion relations by doing operations on the homogeneous Maxwell equations (dropping the source terms about $\vec{P}$ and $\vec{M}$), and one has

$$\nabla \times \left(\nabla \times \vec{E}\left(\vec{r}\right)\right) - \tilde{\omega}^2 \mu_r \overleftrightarrow{\varepsilon}_r \cdot \vec{E}\left(\vec{r}\right) = 0. \tag{3}$$

Taking into account the plane wave ansatz, we can have the matrix equation determining the eigenmodes for given regions:

$$\begin{pmatrix} \tilde{\omega}^2\varepsilon_x\mu_r - k_y^2 - k_z^2 & k_x k_y & k_x k_z \\ k_x k_y & \tilde{\omega}^2\varepsilon_y\mu_r - k_x^2 - k_z^2 & k_y k_z \\ k_x k_z & k_y k_z & \tilde{\omega}^2\varepsilon_z\mu_r - k_y^2 - k_x^2 \end{pmatrix} \times \begin{pmatrix} E_x \\ E_y \\ E_z \end{pmatrix} = 0, \tag{4}$$

where $\varepsilon_x = \varepsilon_1$, $\varepsilon_y = \varepsilon_2$, $\varepsilon_z = \varepsilon_3$ in region II, $\varepsilon_x = \varepsilon_y = \varepsilon_z = 1$ in regions I and III, $\mu_r = \mu$ in region II, and $\mu_r = 1$ in regions I and III. For a nontrivial mode in the medium, the determinant of the coefficient matrix in (4) should vanish. Taking the homogeneous form of the first Maxwell equation in (2) as a constraint, the equation determining eigenmodes is arrived at

$$\begin{aligned} \tilde{\omega}^4 - \tilde{\omega}^2 &\left(\frac{k_x^2 + k_y^2}{\varepsilon_z\mu_r} + \frac{k_x^2 + k_z^2}{\varepsilon_y\mu_r} + \frac{k_z^2 + k_y^2}{\varepsilon_x\mu_r} \right) \\ &+ \left(\frac{k_x^2}{\varepsilon_y\varepsilon_z{\mu_r}^2} + \frac{k_y^2}{\varepsilon_x\varepsilon_z\mu_r^2} + \frac{k_z^2}{\varepsilon_x\varepsilon_y\mu_r^2} \right) \\ &\times \left(k_x^2 + k_z^2 + k_y^2 \right) = 0. \end{aligned} \tag{5}$$

From (5) $k_z(\tilde{\omega}, k_x, k_y)$ can be solved out as the function of $\tilde{\omega}$, k_x and k_y, and there are 4 solutions for k_z, namely, $\{k_{z,1}, -k_{z,1}; k_{z,2}, -k_{z,2}\}$ ($k_{z,1}$ and $k_{z,2}$ are positive real or positive imaginary numbers to denote the wave propagating or decaying along the positive z direction.). To get the corresponding polarizations of the eigenmodes, we can solve (4) with the help of the homogeneous form of the first Maxwell equation in (2) and the corresponding dispersion relation of the given eigenmode $k_{z,i}^2 - [k_{z,i}(\tilde{\omega}, k_x, k_y)]^2 = 0$, where the index i is 1 (2), when we solve the corresponding polarization of the first (second) eigenmode. For the convenience, we denote the unit vectors of them by $\hat{e}_{1,\pm}$ and $\hat{e}_{2,\pm}$, and conveniently the corresponding unit vectors of electric displacement vectors and magnetic field vectors are gotten by $\hat{d}_{i,\pm} = \overleftrightarrow{\varepsilon}_r \cdot \hat{e}_{i,\pm} / |\overleftrightarrow{\varepsilon}_r \cdot \hat{e}_{i,\pm}|$ and $\hat{h}_{i,\pm} = \vec{k}_\pm \times \hat{e}_{i,\pm} / |\vec{k}_\pm \times \hat{e}_{i,\pm}|$. Then physics of propagating wave in the medium is quite clear: for propagating wave in the medium with arbitrary polarization its electric displacement vector is always perpendicular to wave vector; from the previous

analysis, the electric displacement vector can be always decomposed in the plane perpendicular to the wave vector $\vec{k}$ into two components along $\hat{d}_1$ and $\hat{d}_2$, respectively. These two components obey different but definite dispersions, once the three parameters ($\tilde{\omega}$, k_x, and k_y) are known.

2.2. Treatment of Sources. We now restore the source terms in Maxwell equations so that sources enter the picture. The analysis in the last section illuminates that the property of propagating modes in one medium is totally clear, when any three parameters of $\tilde{\omega}$, k_x, k_y, and k_z are determined. On the other hand, when the spatial distribution and time evolution of the random sources are known, Fourier transformation can always help us to count the modes in a desired way (since we have limited in a given frequency case, $\tilde{\omega}$ is known now):

$$\begin{aligned}\vec{P}\left(\vec{r}\right) &= \sum_{i=1,2}\int dz_0 e^{\mp ik_{z,i}z_0}\int \frac{d\vec{k}}{(2\pi)^3}\vec{P}_{\vec{k}_i}e^{i\vec{k}_i\cdot\vec{r}}\\ &= \int dz_0\int\frac{d\vec{\kappa}}{(2\pi)^2}\delta(z-z_0)\vec{P}_{\vec{\kappa}}e^{i\vec{\kappa}\cdot\vec{R}},\\ \vec{M}\left(\vec{r}\right) &= \sum_{i=1,2}\int dz_0 e^{\pm ik_{z,i}z_0}\int \frac{d\vec{k}}{(2\pi)^3}\vec{M}_{\vec{k}_i}e^{i\vec{k}_i\cdot\vec{r}}\\ &= \int dz_0\int\frac{d\vec{\kappa}}{(2\pi)^2}\delta(z-z_0)\vec{M}_{\vec{\kappa}}e^{i\vec{\kappa}\cdot\vec{R}},\end{aligned} \tag{6}$$

where $z_0 \in [0,h]$, since there should be no random sources in vacuum. Here and below it is convenient to put $\vec{R} = (x,y)$. Such a transformation has clear physical meanings: the modes generated from sources are counted according to their tangential wave vectors, and to make the classification possible the price of cutting the medium into planes along z direction is paid. The advantage of the classification is obvious: for each mode generated we can decompose it into two eigenmodes with definite dispersion relations and the same tangential wave vector.

Similarly, the electromagnetic field of a given position in space can be expressed as

$$\begin{aligned}\vec{E}\left(\vec{R},z\right) &= \int\frac{d\vec{\kappa}}{(2\pi)^2}\,\vec{E}\left(\vec{\kappa},z\right)\exp\left(i\,\vec{\kappa}\cdot\vec{R}\right),\\ \vec{B}\left(\vec{R},z\right) &= \int\frac{d\vec{\kappa}}{(2\pi)^2}\,\vec{B}\left(\vec{\kappa},z\right)\exp\left(i\,\vec{\kappa}\cdot\vec{R}\right),\end{aligned} \tag{7}$$

where

$$\begin{aligned}\vec{E}\left(\vec{\kappa},z\right) &= \int dz_0\,\overleftrightarrow{G}_{EP}\left(\vec{\kappa};z-z_0\right)\vec{P}\left(\vec{\kappa},z_0\right)\\ &\quad+\int dz_0\,\overleftrightarrow{G}_{EM}\left(\vec{\kappa};z-z_0\right)\vec{M}\left(\vec{\kappa},z_0\right),\\ \vec{B}\left(\vec{\kappa},z\right) &= \int dz_0\,\overleftrightarrow{G}_{BP}\left(\vec{\kappa};z-z_0\right)\vec{P}\left(\vec{\kappa},z_0\right)\\ &\quad+\int dz_0\,\overleftrightarrow{G}_{BM}\left(\vec{\kappa};z-z_0\right)\vec{M}\left(\vec{\kappa},z_0\right).\end{aligned} \tag{8}$$

In (8), $\overleftrightarrow{G}_{EP}$, $\overleftrightarrow{G}_{BP}$, $\overleftrightarrow{G}_{BM}$, and $\overleftrightarrow{G}_{BM}$ are Green functions linking the field in space with the source for a given tangential wave vector $\vec{\kappa}$. Once getting the relation between fields in space and source, the forms of Green functions are determined spontaneously. Because of the linearity of Maxwell equation, we can focus to one mode with tangential wave vector $\vec{\kappa}$ generated from a source plane labeled as z_0, and to account all modes one needs only to integrate all $\vec{\kappa}$ and z dimensions of the anisotropic medium.

2.3. Mode Expansion in Each Region. To determine the field generated from source plate locating at z_0 with tangential wave vector $\vec{\kappa}$, the mode expansion method would be found useful [21, 22]. Since we have assumed the anisotropy of permeability and isotropy of permittivity, mode expansion according to magnetic field may be more convenient, and they are demonstrated in Figure 2. For the given frequency $\tilde{\omega}$ and tangential wave vector $\vec{\kappa}$, the fields in region II can be expanded as

$$\begin{aligned}\vec{B}_{\mathrm{II}}\left(\tilde{\omega},\vec{\kappa}\right) &= \left[\vec{B}_{1,g,+}\exp(-ik_{z,1}z_0)+\vec{B}_{2,g,+}\exp(-ik_{z,2}z_0)\right]\\ &\quad\times\Theta(z-z_0)+\vec{B}_{1,b,+}+\vec{B}_{2,b,+}\\ &\quad+\left[\vec{B}_{1,g,-}\exp(ik_{z,1}z_0)+\vec{B}_{2,g,-}\exp(ik_{z,2}z_0)\right]\\ &\quad\times\Theta(z_0-z)+\vec{B}_{1,b,-}+\vec{B}_{2,b,-}\\ &\quad+\vec{B}\,\delta(z-z_0)\exp\left(i\,\vec{\kappa}\cdot\vec{R}\right),\\ \vec{D}_{\mathrm{II}}\left(\tilde{\omega},\vec{\kappa}\right) &= \left[\vec{D}_{1,g,+}\exp(-ik_{z,1}z_0)+\vec{D}_{2,g,+}\exp(-ik_{z,2}z_0)\right]\\ &\quad\times\Theta(z-z_0)+\vec{D}_{1,b,+}+\vec{D}_{2,b,+}\\ &\quad+\left[\vec{D}_{1,g,-}\exp(ik_{z,1}z_0)+\vec{D}_{2,g,-}\exp(ik_{z,2}z_0)\right]\\ &\quad\times\Theta(z_0-z)+\vec{D}_{1,b,-}+\vec{D}_{2,b,-}\\ &\quad+\vec{D}\,\delta(z-z_0)\exp\left(i\,\vec{\kappa}\cdot\vec{R}\right),\\ \vec{E}_{\mathrm{II}}\left(\tilde{\omega},\vec{\kappa}\right) &= \left[\vec{E}_{1,g,+}\exp(-ik_{z,1}z_0)+\vec{E}_{2,g,+}\exp(-ik_{z,2}z_0)\right]\\ &\quad\times\Theta(z-z_0)+\vec{E}_{1,b,+}+\vec{E}_{2,b,+}\\ &\quad+\left[\vec{E}_{1,g,-}\exp(ik_{z,1}z_0)+\vec{E}_{2,g,-}\exp(ik_{z,2}z_0)\right]\\ &\quad\times\Theta(z_0-z)+\vec{E}_{1,b,-}+\vec{E}_{2,b,-}\\ &\quad+\vec{E}\,\delta(z-z_0)\exp\left(i\,\vec{\kappa}\cdot\vec{R}\right),\end{aligned} \tag{9}$$

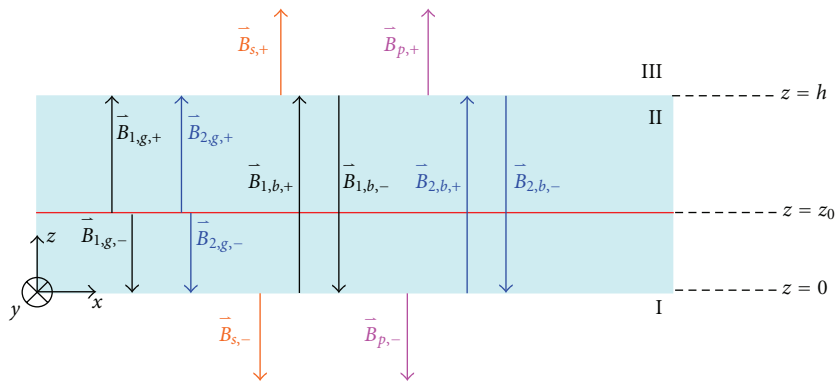

FIGURE 2: Schematic illustration of eigenmode expansion in three regions: $\vec{B}_{s,-}$ and $\vec{B}_{p,-}$ denote the eigen-plane-wave modes in region I, and the minus sign is to denote the direction of propagating is along $z-$ direction; $\vec{B}_{1,g,\pm}$ in region II denotes the first eigenmode generated from the source plane, $\vec{B}_{2,g,\pm}$ is to denote the second eigenmode generated from the source plane, $\vec{B}_{1,b,\pm}$ in region II expresses the first eigenmode bouncing back at the upper and lower boundaries, and $\vec{B}_{2,b,\pm}$ gives the second eigenmode bouncing back at the upper and lower boundaries (the plus and minus signs denotes the propagating along $z+$ and $z-$ directions); $\vec{B}_{s,+}$ and $\vec{B}_{p,+}$ denote the eigen-plane wave modes in region III, and the minus sign is to denote the direction of propagating is along $z+$ direction.

where

$$\begin{aligned}
\vec{B}_{i,g,\pm} &= B_{i,g,\pm}\exp\left(i\,\vec{\kappa}\cdot\vec{R}\right)\exp(\pm ik_{z,i}z)\hat{h}_{i,\pm},\\
\vec{B}_{i,b,\pm} &= B_{i,b,\pm}\exp\left(i\,\vec{\kappa}\cdot\vec{R}\right)\exp(\pm ik_{z,i}z)\hat{h}_{i,\pm},\\
\vec{D}_{i,g,\pm} &= \frac{-1}{i\tilde{\omega}\mu}\nabla\times\vec{B}_{i,g,\pm},\\
\vec{E}_{i,g,\pm} &= \overleftrightarrow{\varepsilon}^{-1}\cdot\vec{D}_{i,g,\pm}\\
\vec{D}_{i,b,\pm} &= \frac{-1}{i\tilde{\omega}\mu}\nabla\times\vec{B}_{i,b,\pm},\\
\vec{E}_{i,b,\pm} &= \overleftrightarrow{\varepsilon}^{-1}\cdot\vec{D}_{i,b,\pm}.
\end{aligned}\qquad i=1,2, \tag{10}$$

$\vec{B}(\vec{D},\ \vec{E})$ is to account the local (nonpropagating) field locating on the source plane, and $\Theta(z-z_0)$ is step function to denote the directions of modes launching from the source plane. In regions I and III, the eigenmodes are s- and p-polarized modes, and field can be expanded as

$$\begin{aligned}
\vec{B}_{\mathrm{I}}\left(\tilde{\omega},\vec{\kappa}\right) &= \left(B_{s,-}\hat{h}^{\mathrm{I}}_{s,-}+B_{p,-}\hat{h}^{\mathrm{I}}_{p,-}\right)\\
&\quad\times\exp\left(i\,\vec{\kappa}\cdot\vec{R}\right)\exp(-ik_{z,\mathrm{I}}z),\\
\vec{D}_{\mathrm{I}}\left(\tilde{\omega},\vec{\kappa}\right) &= \vec{E}_{\mathrm{I}}\left(\tilde{\omega},\vec{\kappa}\right)\\
&= \left(B_{s,-}\hat{e}^{\mathrm{I}}_{s,-}+B_{p,-}\hat{e}^{\mathrm{I}}_{p,-}\right)\\
&\quad\times\exp\left(i\,\vec{\kappa}\cdot\vec{R}\right)\exp(-ik_{z,\mathrm{I}}z),\\
\vec{B}_{\mathrm{III}}\left(\tilde{\omega},\vec{\kappa}\right) &= \left(B_{s,+}\hat{h}^{\mathrm{III}}_{s,+}+B_{p,+}\hat{h}^{\mathrm{III}}_{p,+}\right)\\
&\quad\times\exp\left(i\,\vec{\kappa}\cdot\vec{R}\right)\exp(ik_{z,\mathrm{III}}z),\\
\vec{D}_{\mathrm{III}}\left(\tilde{\omega},\vec{\kappa}\right) &= \vec{E}_{\mathrm{III}}\left(\tilde{\omega},\vec{\kappa}\right)\\
&= \left(B_{s,+}\hat{e}^{\mathrm{III}}_{s,+}+B_{p,+}\hat{e}^{\mathrm{III}}_{p,+}\right)\\
&\quad\times\exp\left(i\,\vec{\kappa}\cdot\vec{R}\right)\exp(ik_{z,\mathrm{III}}z),
\end{aligned}\tag{11}$$

where the unit vectors are defined as

$$\begin{aligned}
\hat{e}^{\alpha}_{s,\pm} &= \frac{\vec{k}_{s,\pm}\times\hat{z}}{\left|\vec{k}_{s,\pm}\times\hat{z}\right|} = \begin{pmatrix}\kappa\cos\theta\\ \kappa\sin\theta\\ \pm k_z\end{pmatrix}\times\begin{pmatrix}0\\0\\1\end{pmatrix} = \begin{pmatrix}\sin\theta\\ -\cos\theta\\ 0\end{pmatrix},\\
\hat{h}^{\alpha}_{s,\pm} &= \frac{\vec{k}_{s,\pm}\times\hat{e}_{s,\pm}}{\left|\vec{k}_{s,\pm}\times\hat{e}_{s,\pm}\right|} = \frac{1}{\tilde{\omega}\sqrt{\varepsilon_r\mu_r}}\begin{pmatrix}\pm k_z\cos\theta\\ \pm k_z\sin\theta\\ -\kappa\end{pmatrix},\\
\hat{h}^{\alpha}_{p,\pm} &= \frac{\vec{k}_{p,\pm}\times\hat{z}}{\left|\vec{k}_{p,\pm}\times\hat{z}\right|} = \begin{pmatrix}\kappa\cos\theta\\ \kappa\sin\theta\\ \pm k_z\end{pmatrix}\times\begin{pmatrix}0\\0\\1\end{pmatrix} = \begin{pmatrix}\sin\theta\\ -\cos\theta\\ 0\end{pmatrix},\\
\hat{e}^{\alpha}_{p,\pm} &= \frac{-\vec{k}_{p,\pm}\times\hat{h}_{p,\pm}}{\left|\vec{k}_{p,\pm}\times\hat{h}_{p,\pm}\right|} = \frac{1}{\tilde{\omega}\sqrt{\varepsilon_r\mu_r}}\begin{pmatrix}\mp k_z\cos\theta\\ \mp k_z\sin\theta\\ \kappa\end{pmatrix},
\end{aligned}\tag{12}$$

where α = I, II, III denotes the region where the unit vectors belong.

2.4. Determination of Generated Field in Each Region and Green Functions. The amplitudes of the four eigenmodes

launching from source plane for the given frequency $\tilde{\omega}$ and tangential wave vector $\vec{\kappa}$ can be determined by putting the fields in region II into the second and the last Maxwell equations in (2). The propagating modes in the mode expansion fulfill homogeneous Maxwell equation, and thus the electric fields and the magnetic fields of these propagating modes cancel. The second and the last Maxwell equations in (2), respectively, read

$$\begin{aligned}
&\delta(z-z_0)\hat{z}\\
&\quad\times\left[\vec{B}_{1,g,+}\exp(-ik_{z,1}z_0)+\vec{B}_{2,g,+}\exp(-ik_{z,2}z_0)\right.\\
&\qquad\left.-\vec{B}_{1,g,-}\exp(ik_{z,1}z_0)-\vec{B}_{2,g,-}\exp(ik_{z,2}z_0)\right]\\
&\quad+\ \hat{z}\times\vec{B}\,\delta'(z-z_0)\exp\left(i\,\vec{\kappa}\cdot\vec{R}\right)+i\,\vec{\kappa}\\
&\quad\times\vec{B}\exp\left(i\,\vec{\kappa}\cdot\vec{R}\right)\delta(z-z_0)\\
&\quad+i\tilde{\omega}\mu\,\overleftrightarrow{\varepsilon}\cdot\vec{E}\,\delta(z-z_0)\exp\left(i\,\vec{\kappa}\cdot\vec{R}\right)\\
&=-\,4\pi i\tilde{\omega}\mu\,\vec{P}\,\delta(z-z_0)\exp\left(i\,\vec{\kappa}\cdot\vec{R}\right)+4\pi\mu i\,\vec{\kappa}\\
&\quad\times\vec{M}\exp\left(i\,\vec{\kappa}\cdot\vec{R}\right)\delta(z-z_0)\\
&\quad+\ 4\pi\mu\delta'(z-z_0)\hat{z}\times\vec{M}\exp\left(i\,\vec{\kappa}\cdot\vec{R}\right),
\end{aligned}\tag{13}$$

$$\begin{aligned}
&\delta(z-z_0)\hat{z}\\
&\quad\times\left[\vec{E}_{1,g,+}\exp(-ik_{z,1}z_0)-\vec{E}_{1,g,-}\exp(ik_{z,1}z_0)\right.\\
&\qquad\left.+\vec{E}_{2,g,+}\exp(-ik_{z,2}z_0)-\vec{E}_{2,g,-}\exp(ik_{z,2}z_0)\right]\\
&\quad+\ \hat{z}\times\vec{E}\,\delta'(z-z_0)\exp\left(i\,\vec{\kappa}\cdot\vec{R}\right)+i\,\vec{\kappa}\\
&\quad\times\ \vec{E}\exp\left(i\,\vec{\kappa}\cdot\vec{R}\right)\delta(z-z_0)\\
&=i\tilde{\omega}\,\vec{B}\,\delta(z-z_0)\exp\left(i\,\vec{\kappa}\cdot\vec{R}\right),
\end{aligned}\tag{14}$$

where we have used $\nabla\Theta(z-z_0)=\hat{z}\delta(z-z_0)$ and $\nabla\delta(z-z_0)=\hat{z}\delta'(z-z_0)$. By requiring the coefficients in front of $\delta(z-z_0)$ and $\delta'(z-z_0)$ equal for the two sides, the amplitudes $B_{i,g,\pm}$ can be solved out. The fields generated in the regions outside of the medium can be determined by imposing the condition of continuity of tangential field at two boundaries ($z=0$ and $z=h$):

$$\begin{aligned}
&\vec{E}_{\mathrm{II}}\left(\tilde{\omega},\vec{\kappa};z=0\right)\cdot(\hat{x}\hat{x}+\hat{y}\hat{y})\\
&\quad=\left(B_{s,-}\hat{e}_{s,-}+B_{p,-}\hat{e}_{p,-}\right)\cdot(\hat{x}\hat{x}+\hat{y}\hat{y})\exp\left(i\,\vec{\kappa}\cdot\vec{R}\right),\\
&\vec{B}_{\mathrm{II}}\left(\tilde{\omega},\vec{\kappa};z=0\right)\cdot(\hat{x}\hat{x}+\hat{y}\hat{y})\\
&\quad=\left(B_{s,-}\hat{h}_{s,-}+B_{p,-}\hat{h}_{p,-}\right)\cdot(\hat{x}\hat{x}+\hat{y}\hat{y})\exp\left(i\,\vec{\kappa}\cdot\vec{R}\right),
\end{aligned}\tag{15}$$

for $z=0$ boundary, where $\hat{x}$ and $\hat{y}$ are the unit vectors of x and y directions,

$$\begin{aligned}
&\vec{E}_{\mathrm{II}}\left(\tilde{\omega},\vec{\kappa};z=h\right)\cdot(\hat{x}\hat{x}+\hat{y}\hat{y})\\
&=\left(B_{s,+}\hat{e}_{s,+}+B_{p,+}\hat{e}_{p,+}\right)\cdot(\hat{x}\hat{x}+\hat{y}\hat{y})\exp\left(i\,\vec{\kappa}\cdot\vec{R}\right)\exp(ikh),\\
&\vec{B}_{\mathrm{II}}\left(\tilde{\omega},\vec{\kappa};z=h\right)\cdot(\hat{x}\hat{x}+\hat{y}\hat{y})\\
&=\left(B_{s,+}\hat{h}_{s,+}+B_{p,+}\hat{h}_{p,+}\right)\cdot(\hat{x}\hat{x}+\hat{y}\hat{y})\exp\left(i\,\vec{\kappa}\cdot\vec{R}\right)\exp(ikh),
\end{aligned}\tag{16}$$

for $z=h$ boundary.

2.5. Correction of the Formulism: Isotropic Case. To prove the correction of the formulism, in this subsection we apply it to isotropic medium and compare the results gotten with well-known results in [17]. Equations from (13) to (16) are solved under the current case to get the Green functions. Since now the relative permittivity in region II then reduces to a scalar (we denote it by ε), the eigenmodes in the region are also s- and p-polarized modes. The dispersions for s- and p-polarized modes are the same and given as $\tilde{\omega}^2\varepsilon\mu=\kappa^2+k_z^2$ in region II and $\tilde{\omega}^2=\kappa^2+k_z^2$ in region I and III. The unit vectors of electric field and magnetic field are given in (12). The further convenience is that $\hat{e}_{s\pm}$, $\hat{\kappa}$ and $\hat{z}$ build up a right-hand coordinate, which can simplify the solution of (13) and (14) by decomposing the fields according to the three directions. After equating the coefficients in front of $\delta'(z-z_0)$ in (13) and (14), the following relations are found:

$$\begin{aligned}
\hat{z}\times\vec{B}&=4\pi\mu\hat{z}\times\vec{M},\\
\hat{z}\times\vec{E}&=0.
\end{aligned}\tag{17}$$

The local magnetic source relates with local magnetic field as $B_{\hat{e}_{s\pm}}=4\pi\mu M_{\hat{e}_{s\pm}}$ and $B_{\hat{\kappa}}=4\pi\mu M_{\hat{\kappa}}$ and $\hat{e}_{s,\pm}$ and $\hat{\kappa}$ components of local electric field vanish ($E_{\hat{e}_{s\pm}}=E_{\hat{\kappa}}=0$). From the equality of the coefficients in front of $\delta(z-z_0)$, we can get the other equations, and we write them according to the components along $\hat{e}_{s\pm}$, $\hat{\kappa}$, and $\hat{z}$ directions for (13), and (14) respectively,

$$\begin{aligned}
\frac{1}{\sqrt{\varepsilon\mu}}\left(B_{s,g,+}+B_{s,g,-}\right)&=\frac{4\pi i\tilde{\omega}^2\mu}{k_z}P_{\hat{e}_{s,\pm}}-\frac{4\pi\mu i\kappa\tilde{\omega}}{k_z}M_{\hat{z}},\\
B_{p,g,+}-B_{p,g,-}&=-4\pi i\tilde{\omega}\mu P_{\hat{\kappa}},\\
i\omega\varepsilon\mu E_{\hat{z}}&=-i4\pi\tilde{\omega}\mu P_{\hat{z}},\\
\frac{1}{\sqrt{\mu\varepsilon}}\left(B_{p,g,+}+B_{p,g,-}\right)+\frac{\kappa k_{\mathrm{II}}}{k_{z,\mathrm{II}}}&=\frac{i\tilde{\omega}k_{\mathrm{II}}}{k_{z,\mathrm{II}}}B_{\hat{e}_{s,\pm}},\\
\frac{1}{\sqrt{\mu\varepsilon}}\left(B_{s,g,+}-B_{s,g,-}\right)&=i\tilde{\omega}B_{\hat{\kappa}},\\
B_{\hat{z}}&=0.
\end{aligned}\tag{18}$$

The fields launching from the source can be gotten by solving (18) and the results are collected as follows:

$$B_{s,g,+} = \left(\frac{2\pi i\tilde{\omega}^2\mu}{k_{z,\mathrm{II}}}\sqrt{\mu\varepsilon}\left(\hat{e}^{\mathrm{II}}_{s,\pm}\cdot\vec{P}\right) + \frac{2\pi\mu i\tilde{\omega}^2\mu\varepsilon}{k_{z,\mathrm{II}}}\left(\hat{h}^{\mathrm{II}}_{s,+}\cdot\vec{M}\right)\right),$$

$$B_{s,g,-} = \left(\frac{2\pi i\tilde{\omega}^2\mu}{k_{z,\mathrm{II}}}\sqrt{\mu\varepsilon}\left(\hat{e}^{\mathrm{II}}_{s,\pm}\cdot\vec{P}\right) + \frac{2\pi\mu i\tilde{\omega}^2\mu\varepsilon}{k_{z,\mathrm{II}}}\left(\hat{h}^{\mathrm{II}}_{s,-}\cdot\vec{M}\right)\right),$$

$$B_{p,g,+} = \left(\frac{2\pi i\mu\tilde{\omega}k_{\mathrm{II}}}{k_{z,\mathrm{II}}}\sqrt{\varepsilon\mu}\left(\hat{e}^{\mathrm{II}}_{s,\pm}\cdot\vec{M}\right) - \frac{2\pi i\tilde{\omega}k_{\mathrm{II}}\mu}{k_{z,\mathrm{II}}}\left(\hat{h}^{\mathrm{II}}_{s,+}\cdot\vec{P}\right)\right),$$

$$B_{p,g,-} = \left(\frac{2\pi i\mu\tilde{\omega}k_{\mathrm{II}}}{k_{z,\mathrm{II}}}\sqrt{\varepsilon\mu}\left(\hat{e}^{\mathrm{II}}_{s,\pm}\cdot\vec{M}\right) - \frac{2\pi i\tilde{\omega}k_{\mathrm{II}}\mu}{k_{z,\mathrm{II}}}\left(\hat{h}^{\mathrm{II}}_{s,-}\cdot\vec{P}\right)\right), \tag{19}$$

where the results are written in a compact form with the help of the unit vectors defined and the same with (2.37) in [17], and thus Green functions in infinite bulk isotropic medium gotten by present method are correct.

To determine the fields in regions I and III, the boundary equations (15) and (16) should be solved. Isotropy of the medium in region II provides great simplification: since the orthogonality between tangential wave vectors $\hat{e}^{T}_{s,\pm} = \hat{h}^{T}_{p,\pm}$ and $\hat{h}^{T}_{s,\pm} = -\hat{e}^{T}_{p,\pm}$ always holds, it is not necessary to arrange the equations in x-y-z coordinate. Taking the advantage, the boundary equation (15) for $z = 0$ becomes

$$\begin{aligned}
&B_{s,-}\hat{e}^{T,\mathrm{I}}_{s,-}\\
&\quad= \frac{1}{\sqrt{\mu\varepsilon}}\left(B_{s,b,+}\hat{e}^{T,\mathrm{II}}_{s,+} + B_{s,g,-}\exp(ik_{z,\mathrm{II}}z_0)\hat{e}^{T,\mathrm{II}}_{s,-} + B_{s,b,-}\hat{e}^{T,\mathrm{II}}_{s,-}\right),\\
&B_{p,-}\hat{e}^{T,\mathrm{I}}_{p,-}\\
&\quad= \frac{1}{\sqrt{\mu\varepsilon}}\left(B_{p,b,+}\hat{e}^{T,\mathrm{II}}_{p,+} + B_{p,g,-}\exp(ik_{z,\mathrm{II}}z_0)\hat{e}^{T,\mathrm{II}}_{p,-} + B_{p,b,-}\hat{e}^{T,\mathrm{II}}_{p,-}\right),\\
&B_{p,-}\hat{h}^{T,\mathrm{I}}_{p,-}\\
&\quad= B_{p,b,+}\hat{h}^{T,\mathrm{II}}_{p,+} + B_{p,g,-}\exp(ik_{z,\mathrm{II}}z_0)\hat{h}^{T,\mathrm{II}}_{p,-} + B_{p,b,-}\hat{h}^{T,\mathrm{II}}_{p,-},\\
&B_{s,-}\hat{h}^{T,\mathrm{I}}_{s,-}\\
&\quad= B_{s,b,+}\hat{h}^{T,\mathrm{II}}_{s,+} + B_{s,g,-}\exp(ik_{z,\mathrm{II}}z_0)\hat{h}^{T,\mathrm{II}}_{s,-} + B_{s,b,-}\hat{h}^{T,\mathrm{II}}_{s,-}.
\end{aligned} \tag{20}$$

Similarly, the boundary equation (16) for $z = h$ gives

$$\begin{aligned}
&B_{s,+}\exp(ik_{z,\mathrm{I}}h)\hat{e}^{T,\mathrm{III}}_{s,+}\\
&\quad= \frac{1}{\sqrt{\mu\varepsilon}}\Big(B_{s,g,+}\exp[ik_{z,\mathrm{II}}(h-z_0)]\hat{e}^{T,\mathrm{II}}_{s,+}\\
&\qquad+ B_{s,b,+}\exp(ik_{z,\mathrm{II}}h)\hat{e}^{T,\mathrm{II}}_{s,+}\\
&\qquad+ B_{s,b,-}\exp(-ik_{z,\mathrm{II}}h)\hat{e}^{T,\mathrm{II}}_{s,-}\Big),\\
&B_{p,+}\exp(ik_{z,\mathrm{I}}h)\hat{e}^{T,\mathrm{III}}_{p,+}\\
&\quad= \frac{1}{\sqrt{\mu\varepsilon}}\Big(B_{p,g,+}\exp[ik_{z,\mathrm{II}}(h-z_0)]\hat{e}^{T,\mathrm{II}}_{p,+}\\
&\qquad+ B_{p,b,+}\exp(ik_{z,\mathrm{II}}h)\hat{e}^{T,\mathrm{II}}_{p,+}\\
&\qquad+ B_{p,b,-}\exp(-ik_{z,\mathrm{II}}h)\hat{e}^{T,\mathrm{II}}_{p,-}\Big),\\
&B_{p,+}\exp(ik_{z,\mathrm{I}}h)\hat{h}^{T,\mathrm{III}}_{p,+}\\
&\quad= B_{p,g,+}\exp[ik_{z,\mathrm{II}}(h-z_0)]\hat{h}^{T,\mathrm{II}}_{p,+}\\
&\qquad+ B_{p,b,+}\exp(ik_{z,\mathrm{II}}h)\hat{h}^{T,\mathrm{II}}_{p,+} + B_{p,b,-}\exp(-ik_{z,\mathrm{II}}h)\hat{h}^{T,\mathrm{II}}_{p,-},\\
&B_{s,+}\exp(ik_{z,\mathrm{I}}h)\hat{h}^{T,\mathrm{III}}_{s,+}\\
&\quad= B_{s,g,+}\exp[ik_{z,\mathrm{II}}(h-z_0)]\hat{h}^{T,\mathrm{II}}_{s,+}\\
&\qquad+ B_{s,b,+}\exp(ik_{z,\mathrm{II}}h)\hat{h}^{T,\mathrm{II}}_{s,+} + B_{s,b,-}\exp(-ik_{z,\mathrm{II}}h)\hat{h}^{T,\mathrm{II}}_{s,-},
\end{aligned} \tag{21}$$

where $\hat{e}^{T,\mathrm{I(III)}}_{s,\pm}$, $\hat{e}^{T,\mathrm{II}}_{s,\pm}$, $\hat{e}^{T,\mathrm{I(III)}}_{p,\pm}$, $\hat{e}^{T,\mathrm{II}}_{p,\pm}$, $\hat{h}^{T,\mathrm{I(III)}}_{p,\pm}$, $\hat{h}^{T,\mathrm{II}}_{p,\pm}$, $\hat{h}^{T,\mathrm{I(III)}}_{s,\pm}$, $\hat{h}^{T,\mathrm{II}}_{s,\pm}$ are the tangential parts of these unit vectors in different regions and $k_{z,\mathrm{II}} = k_{z,s} = k_{z,p}$. Once $B_{s,-}$ and $B_{p,-}$($B_{s,+}$ and $B_{p,+}$) are solved from (20) and (21), the generated fields in region I (III) from the source plane are determined. The fields in region I are given as follows:

$$\begin{aligned}
&\vec{B}_{\mathrm{I}}\left(\tilde{\omega},\vec{\kappa}\right)\\
&\quad= \frac{1}{\sqrt{\mu\varepsilon}}\left[\frac{r^{s}_{\mathrm{II,I}}e^{ik_{z,\mathrm{II}}z_0}}{1-t^{s}_{\mathrm{II,I}}{}^{2}e^{i2k_{z,\mathrm{II}}h}}B_{s,g,-}\right.\\
&\qquad\left.+\frac{r^{s}_{\mathrm{II,I}}t^{s}_{\mathrm{II,I}}e^{ik_{z,\mathrm{II}}(2h-z_0)}}{1-t^{s}_{\mathrm{II,I}}{}^{2}e^{i2k_{z,\mathrm{II}}h}}B_{s,g,+}\right]\\
&\qquad\times\hat{h}_{s,-}\exp\left(i\,\vec{\kappa}\cdot\vec{R}\right)\exp(-ik_{z,\mathrm{I}}z)\\
&\quad+\frac{1}{\sqrt{\mu\varepsilon}}\left[\frac{r^{p}_{\mathrm{II,I}}e^{ik_{z,\mathrm{II}}z_0}}{1-t^{p}_{\mathrm{II,I}}{}^{2}e^{i2k_{z,\mathrm{II}}h}}B_{p,g,-}\right.\\
&\qquad\left.+\frac{r^{p}_{\mathrm{II,I}}t^{p}_{\mathrm{II,I}}e^{ik_{z,\mathrm{II}}(2h-z_0)}}{1-t^{p}_{\mathrm{II,I}}{}^{2}e^{i2k_{z,\mathrm{II}}h}}B_{p,g,+}\right]\\
&\qquad\times\hat{h}_{p,-}\exp\left(i\,\vec{\kappa}\cdot\vec{R}\right)\exp(-ik_{z,\mathrm{I}}z),\\
&\vec{E}_{\mathrm{I}}\left(\tilde{\omega},\vec{\kappa}\right)\\
&\quad= \frac{1}{\sqrt{\mu\varepsilon}}\left[\frac{r^{s}_{\mathrm{II,I}}e^{ik_{z,\mathrm{II}}z_0}}{1-t^{s}_{\mathrm{II,I}}{}^{2}e^{i2k_{z,\mathrm{II}}h}}B_{s,g,-}\right.\\
&\qquad\left.+\frac{r^{s}_{\mathrm{II,I}}t^{s}_{\mathrm{II,I}}e^{ik_{z,\mathrm{II}}(2h-z_0)}}{1-t^{s}_{\mathrm{II,I}}{}^{2}e^{i2k_{z,\mathrm{II}}h}}B_{s,g,+}\right]\\
&\qquad\times\hat{e}_{s,-}\exp\left(i\,\vec{\kappa}\cdot\vec{R}\right)\exp(-ik_{z,\mathrm{I}}z)\\
&\quad+\frac{1}{\sqrt{\mu\varepsilon}}\left[\frac{r^{p}_{\mathrm{II,I}}e^{ik_{z,\mathrm{II}}z_0}}{1-t^{p}_{\mathrm{II,I}}{}^{2}e^{i2k_{z,\mathrm{II}}h}}B_{p,g,-}\right.\\
&\qquad\left.+\frac{r^{p}_{\mathrm{II,I}}t^{p}_{\mathrm{II,I}}e^{ik_{z,\mathrm{II}}(2h-z_0)}}{1-t^{p}_{\mathrm{II,I}}{}^{2}e^{i2k_{z,\mathrm{II}}h}}B_{p,g,+}\right]\\
&\qquad\times\hat{e}_{p,-}\exp\left(i\,\vec{\kappa}\cdot\vec{R}\right)\exp(-ik_{z,\mathrm{I}}z).
\end{aligned} \tag{22}$$

The fields generated in region III are gotten as

$$\begin{aligned}
&\vec{B}_{\mathrm{III}}\left(\widetilde{\omega},\vec{\kappa}\right)\\
&\quad=\frac{1}{\sqrt{\varepsilon\mu}}\left[\frac{r^{s}_{\mathrm{II,III}}t^{s}_{\mathrm{II,III}}e^{ik_{z,\mathrm{II}}(z_0+h)}}{1-{t^{s}_{\mathrm{II,III}}}^{2}e^{i2k_{z,\mathrm{II}}h}}B_{s,g,-}\right.\\
&\qquad\left.+\frac{r^{s}_{\mathrm{II,III}}e^{ik_{z,\mathrm{II}}(h-z_0)}}{1-{t^{s}_{\mathrm{II,III}}}^{2}e^{i2k_{z,\mathrm{II}}h}}B_{s,g,+}\right]\\
&\qquad\times\hat{h}_{s,+}e^{-ik_{z,\mathrm{I}}h}\exp\left(i\,\vec{\kappa}\cdot\vec{R}\right)\exp\left(ik_{z,\mathrm{III}}z\right)\\
&\qquad+\frac{1}{\sqrt{\varepsilon\mu}}\left[\frac{r^{p}_{\mathrm{II,III}}t^{p}_{\mathrm{II,III}}e^{ik_{z,\mathrm{II}}(z_0+h)}}{1-{t^{p}_{\mathrm{II,III}}}^{2}e^{i2k_{z,\mathrm{II}}h}}B_{p,g,-}\right.\\
&\qquad\left.+\frac{r^{p}_{\mathrm{II,III}}e^{ik_{z,\mathrm{II}}(h-z_0)}}{1-{t^{p}_{\mathrm{II,III}}}^{2}e^{i2k_{z,\mathrm{II}}h}}B_{p,g,+}\right]\\
&\qquad\times\hat{h}_{p,+}e^{-ik_{z,\mathrm{I}}h}\exp\left(i\,\vec{\kappa}\cdot\vec{R}\right)\exp\left(ik_{z,\mathrm{III}}z\right),\\
&\vec{E}_{\mathrm{III}}\left(\widetilde{\omega},\vec{\kappa}\right)\\
&\quad=\frac{1}{\sqrt{\varepsilon\mu}}\left[\frac{r^{s}_{\mathrm{II,III}}t^{s}_{\mathrm{II,III}}e^{ik_{z,\mathrm{II}}(z_0+h)}}{1-{t^{s}_{\mathrm{II,III}}}^{2}e^{i2k_{z,\mathrm{II}}h}}B_{s,g,-}\right.\\
&\qquad\left.+\frac{r^{s}_{\mathrm{II,III}}e^{ik_{z,\mathrm{II}}(h-z_0)}}{1-{t^{s}_{\mathrm{II,III}}}^{2}e^{i2k_{z,\mathrm{II}}h}}B_{s,g,+}\right]\\
&\qquad\times\hat{e}_{s,+}e^{-ik_{z,\mathrm{I}}h}\exp\left(i\,\vec{\kappa}\cdot\vec{R}\right)\exp\left(ik_{z,\mathrm{III}}z\right)\\
&\qquad+\frac{1}{\sqrt{\varepsilon\mu}}\left[\frac{r^{p}_{\mathrm{II,III}}t^{p}_{\mathrm{II,III}}e^{ik_{z,\mathrm{II}}(z_0+h)}}{1-{t^{p}_{\mathrm{II,III}}}^{2}e^{i2k_{z,\mathrm{II}}h}}B_{p,g,-}\right.\\
&\qquad\left.+\frac{r^{p}_{\mathrm{II,III}}e^{ik_{z,\mathrm{II}}(h-z_0)}}{1-{t^{p}_{\mathrm{II,III}}}^{2}e^{i2k_{z,\mathrm{II}}h}}B_{p,g,+}\right]\\
&\qquad\times\hat{e}_{p,+}e^{-ik_{z,\mathrm{I}}h}\exp\left(i\,\vec{\kappa}\cdot\vec{R}\right)\exp\left(ik_{z,\mathrm{III}}z\right),
\end{aligned}\tag{23}$$

where $t^{s}_{i,j}=(k_{z,i}-k_{z,j})/(k_{z,i}+k_{z,j})$, $t^{s}_{i,j}=2k_{z,i}/(k_{z,i}+k_{z,j})$, $t^{p}_{i,j}=(k_{z,i}\varepsilon_j\mu_j-k_{z,j}\varepsilon_i\mu_i)/(k_{z,i}\varepsilon_j\mu_j+k_{z,j}\varepsilon_i\mu_i)$, $r^{p}_{i,j}=2k_{z,i}\sqrt{\varepsilon_j\mu_j}\sqrt{\varepsilon_i\mu_i}/(k_{z,i}\varepsilon_j\mu_j+k_{z,j}\varepsilon_i\mu_i)$ are Fresnel coefficients. Since $B_{s,g,\pm}$ and $B_{p,g,\pm}$ have been related with the sources, the fields in regions I and III in fact can spontaneously relate with the sources. Thus, Green functions linking the fields in these regions and source plane are ready to be gotten by following definition (8):

$$\begin{aligned}
&\overleftrightarrow{G}^{\mathrm{I}}_{BM}\left(\vec{\kappa};z-z_0\right)\\
&\quad=\frac{2\pi\mu i\widetilde{\omega}k_{\mathrm{II}}}{k_{z,\mathrm{II}}}\left(\frac{t^{s}_{\mathrm{II,I}}\left(r^{s}_{\mathrm{II,I}}e^{ik_{z,\mathrm{II}}(2h-z_0)}\hat{h}^{\mathrm{I}}_{s,-}\hat{h}^{\mathrm{II}}_{s,+}+e^{ik_{z,\mathrm{II}}z_0}\hat{h}^{\mathrm{I}}_{s,-}\hat{h}^{\mathrm{II}}_{s,-}\right)}{1-{r^{s}_{\mathrm{II,I}}}^{2}e^{i2k_{z,\mathrm{II}}h}}\right.\\
&\qquad\left.+\frac{t^{p}_{\mathrm{II,I}}\left(e^{ik_{z,\mathrm{II}}z_0}+r^{p}_{\mathrm{II,I}}e^{ik_{z,\mathrm{II}}(2h-z_0)}\right)}{1-{r^{p}_{\mathrm{II,I}}}^{2}e^{i2k_{z,\mathrm{II}}h}}\hat{h}^{\mathrm{I}}_{p,-}\hat{e}^{\mathrm{II}}_{s,\pm}\right)\\
&\qquad\times e^{i\vec{\kappa}\cdot\vec{R}}e^{-ik_{z,\mathrm{I}}z},\\
&\overleftrightarrow{G}^{\mathrm{I}}_{BP}\left(\vec{\kappa};z-z_0\right)\\
&\quad=\frac{2\pi i\widetilde{\omega}^{2}\mu}{k_{z,\mathrm{II}}}\\
&\qquad\times\left(\frac{t^{s}_{\mathrm{II,I}}\left(e^{ik_{z,\mathrm{II}}z_0}+r^{s}_{\mathrm{II,I}}e^{ik_{z,\mathrm{II}}(2h-z_0)}\right)}{1-{r^{s}_{\mathrm{II,I}}}^{2}e^{i2k_{z,\mathrm{II}}h}}\hat{h}^{\mathrm{I}}_{s,-}\hat{e}^{\mathrm{II}}_{s,\pm}\right.\\
&\qquad\left.-\frac{t^{p}_{\mathrm{II,I}}\left(e^{ik_{z,\mathrm{II}}z_0}\hat{h}^{\mathrm{I}}_{p,-}\hat{h}^{\mathrm{II}}_{s,-}+r^{p}_{\mathrm{II,I}}e^{ik_{z,\mathrm{II}}(2h-z_0)}\hat{h}^{\mathrm{I}}_{p,-}\hat{h}^{\mathrm{II}}_{s,+}\right)}{1-{r^{p}_{\mathrm{II,I}}}^{2}e^{i2k_{z,\mathrm{II}}h}}\right)\\
&\qquad\times e^{i\vec{\kappa}\cdot\vec{R}}e^{-ik_{z,\mathrm{I}}z},\\
&\overleftrightarrow{G}^{\mathrm{I}}_{EM}\left(\vec{\kappa};z-z_0\right)\\
&\quad=\frac{2\pi\mu i\widetilde{\omega}k_{\mathrm{II}}}{k_{z,\mathrm{II}}}\\
&\qquad\times\left[\frac{r^{s}_{\mathrm{II,I}}\left(t^{s}_{\mathrm{II,I}}e^{ik_{z,\mathrm{II}}(2h-z_0)}\hat{e}^{\mathrm{I}}_{s,-}\hat{h}^{\mathrm{II}}_{s,+}+e^{ik_{z,\mathrm{II}}z_0}\hat{e}^{\mathrm{I}}_{s,-}\hat{h}^{\mathrm{II}}_{s,-}\right)}{1-{t^{s}_{\mathrm{II,I}}}^{2}e^{i2k_{z,\mathrm{II}}h}}\right.\\
&\qquad\left.+\frac{r^{p}_{\mathrm{II,I}}\left(e^{ik_{z,\mathrm{II}}z_0}+t^{p}_{\mathrm{II,I}}e^{ik_{z,\mathrm{II}}(2h-z_0)}\right)}{1-{t^{p}_{\mathrm{II,I}}}^{2}e^{i2k_{z,\mathrm{II}}h}}\hat{e}^{\mathrm{I}}_{p,-}\hat{e}^{\mathrm{II}}_{s,\pm}\right]\\
&\qquad\times e^{i\vec{\kappa}\cdot\vec{R}}e^{-ik_{z,\mathrm{I}}z},\\
&\overleftrightarrow{G}^{\mathrm{I}}_{EM}\left(\vec{\kappa};z-z_0\right)\\
&\quad=\frac{2\pi i\widetilde{\omega}^{2}\mu}{k_{z,\mathrm{II}}}\left[\frac{t^{s}_{\mathrm{II,I}}\left(e^{ik_{z,\mathrm{II}}z_0}+r^{s}_{\mathrm{II,I}}e^{ik_{z,\mathrm{II}}(2h-z_0)}\right)}{1-{r^{s}_{\mathrm{II,I}}}^{2}e^{i2k_{z,\mathrm{II}}h}}\hat{e}^{\mathrm{I}}_{s,-}\hat{e}^{\mathrm{II}}_{s,\pm}\right.\\
&\qquad\left.-\frac{t^{p}_{\mathrm{II,I}}\left(e^{ik_{z,\mathrm{II}}z_0}\hat{e}^{\mathrm{I}}_{p,-}\hat{h}^{\mathrm{II}}_{s,-}+r^{p}_{\mathrm{II,I}}e^{ik_{z,\mathrm{II}}(2h-z_0)}\hat{e}^{\mathrm{I}}_{p,-}\hat{h}^{\mathrm{II}}_{s,+}\right)}{1-{r^{p}_{\mathrm{II,I}}}^{2}e^{i2k_{z,\mathrm{II}}h}}\right]\\
&\qquad\times e^{i\vec{\kappa}\cdot\vec{R}}e^{-ik_{z,\mathrm{I}}z},\\
&\overleftrightarrow{G}^{\mathrm{III}}_{BM}\left(\vec{\kappa};z-z_0\right)\\
&\quad=\frac{2\pi\mu i\widetilde{\omega}k_{\mathrm{II}}}{k_{z,\mathrm{II}}}\\
&\qquad\times\left[\frac{t^{s}_{\mathrm{II,III}}\left(r^{s}_{\mathrm{II,III}}e^{ik_{z,\mathrm{II}}(z_0+h)}\hat{h}^{\mathrm{III}}_{s,+}\hat{h}^{\mathrm{II}}_{s,-}+e^{ik_{z,\mathrm{II}}(h-z_0)}\hat{h}^{\mathrm{III}}_{s,+}\hat{h}^{\mathrm{II}}_{s,+}\right)}{1-{r^{s}_{\mathrm{II,III}}}^{2}e^{i2k_{z,\mathrm{II}}h}}\right.\\
&\qquad\left.+\frac{t^{p}_{\mathrm{II,III}}\left(r^{p}_{\mathrm{II,III}}e^{ik_{z,\mathrm{II}}(z_0+h)}+e^{ik_{z,\mathrm{II}}(h-z_0)}\right)}{1-{r^{p}_{\mathrm{II,III}}}^{2}e^{i2k_{z,\mathrm{II}}h}}\hat{h}^{\mathrm{III}}_{p,+}\hat{e}^{\mathrm{II}}_{s,\pm}\right]\\
&\qquad\times e^{i\kappa_{z,\mathrm{III}}(z-h)}e^{i\vec{k}\cdot\vec{R}},
\end{aligned}$$

$$
\begin{aligned}
&\overleftrightarrow{G}^{\mathrm{III}}_{BP}\left(\vec{\kappa}; z-z_0\right)\\
&=\frac{2\pi i\tilde{\omega}^2\mu}{k_{z,\mathrm{II}}}\\
&\quad\times\left[\frac{t^s_{\mathrm{II,III}}\left(r^s_{\mathrm{II,III}}e^{ik_{z,\mathrm{II}}(z_0+h)}+e^{ik_{z,\mathrm{II}}(h-z_0)}\right)}{1-{r^s_{\mathrm{II,III}}}^2e^{i2k_{z,\mathrm{II}}h}}\hat{h}^{\mathrm{III}}_{s,+}\hat{e}^{\mathrm{II}}_{s,\pm}\right.\\
&\qquad\left.-\frac{t^p_{\mathrm{II,III}}\left(r^p_{\mathrm{II,III}}e^{ik_{z,\mathrm{II}}(z_0+h)}\hat{h}^{\mathrm{III}}_{p,+}\hat{h}^{\mathrm{II}}_{s,-}+e^{ik_{z,\mathrm{II}}(h-z_0)}\hat{h}^{\mathrm{III}}_{p,+}\hat{h}^{\mathrm{II}}_{s,+}\right)}{1-{r^p_{\mathrm{II,III}}}^2e^{i2k_{z,\mathrm{II}}h}}\right]\\
&\quad\times e^{i\kappa_{z,\mathrm{III}}(z-h)}e^{i\vec{k}\cdot\vec{R}}\\
&\overleftrightarrow{G}^{\mathrm{III}}_{EM}\left(\vec{\kappa}\ z-z_0\right)\\
&=\frac{2\pi\mu i\tilde{\omega}k_{\mathrm{II}}}{k_{z,\mathrm{II}}}\\
&\quad\times\left[\frac{t^s_{\mathrm{II,III}}\left(r^s_{\mathrm{II,III}}e^{ik_{z,\mathrm{II}}(z_0+h)}\hat{e}^{\mathrm{III}}_{s,+}\hat{h}^{\mathrm{II}}_{s,-}+e^{ik_{z,\mathrm{II}}(h-z_0)}\hat{e}^{\mathrm{III}}_{s,+}\hat{h}^{\mathrm{II}}_{s,+}\right)}{1-{r^s_{\mathrm{II,III}}}^2e^{i2k_{z,\mathrm{II}}h}}\right.\\
&\qquad\left.+\frac{t^p_{\mathrm{II,III}}\left(r^p_{\mathrm{II,III}}e^{ik_{z,\mathrm{II}}(z_0+h)}+e^{ik_{z,\mathrm{II}}(h-z_0)}\right)}{1-{r^p_{\mathrm{II,III}}}^2e^{i2k_{z,\mathrm{II}}h}}\hat{e}^{\mathrm{III}}_{p,+}\hat{e}^{\mathrm{II}}_{s,\pm}\right]\\
&\quad\times e^{i\kappa_{z,\mathrm{III}}(z-h)}e^{i\vec{k}\cdot\vec{R}},\\
&\overleftrightarrow{G}^{\mathrm{III}}_{EP}\left(\vec{\kappa}\ z-z_0\right)\\
&=\frac{2\pi i\tilde{\omega}^2\mu}{k_{z,\mathrm{II}}}\\
&\quad\times\left[\frac{t^s_{\mathrm{II,III}}\left(r^s_{\mathrm{II,III}}e^{ik_{z,\mathrm{II}}(z_0+h)}+e^{ik_{z,\mathrm{II}}(h-z_0)}\right)}{1-{r^s_{\mathrm{II,III}}}^2e^{i2k_{z,\mathrm{II}}h}}\hat{e}^{\mathrm{III}}_{s,+}\hat{e}^{\mathrm{II}}_{s,\pm}\right.\\
&\qquad\left.-\frac{t^p_{\mathrm{II,III}}\left(r^p_{\mathrm{II,III}}e^{ik_{z,\mathrm{II}}(z_0+h)}\hat{e}^{\mathrm{III}}_{p,+}\hat{h}^{\mathrm{II}}_{s,-}+e^{ik_{z,\mathrm{II}}(h-z_0)}\hat{e}^{\mathrm{III}}_{p,+}\hat{h}^{\mathrm{II}}_{s,+}\right)}{1-{r^p_{\mathrm{II,III}}}^2e^{i2k_{z,\mathrm{II}}h}}\right]\\
&\quad\times e^{i\kappa_{z,\mathrm{III}}(z-h)}e^{i\vec{k}\cdot\vec{R}}.
\end{aligned}
\tag{24}
$$

These results exactly recover (4.18) in [17], and thus the correction of current formulism is proved.

3. Green Functions for Sources in Anisotropic Medium

The formulism developed in the last section is then applied to obtain Green functions linking sources in anisotropic medium and fields in space. The advantage of mode expansion method would be obviously shown in the following study.

3.1. Sources in Uniaxial Crystal. Under the situation, the permittivity tensor in region II would be read as $\mathrm{diag}(\varepsilon_o, \varepsilon_e, \varepsilon_o)$, where without losing generality we have assumed the anisotropy is along y direction (so that mode conversion still happens at the interface). Then the equation determining eigenmodes (5) becomes

$$
\left(\tilde{\omega}^2-\frac{k_x^2}{\varepsilon_o\mu}-\frac{k_y^2}{\varepsilon_o\mu}-\frac{k_z^2}{\varepsilon_o\mu}\right)\left(\tilde{\omega}^2-\frac{k_x^2}{\varepsilon_e\mu}-\frac{k_y^2}{\varepsilon_o\mu}-\frac{k_z^2}{\varepsilon_e\mu}\right)=0.
\tag{25}
$$

Thus, there are two dispersions gotten: the mode with dispersion $\tilde{\omega}^2-k_x^2/\varepsilon_o\mu-k_y^2/\varepsilon_o\mu-k_z^2/\varepsilon_o\mu=0$ is known as o-light, and the mode with dispersion $\tilde{\omega}^2-k_x^2/\varepsilon_e\mu-k_y^2/\varepsilon_o\mu-k_z^2/\varepsilon_e\mu=0$ is known as e-light. The corresponding unit vector for electric field can be solved from (4) and the constraint (the homogeneous form of the first Maxwell equation in (2)) and given as

$$
\begin{aligned}
\hat{e}_{o,\pm}&=\frac{1}{\sqrt{\kappa^2\cos^2\theta+k_{z,o}^2}}\begin{pmatrix}\pm k_{z,o}\\0\\-\kappa\cos\theta\end{pmatrix},\\
\hat{e}_{e,\pm}&=\frac{1}{\sqrt{\dfrac{\left(\kappa^2\cos^2\theta+k_{z,e}^2\right)}{\varepsilon_e^2}+\dfrac{\kappa^2\sin^2\theta}{\varepsilon_o^2}}\sqrt{\kappa^2\cos^2\theta+k_{z,e}^2}}\\
&\quad\times\begin{pmatrix}\varepsilon_o^{-1}\kappa^2\sin\theta\cos\theta\\ \varepsilon_e^{-1}\left(-k_{z,e}^2-\kappa^2\cos^2\theta\right)\\ \pm\varepsilon_o^{-1}k_{z,e}\kappa\sin\theta\end{pmatrix}.
\end{aligned}
\tag{26}
$$

Thus, we can have the unit vectors for magnetic field and electric displacement vector as

$$
\begin{aligned}
\hat{h}_{o\pm}&=\frac{1}{k_o\sqrt{\kappa^2\cos^2\theta+k_{z,o}^2}}\begin{pmatrix}-\kappa^2\sin\theta\cos\theta\\ k_{z,o}^2+\kappa^2\cos^2\theta\\ \mp k_{z,o}\kappa\sin\theta\end{pmatrix},\\
\hat{h}_{e\pm}&=\frac{1}{\sqrt{\kappa^2\cos^2\theta+k_{z,e}^2}}\begin{pmatrix}\pm k_{z,e}\\0\\-\kappa\cos\theta\end{pmatrix},\\
\hat{d}_{o,\pm}&=\frac{1}{\sqrt{\kappa^2\cos^2\theta+k_{z,o}^2}}\begin{pmatrix}\pm k_{z,o}\\0\\-\kappa\cos\theta\end{pmatrix},\\
\hat{d}_{e\pm}&=\frac{1}{k_e\sqrt{\kappa^2\cos^2\theta+k_{z,e}^2}}\begin{pmatrix}\kappa^2\sin\theta\cos\theta\\ -k_{z,e}^2-\kappa^2\cos^2\theta\\ \pm k_{z,e}\kappa\sin\theta\end{pmatrix},
\end{aligned}
\tag{27}
$$

where $k_o = \sqrt{\kappa^2 + k_{z,o}^2}$ and $k_e = \sqrt{\kappa^2 + k_{z,e}^2}$. Following the mode expansion denoted in Section 2.3 the equations determining the fields launching from source plane can be gotten by applying (13) and (14) under current situation; the equality of coefficients in front of $\delta(z - z_0)$ and $\delta'(z - z_0)$ provides the equations determining these fields and constraints about the local field $(B_x, B_y) = 4\pi\mu(M_x, M_y)$ and $(E_x, E_y) = 0$. We summarize them from (13) and (14), respectively, for x, y, and z directions:

$$\begin{aligned}
&\frac{\sqrt{\kappa^2 \cos^2\theta + k_{z,o}^2}}{k_o}\left(B_{o,g,-} - B_{o,g,+}\right) \\
&\quad = -i4\pi\tilde{\omega}\mu P_x + i4\pi\mu\kappa \sin\theta M_z, \\
&\frac{\kappa^2 \sin\theta\cos\theta}{k_o\sqrt{\kappa^2 \cos^2\theta + k_{z,o}^2}}\left(B_{o,g,-} - B_{o,g,+}\right) \\
&\quad + \frac{k_{z,e}}{\sqrt{\kappa^2 \cos^2\theta + k_{z,e}^2}}\left(B_{e,g,+} + B_{e,g,-}\right) \\
&\quad = -i4\pi\tilde{\omega}\mu P_y - i4\pi\mu\kappa\cos\theta M_z, \\
&\quad E_z = -\frac{4\pi}{\varepsilon_o}P_z, \\
&\frac{\sqrt{\kappa^2 \cos^2\theta + k_{z,e}^2}}{\tilde{\omega}\mu\varepsilon_e}\left(B_{e,g,+} - B_{e,g,-}\right) \\
&\quad + iE_z\kappa\sin\theta - i\tilde{\omega}B_x = 0, \\
&\frac{k_o}{\tilde{\omega}\mu\varepsilon_o}\frac{k_{z,o}}{\sqrt{k_{z,o}^2 + \kappa^2\cos^2\theta}}\left(B_{o,g,+} + B_{o,g,-}\right) \\
&\quad + \frac{1}{\tilde{\omega}\mu\varepsilon_o}\frac{\kappa^2\sin\theta\cos\theta}{\sqrt{\kappa^2\cos^2\theta + k_{z,e}^2}}\left(B_{e,g,+} - B_{e,g,-}\right) \\
&\quad - iE_z\kappa\cos\theta - i\tilde{\omega}B_y = 0, \\
&\quad B_z = 0.
\end{aligned} \tag{28}$$

After solving (28), the fields launching from the source plane are determined:

$$\begin{aligned}
B_{o,g,+} &= -O_1P_z + O_2P_x + O_3M_y - O_4M_x - O_5M_z, \\
B_{o,g,-} &= -O_1P_z - O_2P_x + O_3M_y - O_4M_x + O_5M_z, \\
B_{e,g,+} &= -\overline{O}_1P_y + \overline{O}_2P_x + \overline{O}_3P_z + \overline{O}_4M_x - \overline{O}_5M_z, \\
B_{e,g,-} &= -\overline{O}_1P_y + \overline{O}_2P_x - \overline{O}_3P_z - \overline{O}_4M_x - \overline{O}_5M_z,
\end{aligned} \tag{29}$$

where the coefficients in front of the source are

$$\begin{aligned}
O_1 &= \left(\frac{i2\pi\kappa\sqrt{\kappa^2\cos^2\theta + k_{z,e}^2}\tilde{\omega}\mu R\cos\theta}{k_o k_{z,o}}\right. \\
&\quad \left. + \frac{i2\pi\kappa^3\tilde{\omega}\mu\varepsilon_e R\sin^2\theta\cos\theta}{k_o k_{z,o}\varepsilon_o\sqrt{\kappa^2\cos^2\theta + k_{z,e}^2}}\right), \\
O_2 &= \frac{i2\pi\tilde{\omega}k_o\mu}{\sqrt{\kappa^2\cos^2\theta + k_{z,o}^2}}, \\
O_3 &= \frac{i2\pi\tilde{\omega}^2\sqrt{\kappa^2\cos^2\theta + k_{z,e}^2}\mu^2\varepsilon_o R}{k_o k_{z,o}}, \\
O_4 &= \frac{i2\pi\tilde{\omega}^2\kappa^2\mu^2\varepsilon_e R\sin\theta\cos\theta}{k_o k_{z,o}\sqrt{\kappa^2\cos^2\theta + k_{z,e}^2}}, \\
O_5 &= \frac{i2\pi\mu\kappa k_o\sin\theta}{\sqrt{\kappa^2\cos^2\theta + k_{z,o}^2}}, \\
\overline{O}_1 &= \frac{i2\pi\tilde{\omega}\sqrt{\kappa^2\cos^2\theta + k_{z,o}^2}\mu}{k_{z,e}R}, \\
\overline{O}_2 &= \frac{i2\pi\tilde{\omega}\kappa^2\mu\sin\theta\cos\theta}{k_{z,e}\sqrt{\kappa^2\cos^2\theta + k_{z,o}^2}R}, \\
\overline{O}_3 &= \frac{i2\pi\tilde{\omega}\kappa\mu\varepsilon_e\sin\theta}{\varepsilon_o\sqrt{\kappa^2\cos^2\theta + k_{z,e}^2}}, \\
\overline{O}_4 &= \frac{i2\pi\tilde{\omega}^2\mu^2\varepsilon_e}{\sqrt{\kappa^2\cos^2\theta + k_{z,e}^2}}, \\
\overline{O}_5 &= \left[\frac{i2\pi\sqrt{\kappa^2\cos^2\theta + k_{z,o}^2}\kappa\mu\cos\theta}{k_{z,e}R}\right. \\
&\quad \left. + \frac{i2\pi\kappa^3\mu\sin^2\theta\cos\theta}{k_{z,e}\sqrt{\kappa^2\cos^2\theta + k_{z,o}^2}R}\right],
\end{aligned} \tag{30}$$

where the coefficient R in (30) is given as $R = \sqrt{k_{z,o}^2 + \kappa^2\cos^2\theta}/\sqrt{k_{z,e}^2 + \kappa^2\cos^2\theta}$. The fields in the regions outside of the anisotropic medium can be determined by

solving boundary equations, and they can be written for $z = 0$ and $z = h$, respectively, as

$$\begin{aligned}
&\frac{-\kappa^2 \sin\theta\cos\theta}{k_o\sqrt{\kappa^2 \cos^2\theta + k_{z,o}^2}}\left(B_{o,b,+} + B_{o,b,-} + B_{o,g,-}e^{ik_{z,o}z_0}\right)\\
&\quad + \frac{k_{z,e}}{\sqrt{\kappa^2 \cos^2\theta + k_{z,e}^2}}\left(B_{e,b,+} - B_{e,b,-} - B_{e,g,-}e^{ik_{z,e}z_0}\right)\\
&\quad = \frac{-B_{s,-}k_{z,\mathrm{I}}}{\widetilde{\omega}}\cos\theta + B_{p,-}\sin\theta,\\
&\frac{\sqrt{\kappa^2 \cos^2\theta + k_{z,o}^2}}{k_o}\left(B_{o,b,+} + B_{o,b,-} + B_{o,g,-}e^{ik_{z,o}z_0}\right)\\
&\quad = \frac{-B_{s,-}k_{z,\mathrm{I}}}{\widetilde{\omega}}\sin\theta - B_{p,-}\cos\theta,\\
&\left(B_{o,b,+} - B_{o,b,-} - B_{o,g,-}e^{ik_{z,o}z_0}\right)\frac{k_o k_{z,o}}{\widetilde{\omega}\mu\varepsilon_o\sqrt{\kappa^2\cos^2\theta + k_{z,o}^2}}\\
&\quad + \left(B_{e,b,+} + B_{e,b,-} + B_{e,g,-}e^{ik_{z,e}z_0}\right)\frac{\kappa^2\sin\theta\cos\theta}{\widetilde{\omega}\mu\varepsilon_o\sqrt{\kappa^2\cos^2\theta + k_{z,e}^2}}\\
&\quad = B_{s,-}\sin\theta + B_{p,-}\frac{k_{z,\mathrm{I}}}{\widetilde{\omega}}\cos\theta,\\
&\left(B_{e,b,+} + B_{e,b,-} + B_{e,g,-}e^{ik_{z,e}z_0}\right)\frac{\left(-k_{z,e}^2 - \kappa^2\cos^2\theta\right)}{\widetilde{\omega}\mu\varepsilon_e\sqrt{\kappa^2\cos^2\theta + k_{z,e}^2}}\\
&\quad = -B_{s,-}\cos\theta + B_{p,-}\frac{k_{z,\mathrm{I}}}{\widetilde{\omega}}\sin\theta,\\
&\left(B_{o,b,+}e^{ik_{z,o}h} + B_{o,g,+}e^{ik_{z,o}(h-z_0)} + B_{o,b,-}e^{-ik_{z,o}h}\right)\\
&\quad \times \frac{-\kappa^2\sin\theta\cos\theta}{k_o\sqrt{\kappa^2\cos^2\theta + k_{z,o}^2}}\\
&\quad + \left(B_{e,b,+}e^{ik_{z,e}h} + B_{e,g,+}e^{ik_{z,e}(h-z_0)} - B_{e,b,-}e^{-ik_{z,e}h}0\right)\\
&\quad \times \frac{k_{z,e}}{\sqrt{\kappa^2\cos^2\theta + k_{z,e}^2}}\\
&\quad = \frac{k_{z,\mathrm{III}}B_{s,+}e^{ik_{z,\mathrm{III}}h}}{\widetilde{\omega}}\cos\theta + B_{p,+}e^{ik_{z,\mathrm{III}}h}\sin\theta\\
&\left(B_{o,b,+}e^{ik_{z,o}h} + B_{o,g,+}e^{ik_{z,o}(h-z_0)} + B_{o,b,-}e^{-ik_{z,o}h}\right)\\
&\quad \times \frac{\sqrt{\kappa^2\cos^2\theta + k_{z,o}^2}}{k_o}\\
&\quad = \frac{k_{z,\mathrm{III}}B_{s,+}e^{ik_{z,\mathrm{III}}h}}{\widetilde{\omega}}\sin\theta - B_{p,+}e^{ik_{z,\mathrm{III}}h}\cos\theta\\
&\left(B_{o,b,+}e^{ik_{z,o}h} + B_{o,g,+}e^{ik_{z,o}(h-z_0)} - B_{o,b,-}e^{-ik_{z,o}h}\right)\\
&\quad \times \frac{k_o k_{z,o}}{\varepsilon_o\widetilde{\omega}\mu\sqrt{\kappa^2\cos^2\theta + k_{z,o}^2}}\\
&\quad + \left(B_{e,b,+}e^{ik_{z,e}h} + B_{e,g,+}e^{ik_{z,e}(h-z_0)} + B_{e,b,-}e^{-ik_{z,e}h}\right)\\
&\quad \times \frac{\kappa^2\sin\theta\cos\theta}{\varepsilon_o\widetilde{\omega}\mu\sqrt{\kappa^2\cos^2\theta + k_{z,e}^2}}\\
&\quad = B_{s,+}e^{ik_{z,\mathrm{III}}h}\sin\theta - B_{p,+}e^{ik_{z,\mathrm{III}}h}\frac{k_{z,\mathrm{III}}}{\widetilde{\omega}}\cos\theta\\
&\left(B_{e,b,+}e^{ik_{z,e}h} + B_{e,g,+}e^{ik_{z,e}(h-z_0)} + B_{e,b,-}e^{-ik_{z,e}h}\right)\\
&\quad \times \frac{-k_{z,e}^2 - \kappa^2\cos^2\theta}{\widetilde{\omega}\mu\varepsilon_e\sqrt{\kappa^2\cos^2\theta + k_{z,e}^2}}\\
&\quad = -B_{s,+}e^{ik_{z,\mathrm{III}}h}\cos\theta - B_{p,+}e^{ik_{z,\mathrm{III}}h}\frac{k_{z,\mathrm{III}}}{\widetilde{\omega}}\sin\theta.
\end{aligned} \tag{31}$$

From these equations, the origin of mode conversion is obviously accounted by the equations with both o- and e-mode. After solving the fields in regions I and III and linking to the sources with the help of (29), we can get Green functions for these regions:

$$\begin{aligned}
G_{B,P}^{\mathrm{I}} = &\left(\begin{bmatrix}
\left(-W_2O_2e^{ik_{z,o}z_0} - W_1O_2e^{-ik_{z,o}z_0} + W_5\overline{O}_2e^{ik_{z,e}z_0} + W_4\overline{O}_2e^{-ik_{z,e}z_0}\right)\hat{h}_{s,-}^{\mathrm{I}}\hat{x}\\
-\left(W_5\overline{O}_1e^{ik_{z,e}z_0} + W_4\overline{O}_1e^{-ik_{z,e}z_0}\right)\hat{h}_{s,-}^{\mathrm{I}}\hat{y}\\
+\left(-W_2O_1e^{ik_{z,o}z_0} + W_1O_1e^{-ik_{z,o}z_0} - W_5\overline{O}_3e^{ik_{z,e}z_0} + W_4\overline{O}_3e^{-ik_{z,e}z_0}\right)\hat{h}_{s,-}^{\mathrm{I}}\hat{z}
\end{bmatrix}\right.\\
&\left.+\begin{bmatrix}
\left(W_3O_2e^{ik_{z,o}z_0} - W_1O_2e^{-ik_{z,o}z_0} - W_7\overline{O}_2e^{ik_{z,e}z_0} - W_6\overline{O}_2e^{-ik_{z,e}z_0}\right)\hat{h}_{p,-}^{\mathrm{I}}\hat{x}\\
+\left(W_7\overline{O}_1e^{ik_{z,e}z_0} + W_6\overline{O}_1e^{-ik_{z,e}z_0}\right)\hat{h}_{p,-}^{\mathrm{I}}\hat{y}\\
+\left(W_3O_1e^{ik_{z,o}z_0} + W_1O_1e^{-ik_{z,o}z_0} + W_7\overline{O}_3e^{ik_{z,e}z_0} - W_6\overline{O}_3e^{-ik_{z,e}z_0}\right)
\end{bmatrix}\right)\\
&\times \exp\left(i\,\vec{\kappa}\cdot\vec{R}\right)\exp(-ik_{z,\mathrm{I}}z),
\end{aligned}$$

$$G^{\mathrm{I}}_{E,P} = \left(\begin{bmatrix} \left(-W_2O_2e^{ik_{z,o}z_0} - W_1O_2e^{-ik_{z,o}z_0} + W_5\overline{O}_2e^{ik_{z,e}z_0} + W_4\overline{O}_2e^{-ik_{z,e}z_0}\right)\hat{e}^{\mathrm{I}}_{s,-}\hat{x} \\ -\left(W_5\overline{O}_1e^{ik_{z,e}z_0} + W_4\overline{O}_1e^{-ik_{z,e}z_0}\right)\hat{e}^{\mathrm{I}}_{s,-}\hat{y} \\ +\left(-W_2O_1e^{ik_{z,o}z_0} + W_1O_1e^{-ik_{z,o}z_0} - W_5\overline{O}_3e^{ik_{z,e}z_0} + W_4\overline{O}_3e^{-ik_{z,e}z_0}\right)\hat{e}^{\mathrm{I}}_{s,-}\hat{z} \end{bmatrix} + \begin{bmatrix} \left(W_3O_2e^{ik_{z,o}z_0} - W_1O_2e^{-ik_{z,o}z_0} - W_7\overline{O}_2e^{ik_{z,e}z_0} - W_6\overline{O}_2e^{-ik_{z,e}z_0}\right)\hat{e}^{\mathrm{I}}_{p,-}\hat{x} \\ +\left(W_7\overline{O}_1e^{ik_{z,e}z_0} + W_6\overline{O}_1e^{-ik_{z,e}z_0}\right)\hat{e}^{\mathrm{I}}_{p,-}\hat{y} \\ +\left(W_3O_1e^{ik_{z,o}z_0} + W_1O_1e^{-ik_{z,o}z_0} + W_7\overline{O}_3e^{ik_{z,e}z_0} - W_6\overline{O}_3e^{-ik_{z,e}z_0}\right)\hat{e}^{\mathrm{I}}_{p,-}\hat{z} \end{bmatrix} \right) \times \exp\left(i\,\vec{\kappa}\cdot\vec{R}\right)\exp(-ik_{z,1}z),$$

$$G^{\mathrm{I}}_{B,M} = \left(\begin{bmatrix} \left(-W_2O_4e^{ik_{z,o}z_0} + W_1O_4e^{-ik_{z,o}z_0} - W_5\overline{O}_4e^{ik_{z,e}z_0} + W_4\overline{O}_4e^{-ik_{z,e}z_0}\right)\hat{h}^{\mathrm{I}}_{s,-}\hat{x} \\ +\left(W_2O_3e^{ik_{z,o}z_0} - W_1O_3e^{-ik_{z,o}z_0}\right)\hat{h}^{\mathrm{I}}_{s,-}\hat{y} \\ +\left(W_2O_5e^{ik_{z,o}z_0} + W_1O_5e^{-ik_{z,o}z_0} - W_5\overline{O}_5e^{ik_{z,e}z_0} - W_4\overline{O}_5e^{-ik_{z,e}z_0}\right)\hat{h}^{\mathrm{I}}_{s,-}\hat{z} \end{bmatrix} + \begin{bmatrix} \left(W_3O_4e^{ik_{z,o}z_0} + W_1O_4e^{-ik_{z,o}z_0} + W_7\overline{O}_4e^{ik_{z,e}z_0} - W_6\overline{O}_4e^{-ik_{z,e}z_0}\right)\hat{h}^{\mathrm{I}}_{p,-}\hat{x} \\ -\left(W_3O_3e^{ik_{z,o}z_0}M_y + W_1O_3e^{-ik_{z,o}z_0}\right)\hat{h}^{\mathrm{I}}_{p,-}\hat{y} \\ +\left(-W_3O_5e^{ik_{z,o}z_0} + W_1O_5e^{-ik_{z,o}z_0} + W_7\overline{O}_5e^{ik_{z,e}z_0} + W_6\overline{O}_5e^{-ik_{z,e}z_0}\right)\hat{h}^{\mathrm{I}}_{p,-}\hat{z} \end{bmatrix} \right) \times \exp\left(i\,\vec{\kappa}\cdot\vec{R}\right)\exp(-ik_{z,1}z),$$

$$G^{\mathrm{I}}_{E,M} = \left(\begin{bmatrix} \left(-W_2O_4e^{ik_{z,o}z_0} + W_1O_4e^{-ik_{z,o}z_0} - W_5\overline{O}_4e^{ik_{z,e}z_0} + W_4\overline{O}_4e^{-ik_{z,e}z_0}\right)\hat{e}^{\mathrm{I}}_{s,-}\hat{x} \\ +\left(W_2O_3e^{ik_{z,o}z_0} - W_1O_3e^{-ik_{z,o}z_0}\right)\hat{e}^{\mathrm{I}}_{s,-}\hat{y} \\ +\left(W_2O_5e^{ik_{z,o}z_0} + W_1O_5e^{-ik_{z,o}z_0} - W_5\overline{O}_5e^{ik_{z,e}z_0} - W_4\overline{O}_5e^{-ik_{z,e}z_0}\right)\hat{e}^{\mathrm{I}}_{s,-}\hat{z} \end{bmatrix} + \begin{bmatrix} \left(W_3O_4e^{ik_{z,o}z_0} + W_1O_4e^{-ik_{z,o}z_0} + W_7\overline{O}_4e^{ik_{z,e}z_0} - W_6\overline{O}_4e^{-ik_{z,e}z_0}\right)\hat{e}^{\mathrm{I}}_{p,-}\hat{x} \\ -\left(W_3O_3e^{ik_{z,o}z_0}M_y + W_1O_3e^{-ik_{z,o}z_0}\right)\hat{e}^{\mathrm{I}}_{p,-}\hat{y} \\ +\left(-W_3O_5e^{ik_{z,o}z_0} + W_1O_5e^{-ik_{z,o}z_0} + W_7\overline{O}_5e^{ik_{z,e}z_0} + W_6\overline{O}_5e^{-ik_{z,e}z_0}\right)\hat{e}^{\mathrm{I}}_{p,-}\hat{z} \end{bmatrix} \right) \times \exp\left(i\,\vec{\kappa}\cdot\vec{R}\right)\exp(-ik_{z,1}z),$$

$$G^{\mathrm{III}}_{B,P} = \left(\begin{bmatrix} \left(-W_1O_2e^{-ik_{z,o}(h-z_0)} - W_2O_2e^{ik_{z,o}(h-z_0)} + W_4\overline{O}_2e^{-ik_{z,e}(h-z_0)} + W_5\overline{O}_2e^{ik_{z,e}(h-z_0)}\right)\hat{h}^{\mathrm{III}}_{s,+}\hat{x} \\ -\left(W_4\overline{O}_1e^{-ik_{z,e}(h-z_0)} + W_5\overline{O}_1e^{ik_{z,e}(h-z_0)}\right)\hat{h}^{\mathrm{III}}_{s,+}\hat{y} \\ +\left(-W_1O_1e^{-ik_{z,o}(h-z_0)} + W_2O_1e^{ik_{z,o}(h-z_0)} - W_4\overline{O}_3e^{-ik_{z,e}(h-z_0)} + W_5\overline{O}_3e^{ik_{z,e}(h-z_0)}\right)\hat{h}^{\mathrm{III}}_{s,+}\hat{z} \end{bmatrix} + \begin{bmatrix} \left(W_1O_2e^{-ik_{z,o}(h-z_0)} - W_3O_2e^{ik_{z,o}(h-z_0)} + W_6\overline{O}_2e^{-ik_{z,e}(h-z_0)} + W_7\overline{O}_2e^{ik_{z,e}(h-z_0)}\right)\hat{h}^{\mathrm{III}}_{p,+}\hat{x} \\ -\left(W_6\overline{O}_1e^{-ik_{z,e}(h-z_0)} + W_7\overline{O}_1e^{ik_{z,e}(h-z_0)}\right)\hat{h}^{\mathrm{III}}_{p,+}\hat{y} \\ +\left(W_1O_1e^{-ik_{z,o}(h-z_0)} + W_3O_1e^{ik_{z,o}(h-z_0)} - W_6\overline{O}_3e^{-ik_{z,e}(h-z_0)} + W_7\overline{O}_3e^{ik_{z,e}(h-z_0)}\right)\hat{h}^{\mathrm{III}}_{p,+}\hat{z} \end{bmatrix} \right) \times \exp\left(i\,\vec{\kappa}\cdot\vec{R}\right)\exp(ik_{z,\mathrm{III}}(z-h)),$$

$$
G^{\mathrm{III}}_{E,P} = \left(\begin{bmatrix} \left(-W_1 O_2 e^{-ik_{z,o}(h-z_0)} - W_2 O_2 e^{ik_{z,o}(h-z_0)} + W_4 \overline{O}_2 e^{-ik_{z,e}(h-z_0)} + W_5 \overline{O}_2 e^{ik_{z,e}(h-z_0)}\right) \hat{e}^{\mathrm{III}}_{s,+} \hat{x} \\ -\left(W_4 \overline{O}_1 e^{-ik_{z,e}(h-z_0)} + W_5 \overline{O}_1 e^{ik_{z,e}(h-z_0)}\right) \hat{e}^{\mathrm{III}}_{s,+} \hat{y} \\ +\left(-W_1 O_1 e^{-ik_{z,o}(h-z_0)} + W_2 O_1 e^{ik_{z,o}(h-z_0)} - W_4 \overline{O}_3 e^{-ik_{z,e}(h-z_0)} + W_5 \overline{O}_3 e^{ik_{z,e}(h-z_0)}\right) \hat{e}^{\mathrm{III}}_{s,+} \hat{z} \end{bmatrix} \right.
$$

$$
\left. + \begin{bmatrix} \left(W_1 O_2 e^{-ik_{z,o}(h-z_0)} - W_3 O_2 e^{ik_{z,o}(h-z_0)} + W_6 \overline{O}_2 e^{-ik_{z,e}(h-z_0)} + W_7 \overline{O}_2 e^{ik_{z,e}(h-z_0)}\right) \hat{e}^{\mathrm{III}}_{p,+} \hat{x} \\ -\left(W_6 \overline{O}_1 e^{-ik_{z,e}(h-z_0)} + W_7 \overline{O}_1 e^{ik_{z,e}(h-z_0)}\right) \hat{e}^{\mathrm{III}}_{p,+} \hat{y} \\ +\left(W_1 O_1 e^{-ik_{z,o}(h-z_0)} + W_3 O_1 e^{ik_{z,o}(h-z_0)} - W_6 \overline{O}_3 e^{-ik_{z,e}(h-z_0)} + W_7 \overline{O}_3 e^{ik_{z,e}(h-z_0)}\right) \hat{e}^{\mathrm{III}}_{p,+} \hat{z} \end{bmatrix} \right)
$$

$$
\times \exp\left(i \vec{\kappa} \cdot \vec{R}\right) \exp\left(ik_{z,\mathrm{III}}(z-h)\right),
$$

$$
G^{\mathrm{III}}_{B,M} = \left(\begin{bmatrix} \left(-W_1 O_4 e^{-ik_{z,o}(h-z_0)} + W_2 O_4 e^{ik_{z,o}(h-z_0)} - W_4 \overline{O}_4 e^{-ik_{z,e}(h-z_0)} + W_5 \overline{O}_4 e^{ik_{z,e}(h-z_0)}\right) \hat{h}^{\mathrm{III}}_{s,+} \hat{x} \\ +\left(W_1 O_3 e^{-ik_{z,o}(h-z_0)} - W_2 O_3 e^{ik_{z,o}(h-z_0)}\right) \hat{h}^{\mathrm{III}}_{s,+} \hat{y} \\ +\left(-W_4 \overline{O}_5 e^{-ik_{z,e}(h-z_0)} + W_2 O_5 e^{ik_{z,o}(h-z_0)} e^{-ik_z h} + W_1 O_5 e^{-ik_{z,o}(h-z_0)} - W_5 \overline{O}_5 e^{ik_{z,e}(h-z_0)}\right) \hat{h}^{\mathrm{III}}_{s,+} \hat{z} \end{bmatrix} \right.
$$

$$
\left. + \begin{bmatrix} \left(W_1 O_4 e^{-ik_{z,o}(h-z_0)} + W_3 O_4 e^{ik_{z,o}(h-z_0)} - W_6 \overline{O}_4 e^{-ik_{z,e}(h-z_0)} + W_7 \overline{O}_4 e^{ik_{z,e}(h-z_0)}\right) \hat{h}^{\mathrm{III}}_{p,+} \hat{x} \\ -\left(W_1 O_3 e^{-ik_{z,o}(h-z_0)} + W_3 O_3 e^{ik_{z,o}(h-z_0)}\right) \hat{h}^{\mathrm{III}}_{p,+} \hat{y} \\ +\left(-W_1 O_5 e^{-ik_{z,o}(h-z_0)} + W_3 O_5 e^{ik_{z,o}(h-z_0)} - W_6 \overline{O}_5 e^{-ik_{z,e}(h-z_0)} - W_7 \overline{O}_5 e^{ik_{z,e}(h-z_0)}\right) \hat{h}^{\mathrm{III}}_{p,+} \hat{z} \end{bmatrix} \right)
$$

$$
\times \exp\left(i \vec{\kappa} \cdot \vec{R}\right) \exp\left(ik_{z,\mathrm{III}}(z-h)\right),
$$

$$
G^{\mathrm{III}}_{E,M} = \left(\begin{bmatrix} \left(-W_1 O_4 e^{-ik_{z,o}(h-z_0)} + W_2 O_4 e^{ik_{z,o}(h-z_0)} - W_4 \overline{O}_4 e^{-ik_{z,e}(h-z_0)} + W_5 \overline{O}_4 e^{ik_{z,e}(h-z_0)}\right) \hat{e}^{\mathrm{III}}_{s,+} \hat{x} \\ +\left(W_1 O_3 e^{-ik_{z,o}(h-z_0)} - W_2 O_3 e^{ik_{z,o}(h-z_0)}\right) \hat{e}^{\mathrm{III}}_{s,+} \hat{y} \\ +\left(-W_4 \overline{O}_5 e^{-ik_{z,e}(h-z_0)} + W_2 O_5 e^{ik_{z,o}(h-z_0)} e^{-ik_z h} + W_1 O_5 e^{-ik_{z,o}(h-z_0)} - W_5 \overline{O}_5 e^{ik_{z,e}(h-z_0)}\right) \hat{e}^{\mathrm{III}}_{s,+} \hat{z} \end{bmatrix} \right.
$$

$$
\left. + \begin{bmatrix} \left(W_1 O_4 e^{-ik_{z,o}(h-z_0)} + W_3 O_4 e^{ik_{z,o}(h-z_0)} - W_6 \overline{O}_4 e^{-ik_{z,e}(h-z_0)} + W_7 \overline{O}_4 e^{ik_{z,e}(h-z_0)}\right) \hat{e}^{\mathrm{III}}_{p,+} \hat{x} \\ -\left(W_1 O_3 e^{-ik_{z,o}(h-z_0)} + W_3 O_3 e^{ik_{z,o}(h-z_0)}\right) \hat{e}^{\mathrm{III}}_{p,+} \hat{y} \\ +\left(-W_1 O_5 e^{-ik_{z,o}(h-z_0)} + W_3 O_5 e^{ik_{z,o}(h-z_0)} - W_6 \overline{O}_5 e^{-ik_{z,e}(h-z_0)} - W_7 \overline{O}_5 e^{ik_{z,e}(h-z_0)}\right) \hat{e}^{\mathrm{III}}_{p,+} \hat{z} \end{bmatrix} \right)
$$

$$
\times \exp\left(i \vec{\kappa} \cdot \vec{R}\right) \exp\left(ik_{z,\mathrm{III}}(z-h)\right). \tag{32}
$$

The green functions in (32) describe the relation between the fields generated outside of the uniaxial crystal and the source embedded in uniaxial crystal. (The parameters (W_i, $i = 1, 2, \ldots, 7$) in (32) will be given in Appendix A.)

3.2. Sources in Biaxial Crystal. In the subsection, the Green functions linking the fields in region I and III and sources embedded in biaxial crystal in region II are given. The relative permittivity tensor now has the form diag($\varepsilon_1, \varepsilon_2, \varepsilon_3$) with

$\varepsilon_1 \neq \varepsilon_2 \neq \varepsilon_3$. Thus, the equation determining the dispersions of eigenmodes now becomes

$$\widetilde{\omega}^4 - \widetilde{\omega}^2\left(\frac{k_x^2+k_y^2}{\varepsilon_3\mu}+\frac{k_x^2+k_z^2}{\varepsilon_2\mu}+\frac{k_z^2+k_y^2}{\varepsilon_1\mu}\right) + \left(\frac{k_x^2}{\varepsilon_2\varepsilon_3\mu^2}+\frac{k_y^2}{\varepsilon_1\varepsilon_3\mu^2}+\frac{k_z^2}{\varepsilon_1\varepsilon_3\mu^2}\right)\left(k_x^2+k_z^2+k_y^2\right) = 0. \tag{33}$$

The dispersion can be gotten as followes: $k_{z,1}^2 = (-b+\sqrt{b^2-4ac})/2a$ and $k_{z,2}^2 = (-b-\sqrt{b^2-4ac})/2a$ (each of them denotes two modes propagating (or decaying) along positive and negative z direction), where a, b, and c are, respectively, the coefficients in front of the fourth-order, second-order and zeroth-order terms of k_z, and they have the following concrete forms:

$$a = \frac{1}{\varepsilon_1\varepsilon_3\mu}, \qquad b = \frac{k_x^2}{\varepsilon_2\varepsilon_3\mu}+\frac{k_y^2}{\varepsilon_1\varepsilon_3\mu}-\frac{\widetilde{\omega}^2}{\varepsilon_2\mu}-\frac{\widetilde{\omega}^2}{\varepsilon_1\mu},$$

$$c = \left(k_x^2+k_y^2\right)\left(\frac{k_x^2}{\varepsilon_2\varepsilon_3\mu}+\frac{k_y^2}{\varepsilon_1\varepsilon_3\mu}\right) + k_x^2\left(\frac{1}{\varepsilon_3\mu}+\frac{\widetilde{\omega}^2}{\varepsilon_2\mu}\right)+k_y^2\left(\frac{1}{\varepsilon_3\mu}+\frac{\widetilde{\omega}^2}{\varepsilon_1\mu}\right)+\widetilde{\omega}^4. \tag{34}$$

The corresponding unit vectors of electric fields of eigenmodes can be solved as [23]

$$\hat{e}_{i,\pm} = \left(X_i^2+1+Z_i^2\right)^{-1/2}(X_i, 1, \pm Z_i), \tag{35}$$

where

$$X_i = \frac{\kappa^2\cos\theta\sin\theta\left(\kappa^2+k_{z,i}^2-\widetilde{\omega}^2\varepsilon_3\mu\right)}{\left(\widetilde{\omega}^2\varepsilon_1\mu-k_{z,i}^2-\kappa^2\sin^2\theta\right)\left(\widetilde{\omega}^2\varepsilon_3\mu-\kappa^2\right)-\kappa^2\cos^2\theta k_{z,i}^2}$$

$$Z_i = \frac{k_{z,i}\kappa\sin\theta\left(\kappa^2+k_{z,i}^2-\widetilde{\omega}^2\varepsilon_1\mu\right)}{\left(\widetilde{\omega}^2\varepsilon_1\mu-\kappa^2\sin^2\theta-k_{z,i}^2\right)\left(\widetilde{\omega}^2\varepsilon_3\mu-\kappa^2\right)-\kappa^2\cos^2\theta k_{z,i}^2}. \tag{36}$$

In (36) $k_{z,i}$ is a positive square root from $k_{z,i}^2$ so that it denotes the propagating or decaying wave along positive z direction. Thus, the unit vectors of electric displacement vector and magnetic field can be gotten as

$$\hat{d}_{i,\pm} = \left(\varepsilon_1^2X_i^2+\varepsilon_2^2+\varepsilon_3^2Z_i^2\right)^{-1/2}(\varepsilon_1X_i, \varepsilon_2, \pm\varepsilon_3Z_i),$$

$$\hat{h}_{i,\pm} = \frac{1}{N_i}\left(\pm\left(\kappa\sin\theta Z_i-k_{z,i}\right), \pm\left(k_{z,i}X_i-Z_i\kappa\cos\theta\right), \left(\kappa\cos\theta-\kappa\sin\theta X_i\right)\right), \tag{37}$$

$$\text{where } N_i = \sqrt{\left(\kappa\sin\theta Z_i-k_{z,i}\right)^2+\left(k_{z,i}X_i-Z_i\kappa\cos\theta\right)^2+\left(\kappa\cos\theta-\kappa\sin\theta X_i\right)^2}.$$

Then we can determine the fields launching from the source plane with the help of these unit vectors defined. The general equations (13) and (14) can be mapped to concrete forms with each equation gotten giving the field equality in different directions. The relations, $(B_x, B_y) = 4\pi\mu(M_x, M_y)$ and $(E_x, E_y) = 0$, are found again by following the fact of vanishing of the coefficients in front of δ' function. The equations determining the fields launching from the source plane are:

$$\begin{aligned}
&\frac{k_1}{\widetilde{\omega}\mu\left(\varepsilon_1^2X_1^2+\varepsilon_2^2+\varepsilon_3^2Z_1^2\right)^{1/2}}\left[B_{1,g,-}-B_{1,g,+}\right]\\
&+\frac{k_2}{\widetilde{\omega}\mu\left(\varepsilon_1^2X_2^2+\varepsilon_2^2+\varepsilon_3^2Z_2^2\right)^{1/2}}\left[B_{2,g,-}-B_{2,g,+}\right]\\
&+iE_z\kappa\sin\theta = i\widetilde{\omega}B_x,\\
&\frac{X_1k_1}{\widetilde{\omega}\mu\left(\varepsilon_1^2X_1^2+\varepsilon_2^2+\varepsilon_3^2Z_1^2\right)^{1/2}}\left[B_{1,g,-}-B_{1,g,+}\right]\\
&+\frac{X_2k_2}{\widetilde{\omega}\mu\left(\varepsilon_1^2X_2^2+\varepsilon_2^2+\varepsilon_3^2Z_2^2\right)^{1/2}}\left[B_{2,g,-}-B_{2,g,+}\right]\\
&-iE_z\kappa\cos\theta = i\widetilde{\omega}B_y,
\end{aligned}$$

$$\begin{aligned}
&B_z = 0\\
&-\frac{\left(k_{z,1}X_1-Z_1\kappa\cos\theta\right)}{N_1}\left(B_{1,g,+}+B_{1,g,-}\right)\\
&-\frac{\left(k_{z,2}X_2-Z_2\kappa\cos\theta\right)}{N_2}\left(B_{2,g,+}+B_{2,g,-}\right)\\
&= -i4\pi\widetilde{\omega}\mu P_x + i4\pi\mu\kappa\sin\theta M_z,\\
&\frac{\left(\kappa\sin\theta Z_1-k_{z,1}\right)}{N_1}\left(B_{1,g,+}+B_{1,g,-}\right)\\
&+\frac{\left(\kappa\sin\theta Z_2-k_{z,2}\right)}{N_2}\left(B_{2,g,+}+B_{2,g,-}\right)\\
&= -i4\pi\widetilde{\omega}\mu P_y - i4\pi\mu\kappa\cos\theta M_z,\\
&E_z = -\frac{4\pi}{\varepsilon_3}P_z,
\end{aligned} \tag{38}$$

where $k_1 = \sqrt{\kappa^2+k_{z,1}^2}$ and $k_2 = \sqrt{\kappa^2+k_{z,2}^2}$. The solutions of (35) and (36) give the relations between the fields launching

from the source plane and the sources as

$$
\begin{aligned}
B_{1,g,-} &= \frac{1}{2}\left(V_{10}P_x + V_{11}P_y + V_{12}M_z + V_1M_x + V_2M_y + V_3P_z\right)\\
B_{1,g,+} &= \frac{1}{2}\left(V_{10}P_x + V_{11}P_y + V_{12}M_z - V_1M_x - V_2M_y - V_3P_z\right)\\
B_{2,g,-} &= \frac{1}{2}\left(V_7P_x + V_8P_y + V_9M_z + V_4M_x + V_5M_y + V_6P_z\right)\\
B_{2,g,+} &= \frac{1}{2}\left(V_7P_x + V_8P_y + V_9M_z - V_4M_x - V_5M_y - V_6P_z\right).
\end{aligned}
\tag{39}
$$

The details of the definitions of parameters V_i ($i = 1, 2, \ldots, 12$) in (39) are given in Appendix B. To determine the fields generated in regions I and III, the boundary equations should be solved, and we firstly write down their concrete forms from the continuity of the tangential fields for the interfaces at $z = 0$ and $z = h$, respectively (we have used the fact that $k_z = k_{z,\mathrm{I}} = k_{z,\mathrm{III}}$ in the following equations, when $\vec{\kappa}$ is the same),

$$
\begin{aligned}
&S_1\left(B_{1,b,+} - B_{1,b,-} - B_{1,g,-}e^{ik_{z,1}z_0}\right)\\
&\quad + S_2\left(B_{2,b,+} - B_{2,b,-} - B_{2,g,-}e^{ik_{z,2}z_0}\right)\\
&\quad = \frac{-B_{s,-}k_z}{\widetilde{\omega}}\cos\theta + B_{p,-}\sin\theta,\\
&S_3\left(B_{1,b,+} - B_{1,b,-} - B_{1,g,-}e^{ik_{z,1}z_0}\right)\\
&\quad + S_4\left(B_{2,b,+} - B_{2,b,-} - B_{2,g,-}e^{ik_{z,2}z_0}\right)\\
&\quad = \frac{-B_{s,-}k_z}{\widetilde{\omega}}\sin\theta - B_{p,-}\cos\theta,\\
&S_5X_1\left(B_{1,b,+} + B_{1,b,-} + B_{1,g,-}e^{ik_{z,1}z_0}\right)\\
&\quad + S_6X_2\left(B_{2,b,+} + B_{2,b,-} + B_{2,g,-}e^{ik_{z,2}z_0}\right)\\
&\quad = B_{s,-}\sin\theta + B_{p,-}\frac{k_z}{\widetilde{\omega}}\cos\theta,\\
&S_5\left(B_{1,b,+} + B_{1,b,-} + B_{1,g,-}e^{ik_{z,1}z_0}\right)\\
&\quad + S_6\left(B_{2,b,+} + B_{2,b,-} + B_{2,g,-}e^{ik_{z,2}z_0}\right)\\
&\quad = -B_{s,-}\cos\theta + B_{p,-}\frac{k_z}{\widetilde{\omega}}\sin\theta,\\
&S_1\left(B_{1,b,+}e^{ik_{z,1}h} - B_{1,b,-}e^{-ik_{z,1}h} + B_{1,g,+}e^{ik_{z,1}(h-z_0)}\right)\\
&\quad + S_2\left(B_{2,b,+}e^{ik_{z,2}h} - B_{2,b,-}e^{-ik_{z,2}h} + B_{2,g,+}e^{ik_{z,2}(h-z_0)}\right)\\
&\quad = \frac{k_z\cos\theta}{\widetilde{\omega}}B_{s,+}e^{ik_zh} + \sin\theta B_{p,+}e^{ik_zh},\\
&S_3\left(B_{1,b,+}e^{ik_{z,1}h} - B_{1,b,-}e^{-ik_{z,1}h} + B_{1,g,+}e^{ik_{z,1}(h-z_0)}\right)\\
&\quad + S_4\left(B_{2,b,+}e^{ik_{z,2}h} - B_{2,b,-}e^{-ik_{z,2}h} + B_{2,g,+}e^{ik_{z,2}(h-z_0)}\right)\\
&\quad = \frac{k_z\sin\theta}{\widetilde{\omega}}B_{s,+}e^{ik_zh} - \cos\theta B_{p,+}e^{ik_zh},\\
&S_5X_1\left(B_{1,b,+}e^{ik_{z,1}h} + B_{1,b,-}e^{-ik_{z,1}h} + B_{1,g,+}e^{ik_{z,1}(h-z_0)}\right)\\
&\quad + S_6X_2\left(B_{2,b,+}e^{ik_{z,2}h} + B_{2,b,-}e^{-ik_{z,2}h} + B_{2,g,+}e^{ik_{z,2}(h-z_0)}\right)\\
&\quad = \sin\theta B_{s,+}e^{ik_zh} - \frac{k_z\cos\theta}{\widetilde{\omega}}B_{p,+}e^{ik_zh}\\
&S_5\left(B_{1,b,+}e^{ik_{z,1}h} + B_{1,b,-}e^{-ik_{z,1}h} + B_{1,g,+}e^{ik_{z,1}(h-z_0)}\right)\\
&\quad + S_6\left(B_{2,b,+}e^{ik_{z,2}h} + B_{2,b,-}e^{-ik_{z,2}h} + B_{2,g,+}e^{ik_{z,2}(h-z_0)}\right)\\
&\quad = -\cos\theta B_{s,+}e^{ik_zh} - \frac{k_z\sin\theta}{\widetilde{\omega}}B_{p,+}e^{ik_zh},
\end{aligned}
\tag{40}
$$

where the parameters are given as

$$
\begin{aligned}
S_1 &= \frac{\kappa\sin\theta Z_1 - k_{z,1}}{N_1}, \qquad S_2 = \frac{\kappa\sin\theta Z_2 - k_{z,2}}{N_2},\\
S_3 &= \frac{k_{z,1}X_1 - Z_1\kappa\cos\theta}{N_1}, \qquad S_4 = \frac{k_{z,2}X_2 - Z_2\kappa\cos\theta}{N_2},\\
S_5 &= \frac{k_1}{\widetilde{\omega}\mu\sqrt{\varepsilon_1^2X_1^2 + \varepsilon_2^2 + \varepsilon_3^2Z_1^2}},\\
S_6 &= \frac{k_2}{\widetilde{\omega}\mu\sqrt{\varepsilon_1^2X_2^2 + \varepsilon_2^2 + \varepsilon_3^2Z_2^2}}.
\end{aligned}
\tag{41}
$$

The fields in regions I and III can be solved out from (40) and (41). Consequently, the Green functions relating them to the sources in biaxial crystal can be gotten with the help of (39) and the definitions given in (8):

$$
\begin{aligned}
G^{\mathrm{I}}_{B,P} = \frac{1}{2}\Bigg(&\begin{bmatrix}
\left(U_2V_{10}e^{ik_{z,1}z_0} - U_1V_{10}e^{-ik_{z,1}z_0} + U_5V_7e^{ik_{z,2}z_0} + U_4V_7e^{-ik_{z,2}z_0}\right)\hat{h}^{\mathrm{I}}_{s,-}\hat{x}\\
+\left(U_2V_{11}e^{ik_{z,1}z_0} - U_1V_{11}e^{-ik_{z,1}z_0} + U_5V_8e^{ik_{z,2}z_0} + U_4V_8e^{-ik_{z,2}z_0}\right)\hat{h}^{\mathrm{I}}_{s,-}\hat{y}\\
+\left(U_2V_3e^{ik_{z,1}z_0} + U_1V_3e^{-ik_{z,1}z_0} + U_5V_6e^{ik_{z,2}z_0} - U_4V_6e^{-ik_{z,2}z_0}\right)\hat{h}^{\mathrm{I}}_{s,-}\hat{z}
\end{bmatrix}\\
&+\begin{bmatrix}
\left(-U_3V_{10}e^{ik_{z,1}z_0} - U_1V_{10}e^{-ik_{z,1}z_0} - U_7V_7e^{ik_{z,2}z_0} - U_6V_7e^{-ik_{z,2}z_0}\right)\hat{h}^{\mathrm{I}}_{p,-}\hat{x}\\
+\left(-U_3V_{11}e^{ik_{z,1}z_0} - U_1V_{11}e^{-ik_{z,1}z_0} - U_7V_8e^{ik_{z,2}z_0} - U_6V_8e^{-ik_{z,2}z_0}\right)\hat{h}^{\mathrm{I}}_{p,-}\hat{y}\\
+\left(-U_3V_3e^{ik_{z,1}z_0} + U_1V_3e^{-ik_{z,1}z_0} - U_7V_6e^{ik_{z,2}z_0} + U_6V_6e^{-ik_{z,2}z_0}\right)\hat{h}^{\mathrm{I}}_{p,-}\hat{z}
\end{bmatrix}\Bigg)\\
&\times\exp\left(i\,\vec{\kappa}\cdot\vec{R}\right)\exp(-ik_{z,1}z),
\end{aligned}
$$

$$G^{\mathrm{I}}_{E,P} = \frac{1}{2}\left(\begin{bmatrix} \left(U_2V_{10}e^{ik_{z,1}z_0} - U_1V_{10}e^{-ik_{z,1}z_0} + U_5V_7e^{ik_{z,2}z_0} + U_4V_7e^{-ik_{z,2}z_0}\right)\hat{e}^{\mathrm{I}}_{s,-}\hat{x} \\ +\left(U_2V_{11}e^{ik_{z,1}z_0} - U_1V_{11}e^{-ik_{z,1}z_0} + U_5V_8e^{ik_{z,2}z_0} + U_4V_8e^{-ik_{z,2}z_0}\right)\hat{e}^{\mathrm{I}}_{s,-}\hat{y} \\ +\left(U_2V_3e^{ik_{z,1}z_0} + U_1V_3e^{-ik_{z,1}z_0} + U_5V_6e^{ik_{z,2}z_0} - U_4V_6e^{-ik_{z,2}z_0}\right)\hat{e}^{\mathrm{I}}_{s,-}\hat{z} \end{bmatrix} + \begin{bmatrix} \left(-U_3V_{10}e^{ik_{z,1}z_0} - U_1V_{10}e^{-ik_{z,1}z_0} - U_7V_7e^{ik_{z,2}z_0} - U_6V_7e^{-ik_{z,2}z_0}\right)\hat{e}^{\mathrm{I}}_{p,-}\hat{x} \\ +\left(-U_3V_{11}e^{ik_{z,1}z_0} - U_1V_{11}e^{-ik_{z,1}z_0} - U_7V_8e^{ik_{z,2}z_0} - U_6V_8e^{-ik_{z,2}z_0}\right)\hat{e}^{\mathrm{I}}_{p,-}\hat{y} \\ +\left(-U_3V_3e^{ik_{z,1}z_0} + U_1V_3e^{-ik_{z,1}z_0} - U_7V_6e^{ik_{z,2}z_0} + U_6V_6e^{-ik_{z,2}z_0}\right)\hat{e}^{\mathrm{I}}_{p,-}\hat{z} \end{bmatrix}\right) \times \exp\left(i\,\vec{\kappa}\cdot\vec{R}\right)\exp(-ik_{z,1}z),$$

$$G^{\mathrm{I}}_{B,M} = \left(\begin{bmatrix} \left(U_2V_1e^{ik_{z,1}z_0} + U_1V_1e^{-ik_{z,1}z_0} + U_5V_4e^{ik_{z,2}z_0} - U_4V_4e^{-ik_{z,2}z_0}\right)\hat{h}^{\mathrm{I}}_{s,-}\hat{x} \\ +\left(U_2V_2e^{ik_{z,1}z_0} + U_1V_2e^{-ik_{z,1}z_0} + U_5V_5e^{ik_{z,2}z_0} - U_4V_5e^{-ik_{z,2}z_0}\right)\hat{h}^{\mathrm{I}}_{s,-}\hat{y} \\ +\left(U_2V_{12}e^{ik_{z,1}z_0} - U_1V_{12}e^{-ik_{z,1}z_0} + U_5V_9e^{ik_{z,2}z_0} + U_4V_9e^{-ik_{z,2}z_0}\right)\hat{h}^{\mathrm{I}}_{s,-}\hat{z} \end{bmatrix} + \begin{bmatrix} \left(-U_3V_1e^{ik_{z,1}z_0} + U_1V_1e^{-ik_{z,1}z_0} - U_7V_4e^{ik_{z,2}z_0} + U_6V_4e^{-ik_{z,2}z_0}\right)\hat{h}^{\mathrm{I}}_{p,-}\hat{x} \\ +\left(-U_3V_2e^{ik_{z,1}z_0} + U_1V_2e^{-ik_{z,1}z_0} - U_7V_5e^{ik_{z,2}z_0} + U_6V_5e^{-ik_{z,2}z_0}\right)\hat{h}^{\mathrm{I}}_{p,-}\hat{y} \\ +\left(-U_3V_{12}e^{ik_{z,1}z_0} - U_1V_{12}e^{-ik_{z,1}z_0} - U_7V_9e^{ik_{z,2}z_0} - U_6V_9e^{-ik_{z,2}z_0}\right)\hat{h}^{\mathrm{I}}_{p,-}\hat{z} \end{bmatrix}\right) \times \exp\left(i\,\vec{\kappa}\cdot\vec{R}\right)\exp(-ik_{z,1}z),$$

$$G^{\mathrm{I}}_{E,M} = \left(\begin{bmatrix} \left(U_2V_1e^{ik_{z,1}z_0} + U_1V_1e^{-ik_{z,1}z_0} + U_5V_4e^{ik_{z,2}z_0} - U_4V_4e^{-ik_{z,2}z_0}\right)\hat{e}^{\mathrm{I}}_{s,-}\hat{x} \\ +\left(U_2V_2e^{ik_{z,1}z_0} + U_1V_2e^{-ik_{z,1}z_0} + U_5V_5e^{ik_{z,2}z_0} - U_4V_5e^{-ik_{z,2}z_0}\right)\hat{e}^{\mathrm{I}}_{s,-}\hat{y} \\ +\left(U_2V_{12}e^{ik_{z,1}z_0} - U_1V_{12}e^{-ik_{z,1}z_0} + U_5V_9e^{ik_{z,2}z_0} + U_4V_9e^{-ik_{z,2}z_0}\right)\hat{e}^{\mathrm{I}}_{s,-}\hat{z} \end{bmatrix} + \begin{bmatrix} \left(-U_3V_1e^{ik_{z,1}z_0} + U_1V_1e^{-ik_{z,1}z_0} - U_7V_4e^{ik_{z,2}z_0} + U_6V_4e^{-ik_{z,2}z_0}\right)\hat{e}^{\mathrm{I}}_{p,-}\hat{x} \\ +\left(-U_3V_2e^{ik_{z,1}z_0} + U_1V_2e^{-ik_{z,1}z_0} - U_7V_5e^{ik_{z,2}z_0} + U_6V_5e^{-ik_{z,2}z_0}\right)\hat{e}^{\mathrm{I}}_{p,-}\hat{y} \\ +\left(-U_3V_{12}e^{ik_{z,1}z_0} - U_1V_{12}e^{-ik_{z,1}z_0} - U_7V_9e^{ik_{z,2}z_0} - U_6V_9e^{-ik_{z,2}z_0}\hat{e}^{\mathrm{I}}_{p,-}\hat{z}\right) \end{bmatrix}\right) \times \exp\left(i\,\vec{\kappa}\cdot\vec{R}\right)\exp(-ik_{z,1}z),$$

$$G^{\mathrm{III}}_{B,P} = \frac{1}{2}\left(\begin{bmatrix} \left(U_1V_{10}e^{-ik_{z,1}(h-z_0)} - U_2V_{10}e^{ik_{z,1}(h-z_0)} + U_4V_7e^{-ik_{z,2}(h-z_0)} + U_5V_7e^{ik_{z,2}(h-z_0)}\right)\hat{h}^{\mathrm{III}}_{s,+}\hat{x} \\ +\left(U_1V_{11}e^{-ik_{z,1}(h-z_0)} - U_2V_{11}e^{ik_{z,1}(h-z_0)} + U_4V_8e^{-ik_{z,2}(h-z_0)} + U_5V_8e^{ik_{z,2}(h-z_0)}\right)\hat{h}^{\mathrm{III}}_{s,+}\hat{y} \\ +\left(U_1V_3e^{-ik_{z,1}(h-z_0)} + U_2V_3e^{ik_{z,1}(h-z_0)} + U_4V_6e^{-ik_{z,2}(h-z_0)} - U_5V_6e^{ik_{z,2}(h-z_0)}\right)\hat{h}^{\mathrm{III}}_{s,+}\hat{z} \end{bmatrix} + \begin{bmatrix} \left(-U_1V_{10}e^{-ik_{z,1}(h-z_0)} - U_3V_{10}e^{ik_{z,1}(h-z_0)} + U_6V_7e^{-ik_{z,2}(h-z_0)} + U_7V_7e^{ik_{z,2}(h-z_0)}\right)\hat{h}^{\mathrm{III}}_{p,+}\hat{x} \\ +\left(-U_1V_{11}e^{-ik_{z,1}(h-z_0)} - U_3V_{11}e^{ik_{z,1}(h-z_0)} + U_6V_8e^{-ik_{z,2}(h-z_0)} + U_7V_8e^{ik_{z,2}(h-z_0)}\right)\hat{h}^{\mathrm{III}}_{p,+}\hat{y} \\ +\left(-U_1V_3e^{-ik_{z,1}(h-z_0)} + U_3V_3e^{ik_{z,1}(h-z_0)} + U_6V_6e^{-ik_{z,2}(h-z_0)} - U_7V_6e^{ik_{z,2}(h-z_0)}\right)\hat{h}^{\mathrm{III}}_{p,+}\hat{z} \end{bmatrix}\right) \times \exp\left(i\,\vec{\kappa}\cdot\vec{R}\right)\exp(ik_{z,\mathrm{III}}(z-h)),$$

$$G^{\mathrm{III}}_{E,P} = \frac{1}{2}\left(\begin{bmatrix} \left(U_1V_{10}e^{-ik_{z,1}(h-z_0)} - U_2V_{10}e^{ik_{z,1}(h-z_0)} + U_4V_7e^{-ik_{z,2}(h-z_0)} + U_5V_7e^{ik_{z,2}(h-z_0)}\right)\hat{e}^{\mathrm{III}}_{s,+}\hat{x} \\ +\left(U_1V_{11}e^{-ik_{z,1}(h-z_0)} - U_2V_{11}e^{ik_{z,1}(h-z_0)} + U_4V_8e^{-ik_{z,2}(h-z_0)} + U_5V_8e^{ik_{z,2}(h-z_0)}\right)\hat{e}^{\mathrm{III}}_{s,+}\hat{y} \\ +\left(U_1V_3e^{-ik_{z,1}(h-z_0)} + U_2V_3e^{ik_{z,1}(h-z_0)} + U_4V_6e^{-ik_{z,2}(h-z_0)} - U_5V_6e^{ik_{z,2}(h-z_0)}\right)\hat{e}^{\mathrm{III}}_{s,+}\hat{z} \end{bmatrix} + \begin{bmatrix} \left(-U_1V_{10}e^{-ik_{z,1}(h-z_0)} - U_3V_{10}e^{ik_{z,1}(h-z_0)} + U_6V_7e^{-ik_{z,2}(h-z_0)} + U_7V_7e^{ik_{z,2}(h-z_0)}\right)\hat{e}^{\mathrm{III}}_{p,+}\hat{x} \\ +\left(-U_1V_{11}e^{-ik_{z,1}(h-z_0)} - U_3V_{11}e^{ik_{z,1}(h-z_0)} + U_6V_8e^{-ik_{z,2}(h-z_0)} + U_7V_8e^{ik_{z,2}(h-z_0)}\right)\hat{e}^{\mathrm{III}}_{p,+}\hat{y} \\ +\left(-U_1V_3e^{-ik_{z,1}(h-z_0)} + U_3V_3e^{ik_{z,1}(h-z_0)} + U_6V_6e^{-ik_{z,2}(h-z_0)} - U_7V_6e^{ik_{z,2}(h-z_0)}\right)\hat{e}^{\mathrm{III}}_{p,+}\hat{z} \end{bmatrix}\right) \times \exp\left(i\,\vec{\kappa}\cdot\vec{R}\right)\exp(ik_{z,\mathrm{III}}(z-h)),$$

$$G^{\mathrm{III}}_{B,M} = \frac{1}{2}\left(\begin{bmatrix} \left(U_1V_1e^{-ik_{z,1}(h-z_0)} + U_2V_1e^{ik_{z,1}(h-z_0)} + U_4V_4e^{-ik_{z,2}(h-z_0)} - U_5V_4e^{ik_{z,2}(h-z_0)}\right)\hat{h}^{\mathrm{III}}_{s,+}\hat{x} \\ +\left(U_1V_2e^{-ik_{z,1}(h-z_0)} + U_2V_2e^{ik_{z,1}(h-z_0)} + U_4V_5e^{-ik_{z,2}(h-z_0)} - U_5V_5e^{ik_{z,2}(h-z_0)}\right)\hat{h}^{\mathrm{III}}_{s,+}\hat{y} \\ +\left(U_1V_{12}e^{-ik_{z,1}(h-z_0)} - U_2V_{12}e^{ik_{z,1}(h-z_0)} + U_4V_9e^{-ik_{z,2}(h-z_0)} + U_5V_9e^{ik_{z,2}(h-z_0)}\right)\hat{h}^{\mathrm{III}}_{s,+}\hat{z} \end{bmatrix} + \begin{bmatrix} \left(-U_1V_1e^{-ik_{z,1}(h-z_0)} + U_3V_1e^{ik_{z,1}(h-z_0)} + U_6V_4e^{-ik_{z,2}(h-z_0)} - U_7V_4e^{ik_{z,2}(h-z_0)}\right)\hat{h}^{\mathrm{III}}_{p,+}\hat{x} \\ +\left(-U_1V_2e^{-ik_{z,1}(h-z_0)} + U_3V_2e^{ik_{z,1}(h-z_0)} + U_6V_5e^{-ik_{z,2}(h-z_0)} - U_7V_5e^{ik_{z,2}(h-z_0)}\right)\hat{h}^{\mathrm{III}}_{p,+}\hat{y} \\ +\left(-U_1V_{12}e^{-ik_{z,1}(h-z_0)} - U_3V_{12}e^{ik_{z,1}(h-z_0)} + U_6V_9e^{-ik_{z,2}(h-z_0)} + U_7V_9e^{ik_{z,2}(h-z_0)}\right)\hat{h}^{\mathrm{III}}_{p,+}\hat{z} \end{bmatrix}\right) \times \exp\left(i\,\vec{\kappa}\cdot\vec{R}\right)\exp(ik_{z,\mathrm{III}}(z-h)),$$

$$G_{E,M}^{\mathrm{III}} = \frac{1}{2}\left(\begin{array}{l}\left[\begin{array}{l}\left(U_1V_1e^{-ik_{z,1}(h-z_0)} + U_2V_1e^{ik_{z,1}(h-z_0)} + U_4V_4e^{-ik_{z,2}(h-z_0)} - U_5V_4e^{ik_{z,2}(h-z_0)}\right)\hat{e}_{s,+}^{\mathrm{III}}\hat{x} \\ +\left(U_1V_2e^{-ik_{z,1}(h-z_0)} + U_2V_2e^{ik_{z,1}(h-z_0)} + U_4V_5e^{-ik_{z,2}(h-z_0)} - U_5V_5e^{ik_{z,2}(h-z_0)}\right)\hat{e}_{s,+}^{\mathrm{III}}\hat{y} \\ +\left(U_1V_{12}e^{-ik_{z,1}(h-z_0)} - U_2V_{12}e^{ik_{z,1}(h-z_0)} + U_4V_9e^{-ik_{z,2}(h-z_0)} + U_5V_9e^{ik_{z,2}(h-z_0)}\right)\hat{e}_{s,+}^{\mathrm{III}}\hat{z}\end{array}\right] \\ +\left[\begin{array}{l}\left(-U_1V_1e^{-ik_{z,1}(h-z_0)} + U_3V_1e^{ik_{z,1}(h-z_0)} + U_6V_4e^{-ik_{z,2}(h-z_0)} - U_7V_4e^{ik_{z,2}(h-z_0)}\right)\hat{e}_{p,+}^{\mathrm{III}}\hat{x} \\ +\left(-U_1V_2e^{-ik_{z,1}(h-z_0)} + U_3V_2e^{ik_{z,1}(h-z_0)} + U_6V_5e^{-ik_{z,2}(h-z_0)} - U_7V_5e^{ik_{z,2}(h-z_0)}\right)\hat{e}_{p,+}^{\mathrm{III}}\hat{y} \\ +\left(-U_1V_{12}e^{-ik_{z,1}(h-z_0)} - U_3V_{12}e^{ik_{z,1}(h-z_0)} + U_6V_9e^{-ik_{z,2}(h-z_0)} + U_7V_9e^{ik_{z,2}(h-z_0)}\right)\hat{e}_{p,+}^{\mathrm{III}}\hat{z}\end{array}\right]\end{array}\right)$$
$$\times \exp\left(i\,\vec{\kappa}\cdot\vec{R}\right)\exp\left(ik_{z,\mathrm{III}}(z-h)\right). \tag{42}$$

Green functions gotten in (42) give the relations between the fields generated in region I (or region III) and the sources embedded in biaxial crystal (region II). The definitions of parameters ($U_i, i = 1,2,\ldots,7$) in (42) will be given in Appendix C.

4. Conclusion Remark

In summary, a new Green function formulism is developed by combining eigenmode expansion method and conventional formulism. The correction of the formulism is supported by recovering well-known results gotten by conventional formulism. The powerful eigenmode expansion method removes the difficulties brought by the interface between anisotropic media. Given to the advantage, the Green functions relating the fields generated outside of anisotropic medium and the sources inside were calculated and shown. They may have potential applications in studying the electromagnetic response and its spatial distribution of anisotropic metamaterial medium, which has well-defined effective medium tensor.

Appendices

A. Definitions of Parameters W_i in (32)

The parameters W_i come out, when one solves the equation groups (31). Thus, it can be related to the coefficients in front of the field amplitudes. In the solution processes, they firstly relate to parameters I_i, $i = 1,2,\ldots,6$, and F_i, $i = 1,2,\ldots,9$, as

$$W_1 = \left[\frac{I_3I_5 - I_2I_6}{I_1I_5 - I_2I_4}e^{ik_{z,o}h}\right],$$
$$W_2 = \left[\frac{F_1I_5 - F_4I_2}{F_7(I_1I_5 - I_2I_4)}e^{-ik_{z,o}h}\right],$$
$$W_3 = \left[\frac{F_1I_4 - F_4I_1}{F_7(I_2I_4 - I_1I_5)}e^{-ik_{z,o}h}\right],$$
$$W_4 = \frac{I_2}{I_1I_5 - I_2I_4}e^{ik_{z,o}h},$$
$$W_5 = \frac{I_5}{I_1I_5 - I_2I_4}e^{-ik_{z,o}h},$$
$$W_6 = \frac{I_1}{I_2I_4 - I_1I_5}e^{ik_{z,o}h},$$
$$W_7 = \frac{I_4}{I_2I_4 - I_1I_5}e^{-ik_{z,o}h}. \tag{A.1}$$

The definitions of parameters I_i, $i = 1,2,\ldots,6$, are the following:

$$I_1 = F_2 - \frac{F_1F_8}{F_7},$$
$$I_2 = F_3 - \frac{F_1F_9}{F_7},$$
$$I_3 = \frac{F_1D_6}{F_7D_5} + \frac{D_2}{D_5}, \tag{A.2}$$
$$I_4 = F_5 - \frac{F_4F_8}{F_7},$$
$$I_5 = F_6 - \frac{F_4F_9}{F_7}, I_6 = \frac{F_4D_6}{F_7D_5} - \frac{D_1}{D_5}.$$

The definitions of parameters F_i, $i = 1,2,\ldots,9$, are given as

$$F_1 = \frac{D_2D_7}{D_5} + D_4,$$
$$F_2 = D_1e^{-ik_{z,e}h} + \frac{D_2D_6}{D_5}e^{ik_{z,o}h},$$
$$F_3 = D_3e^{-ik_{z,e}h} - \frac{D_2D_8}{D_5}e^{ik_{z,o}h},$$
$$F_4 = -\frac{D_1D_7}{D_5} - D_3,$$
$$F_5 = -D_2e^{ik_{z,e}h} - \frac{D_1D_6}{D_5}e^{ik_{z,o}h},$$
$$F_6 = -D_4e^{ik_{z,e}h} + \frac{D_1D_8}{D_5}e^{ik_{z,o}h},$$

$$F_7 = D_8 - \frac{D_6 D_7}{D_5},$$

$$F_8 = D_5 e^{-ik_{z,o}h} - \frac{D_6^2}{D_5} e^{ik_{z,o}h},$$

$$F_9 = -D_7 e^{-ik_{z,o}h} + \frac{D_6 D_8}{D_5} e^{ik_{z,o}h}. \tag{A.3}$$

The parameters D_i, $i = 1, 2, \ldots, 8$, relate to the coefficients in (31) directly (since the media in region I and region III are the same, we used the fact that $k_z = k_{z,\mathrm{I}} = k_{z,\mathrm{III}}$, when $\vec{\kappa}$ is the same):

$$D_1 = \frac{k_z}{2A_2A_3\widetilde{\omega}}(A_3\cos\theta + A_1\sin\theta) + \frac{\widetilde{\omega}\mu\varepsilon_e R}{2k_oA_3}\cos\theta,$$

$$D_2 = \frac{k_z}{2A_2A_3\widetilde{\omega}}(A_3\cos\theta + A_1\sin\theta) - \frac{\widetilde{\omega}\mu\varepsilon_e R}{2k_oA_3}\cos\theta,$$

$$D_3 = \frac{1}{2A_2A_3}(A_3\sin\theta - A_1\cos\theta) + \frac{k_z\mu\varepsilon_e R}{2k_oA_3}\sin\theta,$$

$$D_4 = \frac{1}{2A_2A_3}(A_3\sin\theta - A_1\cos\theta) - \frac{k_z\mu\varepsilon_e R}{2k_oA_3}\sin\theta,$$

$$D_5 = \frac{k_{z,e}\widetilde{\omega}\mu\varepsilon_e\sqrt{\mu\varepsilon_o}R^2}{2k_{z,o}k_oA_2A_3}\left(\frac{k_o\sin\theta}{\widetilde{\omega}\mu\varepsilon_e R}A_3 - \frac{R\cos\theta}{\sqrt{\mu\varepsilon_o}}A_1\right) + \frac{k_z\sin\theta}{2A_3\widetilde{\omega}},$$

$$D_6 = \frac{k_{z,e}\widetilde{\omega}\mu\varepsilon_e\sqrt{\mu\varepsilon_o}R^2}{2k_{z,o}k_oA_2A_3}\left(\frac{k_o\sin\theta}{\widetilde{\omega}\mu\varepsilon_e R}A_3 - \frac{R\cos\theta}{\sqrt{\mu\varepsilon_o}}A_1\right) - \frac{k_z\sin\theta}{2A_3\widetilde{\omega}},$$

$$D_7 = \frac{k_{z,e}\widetilde{\omega}\mu\varepsilon_e\sqrt{\mu\varepsilon_o}R^2}{2k_{z,o}k_oA_2A_3}\left(\frac{k_ok_z\cos\theta}{\widetilde{\omega}^2\mu\varepsilon_e R}A_3 + \frac{Rk_z\sin\theta}{\widetilde{\omega}\sqrt{\mu\varepsilon_o}}A_1\right) + \frac{\cos\theta}{2A_3},$$

$$D_8 = \frac{k_{z,e}\widetilde{\omega}\mu\varepsilon_e\sqrt{\mu\varepsilon_o}R^2}{2k_{z,o}k_oA_2A_3}\left(\frac{k_ok_z\cos\theta}{\widetilde{\omega}^2\mu\varepsilon_e R}A_3 + \frac{Rk_z\sin\theta}{\widetilde{\omega}\sqrt{\mu\varepsilon_o}}A_1\right) - \frac{\cos\theta}{2A_3}, \tag{A.4}$$

where the parameters A_i $(i = 1, 2, 3)$ are given as

$$A_1 = \frac{\kappa^2\sin\theta\cos\theta}{k_o\sqrt{\kappa^2\cos^2\theta + k_{z,o}^2}},$$

$$A_2 = \frac{k_{z,e}}{\sqrt{\kappa^2\cos^2\theta + k_{z,e}^2}}, \tag{A.5}$$

$$A_3 = \frac{\sqrt{\kappa^2\cos^2\theta + k_{z,o}^2}}{k_o}.$$

B. Definitions of Parameters V_i in (39)

The parameters come from the processes of solving equation groups (38), and they can relate to the coefficients of them as

$$V_1 = \frac{-\widetilde{\omega}\mu\left(\varepsilon_1^2X_1^2 + \varepsilon_2^2 + \varepsilon_3^2Z_1^2\right)^{1/2}i4\pi\widetilde{\omega}\mu X_2}{k_1(X_1 - X_2)},$$

$$V_2 = \frac{\widetilde{\omega}\mu\left(\varepsilon_1^2X_1^2 + \varepsilon_2^2 + \varepsilon_3^2Z_1^2\right)^{1/2}i4\pi\widetilde{\omega}\mu}{k_1(X_1 - X_2)},$$

$$V_3 = \frac{-i4\pi\kappa\widetilde{\omega}\mu\left(\varepsilon_1^2X_1^2 + \varepsilon_2^2 + \varepsilon_3^2Z_1^2\right)^{1/2}(\cos\theta + X_1\sin\theta)}{k_1\varepsilon_3(X_1 - X_2)},$$

$$V_4 = \frac{-\widetilde{\omega}\mu\left(\varepsilon_1^2X_2^2 + \varepsilon_2^2 + \varepsilon_3^2Z_2^2\right)^{1/2}i4\pi\mu\widetilde{\omega}X_1}{k_2(X_2 - X_1)},$$

$$V_5 = \frac{\widetilde{\omega}\mu\left(\varepsilon_1^2X_2^2 + \varepsilon_2^2 + \varepsilon_3^2Z_2^2\right)^{1/2}i4\pi\mu\widetilde{\omega}}{k_2(X_2 - X_1)},$$

$$V_6 = \frac{-i4\pi\kappa\widetilde{\omega}\mu\left(\varepsilon_1^2X_2^2 + \varepsilon_2^2 + \varepsilon_3^2Z_2^2\right)^{1/2}(\cos\theta + X_1\sin\theta)}{\varepsilon_3k_2(X_2 - X_1)},$$

$$V_7 = \frac{-i4\pi\widetilde{\omega}\mu N_2(\kappa\sin\theta Z_1 - k_{z,1})}{\mathcal{A}},$$

$$V_8 = \frac{-i4\pi\widetilde{\omega}\mu N_2(k_{z,1}X_1 - Z_1\kappa\cos\theta)}{\mathcal{A}},$$

$$V_9 = \frac{N_2\left[i4\pi\mu\kappa\sin\theta(\kappa\sin\theta Z_1 - k_{z,1}) - \mathcal{B}\right]}{\mathcal{A}},$$

$$V_{10} = \frac{-i4\pi\widetilde{\omega}\mu N_1(\kappa\sin\theta Z_2 - k_{z,2})}{\mathcal{C}},$$

$$V_{11} = \frac{-i4\pi\widetilde{\omega}\mu N_1(k_{z,2}X_2 - Z_2\kappa\cos\theta)}{\mathcal{C}},$$

$$V_{12} = \frac{N_1\left[i4\pi\mu\kappa\sin\theta(\kappa\sin\theta Z_2 - k_{z,2}) - \mathcal{D}\right]}{\mathcal{C}}, \tag{B.1}$$

where $\mathcal{A}$ denotes $(\kappa\sin\theta Z_2 - k_{z,2})(k_{z,1}X_1 - Z_1\kappa\cos\theta) - (k_{z,2}X_2 - Z_2\kappa\cos\theta)(\kappa\sin\theta Z_1 - k_{z,1})$, $\mathcal{B}$ denotes $i4\pi\mu\kappa\cos\theta(k_{z,1}X_1 - Z_1\kappa\cos\theta)$, $\mathcal{C}$ denotes $(\kappa\sin\theta Z_1 - k_{z,1})(k_{z,2}X_2 - Z_2\kappa\cos\theta) - (k_{z,1}X_1 - Z_1\kappa\cos\theta)(\kappa\sin\theta Z_2 - k_{z,2})$, and $\mathcal{D}$ denotes $i4\pi\mu\kappa\cos\theta(k_{z,2}X_2 - Z_2\kappa\cos\theta)$.

C. Definitions of Parameters U_i in (42)

The parameters U_i are gotten in the processes of solving equation groups (40) and (41), and they can be related to the coefficients in front of the field amplitudes. They firstly relate to parameters I_i', $i = 1, 2, \ldots, 6$, and F_i', $i = 1, 2, \ldots, 9$, which will defined later:

$$U_1 = \frac{I_3'I_5' - I_2'I_6'}{I_1'I_5' - I_2'I_4'}e^{ik_{z,1}h},$$

$$U_2 = \frac{F_1'I_5' - F_4'I_2'}{F_7'(I_1'I_5' - I_2'I_4')}e^{-ik_{z,1}h},$$

$$U_3 = \frac{F_1'I_4' - F_4'I_1'}{F_7'(I_2'I_4' - I_1'I_5')}e^{-ik_{z,1}h},$$

$$U_4 = \frac{I_2'}{I_1'I_5' - I_2'I_4'}, \tag{C.1}$$

$$U_5 = \frac{I_5'}{I_1'I_5' - I_2'I_4'}e^{-ik_{z,1}h},$$

$$U_6 = \frac{I_1'}{I_2'I_4' - I_1'I_5'}e^{ik_{z,1}h},$$

$$U_7 = \frac{I_4'}{I_2'I_4' - I_1'I_5'}e^{-ik_{z,1}h}.$$

The parameters I_i', $i = 1, 2, \ldots, 6$, are given as functions of F_i', $i = 1, 2, \ldots, 9$, and Q_i, $i = 1, 2, \ldots, 8$

$$\begin{aligned}
I_1' &= F_2' - \frac{F_1' F_8'}{F_7'}, \\
I_2' &= F_3' - \frac{F_1' F_9'}{F_7'}, \\
I_3' &= \frac{F_1' Q_1}{F_7' Q_3} + \frac{Q_5}{Q_3}, \\
I_4' &= F_5' - \frac{F_4' F_8'}{F_7'}, \\
I_5' &= F_6' - \frac{F_4' F_9'}{F_7'}, \\
I_6' &= \frac{F_4' Q_1}{F_7' Q_3} - \frac{Q_7}{Q_3}.
\end{aligned} \tag{C.2}$$

The parameters F_i', $i = 1, 2, \ldots, 9$, are defined as the functions of Q_i, $i = 1, 2, \ldots, 8$,

$$\begin{aligned}
F_1' &= \frac{Q_4 Q_5}{Q_3} + Q_6, \\
F_2' &= Q_7 e^{-ik_{z,2}h} + \frac{Q_5 Q_1}{Q_3} e^{ik_{z,1}h}, \\
F_3' &= Q_8 e^{-ik_{z,2}h} - \frac{Q_5 Q_2}{Q_3} e^{ik_{z,1}h}, \\
F_4' &= -\frac{Q_7 Q_4}{Q_3} - Q_8, \\
F_5' &= -Q_5 e^{ik_{z,2}h} - \frac{Q_7 Q_1}{Q_3} e^{ik_{z,1}h}, \\
F_6' &= -Q_6 e^{ik_{z,2}h} + \frac{Q_7 Q_2}{Q_3} e^{ik_{z,1}h}, \\
F_7' &= Q_2 - \frac{Q_1 Q_4}{Q_3}, \\
F_8' &= Q_3 e^{-ik_{z,1}h} - \frac{Q_1^2}{Q_3} e^{ik_{z,1}h}, \\
F_9' &= -Q_4 e^{-ik_{z,1}h} + \frac{Q_1 Q_2}{Q_3} e^{ik_{z,1}h}.
\end{aligned} \tag{C.3}$$

The parameters Q_i, $i = 1, 2, \ldots, 8$, relate with the coefficients in (40) and (41) directly:

$$\begin{aligned}
Q_1 &= \left[\frac{[-(X_1 \cos\theta + \sin\theta) X_2 + (X_2 - X_1) \sin\theta]}{2S_5 (X_2 - X_1) X_1} \right. \\
&\quad \left. + \frac{(S_4 \cos\theta - S_2 \sin\theta) k_z}{2(S_2 S_3 - S_1 S_4) \widetilde{\omega}} \right], \\
Q_2 &= \left[\frac{-(S_4 \sin\theta + S_2 \cos\theta)}{2(S_2 S_3 - S_1 S_4)} \right. \\
&\quad \left. + \frac{[(X_1 \sin\theta - \cos\theta) X_2 + (X_2 - X_1) \cos\theta]}{2S_5 (X_2 - X_1) X_1} \frac{k_z}{\widetilde{\omega}} \right], \\
Q_3 &= \left[\frac{[(X_2 - X_1) \sin\theta - X_2 (\sin\theta + \cos\theta X_1)]}{2S_5 X_1 (X_2 - X_1)} \right. \\
&\quad \left. - \frac{(S_4 \cos\theta - S_2 \sin\theta)}{2(S_2 S_3 - S_1 S_4)} \frac{k_z}{\widetilde{\omega}} \right], \\
Q_4 &= \left[\frac{[\cos\theta (X_2 - X_1) - X_2 (\cos\theta - X_1 \sin\theta)]}{2S_5 X_1 (X_2 - X_1)} \frac{k_z}{\widetilde{\omega}} \right. \\
&\quad \left. + \frac{(S_4 \sin\theta + S_2 \cos\theta)}{2(S_2 S_3 - S_1 S_4)} \right] \\
Q_5 &= -\left[\frac{[-(S_2 S_3 - S_1 S_4) \cos\theta - S_1 (S_4 \cos\theta - S_2 \sin\theta)]}{2(S_2 S_3 - S_1 S_4) S_2} \frac{k_z}{\widetilde{\omega}} \right. \\
&\quad \left. + \frac{(X_1 \cos\theta + \sin\theta)}{2S_6 (X_2 - X_1)} \right], \\
Q_6 &= \left[\frac{(\cos\theta - X_1 \sin\theta)}{2S_6 (X_2 - X_1)} \frac{k_z}{\widetilde{\omega}} \right. \\
&\quad \left. + \frac{[(S_2 S_3 - S_1 S_4) \sin\theta + S_1 (S_4 \sin\theta + S_2 \cos\theta)]}{2(S_2 S_3 - S_1 S_4) S_2} \right], \\
Q_7 &= \left[\frac{[\cos\theta (S_2 S_3 - S_1 S_4) + S_1 (S_4 \cos\theta - S_2 \sin\theta)]}{2S_2 (S_2 S_3 - S_1 S_4)} \frac{k_z}{\widetilde{\omega}} \right. \\
&\quad \left. + \frac{(\sin\theta + \cos\theta X_1)}{2S_6 (X_2 - X_1)} \right], \\
Q_8 &= \left[\frac{[\sin\theta (S_2 S_3 - S_1 S_4) + S_1 (S_4 \sin\theta + S_2 \cos\theta)]}{2S_2 (S_2 S_3 - S_1 S_4)} \right. \\
&\quad \left. - \frac{(\cos\theta - X_1 \sin\theta)}{2S_6 (X_2 - X_1)} \frac{k_z}{\widetilde{\omega}} \right].
\end{aligned} \tag{C.4}$$

Acknowledgments

W. Wen would like to thank the support for this work by the Hong Kong RGC Grant HKUST2/CRF/11G. B. Hou would like to acknowledge the support from the National Natural Science Foundation of China (Grant no. 11104198) and from a Project Funded by the Priority Academic Program Development of Jiangsu Higher Education Institutions (PAPD).

References

[1] B. Hou, H. Wen, Y. Leng, and W. Wen, "Enhanced transmission of electromagnetic waves through metamaterials," *Applied Physics A*, vol. 87, no. 2, pp. 217–221, 2007.

[2] X. Xiao, X. Yi, B. Hou et al., "Subwavelength waveguiding and imaging with a one-dimensional array of metallic H-fractals," *New Journal of Physics*, vol. 12, Article ID 073021, 2010.

[3] V. M. Shalaev, "Optical negative-index metamaterials," *Nature Photonics*, vol. 1, no. 1, pp. 41–48, 2007.

[4] D. R. Smith, J. B. Pendry, and M. C. K. Wiltshire, "Metamaterials and negative refractive index," *Science*, vol. 305, no. 5685, pp. 788–792, 2004.

[5] B. Hou and W. Wen, "Transmission resonances of electromagnetic wave through metallic gratings: phase and field characterizations," *Optics Express*, vol. 16, no. 21, pp. 17098–17106, 2008.

[6] X. Xiao, J. Wu, F. Miyamaru et al., "Fano effect of metamaterial resonance in terahertz extraordinary transmission," *Applied Physics Letters*, vol. 98, no. 1, Article ID 011911, 2011.

[7] N. I. Zheludev, "The road ahead for metamaterials," *Science*, vol. 328, no. 5978, pp. 582–583, 2010.

[8] D. R. Smith, S. Schultz, P. Markoš, and C. M. Soukoulis, "Determination of effective permittivity and permeability of metamaterials from reflection and transmission coefficients," *Physical Review B*, vol. 65, no. 19, Article ID 195104, 2002.

[9] A. M. Bratkovsky, E. Ponizovskaya, E. Kim et al., "Properties of nanostructured metamaterials at optical frequencies," in

Optoelectronic Materials and Devices III, vol. 7135, 71352K of *Proceedings of SPIE*, Hangzhou, China, October 2008.

[10] C. Fu and Z. M. Zhang, "Thermal radiative properties of metamaterials and other nanostructured materials: a review," *Frontiers of Energy and Power Engineering in China*, vol. 3, no. 1, pp. 11–26, 2009.

[11] A. V. Kabashin, P. Evans, S. Pastkovsky et al., "Plasmonic nanorod metamaterials for biosensing," *Nature Materials*, vol. 8, no. 11, pp. 867–871, 2009.

[12] C. R. Simovski and S. A. Tretyakov, "On effective electromagnetic parameters of artificial nanostructured magnetic materials," *Photonics and Nanostructures*, vol. 8, no. 4, pp. 254–263, 2010.

[13] W. T. Lu and S. Sridhar, "Superlens imaging theory for anisotropic nanostructured metamaterials with broadband all-angle negative refraction," *Physical Review B*, vol. 77, no. 23, Article ID 233101, 2008.

[14] K. Joulain, J. P. Mulet, F. Marquier, R. Carminati, and J. J. Greffet, "Surface electromagnetic waves thermally excited: radiative heat transfer, coherence properties and Casimir forces revisited in the near field," *Surface Science Reports*, vol. 57, no. 3-4, pp. 59–112, 2005.

[15] R. Carminati and J.-J. Greffet, "Near-field effects in spatial coherence of thermal sources," *Physical Review Letters*, vol. 82, no. 8, pp. 1660–1663, 1999.

[16] W. T. Lau, J.-T. Shen, G. Veronis, and S. Fan, "Spatial coherence of the thermal electromagnetic field in the vicinity of a dielectric slab," *Physical Review E*, vol. 76, no. 1, Article ID 016601, 2007.

[17] J. E. Sipe, "New Green-function formalism for surface optics," *Journal of the Optical Society of America B*, vol. 4, no. 4, pp. 481–489, 1987.

[18] F. S. S. Rosa, D. A. R. Dalvit, and P. W. Milonni, "Casimir-lifshitz theory and metamaterials," *Physical Review Letters*, vol. 100, no. 18, Article ID 183602, 2008.

[19] J. Hao, Y. Yuan, L. Ran et al., "Manipulating electromagnetic wave polarizations by anisotropic metamaterials," *Physical Review Letters*, vol. 99, no. 6, Article ID 063908, 2007.

[20] J. Hao, Q. Ren, Z. An et al., "Optical metamaterial for polarization control," *Physical Review A*, vol. 80, no. 2, Article ID 023807, 2009.

[21] F. J. García-Vidal, L. Martín-Moreno, H. J. Lezec, and T. W. Ebbesen, "Focusing light with a single subwavelength aperture flanked by surface corrugations," *Applied Physics Letters*, vol. 83, no. 22, pp. 4500–4502, 2003.

[22] L. Martín-Moreno, F. J. Garcia-Vidal, H. J. Lezec, A. Degiron, and T. W. Ebbesen, "Theory of highly directional emission from a single subwavelength aperture surrounded by surface corrugations," *Physical Review Letters*, vol. 90, no. 16, Article ID 167401, 2003.

[23] J. Hao and L. Zhou, "Electromagnetic wave scatterings by anisotropic metamaterials: generalized 4×4 transfer-matrix method," *Physical Review B*, vol. 77, no. 9, Article ID 094201, 2008.

Hindawi Publishing Corporation
International Journal of Optics
Volume 2012, Article ID 372048, 13 pages
doi:10.1155/2012/372048

Review Article

Nanoscale Plasmonic Devices Based on Metal-Dielectric-Metal Stub Resonators

Yin Huang,[1,2] Changjun Min,[2] Liu Yang,[1,2] and Georgios Veronis[1,2]

[1] *Department of Electrical and Computer Engineering, Louisiana State University, Baton Rouge, LA 70803, USA*
[2] *Center for Computation and Technology, Louisiana State University, Baton Rouge, LA 70803, USA*

Correspondence should be addressed to Georgios Veronis, gveronis@lsu.edu

Received 10 May 2012; Accepted 10 July 2012

Academic Editor: Qiwen Zhan

Copyright © 2012 Yin Huang et al. This is an open access article distributed under the Creative Commons Attribution License, which permits unrestricted use, distribution, and reproduction in any medium, provided the original work is properly cited.

We review some of the recent research activities on plasmonic devices based on metal-dielectric-metal (MDM) stub resonators for manipulating light at the nanoscale. We first introduce slow-light subwavelength plasmonic waveguides based on plasmonic analogues of periodically loaded transmission lines and electromagnetically induced transparency. In both cases, the structures consist of a MDM waveguide side-coupled to periodic arrays of MDM stub resonators. We then introduce absorption switches consisting of a MDM plasmonic waveguide side-coupled to a MDM stub resonator filled with an active material.

1. Introduction

Light-guiding structures which allow subwavelength confinement of the optical mode are important for achieving compact integrated photonic devices. The minimum confinement of a guided optical mode in dielectric waveguides is set by the diffraction limit and is of the order of λ_0/n, where λ_0 is the wavelength in free space and n is the refractive index.

As opposed to dielectric waveguides, plasmonic waveguides, based on surface plasmons propagating at metal-dielectric interfaces, have shown the potential to guide and manipulate light at deep subwavelength scales [1, 2]. Several different nanoscale plasmonic waveguiding structures have been recently proposed, such as metallic nanowires, metallic nanoparticle arrays, V-shaped grooves, and metal-dielectric-metal (MDM) waveguides [3–10]. Among these, MDM plasmonic waveguides are of particular interest because they support modes with deep subwavelength scale and high group velocity over a very wide range of frequencies extending from DC to visible [11]. Thus, MDM waveguides could be potentially important in providing an interface between conventional optics and subwavelength electronic and optoelectronic devices. Because of the predicted attractive properties of MDM waveguides, their modal structure has been studied in great detail [6, 11–14], and people have also started to explore such structures experimentally [15–17]. Recent research work has therefore focused on the development of functional plasmonic devices, including active devices, for nanoscale plasmonic integrated circuits. Three-dimensional MDM plasmonic waveguides were recently experimentally realized and characterized by several research groups [18–21]. In these experiments, the MDM waveguides are typically defined using electron beam lithography (EBL) and patterned using a focused ion beam (FIB) or other similar processes. In addition, the integration of nanoplasmonic waveguides with active materials, such as photochromic molecules or CdSe quantum dots, has also been recently achieved experimentally by several research groups [22, 23].

Waveguide-cavity systems are particularly useful for the development of several integrated photonic devices, such as tunable filters, optical switches, channel drop filters, reflectors, and impedance matching elements. In MDM plasmonic waveguide devices, a waveguide-cavity system can be created by side-coupling a stub resonator, consisting of a MDM waveguide of finite length, to a MDM waveguide [9]. In this paper, we provide a review of some of our own recent research activities on plasmonic devices based on metal-dielectric-metal stub resonators for manipulating light at the nanoscale [24–26]. The remainder of the paper is organized as follows. In Section 2, we first review the methods used

for the simulation and analysis of such devices. We then introduce slow-light waveguides for enhanced light-matter interaction (Section 3) and absorption switches (Section 4) based on metal-dielectric-metal stub resonators. Finally, our conclusions are summarized in Section 5.

2. Simulation and Analysis Methods

2.1. Full-Wave Finite-Difference Methods. The properties of MDM plasmonic waveguide devices can be investigated using full-wave electromagnetic simulation methods such as finite-difference methods in the time and frequency domains. In particular, the finite-difference frequency-domain (FDFD) method [27, 28] allows to directly use experimental data for the frequency-dependent dielectric constant of metals such as silver [29], including both the real and imaginary parts, with no approximation. Perfectly matched layer (PML) absorbing boundary conditions are used at all boundaries of the simulation domain [30].

Due to the rapid field variation at the metal-dielectric interfaces, a very fine grid resolution of ~1 nm is required at the metal-dielectric interfaces to adequately resolve the local fields. On the other hand, a grid resolution of $\sim \lambda/20$ is sufficient in other regions of the simulation domain. For example, the required grid size in air at $\lambda_0 = 1.55\,\mu$m is ~77.5 nm, which is almost two orders of magnitude larger than the required grid size at the metal-dielectric interfaces. A nonuniform orthogonal grid [31] is therefore commonly used to avoid an unnecessary computational cost. We found that by using such a grid our results are accurate to ~0.05%.

The properties of MDM plasmonic waveguide devices can also be investigated using the finite-element frequency-domain method (FEM). The FEM is a more powerful technique than FDFD, especially for problems with complex geometries. However, FDFD is conceptually simpler and easier to program. The main advantage of FEM is that complex geometric structures can be discretized using a variety of elements of different shapes, while in FDFD a rectangular grid is typically used leading to staircase approximations of particle shapes [30, 32]. In addition, in FEM fields within elements are approximated by shape functions, typically polynomials, while in FDFD a simpler piecewise constant approximation is used [32]. In short, FEM is more complicated than FDFD but achieves better accuracy for a given computational cost [32].

2.2. Transmission Line Theory. The properties of systems, which consist of circuits of deep subwavelength MDM plasmonic waveguides, can be described using the concept of characteristic impedance and transmission line theory [7, 33, 34].

The characteristic impedance of the fundamental TEM mode in a perfect electric conductor (PEC) parallel-plate waveguide with a dielectric layer thickness d is uniquely defined as the ratio of voltage V to surface current density I and is equal to [34]

$$Z_{\mathrm{TEM}} \equiv \frac{V}{I} = \frac{E_x w}{H_y} = \frac{\beta_{\mathrm{TEM}}}{\omega\varepsilon_0} w = \sqrt{\frac{\mu_0}{\varepsilon_0}}\, w, \tag{1}$$

where E_x, H_y are the transverse components of the electric and magnetic field, respectively, and we assumed a unit-length waveguide in the y direction. Non-TEM modes, such as the fundamental MDM mode, voltage, and current, are not uniquely defined. However, metals like silver satisfy the condition $|\varepsilon_{\mathrm{metal}}| \gg \varepsilon_{\mathrm{diel}}$ at the optical communication wavelength of 1.55 μm [29]. Thus, $|E_{x\,\mathrm{metal}}| \ll |E_{x\,\mathrm{diel}}|$, so that the integral of the electric field in the transverse direction can be approximated by $E_{x\,\mathrm{diel}} w$, and we may therefore define the characteristic impedance of the fundamental MDM mode as

$$Z_{\mathrm{MDM}}(w) \equiv \frac{E_{x\,\mathrm{diel}} w}{H_{y\,\mathrm{diel}}} = \frac{\gamma_{\mathrm{MDM}}(w)}{j\omega\varepsilon} w, \tag{2}$$

where $\gamma_{\mathrm{MDM}} = \alpha_{\mathrm{MDM}} + i\beta_{\mathrm{MDM}}$ is the complex wave vector of the fundamental propagating TM mode in a MDM waveguide of width w and ε is the dielectric permittivity of the dielectric region of the MDM waveguide.

2.3. Scattering Matrix Theory. The properties of systems which consist of circuits of deep subwavelength MDM plasmonic waveguides, in which only the fundamental TM mode is propagating, can also be described using scattering matrix theory [35]. As mentioned above, in the transmission line theory method the transmission and reflection coefficients at MDM waveguide junctions are calculated using the concept of the characteristic impedance (2). Unlike the transmission line theory method, in the scattering matrix theory method, the transmission and reflection coefficients at MDM waveguide junctions are directly numerically extracted using a full-wave simulation method such as FDFD [35]. Thus, the use of the scattering matrix theory method results in improved accuracy and increased computational cost associated with the additional full-wave simulations required to extract the transmission and reflection coefficients at MDM waveguide junctions.

2.4. Numerical Example. We now consider a specific numerical example in order to compare the different methods for the analysis and simulation of nanoscale plasmonic devices based on metal-dielectric-metal stub resonators. We consider a plasmonic MDM waveguide side-coupled to two MDM stub resonators (Figure 1(a)). The resonant frequencies of the cavities can be tuned by adjusting the cavity lengths L_1 and L_2. This system is a plasmonic analogue of electromagnetically induced transparency (EIT) [36, 37].

The MDM waveguide and MDM stub resonators have deep subwavelength widths ($w \ll \lambda$), so that only the fundamental TM mode is propagating. Thus, we can use transmission line theory or scattering matrix theory to account for the behavior of the system. First, the properties of such a side-coupled-cavity structure can be described using transmission line theory and the concept of characteristic impedance. Based on transmission line theory, the structure of Figure 1(a) is equivalent to two short-circuited transmission line resonators of lengths L_1 and L_2, propagation constant $\gamma_{\mathrm{MDM}}(w)$, and characteristic impedance $Z_{\mathrm{MDM}}(w)$ (2) which are connected in series to a transmission line with the same characteristic impedance $Z_{\mathrm{MDM}}(w)$ [33]. Based on

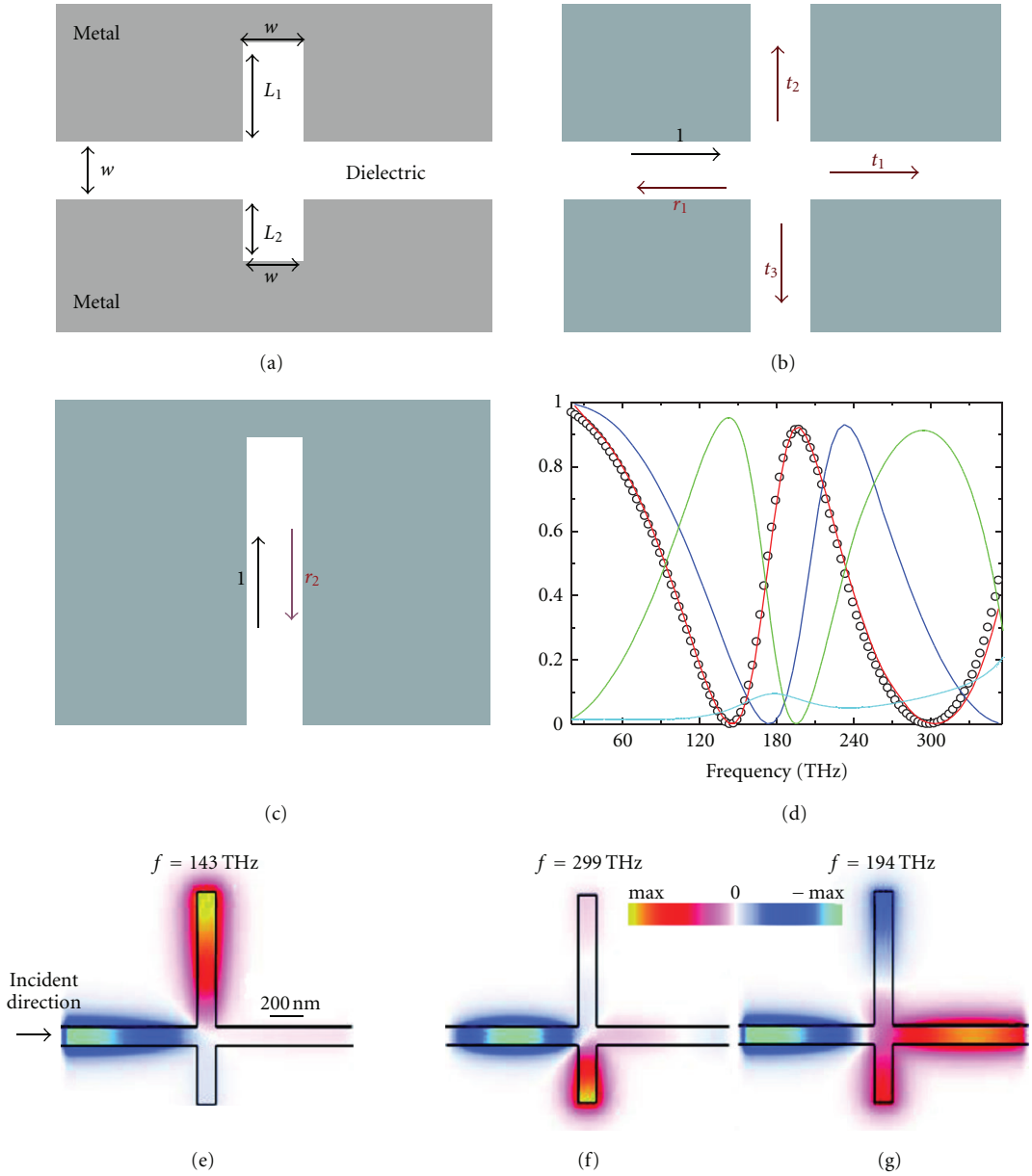

Figure 1: (a) Schematic of a MDM plasmonic waveguide side-coupled to two MDM stub resonators. (b) Schematic defining the reflection coefficient r_1 and transmission coefficients t_1, t_2, t_3 when the fundamental TM mode of the MDM waveguide is incident at a waveguide crossing. Note that $t_2 = t_3$ due to symmetry. (c) Schematic defining the reflection coefficient r_2 of the fundamental TM mode of the MDM waveguide at the boundary of a short-circuited MDM waveguide. (d) Transmission spectra for the structure of (a) calculated using FDFD (circles), transmission line theory (solid blue line), and scattering matrix theory (solid red line) for a silver-air structure with $w = 50$ nm. Also shown are the reflection (solid green line) and absorption (solid cyan line) spectra calculated using FDFD. Results are shown for $L_1 = 360$ nm, $L_2 = 160$ nm. ((e)–(g)) Magnetic field profiles for the structure of (a) for $L_1 = 360$ nm, $L_2 = 160$ nm, $w = 50$ nm at $f = 143$, 299, 194 THz, when the fundamental TM mode of the MDM waveguide is incident from the left.

this model, the transmission T of the structure of Figure 1(a) can be calculated as [33]

$$T = \left| 1 + \frac{1}{2}\left(\tanh\left(\gamma_{\mathrm{MDM}} L_1\right) + \tanh\left(\gamma_{\mathrm{MDM}} L_2\right)\right) \right|^{-2}. \quad (3)$$

Second, the properties of such a side-coupled-cavity structure can also be described using scattering matrix theory. The complex magnetic field reflection coefficient r_1 and transmission coefficients t_1, $t_2 = t_3$ for the fundamental propagating TM mode at a MDM waveguide crossing (Figure 1(b)), as well as the reflection coefficient r_2 at the boundary of a short-circuited MDM waveguide (Figure 1(c)), are numerically extracted using FDFD [35]. The power transmission spectra $T(\omega)$ of the two-cavity system (Figure 1(a)) can then be calculated using scattering matrix theory as

$$T = |t_1 - C|^2. \quad (4)$$

Here, $C = t_2^2(2t_1 - 2r_1 + s_1 + s_2)/(t_1^2 - (r_1 - s_1)(r_1 - s_2))$, $s_i = r_2^{-1}\exp(2\gamma_{\mathrm{MDM}}L_i)$, $i = 1, 2$.

In Figure 1(d) we show the transmission spectra for the structure of Figure 1(a) calculated using FDFD, transmission line theory (3) and scattering matrix theory (4). We observe that there is good agreement between the transmission line theory results and the exact results obtained using FDFD. We note, however, that while the transmission at the transparency peak is correctly predicted by transmission line theory, the resonance frequency obtained using transmission line theory is blue-shifted with respect to the exact result obtained using FDFD (Figure 1(d)). The difference between the transmission line theory results and the exact results obtained using FDFD is due to the error introduced by the transmission line model in the phase of the reflection coefficient [38, 39] at the interfaces of the two-side-coupled cavities. Such limitations of the transmission line model for circuits of MDM plasmonic waveguides are also described in detail in [35]. We also observe that there is excellent agreement between the scattering matrix theory results and the exact results obtained using FDFD. This is due to the fact that, as mentioned above, in the scattering matrix theory method, the transmission and reflection coefficients are directly extracted using FDFD. The improved accuracy of scattering matrix theory with respect to transmission line theory comes at the cost of the additional FDFD simulations required to numerically extract the transmission and reflection coefficients.

The transmission spectra $T(\omega)$ feature two dips (Figure 1(d)). We found that the frequencies ω_1, ω_2 where these dips occur are approximately equal to the first resonant frequencies of the two cavities; that is, $\phi_{r_1}(\omega_i) + \phi_{r_2}(\omega_i) - 2\beta_{\mathrm{MDM}}(\omega_i)L_i \approx -2\pi$, $i = 1, 2$, where $\phi_{r_i} = \arg(r_i)$, $i = 1, 2$. When either one of the cavities is resonant, the field intensity in that cavity is high, while the field intensity in the other cavity is almost zero, since it is far from resonance (Figures 1(e) and 1(f)). In addition, the transmission is almost zero, since the incoming wave interferes destructively with the decaying amplitude into the forward direction of the resonant cavity field. The transmission spectra $T(\omega)$ also feature a transparency peak centered at frequency ω_0. We found that ω_0 is approximately equal to the first resonant frequency of the composite cavity of length $L_1 + L_2 + w$ formed by the two cavities; that is, $2\phi_{r_2}(\omega_0) - 2\beta_{\mathrm{MDM}}(\omega_0)(L_1 + L_2 + w) \approx -2\pi$. Thus, the transmission peak frequency ω_0 is tunable through the cavity lengths L_1, L_2. When $\omega = \omega_0$, the field intensity is high in the entire composite cavity (Figure 1(g)), and the transmission spectra exhibit a peak due to resonant tunneling of the incoming wave through the composite cavity. In Figure 1(d) we also show the reflection and absorption spectra for the structure of Figure 1(a). We note that in all cases considered in this paper the length of the MDM stub resonators is much smaller than the propagation length of the supported optical mode in the stubs. Thus, the absorption in the MDM stub resonators is small. This applied to both the two-stub structures considered in this Section, as well as the single-stub structures considered in Section 4 below.

3. Slow-Light Waveguides

Slowing down light in plasmonic waveguides leads to enhanced light-matter interaction and could therefore enhance the performance of nanoscale plasmonic devices such as switches and sensors [40–45]. However, in conventional MDM plasmonic waveguides, once the operating wavelength and modal size are fixed, the group velocity of light is not tunable.

3.1. Slow-Light Based on a Plasmonic Analog of Periodically Loaded Transmission Lines. In this section, we first introduce a plasmonic waveguide system, which supports a subwavelength broadband slow-light-guided mode with a tunable slow-down factor at a given wavelength. The structure is a plasmonic analog of the periodically loaded transmission lines used in microwave engineering [33]. Such slow-light plasmonic waveguide systems could be potentially used in nonlinear, switching, and sensing applications.

The structure consists of a MDM waveguide side-coupled to a periodic array of MDM stub resonators (Figure 2(a)). Both the MDM waveguide and MDM stub resonators have deep subwavelength widths ($w_0, w \ll \lambda$). The periodicity d is also subwavelength ($d \ll \lambda$), so that the operating wavelength is far from the Bragg wavelength of the waveguide [46] ($\lambda \gg \lambda_{\mathrm{Bragg}}$). In addition, the distance between adjacent side-coupled cavities d-w is chosen large enough so that direct coupling between the cavities has a negligible effect on the dispersion relation of the system. This sets a lower limit on the periodicity d_{min} of the plasmonic waveguide structure. For $w = 50$ nm we found that $d_{\mathrm{min}} \sim 80$ nm.

Using transmission line theory [33], the dispersion relation between ω and the Bloch wave vector $\gamma = \alpha + i\beta$ of the entire system is found to be

$$\cosh(\gamma d) = \cosh^2\left(\gamma_0\frac{d}{2}\right) + \sinh^2\left(\gamma_0\frac{d}{2}\right) + \frac{Z_1}{Z_0}\sinh\left(\gamma_0\frac{d}{2}\right)\cosh\left(\gamma_0\frac{d}{2}\right)\tanh(\gamma_1 L). \quad (5)$$

In Figure 2(b), we show the dispersion relation for the plasmonic waveguiding structure of Figure 2(a) calculated using FDFD, which, similar to surface plasmons propagating at a single metal-dielectric interface [46], exhibits a resonance. In the lossless metal case, the resonance frequency ω_{res} is the cut-off frequency of the fundamental mode, and for $\omega > \omega_{\mathrm{res}}$, the system has a band gap, supporting a nonpropagating mode with $\beta = 0$. In addition, we have $\gamma_0 = i\beta_0$, $\gamma_1 = i\beta_1$, and $\beta(\omega_{\mathrm{res}}) = \pi/d$ at the band edge. Using these and (5), we find that the resonance frequency ω_{res} is a solution of the following equation:

$$Z_1\tan[\beta_1(\omega_{\mathrm{res}})L] = 2Z_0\cot\left[\beta_0(\omega_{\mathrm{res}})\frac{d}{2}\right]. \quad (6)$$

Thus, unlike in conventional MDM waveguides where ω_{res} is equal to the surface plasmon frequency of the metal-dielectric interface ($\omega_{\mathrm{res}} = \omega_{\mathrm{sp}}$) and is fixed for a given metal [46], in such a plasmonic waveguide system the resonance frequency ω_{res} is tunable through its geometric parameters.

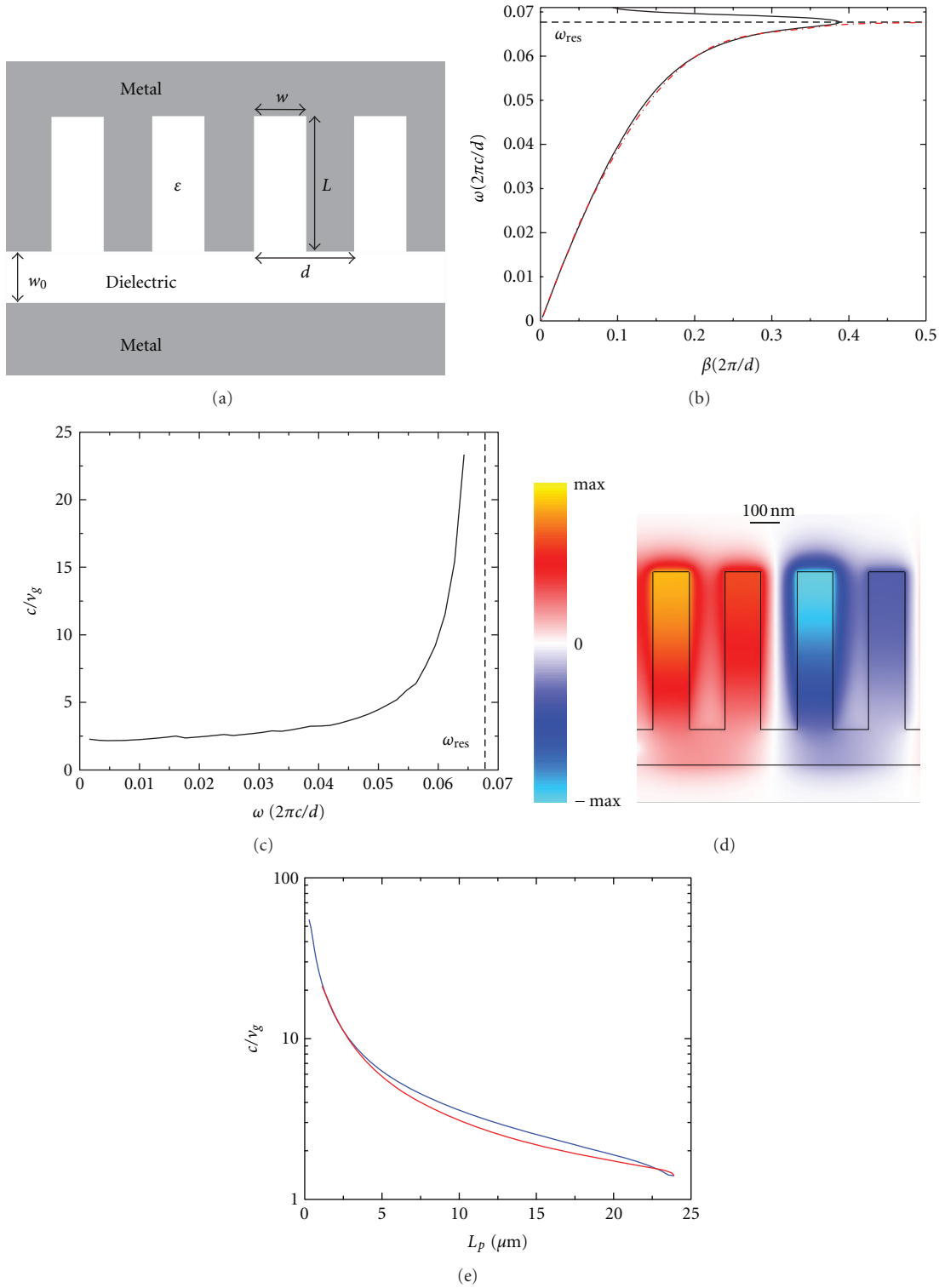

FIGURE 2: (a) Schematic of a plasmonic waveguide system consisting of a metal-dielectric-metal (MDM) waveguide side-coupled to a periodic array of MDM stub resonators. (b) Dispersion relation of the plasmonic waveguide system of (a) calculated using FDFD (black solid line). Results are shown for a silver-air structure with $d = 100\,\text{nm}$, $L = 220\,\text{nm}$, $w_0 = w = 50\,\text{nm}$. Also shown is the dispersion relation for lossless metal (red dash-dotted line) and the resonance frequency ω_{res} (black dashed line) ($\omega_{\text{res}} \cong 0.067 * 2\pi c/d$ corresponding to $\lambda_{\text{res}} \cong 1.5\,\mu m$). (c) Reciprocal of the group velocity v_g of light in the plasmonic waveguide system as a function of frequency. All parameters are as in (b). (d) Magnetic field profile of the supported optical mode in the system at $\lambda_0 = 1.55\,\mu\text{m}$. All other parameters are as in Figure 2(b). (e) Reciprocal of v_g versus propagation length L_p for the plasmonic waveguide system of Figure 2(a) at $\lambda_0 = 1.55\,\mu\text{m}$ calculated using FDFD. Results are shown for $d = 100\,\text{nm}$ (upper blue curve) and $d = 200\,\text{nm}$ (lower red curve) as L is varied. All other parameters are as in (b).

In the presence of loss, we have $\beta(\omega_{\text{res}}) < \pi/d$ (Figure 2(b)). In addition, for $\omega > \omega_{\text{res}}$, the Bloch wave vector γ has an imaginary component ($\beta \neq 0$) and the dispersion relation experiences back-bending [46] with negative group velocity $v_g = \partial\omega/\partial\beta$ (Figure 2(b)).

In such a plasmonic waveguide system, light is slowed down over a very wide frequency range extending from DC to slightly below the resonance frequency (Figure 2(c)). To find the slow-down factor c/v_g in the low-frequency limit, we take the limit of the dispersion relation (5) as $\omega \to 0$. We note that in the limit of $\omega \to 0$, $\gamma_0 \simeq \gamma_1 \simeq i\omega\sqrt{\varepsilon\mu_0}$. Using these, we obtain the low-frequency ($\omega \to 0$) slow-down factor $c/v_g = \sqrt{1 + wL/w_0 d}$. We confirmed that this analytical result is in excellent agreement with the result obtained using FDFD. Thus, the group velocity of the system in the low-frequency regime is entirely controlled by its geometry. When ω approaches ω_{res} ($\omega \leq \omega_{\text{res}}$), the dispersion relation becomes flat, and the group velocity v_g rapidly decreases (Figure 2(c)).

We found that at frequencies far from the resonance frequency, the modal energy of the periodic plasmonic waveguide extends over both the waveguide and the stub resonators. On the other hand, at frequencies near the resonance frequency, the field intensity in the resonators is enhanced, and the modal energy is therefore mostly concentrated in the resonators (Figure 2(d)). In both cases the modal size is subwavelength. In addition, due to the absorption loss in the metal, there is a trade-off between the slow-down factor c/v_g and the propagation length L_p of the supported optical mode in such slow-light plasmonic waveguide systems (Figure 2(e)).

3.2. Slow-Light Based on a Plasmonic Analog of Electromagnetically Induced Transparency. In this section, we introduce an alternative MDM plasmonic waveguide system, based on a plasmonic analogue of EIT, which also supports a guided subwavelength slow-light mode. EIT is a coherent process observed in three-level atomic media, which allows a narrow transparency window in the spectrum of an otherwise opaque medium, and can slow down light pulses by several orders of magnitude [47]. Since the EIT spectrum results from the interference of resonant pathways [47, 48], it has been recognized that similar interference effects can also occur in classical systems, such as optical waveguides coupled to resonators and metamaterials [47, 49–51]. In addition, it has been demonstrated that periodic optical waveguides, resulting from cascading structures with EIT-like response, can slow down and even stop light [48, 52, 53]. Our proposed structure consists of a periodic array of two MDM stub resonators side-coupled to a MDM waveguide.

We consider the plasmonic waveguide system (Figure 3(a)) obtained by periodically cascading the side-coupled-cavity structure of Figure 1(a). The periodicity d is subwavelength ($d \ll \lambda$), so that the operating wavelength is far from the Bragg wavelength of the waveguide [25] ($\lambda \gg \lambda_{\text{Bragg}}$). In addition, the distance between adjacent side-coupled cavities d-w is chosen large enough so that direct coupling between the cavities has a negligible effect on the dispersion relation of the system [25]. Using single-mode scattering matrix theory [35], the dispersion relation between the frequency ω and the Bloch wave vector $\gamma = \alpha + j\beta$ of the entire system is found to be

$$\cosh(\gamma d) = \frac{A}{2}\exp\left[-\gamma_{\text{MDM}}(d-w)\right] + \frac{B}{2}\exp[\gamma_{\text{MDM}}(d-w)], \tag{7}$$

which is in excellent agreement with the exact results obtained using FDFD (Figure 4(a)). Here $A = (t_1 - r_1)((t_1 + r_1 - 2C)/(t_1 - C))$ and $B = (t_1 - C)^{-1}$. In Figure 3(b), we show the dispersion relation for the plasmonic waveguiding structure of Figure 3(a). In the lossless metal case, the system supports three photonic bands in the vicinity of the cavity resonances. The middle band corresponds to a mode with slow group velocity $v_g = \partial\omega/\partial\beta$ and zero group velocity dispersion $\beta_2 = \partial^2\beta/\partial\omega^2$ near the middle of this band (Figure 3(b)). In the two band gaps between the three bands, the system supports nonpropagating modes with $\beta = 0$. Such a band diagram is similar to that of EIT systems [52]. When losses in the metal are included, the band structure is unaffected in the frequency range of the three bands except at the band edges (Figure 3(b)). In addition, in the frequency range of the two band gaps, the Bloch wave vector γ has an imaginary component ($\beta \neq 0$) and the dispersion relation experiences back-bending [25] with negative group velocity. In Figure 3(c) we show the magnetic field profile for the plasmonic waveguide system of Figure 3(a).

In addition, the width of the middle band and the slow-down factor c/v_g strongly depend on the frequency spacing between the resonances $\delta\omega = \omega_2 - \omega_1$. By decreasing the stub lengths difference δL, $\delta\omega$ decreases, and this leads to decreased bandwidth of the middle band (Figure 4(a)). In Figures 4(b) and 4(c) we show the slow-down factor c/v_g and propagation length L_p for the plasmonic waveguide system of Figure 3(a) as a function of frequency for two different values of δL. In both cases we show the frequency range corresponding to the middle band of the system. For a given δL, the propagation length L_p of the supported optical mode is maximized at a frequency very close to the frequency where the group velocity dispersion is zero. As δL and therefore $\delta\omega$ decrease, the slow-down factor c/v_g increases, while the propagation length L_p decreases at the frequency of zero group velocity dispersion. Thus, there is a trade-off between the slow-down factor c/v_g and the propagation length L_p of the supported optical mode in such slow-light plasmonic waveguide systems [25]. For $\delta L = 200\,\text{nm}$ ($\delta L = 75\,\text{nm}$) we have $c/v_g \approx 6$ ($c/v_g \approx 30$) at the frequency where the group velocity dispersion is zero (Figures 4(b) and 4(c)). We found that even larger slow-down factors can be obtained by further decreasing δL at the cost of reduced propagation length. We also note that the propagation length of the system for a given slowdown factor can be increased by incorporating gain media in the structure [46]. The slow-down factor exhibits two maxima near the two edges of this band and a minimum at a frequency near the middle of the band where the group velocity dispersion is zero.

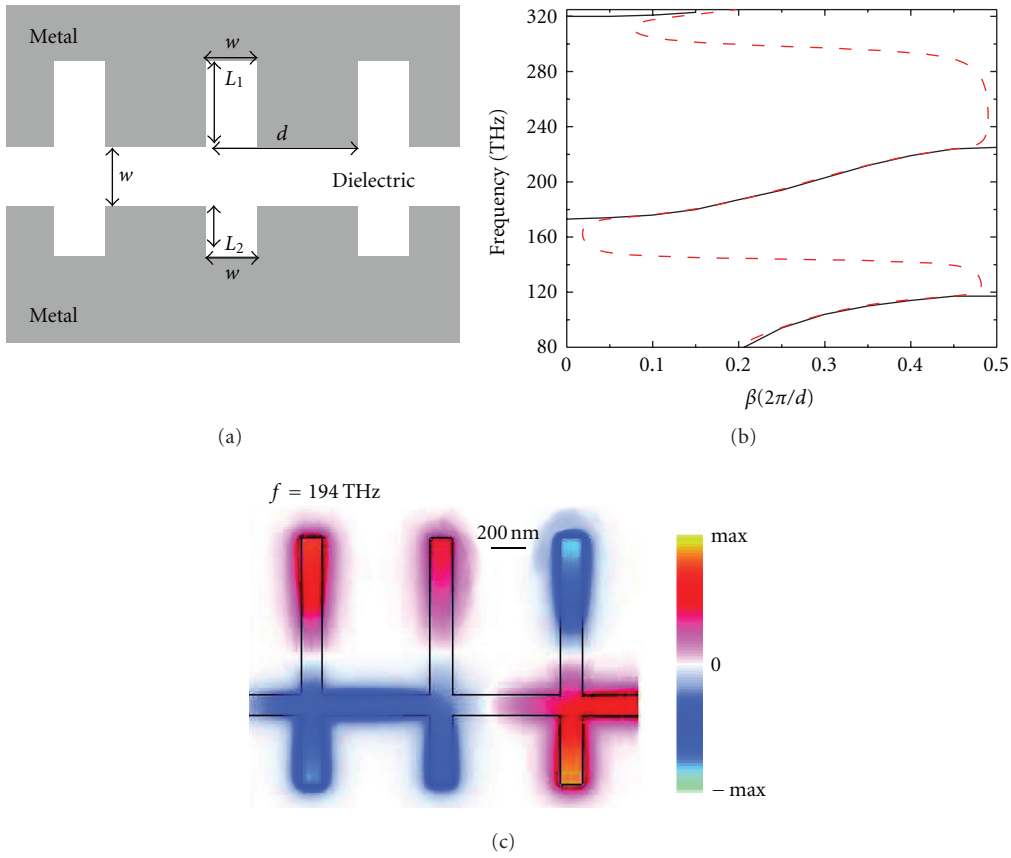

FIGURE 3: (a) Schematic of a plasmonic waveguide system consisting of a periodic array of two MDM stub resonators side-coupled to a MDM waveguide. (b) Dispersion relation of the plasmonic waveguide system of Figure 2(a) calculated using FDFD (red dashed line). Results are shown for a silver-air structure with $d = 300$ nm, $L_1 = 360$ nm, $L_2 = 160$ nm, and $w = 50$ nm. Also shown is the dispersion relation for lossless metal (black solid line). (c) Magnetic field profile for the structure of (a) for $L_1 = 360$ nm, $L_2 = 160$ nm, $w = 50$ nm at $f = 194$ THz.

We also consider the effect of the periodicity d (Figure 3(a)) on the dispersion relation of the system (Figure 4(d)). For large d the distance d-w between adjacent two-cavity structures in the periodic waveguide is large, so that their coupling through the MDM waveguide is weak. In this regime, the frequency range of the middle band of the periodic waveguide system of Figure 3(a) approximately corresponds to the frequency range of the transparency peak of the two-cavity structure of Figure 1(a). As d decreases, the coupling between adjacent two-cavity structures increases. As a result, the slow-light middle band shifts to higher frequencies, while its width slightly broadens (Figure 4(d)). Thus, the periodicity provides us an additional degree of freedom to tune the dispersion relation of the periodic waveguide system.

4. Absorption Switches

One of the main challenges in plasmonics is achieving active control of optical signals in nanoscale plasmonic devices [2]. This challenge has motivated significant recent activities in exploring actively controlled plasmonic devices, such as switches and modulators [22, 23, 54–63]. Several different approaches have been proposed in order to achieve active control of light in nanoscale plasmonic devices [22, 23, 54–63]. These include thermally induced changes in the refractive index [54–56], direct ultrafast optical excitation of the metal [57], as well as the incorporation of nonlinear [58, 59], electrooptic [60, 61], and gain [62] media in plasmonic devices. An alternative approach for active control of optical signals in plasmonic devices is tuning the absorption coefficient. This has been recently achieved experimentally through optical excitation of photochromic molecules [23] or CdSe quantum dots (QDs) [22, 63].

Here, we consider a switch consisting of a silver-air-silver MDM plasmonic waveguide side-coupled to a MDM stub resonator filled with a material with tunable absorption coefficient ($n = 2.02 + i\kappa$) (Figure 5(a)). The properties of such a side-coupled-cavity switch can be described using transmission line theory and the concept of characteristic impedance. Based on transmission line theory, the side-coupled-cavity switch is equivalent to a short-circuited transmission line resonator of length L, propagation constant γ_2, and characteristic impedance Z_2, which is connected in series to a transmission line with characteristic impedance Z_1 [33]. Based on this model, the transmission T of the side-coupled-cavity

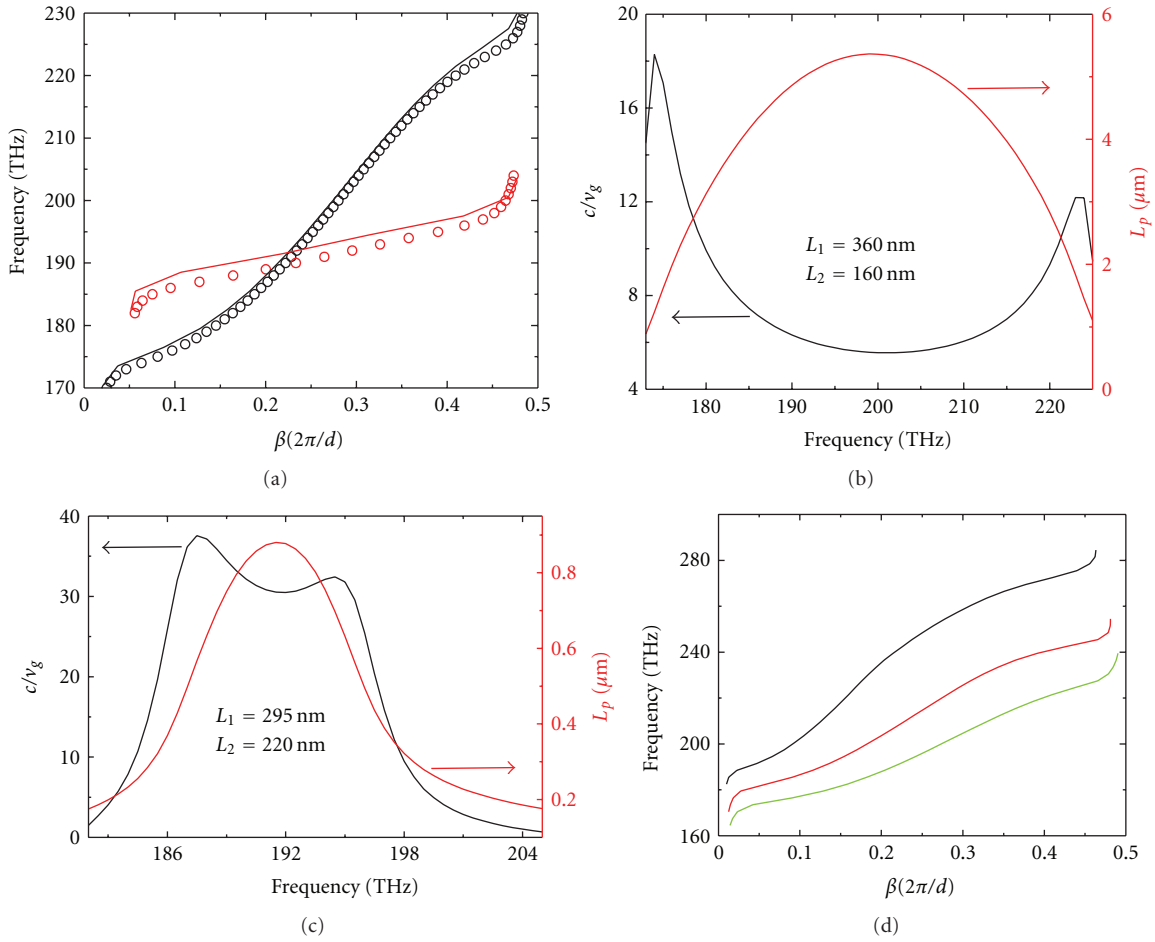

FIGURE 4: (a) Dispersion relation of the plasmonic waveguide system of Figure 3(a) calculated using FDFD (circles) and scattering matrix theory (solid line). Results are shown for $L_1 = 360$ nm, $L_2 = 160$ nm (black line and circles) and $L_1 = 295$ nm, $L_2 = 220$ nm (red line and circles). All other parameters are as in Figure 3(b). In both cases only a portion of the band structure is shown, corresponding to the frequency range of the middle band. ((b)-(c)) Reciprocal of the group velocity v_g and propagation length L_p for the plasmonic waveguide system of Figure 3(a) as a function of frequency calculated using FDFD. Results are shown for $L_1 = 360$ nm, $L_2 = 160$ nm and $L_1 = 295$ nm, $L_2 = 220$ nm. All other parameters are as in Figure 3(b). (d) Dispersion relation of the plasmonic waveguide system of Figure 3(a) calculated using FDFD. Results are shown for $d = 100$ nm (black line), $d = 200$ nm (red line), and $d = 300$ nm (green line). All other parameters are as in Figure 3(b). In all cases only a portion of the band structure is shown, corresponding to the frequency range of the middle band.

switch can be calculated using transmission line theory [33] as

$$T = \left| 1 + \frac{Z_2}{2Z_1} \tanh(\gamma_2 L) \right|^{-2}. \tag{8}$$

As seen from (8), the system exhibits a resonance when $\beta_2 L = (N+1/2)\pi$, where $\gamma_2 = \alpha_2 + j\beta_2$, and N is an integer. We assume that the cavity length L is equal to one of the resonant lengths L_N at frequency ω_0 and consider the response of the system for frequencies ω in the vicinity of $\omega_0 (|\omega - \omega_0|/\omega_0 \ll 1)$. In such a case, we find that (8) can be approximated as

$$T(\omega) \approx \frac{(\omega - \omega_0)^2 + (\omega_0/2Q_0)^2}{(\omega - \omega_0)^2 + ((\omega_0/2Q_0) + (\omega_0/2Q_e))^2}, \tag{9}$$

where

$$Q_0 = \frac{\omega_0}{2\alpha_2 v_g}, \qquad Q_e = \frac{Z_1}{Z_2} \frac{\omega_0 L_N}{v_g}, \tag{10}$$

and $v_g = \partial\omega/\partial\beta_2$. Here Q_0 is the quality factor associated with the internal loss in the cavity due to the propagation loss of the optical mode and Q_e is the quality factor associated with the power escape through the waveguide. We note that (9) can also be directly derived using coupled-mode theory and first-principles calculation of the quality factors Q_0 and Q_e [64, 65]. We observe that the on-resonance transmission is a function of the ratio r of the quality factors; that is,

$$T(\omega_0) \approx \left(\frac{r}{r+1} \right)^2, \qquad r = \frac{Q_e}{Q_0} = \frac{Z_1}{Z_2} 2\alpha_2 L_N. \tag{11}$$

Since both α_2 and Z_2 depend on the imaginary part κ of the refractive index in the cavity, the transmission of the system can be controlled by modifying κ with an external beam.

In Figure 5(b) we show the transmission spectra of the side-coupled-cavity structure for $w = w_0 = 50$ nm in the absence of optical pumping ($\kappa = 0$) calculated using FDFD.

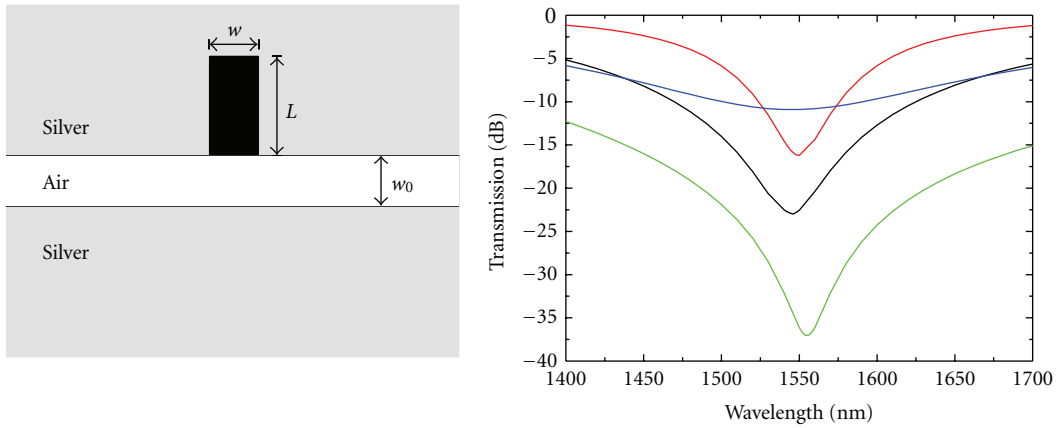

(a) (b)

Figure 5: (a) Schematic of a switch consisting of a silver-air-silver MDM plasmonic waveguide side-coupled to a cavity filled with an absorbing material with refractive index $n = 2.02 + i\kappa$. The imaginary part κ of the refractive index can be modified with an external control beam. (b) Transmission spectra of the switch calculated using FDFD. Results are shown for $w = 50$ nm, $L = 120$ nm, $\kappa = 0$ (black curve), $w = 50$ nm, $L = 405$ nm, $\kappa = 0$ (red curve), $w = 200$ nm, $L = 175$ nm, $\kappa = 0$ (green curve), and $w = 50$ nm, $L = 120$ nm, $\kappa = 0.1$ (blue curve). In all cases $w_0 = 50$ nm and $\lambda_0 = 1.55\,\mu$m.

The length of the cavity L is chosen $L = 120$ nm, so that the system exhibits a resonance at $\lambda_0 = 1.55\,\mu$m. The transmission spectra are characterized by a Lorentzian lineshape, as predicted by (9). We observe that, as $|\omega - \omega_0|$ increases, the transmission increases, and, in the limit $|\omega - \omega_0| \to \infty$, the transmission approaches 1 ($\lim_{|\omega-\omega_0|\to\infty} T(\omega) = 1$). In other words, if ω is far from the resonant frequency ω_0, the incident waveguide mode is almost completely transmitted. At resonance ($\omega = \omega_0$), we observe that the transmission is less than 1% ($T(\omega_0) \approx -23$ dB). When the material filling the cavity is in its transparent state ($\kappa = 0$), the propagation loss of the optical mode is only associated with the loss in the metal. In that case, the propagation length is in the order of tens of micrometers at near-infrared wavelengths [6], so that $\alpha_2 L \ll 1$, and therefore $r \ll 1$ and $T \ll 1$ (11). In addition, since $r \ll 1$, the total quality factor, defined as $Q \equiv (Q_0^{-1} + Q_e^{-1})^{-1}$, is $Q \approx Q_e \approx 4.4$ (10), and the system response is broad (Figure 5(b)). The low-quality factor in this structure is associated with the low reflectivity at the waveguide-cavity interface due to the small impedance mismatch.

If the stub length L increases to the second resonant length ($L = 405$ nm is chosen as before so that the system exhibits a resonance at $\lambda_0 = 1.55\,\mu$m), more energy is stored in the resonant cavity, so that Q_e increases (10), and therefore the on-resonance transmission also increases (11). We indeed observe that for $L = 405$ nm the transmission is higher than that for $L = 120$ nm in the entire frequency range (Figure 5(b)).

If the stub width w increases ($w = 200$ nm, and $L = 175$ nm is chosen as before so that the system exhibits a resonance at $\lambda_0 = 1.55\,\mu$m), the propagation length of the optical mode in the cavity increases, leading to higher Q_0 (10). In addition, the wider w leads to larger power escape through the waveguide and therefore lower Q_e. Hence the on-resonance transmission decreases (11). We indeed observe that for wider w the transmission is lower in the entire frequency range (Figure 5(b)).

In the presence of optical pumping, the material in the stub switches to its absorbing state. The internal loss in the cavity increases, and therefore Q_0 decreases, resulting in higher on-resonance transmission (11). We indeed observe that for $\kappa = 0.1$ the on resonance transmission is significantly larger than that for $\kappa = 0$ (Figure 5(b)). Thus, the side-coupled structure can operate as an absorption switch for MDM plasmonic waveguides, in which the on/off states correspond to the presence/absence of optical pumping.

In Figure 6(a) we show the modulation depth of the switch $T(\kappa = 1)/T(\kappa = 0)$ as a function of the cavity length L at $\lambda_0 = 1.55\,\mu$m calculated with FDFD. We observe that the modulation depth exhibits peaks when L is equal to one of the resonant lengths of the stub. This is due to the fact that the transmission in the absence of pumping $T(\kappa = 0)$ is minimized on resonance, as described above. We also observe that the maximum modulation depth is obtained when the cavity length L is equal to the first resonant length. As described above, if the stub length L increases to a higher-order resonant length, the quality factor Q_e increases and leads to larger on-resonance transmission. This occurs both in the presence and in the absence of pumping; that is, both $T(\kappa = 1)$ and $T(\kappa = 0)$ increase. In the absence of pumping ($\kappa = 0$), we have $r \ll 1$ for the ratio r of the quality factors, as mentioned above. Thus, based on (11), the on-resonance transmission in the absence of pumping varies roughly quadratically with r. On the other hand, in the presence of pumping, r is much larger, and the on-resonance transmission is, therefore, less sensitive to r (11). In other words, if the stub length L increases to a higher-order resonant length, the on-resonance transmission in the absence of pumping $T(\kappa = 0)$ increases more than the on-resonance transmission in the presence of pumping $T(\kappa = 1)$. Thus, the modulation depth $T(\kappa = 1)/T(\kappa = 0)$ decreases (Figure 6(a)). In Figure 6(a)

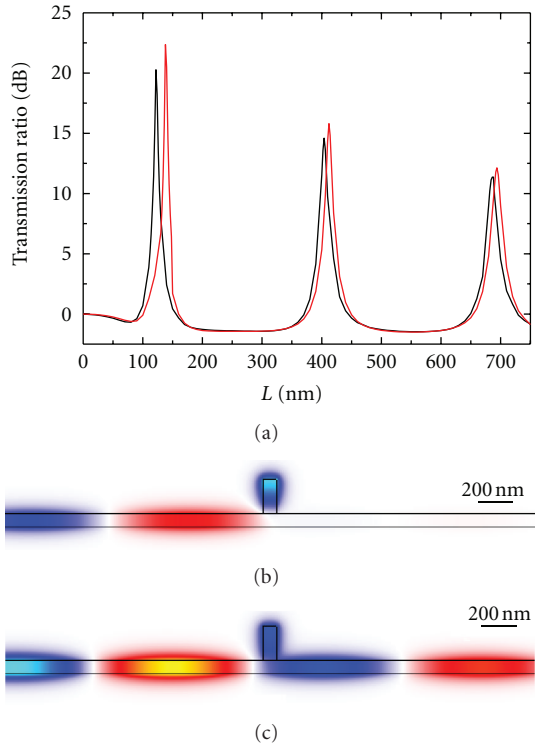

Figure 6: (a) Modulation depth $T(\kappa = 1)/T(\kappa = 0)$ of the side-coupled-cavity switch (Figure 5(a)) as a function of the stub length L calculated using FDFD (black curve), and transmission line theory (red curve). Results are shown for $w = 50$ nm. All other parameters are as in Figure 5(b). (b) Magnetic field profile of the switch for $L = 120$ nm in the absence of pumping ($\kappa = 0$). All other parameters are as in (a). (c) Magnetic field profile of the switch in the presence of pumping ($\kappa = 1$). All other parameters are as in (b).

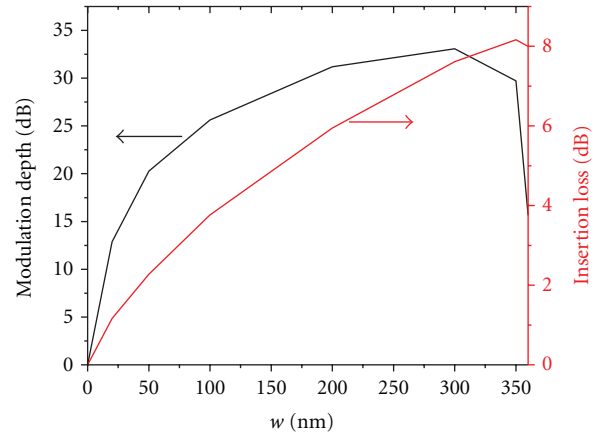

Figure 7: Modulation depth $T(\kappa = 1)/T(\kappa = 0)$ (black curve) and insertion loss (red curve) of the side-coupled-cavity switch (Figure 5(a)) as a function of the stub width w. For each stub width w, the stub length L is equal to the first resonant length of the cavity. All other parameters are as in Figure 5(b).

we also show the modulation depth of the switch calculated by transmission line theory (8). We again observe that there is very good agreement between the transmission line theory results and the exact results obtained using FDFD.

In Figures 6(b) and 6(c) we show the magnetic field profile of the side-coupled-cavity switch corresponding to the *off* and *on* states, respectively. In the absence of pumping, corresponding to the *off* state, the incident optical mode is almost completely reflected. In contrast, in the presence of pumping, corresponding to the *on* state, the transmission increases by more than two orders of magnitude leading to a large modulation depth.

In Figure 7 we show the maximum modulation depth of the side-coupled-cavity switch as a function of the stub width w. As mentioned above, for a given w the maximum modulation depth is achieved when the stub length L is equal to the first resonant length. We observe that for $w < 300$ nm the maximum modulation depth increases with w. As described above, larger w leads to both higher Q_0 and lower Q_e for the resonator. Thus, the quality factors' ratio r decreases, and the on-resonance transmission decreases (11). This occurs both in the presence and in the absence of pumping; that is, both $T(\kappa = 1)$ and $T(\kappa = 0)$ decrease. However, as mentioned above, in the absence of pumping ($\kappa = 0$) the on-resonance transmission is more sensitive to r. Thus, as the stub width w increases, the on-resonance transmission in the absence of pumping $T(\kappa = 0)$ decreases more than the on-resonance transmission in the presence of pumping $T(\kappa = 1)$. Thus, the modulation depth $T(\kappa = 1)/T(\kappa = 0)$ increases with w (Figure 7). We also observe that the modulation depth is maximized for $w \approx 300$ nm. In other words, for a given pumping intensity there is a maximum achievable modulation depth for the side-coupled-cavity structure. We found that the decrease with w of the modulation depth for $w > 300$ nm is associated with the excitation of higher-order modes in the resonator, which occurs when w becomes comparable to the wavelength. In this regime, the transmission line model breaks down, and the system properties are no longer accurately described by (8)–(11).

In Figure 7 we also show the insertion loss of the side-coupled-cavity switch, defined as $-10\log_{10}(T(\kappa = 1))$, as a function of the stub width w. As described above, for $w < 300$ nm the on-resonance transmission in the presence of pumping $T(\kappa = 1)$ decreases with w, and the insertion loss therefore increases (Figure 7). For $w > 300$ nm, the insertion loss decreases with w(Figure 7), due to the excitation of higher-order modes in the resonator, as also described above. We observe that for the side-coupled-cavity switch there is a tradeoff between modulation depth and insertion loss, as the geometrical parameters of the stub are varied. Similar tradeoffs are observed in electroabsorption modulators [66].

In Figure 8, we show the modulation depth $T(\kappa)/T(\kappa = 0)$ of the side-coupled-cavity switch as a function of the imaginary part κ of the refractive index. As expected, the modulation depth increases with κ. We also observe that even for a relatively small variation in the absorption coefficient of the material filling the cavity ($\kappa = 0.01$), we can achieve a modulation depth of ~60% (~4 dB). We note that such modulation depths have been demonstrated experimentally

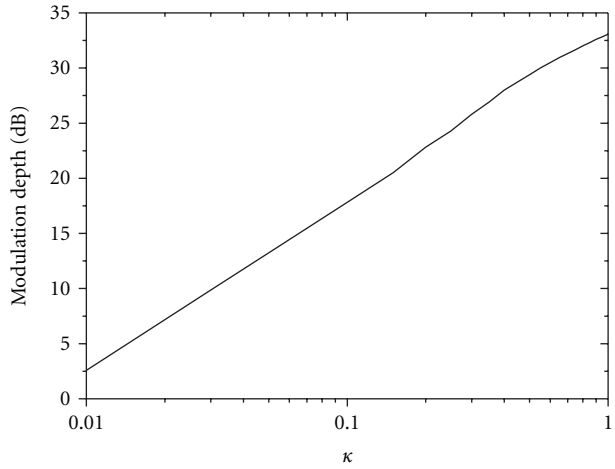

FIGURE 8: Modulation depth $T(\kappa)/T(\kappa = 0)$ of the side-coupled-cavity switch (Figure 5(a)) as a function of the imaginary part κ of the refractive index. Results are shown for $w = 300$ nm, $L = 210$ nm. All other parameters are as in Figure 5(b).

in other plasmonic absorption switches [23, 63]. For a modulation depth of 99%, the required variation is $\kappa = 0.15$.

5. Conclusions

In summary, in this paper we provided a review of some of our recent research activities on plasmonic devices based on MDM stub resonators for manipulating light at the nanoscale. We first briefly reviewed the methods used for the simulation and analysis of such devices. We then introduced slow-light subwavelength plasmonic waveguides based on plasmonic analogues of periodically loaded transmission lines and electromagnetically induced transparency. In both cases, the structures consist of a MDM waveguide side-coupled to periodic arrays of MDM stub resonators. We finally introduced switches consisting of a MDM plasmonic waveguide side-coupled to a MDM stub resonator filled with an active material. As final remarks, we note that plasmonic devices based on MDM stub resonators have also been proposed as compact filters, reflectors, and impedance matching elements for MDM plasmonic waveguides [10, 67–74].

References

[1] W. L. Barnes, A. Dereux, and T. W. Ebbesen, "Surface plasmon subwavelength optics," *Nature*, vol. 424, no. 6950, pp. 824–830, 2003.

[2] E. Ozbay, "Plasmonics: merging photonics and electronics at nanoscale dimensions," *Science*, vol. 311, no. 5758, pp. 189–193, 2006.

[3] J. R. Krenn, B. Lamprecht, H. Ditlbacher et al., "Non-diffraction-limited light transport by gold nanowires," *Europhysics Letters*, vol. 60, no. 5, pp. 663–669, 2002.

[4] S. A. Maier, P. G. Kik, H. A. Atwater et al., "Local detection of electromagnetic energy transport below the diffraction limit in metal nanoparticle plasmon waveguides," *Nature Materials*, vol. 2, no. 4, pp. 229–232, 2003.

[5] S. I. Bozhevolnyi, V. S. Volkov, E. Devaux, J. Y. Laluet, and T. W. Ebbesen, "Channel plasmon subwavelength waveguide components including interferometers and ring resonators," *Nature*, vol. 440, no. 7083, pp. 508–511, 2006.

[6] R. Zia, M. D. Selker, P. B. Catrysse, and M. L. Brongersma, "Geometries and materials for subwavelength surface plasmon modes," *Journal of the Optical Society of America A*, vol. 21, no. 12, pp. 2442–2446, 2004.

[7] G. Veronis and S. Fan, "Bends and splitters in metal-dielectric-metal subwavelength plasmonic waveguides," *Applied Physics Letters*, vol. 87, Article ID 131102, 3 pages, 2005.

[8] A. Hosseini and Y. Massoud, "Nanoscale surface plasmon based resonator using rectangular geometry," *Applied Physics Letters*, vol. 90, no. 18, Article ID 181102, 3 pages, 2007.

[9] Y. Matsuzaki, T. Okamoto, M. Haraguchi, M. Fukui, and M. Nakagaki, "Characteristics of gap plasmon waveguide with stub structures," *Optics Express*, vol. 16, no. 21, pp. 16314–16325, 2008.

[10] X. S. Lin and X. G. Huang, "Tooth-shaped plasmonic waveguide filters with nanometeric sizes," *Optics Letters*, vol. 33, no. 23, pp. 2874–2876, 2008.

[11] E. N. Economou, "Surface plasmons in thin films," *Physical Review*, vol. 182, no. 2, pp. 539–554, 1969.

[12] J. A. Dionne, L. A. Sweatlock, H. A. Atwater, and A. Polman, "Planar metal plasmon waveguides: frequency-dependent dispersion, propagation, localization, and loss beyond the free electron model," *Physical Review B*, vol. 72, Article ID 075405, 11 pages, 2005.

[13] J. A. Dionne, L. A. Sweatlock, H. A. Atwater, and A. Polman, "Plasmon slot waveguides: towards chip-scale propagation with subwavelength-scale localization," *Physical Review B*, vol. 73, Article ID 035407, 9 pages, 2006.

[14] S. E. Kocabas, G. Veronis, D. A. B. Miller, and S. Fan, "Modal analysis and coupling in metal-insulator-metal waveguides," *Physical Review B*, vol. 79, Article ID 035120, 17 pages, 2009.

[15] J. A. Dionne, H. J. Lezec, and H. A. Atwater, "Highly confined photon transport in subwavelength metallic slot waveguides," *Nano Letters*, vol. 6, no. 9, pp. 1928–1932, 2006.

[16] H. J. Lezec, J. A. Dionne, and H. A. Atwater, "Negative refraction at visible frequencies," *Science*, vol. 316, no. 5823, pp. 430–432, 2007.

[17] E. Verhagen, J. A. Dionne, L. Kuipers, H. A. Atwater, and A. Polman, "Near-field visualization of strongly confined surface plasmon polaritons in metal-insulator-metal waveguides," *Nano Letters*, vol. 8, no. 9, pp. 2925–2929, 2008.

[18] Z. Han, A. Y. Elezzabi, and Van, "Experimental realization of subwavelength plasmonic slot waveguides on a silicon platform," *Optics Letters*, vol. 35, no. 4, pp. 502–504, 2010.

[19] Z. Han, A. Y. Elezzabi, and V. Van, "Wideband Y-splitter and aperture-assisted coupler based on sub-diffraction confined plasmonic slot waveguides," *Applied Physics Letters*, vol. 96, no. 13, Article ID 131106, 3 pages, 2010.

[20] S. Zhu, T. Y. Liow, G. Q. Lo, and D. L. Kwong, "Fully complementary metal-oxide-semiconductor compatible nanoplasmonic slot waveguides for silicon electronic photonic integrated circuits," *Applied Physics Letters*, vol. 98, no. 2, Article ID 021107, 3 pages, 2011.

[21] J. Wen, P. Banzer, A. Kriesch, D. Ploss, B. Schmauss, and U. Peschel, "Experimental cross-polarization detection of coupling far-field light to highly confined plasmonic gap modes via nanoantennas," *Applied Physics Letters*, vol. 98, no. 10, Article ID 101109, 2011.

[22] D. Pacifici, H. J. Lezec, and H. A. Atwater, "All-optical modulation by plasmonic excitation of CdSe quantum dots," *Nature Photonics*, vol. 1, no. 7, pp. 402–406, 2007.

[23] R. A. Pala, K. T. Shimizu, N. A. Melosh, and M. L. Brongersma, "A nonvolatile plasmonic switch employing photochromic molecules," *Nano Letters*, vol. 8, no. 5, pp. 1506–1510, 2008.

[24] C. Min and G. Veronis, "Absorption switches in metal-dielectric-metal plasmonic waveguides," *Optics Express*, vol. 17, no. 13, pp. 10757–10766, 2009.

[25] L. Yang, C. Min, and G. Veronis, "Guided subwavelength slow-light mode supported by a plasmonic waveguide system," *Optics Letters*, vol. 35, no. 24, pp. 4184–4186, 2010.

[26] Y. Huang, C. Min, and G. Veronis, "Subwavelength slow-light waveguides based on a plasmonic analogue of electromagnetically induced transparency," *Applied Physics Letters*, vol. 99, no. 14, Article ID 143117, 2011.

[27] S.-D. Wu and E. N. Glytsis, "Finite-number-of-periods holographic gratings with finite-width incident beams: analysis using the finite-difference frequency-domain method," *Journal of the Optical Society of America A*, vol. 19, no. 10, pp. 2018–2029, 2002.

[28] G. Veronis, R. W. Dutton, and S. Fan, "Method for sensitivity analysis of photonic crystal devices," *Optics Letters*, vol. 29, no. 19, pp. 2288–2290, 2004.

[29] E. D. Palik, *Handbook of Optical Constants of Solids*, Academic, Orlando, Fla, USA, 1985.

[30] J. Jin, *The Finite Element Method in Electromagnetics*, Wiley, New York, NY, USA, 2002.

[31] A. Taflove and S. C. Hagness, *Computational Electrodynamics*, Artech House, Boston, Mass, USA, 3rd edition, 2005.

[32] M. N. O. Sadiku, *Numerical Techniques in Electromagnetics*, CRC Press, Boca Raton, Fla, USA, 2001.

[33] D. M. Pozar, *Microwave Engineering*, Wiley, New York, NY, USA, 1998.

[34] S. Ramo, J. R. Whinnery, and T. Van, *Duzer, Fields and Waves in Communication Electronics*, Wiley, New York, NY, USA, 1994.

[35] S. E. Kocabas, G. Veronis, D. A. B. Miller, and S. Fan, "Transmission line and equivalent circuit models for plasmonic waveguide components," *IEEE Journal on Selected Topics in Quantum Electronics*, vol. 14, no. 6, Article ID 4559744, pp. 1462–1472, 2008.

[36] R. D. Kekatpure, E. S. Barnard, W. Cai, and M. L. Brongersma, "Phase-coupled plasmon-induced transparency," *Applied Physics Letters*, vol. 104, Article ID 243902, 4 pages, 2010.

[37] Z. Han and S. I. Bozhevolnyi, "Plasmon-induced transparency with detuned ultracompact Fabry-Perot resonators in integrated plasmonic devices," *Optics Express*, vol. 19, no. 4, pp. 3251–3257, 2011.

[38] D. Pacifici, H. J. Lezec, H. A. Atwater, and J. Weiner, "Quantitative determination of optical transmission through subwavelength slit arrays in Ag films: role of surface wave interference and local coupling between adjacent slits," *Physical Review B*, vol. 77, Article ID 115411, 2008.

[39] D. Pacifici, H. J. Lezec, L. A. Sweatlock, R. J. Walters, and H. A. Atwater, "Universal optical transmission features in periodic and quasiperiodic hole arrays," *Optics Express*, vol. 16, no. 12, pp. 9222–9238, 2008.

[40] A. Karalis, E. Lidorikis, M. Ibanescu, J. Joannopoulos, and M. Soljacic, "Surface-plasmon-assisted guiding of broadband slow and subwavelength light in air," *Physical Review Letters*, vol. 95, Article ID 063901, 2005.

[41] M. Sandtke and L. Kuipers, "Slow guided surface plasmons at telecom frequencies," *Nature Photonics*, vol. 1, no. 10, pp. 573–576, 2007.

[42] Z. Kang, W. Lin, and G. P. Wang, "Dual-channel broadband slow surface plasmon polaritons in metal gap waveguide superlattices," *Journal of the Optical Society of America B*, vol. 26, no. 10, pp. 1944–1948, 2009.

[43] Q. Gan, Y. J. Ding, and F. J. Bartoli, "'Rainbow' trapping and releasing at telecommunication wavelengths," *Physical Review Letters*, vol. 102, Article ID 056801, 4 pages, 2009.

[44] A. Kocabas, S. S. Senlik, and A. Aydinli, "Slowing down surface plasmons on a Moiré surface," *Physical Review Letters*, vol. 102, Article ID 063901, 4 pages, 2009.

[45] E. Feigenbaum and M. Orenstein, "Backward propagating slow light in inverted plasmonic taper," *Optics Express*, vol. 17, no. 4, pp. 2465–2469, 2009.

[46] S. A. Maier, *Plasmonics: Fundamentals and Applications*, Springer, New York, NY, USA, 2007.

[47] P. Tassin, L. Zhang, T. Koschny, E. N. Economou, and C. M. Soukoulis, "Low-loss metamaterials based on classical electromagnetically induced transparency," *Physical Review Letters*, vol. 102, no. 5, Article ID 053901, 2009.

[48] S. Fan, M. F. Yanik, Z. Wang, S. Sandhu, and M. L. Povinelli, "Advances in theory of photonic crystals," *Journal of Lightwave Technology*, vol. 24, no. 12, pp. 4493–4501, 2006.

[49] S. Zhang, D. A. Genov, Y. Wang, M. Liu, and X. Zhang, "Plasmon-induced transparency in metamaterials," *Physical Review Letters*, vol. 101, no. 4, Article ID 047401, 2008.

[50] N. Papasimakis, V. A. Fedotov, and N. I. Zheludev, "Metamaterial analog of electromagnetically induced transparency," *Physical Review Letters*, vol. 101, Article ID 253903, 4 pages, 2008.

[51] N. Liu, L. Langguth, T. Weiss et al., "Plasmonic analogue of electromagnetically induced transparency at the Drude damping limit," *Nature Materials*, vol. 8, no. 9, pp. 758–762, 2009.

[52] M. F. Yanik, W. Suh, Z. Wang, and S. Fan, "Stopping light in a waveguide with an all-optical analog of electromagnetically induced transparency," *Physical Review Letters*, vol. 93, Article ID 233903, 1 pages, 2004.

[53] Q. Xu, S. Sandhu, M. Povinelli, J. Shakya, S. Fan, and M. Lipson, "Experimental realization of an on-chip all-optical analogue to electromagnetically induced transparency," *Physical Review Letters*, vol. 96, no. 12, Article ID 123901, 4 pages, 2006.

[54] A. V. Krasavin and N. I. Zheludev, "Active plasmonics: controlling signals in Au/Ga waveguide using nanoscale structural transformations," *Applied Physics Letters*, vol. 84, no. 8, pp. 1416–1418, 2004.

[55] T. Nikolajsen, K. Leosson, and S. I. Bozhevolnyi, "Surface plasmon polariton based modulators and switches operating at telecom wavelengths," *Applied Physics Letters*, vol. 85, no. 24, pp. 5833–5835, 2004.

[56] A. L. Lereu, A. Passian, J. P. Goudonnet, T. Thundat, and T. L. Ferrell, "Optical modulation processes in thin films based on thermal effects of surface plasmons," *Applied Physics Letters*, vol. 86, no. 15, Article ID 154101, pp. 1–3, 2005.

[57] K. F. MacDonald, Z. L. Sámson, M. I. Stockman, and N. I. Zheludev, "Ultrafast active plasmonics," *Nature Photonics*, vol. 3, no. 1, pp. 55–58, 2009.

[58] G. A. Wurtz and A. V. Zayats, "Nonlinear surface plasmon polaritonic crystals," *Laser and Photonics Reviews*, vol. 2, no. 3, pp. 125–135, 2008.

[59] C. Min, P. Wang, C. Chen et al., "All-optical switching in subwavelength metallic grating structure containing nonlinear optical materials," *Optics Letters*, vol. 33, no. 8, pp. 869–871, 2008.

[60] M. J. Dicken, L. A. Sweatlock, D. Pacifici, H. J. Lezec, K. Bhattacharya, and H. A. Atwater, "Electrooptic modulation in thin film barium titanate plasmonic interferometers," *Nano Letters*, vol. 8, no. 11, pp. 4048–4052, 2008.

[61] W. Dickson, G. A. Wurtz, P. R. Evans, R. J. Pollard, and A. V. Zayats, "Electronically controlled surface plasmon dispersion and optical transmission through metallic hole arrays using liquid crystal," *Nano Letters*, vol. 8, no. 1, pp. 281–286, 2008.

[62] Z. Yu, G. Veronis, S. Fan, and M. L. Brongersma, "Gain-induced switching in metal-dielectric-metal plasmonic waveguides," *Applied Physics Letters*, vol. 92, no. 4, Article ID 041117, 3 pages, 2008.

[63] D. Pacifici, H. J. Lezec, L. A. Sweatlock, C. D. Ruiter, V. Ferry, and H. A. Atwater, *Plasmonic Nanoguides and Circuits*, World Scientific, River Edge, NJ, USA, 2009.

[64] H. A. Haus and Y. Lai, "Narrow-band distributed feedback reflector design," *Journal of Lightwave Technology*, vol. 9, no. 6, pp. 754–760, 1991.

[65] H. A. Haus and Y. Lai, "Theory of cascaded quarter wave shifted distributed feedback resonators," *IEEE Journal of Quantum Electronics*, vol. 28, no. 1, pp. 205–213, 1992.

[66] J. Liu, M. Beals, A. Pomerene et al., "Waveguide-integrated, ultralow-energy GeSi electro-absorption modulators," *Nature Photonics*, vol. 2, no. 7, pp. 433–437, 2008.

[67] A. Pannipitiya, I. D. Rukhlenko, M. Premaratne, H. T. Hattori, and G. P. Agrawal, "Improved transmission model for metal-dielectric-metal plasmonic waveguides with stub structure," *Optics Express*, vol. 18, no. 6, pp. 6191–6204, 2010.

[68] Z. Zhong, Y. Xu, S. Lan, Q. Dai, and L. Wu, "Sharp and asymmetric transmission response in metal-dielectric-metal plasmonic waveguides containing Kerr nonlinear media," *Optics Express*, vol. 18, no. 1, pp. 79–68, 2010.

[69] J. Liu, G. Fang, H. Zhao, Y. Zhang, and S. Liu, "Surface plasmon reflector based on serial stub structure," *Optics Express*, vol. 17, no. 22, pp. 20134–20139, 2009.

[70] F. Hu, H. Yi, and Z. Zhou, "Wavelength demultiplexing structure based on arrayed plasmonic slot cavities," *Optics Letters*, vol. 36, no. 8, pp. 1500–1502, 2011.

[71] Y. Xu, A. E. Miroshnichenko, S. Lan, Q. Guo, and L. J. Wu, "Impedance matching induce high transmission and flat responseb band-pass plasmonic waveguides," *Plasmonics*, vol. 6, no. 2, pp. 337–343, 2011.

[72] Q. Zhang, X. Huang, X. Lin, J. Tao, and X. Jin, "A subwavelength coupler-type MIM optical filter," *Optics Express*, vol. 17, no. 9, pp. 7549–7555, 2009.

[73] J. Tao, Q. J. Wang, and X. G. Huang, "All-optical plasmonic switches based on coupled nano-disk cavity structures containing nonlinear material," *Plasmonics*, vol. 6, no. 4, pp. 753–759, 2011.

[74] S. R. Mirnaziry, A. Setayesh, and M. S. Abrishamian, "Design and analysis of plasmonic filters based on stubs," *Journal of the Optical Society of America B*, vol. 28, no. 5, pp. 1300–1307, 2011.

Hindawi Publishing Corporation
International Journal of Optics
Volume 2012, Article ID 651563, 8 pages
doi:10.1155/2012/651563

Research Article

Passive Infrared Sensing Using Plasmonic Resonant Dust Particles

Mark Mirotznik,[1] William Beck,[2] Kimberly Olver,[2] John Little,[2] and Peter Pa[1]

[1] *Department of Electrical and Computer Engineering, University of Delaware, 106 Evans Hall, Newark, DE 19716, USA*
[2] *Sensors and Electron Devices Directorate, U.S. Army Research Laboratory, Adelphi, MD 20783, USA*

Correspondence should be addressed to Mark Mirotznik, mirotzni@ece.udel.edu

Received 5 May 2012; Accepted 24 June 2012

Academic Editor: Georgios Veronis

Copyright © 2012 Mark Mirotznik et al. This is an open access article distributed under the Creative Commons Attribution License, which permits unrestricted use, distribution, and reproduction in any medium, provided the original work is properly cited.

We present computational and experimental results of dust particles that can be tuned to preferentially reflect or emit IR radiation within the 8–14 μm band. The particles consist of thin metallic subwavelength gratings patterned on the surface of a simple quarter wavelength cavity. This design creates distinct IR absorption resonances by combining the plasmonic resonance of the grating with the natural resonance of the cavity. We show that the resonance peaks are easily tuned by varying either the geometry of the grating or the thickness of the cavity. Here, we present a computational design algorithm along with experimental results that validate the design methodology.

1. Introduction

Most objects, either manmade or found in nature, reflect and emit infrared (IR) radiation in a relatively smooth spectrum; however, by applying structures with resonant absorption to the surface of those materials, the reflection and emission spectra can be enhanced or reduced at particular wavelengths (as illustrated in Figure 1). Moreover, by mixing small resonant particles (<100 μm) designed for several different wavelengths, we can create IR dust that reflects or emits with a characteristic spectral signature. Such material-by-design particles would be useful for a variety of practical applications. For example, when applied to a base surface, the resonant particles could be used to tune an IR reflectance to mimic other natural or manmade surfaces. This could be useful as a calibration standard for hyperspectral imaging systems. Additionally, if the particles are chemically functionalized, there are a number of remote atmospheric sensing applications that could be explored.

2. Infrared Absorbers Using Plasmonic Gratings

It is well known that metallic surfaces patterned on a subwavelength scale exhibit unusual electromagnetic properties at optical wavelengths. In particular, the presence of localized surface plasmon resonances creates well-defined absorption bands. This phenomenon has been studied and exploited by a number of investigators to realize new types of sensors, optical filters, and absorbers [1–5]. The goal of this work was to numerically and experimentally study plasmonic-based resonant absorbers in the long-wavelength IR (LWIR) band (8–14 μm) that could be fashioned into small ($\sim$100 μm $\times$ 100 μm $\times$ 25 μm) dust particles. The dust particles could then be used to tailor the reflectivity/emissivity of a surface or dispersed in air and used for atmospheric sensing applications.

There are a number of small resonant absorbing "dust like" structures that could be used to preferentially absorb, and thus thermally emit, IR radiation at specific wavelengths including dielectric ring resonators, resonant patch antennas, and plasmonic-based resonator. These various structures were compared based on (1) their ability to efficiently absorb IR energy at selected wavelengths within the 8–14 μm band, (2) the ability to easily tune the resonant absorption, (3) ease of fabrication, and (4) manufacturing cost. Based on these criteria, we chose to investigate, in detail, the relatively simple surface plasmon-based designs shown in Figure 2. The building blocks for this design are two thin resonant

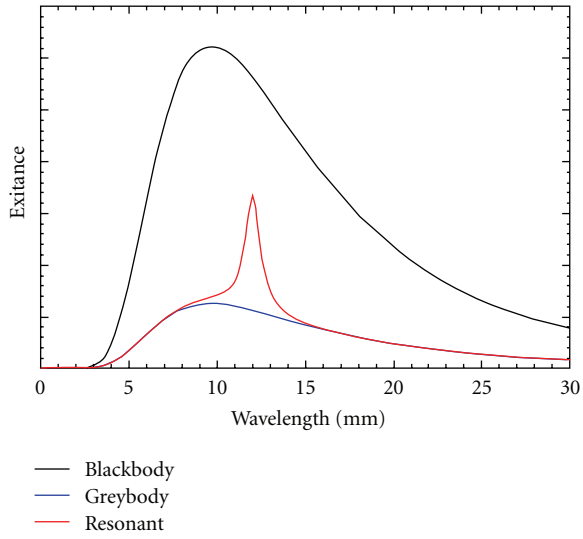

Figure 1: Notional diagram that illustrates the normally smooth thermal exitance curves from blackbody and graybody objects compared to the resonant behavior of our "engineered" IR resonant dust.

cavities, one on the top of Figure 2 and the other on the bottom. Each cavity is composed of a thin gold ground plane, a thin dielectric substrate layer (formed from zinc selenide (ZnSe) in our design), and a subwavelength metallic grating made from gold. In the middle of the structure is a relatively thick silicon layer needed for mechanical rigidity. The symmetry of the top and bottom layers was needed since the particles, when dispersed, would orient themselves randomly.

The strong resonant behavior of this design is due to a combination of two different resonant phenomena. The first is a surface plasmon resonance that is excited within the subwavelength gold grating. The second is a cavity resonance excited in the ZnSe substrate region that is between the grating layer and the metallic ground plane layer. By adjusting the thickness of the ZnSe substrate for a given grating period and duty cycle, a strong absorption resonance can be excited at any wavelength within the 8–14 micron band. To create small dust particles, a large sample is diced into small ($\sim 100\,\mu\text{m} \times 100\,\mu\text{m} \times 25\,\mu\text{m}$) particles.

3. Computational Modeling and Design

Two different computational models were employed to rigorously design and validate the resonant structure shown in Figure 2. The first method is a fully periodic planar method called the rigorous coupled wave method. The second method, finite element method (FEM), was used to investigate finite-sized particle effects. A brief description of these two methods along with simulation results are presented in the next two sections.

3.1. Modeling of Infinitely Periodic Structures Using Rigorous Coupled Wave Analysis. Two approaches are used extensively for simulating the electromagnetic properties of infinitely periodic subwavelength gratings. The first uses effective media theory to provide closed-form approximations for the effective dielectric constants as a function of the grating structure [6]. Although attractive from a computational perspective, the approximate expressions are accurate only for gratings whose period is much smaller than the wavelength of illumination. As the grating period approaches the wavelength, which is referred to as the resonance regime, the assumptions on which these closed-form expressions are based are no longer valid. For our designs, we assumed grating periods only slightly smaller than the material wavelength and thus could not accurately utilize effective media theory.

We instead employed a second approach using a rigorous electromagnetic model. Although computationally more difficult, this approach is capable of generating accurate results for gratings of any period size and shape. Several rigorous electromagnetic models can be used for this calculation. We chose the rigorous coupled wave (RCW) algorithm originally presented by Moharam and Gaylord [7]. Our specific implementation is based on the enhanced transmittance matrix approach introduced by Moharam and Gaylord [7] and later refined by Lalanne [8] and Noponen and Turunen [9]. For the sake of brevity, we refer the reader to the references above for details on the RCW method. While being accurate, the RCW method does assume the grating structure, shown in Figure 2, is infinite in the transverse directions. The effect of finite-sized samples is investigated in Section 3.3.

3.1.1. RCW Simulation Results for Infinitely Periodic Surfaces. Figure 3 presents typical simulation, results calculated using the RCW method. In the figure, the reflectivity of the sample is calculated as a function of wavelength and polarization for a normally Incident Planewave.

For this simulation the ZnSe substrate thickness was assumed to be $1.8\,\mu$m, the gold grating period was $3.0\,\mu$m with a 50% duty cycle. The gold gratings were assumed to be 100 nm thick, and the gold ground planes were 300 nm thick. The electromagnetic material properties of the gold were determined using the model given in [10]. For the ZnSe layer, a lossless index of refraction of $n = 2.41$ was used in all simulations. The incident field was assumed to be normally incident from the top. For this design, a very strong resonance absorption, near-perfect absorption, is predicted near $9.5\,\mu$m for the case of parallel polarization (E-field polarized along the axis of the grating) and only weak resonances occur for the case of perpendicular polarization (E-field polarized perpendicular to the axis of the grating).

3.1.2. Reflectance Sensitivity to Geometrical Parameters. Given a specific substrate and metallization material, such as ZnSe and gold, the dust particle's reflectance can be tuned by proper selection of the geometrical parameters shown in Figure 2: specifically, (1) thickness of the ZnSe layer, denoted by h in Figure 2; (2) grating period, denoted by Λ in Figure 2; (3) the grating's duty cycle given by (w/Λ in

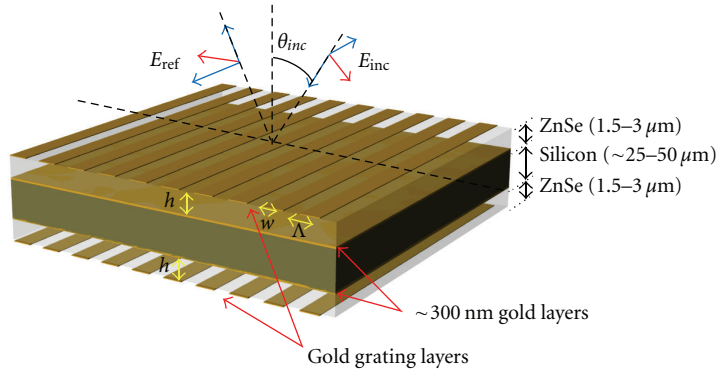

Figure 2: Illustration of our surface plasmon-based IR resonant particles. The gold subwavelength gratings along with cavity resonances produce distinct resonant absorption phenomenon within the LWIR band.

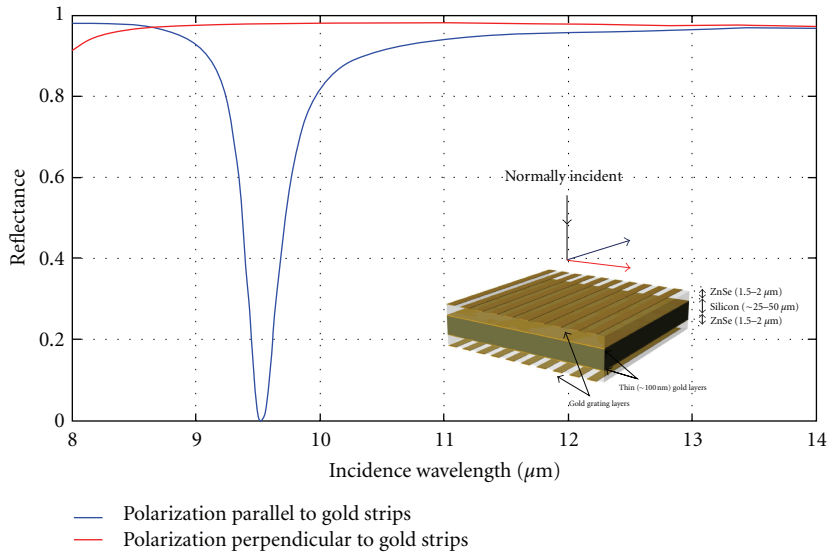

Figure 3: Simulation results, using the RCW method, that present the reflectivity at normal incidence within the LWIR band. The reflectivity as expected is polarization dependent due to the anisotropic nature of the gratings.

Figure 2); (4) thickness of the gold grating layer and gold ground plane. Assuming the gold layers are thick enough to prevent transmission (i.e., much thicker than the penetration depth), the variables given by 1–3 above will have the most effect on the LWIR reflectance.

In Figure 4, we present the effect of the ZnSe substrate thickness on the resonant behavior. As the thickness is increased from 1.5 to 2.5 μm, the resonant dip shifts from 8.3 to 13.2 μm, respectively. Thus the resonant behavior can be tuned by simply varying the thickness of the ZnSe substrate.

Alternatively, for a given substrate thickness, the resonant absorption characteristics can be tuned by varying the grating period and duty cycle. Shown in Figure 5 is the simulated reflectance of a sample in which the substrate thickness was fixed at 2.0 μm and the grating period was varied from 1.0 to 3.0 μm. For this simulation, the duty cycle was fixed at 50%. While the resonant wavelength clearly varied with grating period, the change was less sensitive than varying substrate thickness. Moreover, by just changing the grating period, with all other parameters fixed, the amplitude of the resonance would vary considerably. Lastly, we varied the grating's duty cycle while holding the substrate thickness and grating period fixed at 2.0 and 3.0 μm, respectively. As shown in Figure 6, the grating duty cycle has a large effect on not only the resonant wavelength but also on the amplitude and bandwidth of the resonance.

The sensitivity to incident angle was also evaluated using the RCW code. A typical result for the case of both parallel and perpendicular polarization is shown in Figure 7. Here, the simulation results predict that the resonant frequency for parallel polarization (Figure 7(a)) should slowly increase as the incident angle increases from normal incidence (0 degrees in the figure) to near grazing angles (80 degrees). It is interesting to note that for the case of parallel polarization (Figure 7(a)) the variation in resonant wavelength with incident angle is relatively small (<1 μm) even with near-grazing incident angles. For the given application of resonant dust particles, this is an attractive feature since the orientation of

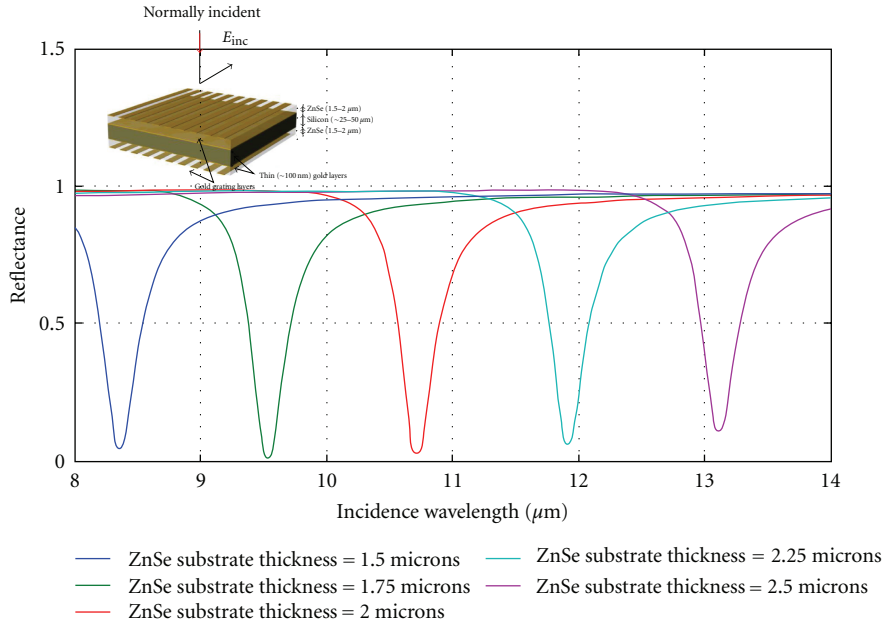

Figure 4: Simulation results, using the RCW method, that present the reflectance at normal incidence within the LWIR band as the ZnSe substrate thickness is varied from 1.5 to 2.5 μm. For this simulation, the grating period is fixed at 3.0 μm with a 50% duty cycle. The incident wave was normally incident with parallel polarization. As the substrate thickness is increased, the resonant absorption peak shifts to longer wavelengths but still remains strong. The bandwidth of the resonance also remains relatively fixed as the substrate thicknesses is varied.

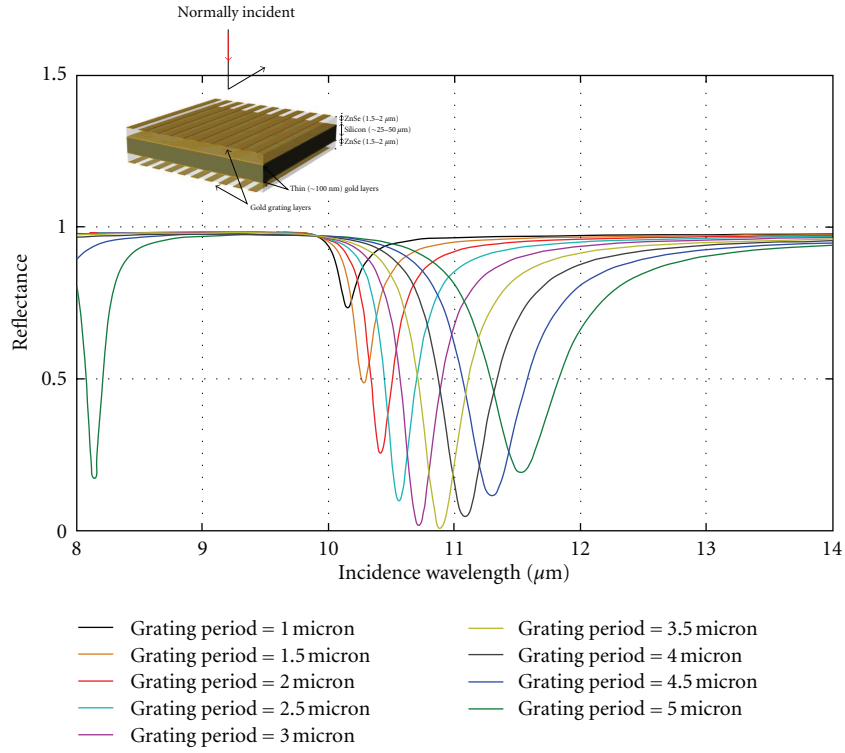

Figure 5: Simulation results, using the RCW method, that present the reflectance at normal incidence within the LWIR band as the gold grating period is varied from 1.0 to 5.0 μm. For this simulation, the substrate thickness is fixed at 2.0 μm with a grating duty cycle of 50%. The incident wave was normally incident with parallel polarization.

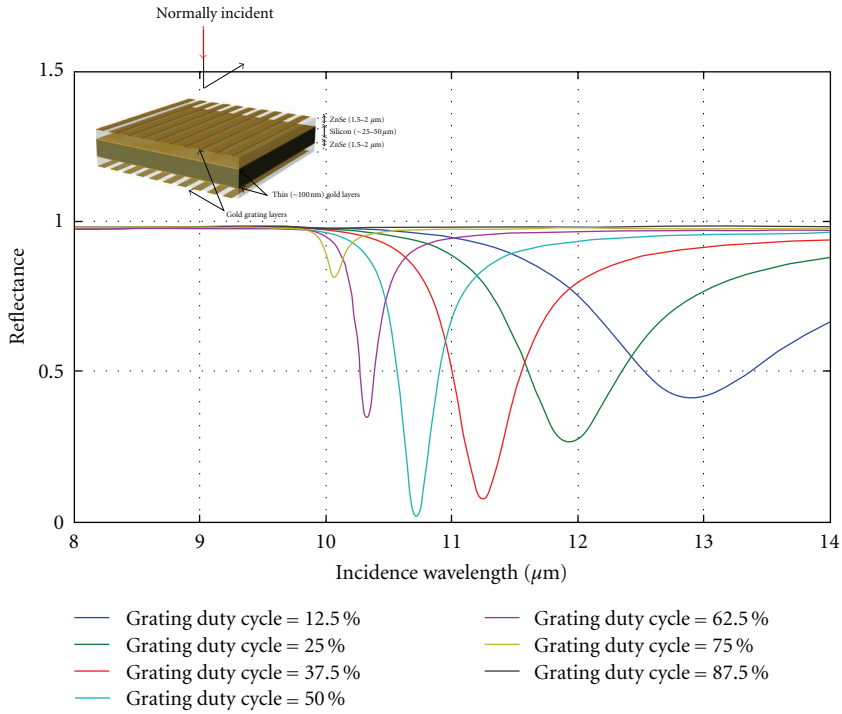

Figure 6: Simulation results using the RCW method that present the reflectance at normal incidence within the LWIR band as the duty cycle of the gold grating period is varied from 12.5% to 87.5%. For this simulation, the substrate thickness is fixed at 2.0 μm with a grating period of 3.0 μm. The incident wave was normally incident with parallel polarization.

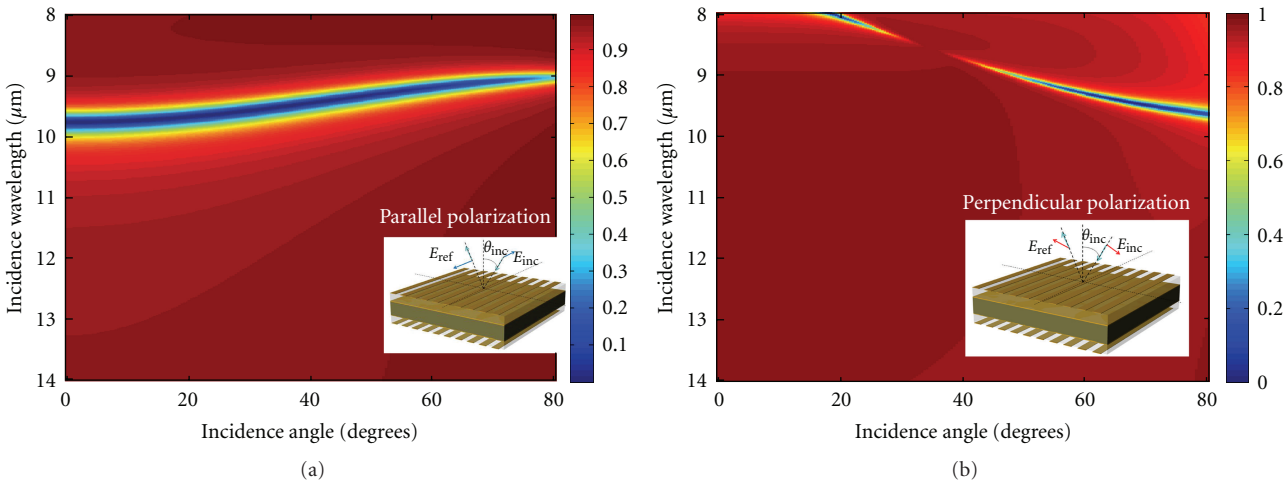

Figure 7: RCW predictions illustrating the sensitivity of our resonant structure with incident angle. The plot on the left (a) is for parallel polarization, while the plot on the right (b) is for perpendicular polarization.

the particles with respect to the incident field cannot be well controlled.

3.2. Iterative Design. As Figures 4 through 7 demonstrate, the resonant absorption properties of the structure shown in Figure 2 have a complicated dependence on a number of geometrical parameters. As a result, it is unlikely that any simple analytical design equation could be derived and used to determine an optimal structure for a given desired response. Consequently, we implemented a numerical iterative design algorithm. Here the RCW method is used to calculate the full wave solution for the reflectance as a function of wavelength, polarization, and angle of incidence for a geometry of a given substrate thickness, grating period, and duty cycle. An optimization algorithm is then used to refine the geometry until an objective function is minimized. The objective function may vary depending on the application, but in most cases we chose to minimize the total reflectance over some desired

wavelength band. A number of iterative optimization algorithms could be employed including traditional derivative-based algorithms, genetic algorithms, or direct pattern search algorithms. An advantage of both genetic and pattern search algorithms is that they do not require derivatives, and as a consequence work well on nondifferentiable, stochastic, and discontinuous objective functions. Both simple genetic algorithms and direct pattern search algorithms were implemented and tested for the application of interest here. While both methods produced comparable results, the pattern search algorithm was often computationally less expensive.

3.3. Modeling of Finite Grating Effects Using the Finite Element Method. The RCW method, while accurate and computationally efficient, assumes the gratings to be infinitely periodic. For our application, the samples are actually diced into small ($\sim 100\,\mu\text{m} \times 100\,\mu\text{m} \times 25\,\mu\text{m}$) particles. Consequently, it is important to understand the effects of relatively small (<10 wavelengths) finite-sized particles on the overall effectiveness of the design. To conduct these simulations we used the commercial EM solver, HFSS from Ansys. Simulations were conducted using HFSS's FEM solver with grating structures that varied from 25 to 100 μm on a side.

Figure 8 plots the simulated current density on the surface of a $50\,\mu\text{m} \times 50\,\mu\text{m} \times 5\,\mu\text{m}$ plasmonic particle at a fixed incident wavelength of 10 μm. The spatial distribution of current is a direct consequence of its finite lateral size and will affect the total absorbed energy. In Figure 9, we plot the average reflectance of the same particle as a function of wavelength. While the total absorption is slightly less and the resonance wavelength is slightly shifted towards longer wavelength, the finite-sized particles still behave with the same general absorption characteristics as the infinitely periodic predictions described previously.

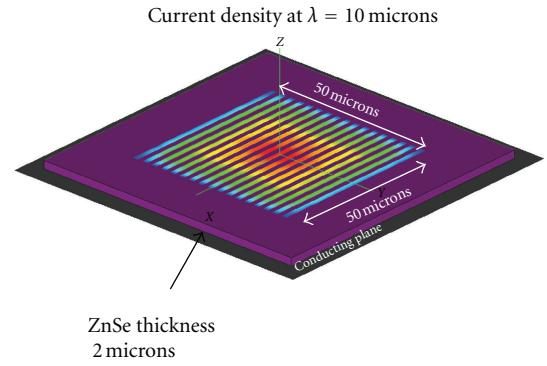

Figure 8: Current density distribution for a finite-sized resonant particle. Simulations were conducted using HFSS FEM solver.

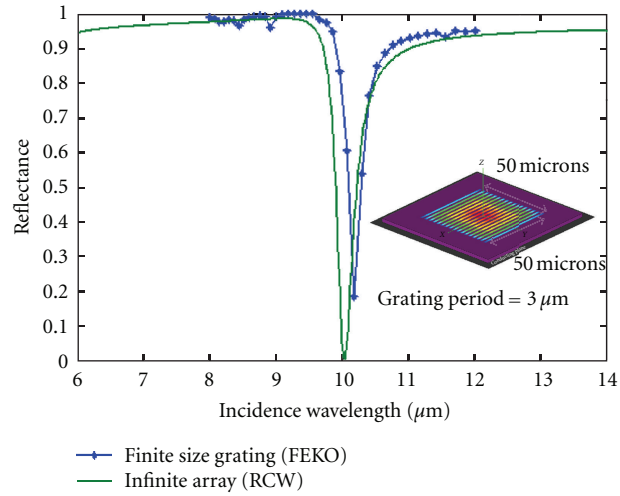

Figure 9: Predicted reflectance curves for a finite-sized particle compared to the infinitely periodic calculations. The edge effects of the finite-sized sample are evident but do not significantly alter the resonant peak.

4. Experimental Fabrication

To fabricate the samples, a thin (80 microns) 2-inch silicon wafer was first mounted onto a 3-inch (350–500 micron) silicon carrier wafer using Aquabond 55 Adhesive Products wax. The carrier wafer was placed on a hot plate at a temperature of 80°C. A small amount of wax was smeared on the surface starting at the center and working outward. The thin silicon wafer was carefully placed on top of the wax. A flat glass plate was placed on top of the thin wafer, followed by a brass weight. This was to keep the silicon wafer as flat as possible during the mounting procedure. The hot plate was turned off, and the wax was allowed to cool to room temperature. Excess wax on and around the mounted silicon wafer was removed by gently swabbing it away with a 1% solution of Aqua Clean. The wafer assembly was placed in a vacuum electron beam evaporator. A blanket metallization of 300 Å of chromium followed by 2000 Å of gold was evaporated on to the wafer. The assembled structure was then moved to another vacuum e-beam evaporator, and a 1.8-micron-thick layer of ZnSe was evaporated onto the surface. Depositions were performed at 145°C, with a base pressure of 1×10^{-6}. A 120-Å layer of yttrium oxide (Y_2O_3) was deposited first to promote adhesion between the substrate and the ZnSe.

Photolithography on the ZnSe was achieved by first spin coating the wafer assembly with AZ # 5214 image reversal photoresist at a speed of 4000 rpm for 40 seconds. This photoresist was hot plate baked at 110°C for 2 minutes, exposed on a JBA vacuum contact aligner for 20 seconds with a bulb intensity of 4 mW/cm^2, hotplate baked (reversal bake) at 124°C for 40 seconds, and flood exposed for 25 seconds. The resist was then developed in AZ 300 MIF photoresist developer for 60 seconds and rinsed in deionized (DI) water for 1 minute. The wafer was then dried with nitrogen gas. The resulting photolithography was inspected under a microscope for clearing. Prior to loading the wafer assembly into the e-beam evaporator for the grating structure, a photoresist cleaning in a barrel plasma asher was performed. The patterned wafer assembly was placed into the vacuum e-beam evaporator and a metallization of 300 Å titanium (Ti) followed by 1000 Å of gold was completed. A metal liftoff

using acetone, isopropyl, and DI water removed the excess metal. This fabrication process is graphically illustrated in Figure 10.

5. Experimental Characterization

Experimental characterization results for samples that were fabricated using the method described earlier are shown in Figures 11 and 12. For these samples, the ZnSe substrate thickness was fixed at 1.8 μm and the linear gold gratings were spaced 3.0 μm with a 50% duty cycle.

The IR reflectance and emission measurements were made using a Nicolet 560 Fourier transform infrared (FTIR) spectrometer with a near-normal incidence reflectivity module and an input port for collecting IR emission or photoluminescence. The reflectivity was taken at room temperature as a function of incident polarization. Although the polarized emission could be easily detected at room temperature, the signal-to-noise ratio was improved by taking the data at an elevated temperature. The experimental results, which closely match the modeled results, demonstrate a strong resonant absorption and thermal emission near the designed wavelength.

6. Alternative Polarization Insensitive Designs

One disadvantage of using the resonant particles described in Figure 2 is their sensitivity to polarization. This reduces the total absorbed energy by one half. To address this issue, we explored a number of designs that were less sensitive to incident field polarization. These structures, shown in Figure 13, consist of 2D arrays of gold strips (known commonly as a fishnet structure), metallic patches, and circular holes. Each of the structures shown in Figure 11 was analyzed using the RCW method. Of those structures analyzed, the inductive grid array (Figure 13(c)) showed the most promise. Figure 12 presents numerical simulations of normal incident reflectance as a function of wavelength. A strong, nearly perfect, absorption is predicted for both parallel and perpendicular polarization. Moreover, as in the previous designs, the resonant wavelength was easily tuned by simply varying the thickness of the dielectric substrate layer. It should be noted that the results shown in Figure 14 have not been experimentally validated yet.

7. Conclusions

In this paper, we presented a design methodology to create small particles characterized by a strong resonant absorption within the LWIR (8–14 μm) band. Our method combined a surface plasmon resonance, created using a subwavelength metallic grating with a dielectric cavity resonance. We showed that by varying the thickness of the cavity substrate the resonances could be tuned anywhere within the LWIR band. Experimental samples were fabricated using photolithography and experimentally characterized. The experimental results compared favorably with the calculated results. We believe that material-by-design particles, such

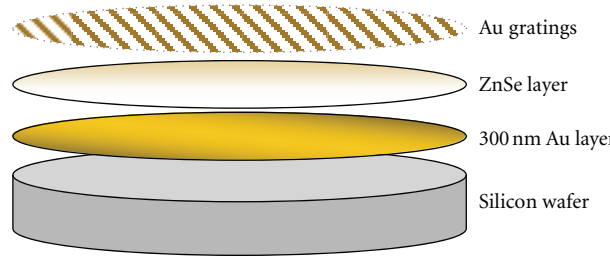

Figure 10: Illustration of the fabrication steps.

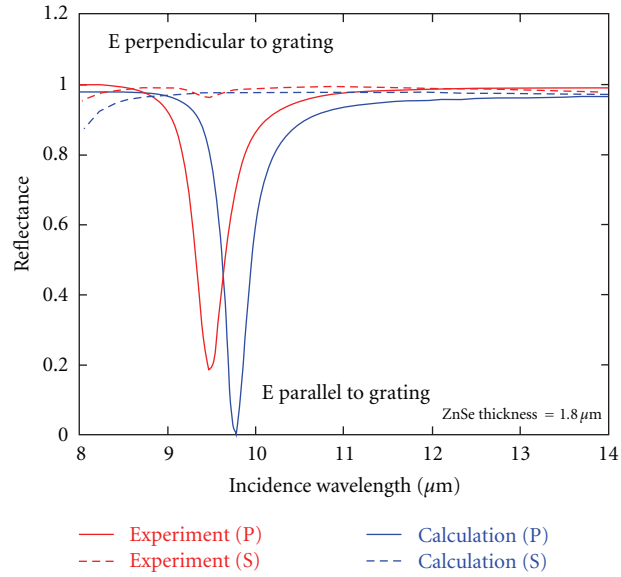

Figure 11: A comparison of predicted (using RCW code) and measured reflectance for both parallel (P type) and perpendicular (S type) polarizations.

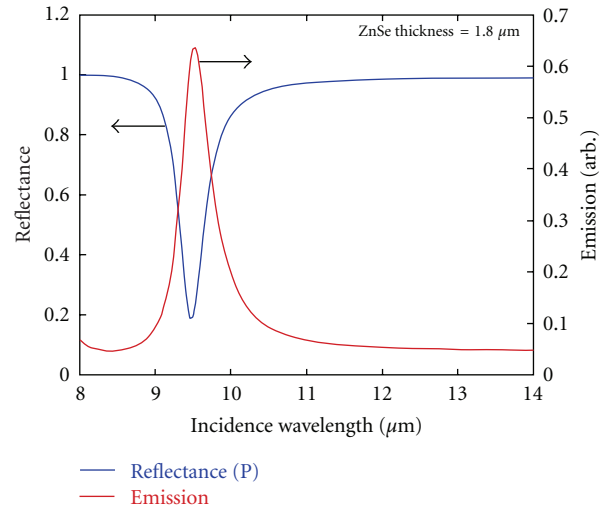

Figure 12: Experimentally measured reflectance curve and emission curve clearly demonstrating the resonant nature of our design.

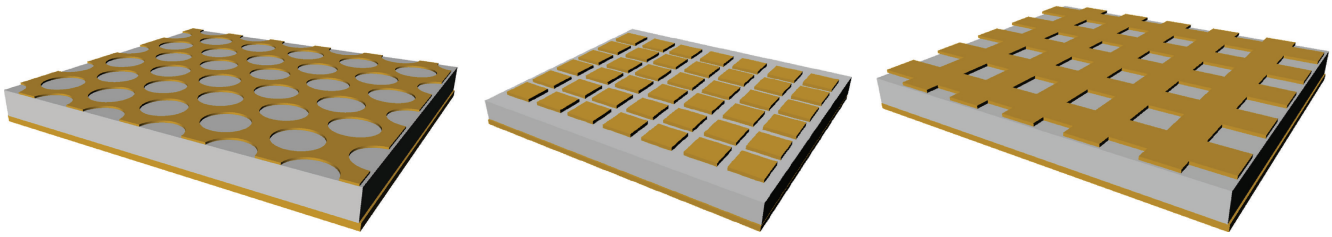

(a) Hole array (b) Capacitive patch array (c) Inductive grid array (fishnet)

Figure 13: Designs less sensitive to polarization effects.

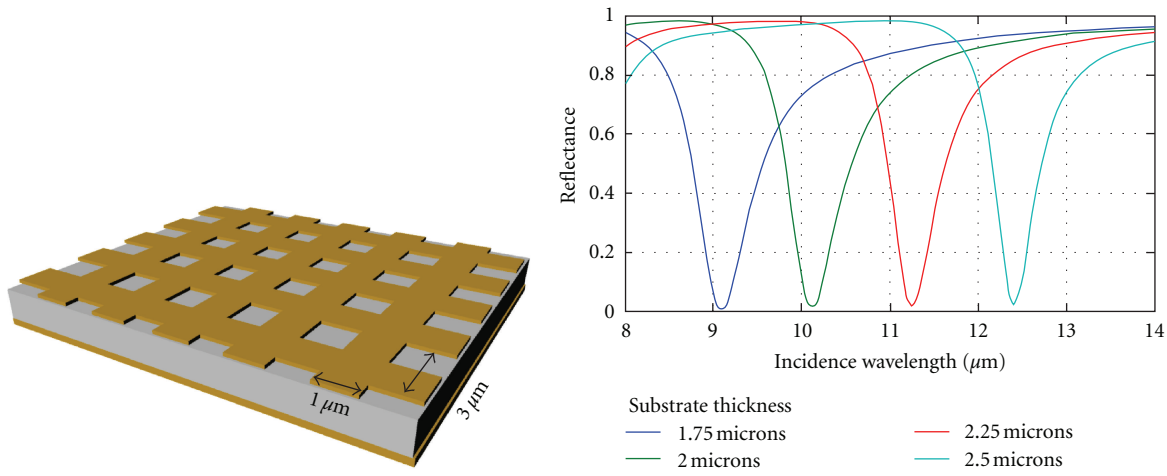

(a) (b)

Figure 14: RCW simulations for inductive grid array shown in Figure 11(c). Here as the substrate, assumed to be ZnSe, is varied from 1.75 to 2.5 μm. The resonant absorption wavelength shifts to longer wavelengths; however, the magnitude of the absorption remains near perfect.

as the ones described here, would be useful for a variety of remote atmospheric sensing applications. In those applications, which require relatively small particles, a custom spectral signature with multiple wavelengths would be achieved by mixing batches of single-wavelength particles designed for the component wavelengths. But in other applications, such as calibrated surfaces for hyperspectral imager testing and training, the surfaces could be larger and the multiple wavelengths could be designed into a single surface by implementing a checkerboard subcells with different grating periods across the surface. By properly selecting the frequencies and relative areas of the emitting subcells, the emission spectrum could be designed to mimic the spectral emission from specific natural surfaces.

References

[1] K. Masuno, S. Kumagai, and M. Sasaki, "Reflection-type wavelength-selective infrared emitter using surface plasmon polaritons," *Optics Letters*, vol. 36, no. 3, pp. 376–378, 2011.

[2] J. Hendrickson, J. Guo, B. Zhang, W. Buchwald, and R. Soref, "Wideband perfect light absorber at midwave infrared using muliplexed metal structures," *Optics Letters*, vol. 37, no. 3, pp. 371–373, 2012.

[3] K. Boratay Alici, A. Burak Turhan, C. M. Soukoulis, and E. Ozbay, "Optically thin composite resonant absorber at the near-infrared band: a polarization independent and spectrally broadband configuration," *Optics Express*, vol. 19, no. 15, pp. 14260–14267, 2011.

[4] N. Liu, M. Mesch, T. Weiss, M. Hentschel, and H. Giessen, "Infrared perfect absorber and its application as plasmonic sensor," *Nano Letters*, vol. 10, no. 7, pp. 2342–2348, 2010.

[5] C. H. Lin, R. L. Chern, and H. Y. Lin, "Polarization-independent broad-band nearly perfect absorbers in the visible regime," *Optics Express*, vol. 19, no. 2, pp. 415–424, 2011.

[6] P. Lalanne and J. P. Hugonin, "High-order effective-medium theory of subwavelength gratings in classical mounting: application to volume holograms," *Journal of the Optical Society of America A*, vol. 15, no. 7, pp. 1843–1851, 1998.

[7] M. G. Moharam and T. K. Gaylord, "Rigorous coupled-wave analysis of planar-grating diffraction," *Journal of the Optical Society of America*, vol. 71, no. 7, pp. 811–818, 1981.

[8] P. Lalanne, "Improved formulation of the coupled-wave method for two-dimensional gratings," *Journal of the Optical Society of America A*, vol. 14, no. 7, pp. 1592–1598, 1997.

[9] E. Noponen and J. Turunen, "Eigenmode method for electromagnetic synthesis of diffractive elements with three-dimensional profiles," *Journal of the Optical Society of America A*, vol. 11, no. 9, pp. 2494–2502, 1994.

[10] P. G. Etchegoin, E. C. Le Ru, and M. Meyer, "An analytic model for the optical properties of gold," *Journal of Chemical Physics*, vol. 125, no. 16, Article ID 164705, 3 pages, 2006.

Hindawi Publishing Corporation
International Journal of Optics
Volume 2012, Article ID 258013, 12 pages
doi:10.1155/2012/258013

Review Article

Subwavelength Plasmonic Waveguides and Plasmonic Materials

Ruoxi Yang and Zhaolin Lu

Microsystems Engineering, Kate Gleason College of Engineering, Rochester Institute of Technology, Rochester, NY 14623, USA

Correspondence should be addressed to Zhaolin Lu, zxleen@rit.edu

Received 29 March 2012; Accepted 8 June 2012

Academic Editor: Xiaoyue Huang

Copyright © 2012 R. Yang and Z. Lu. This is an open access article distributed under the Creative Commons Attribution License, which permits unrestricted use, distribution, and reproduction in any medium, provided the original work is properly cited.

With the fast development of microfabrication technology and advanced computational tools, nanophotonics has been widely studied for high-speed data transmission, sensitive optical detection, manipulation of ultrasmall objects, and visualization of nanoscale patterns. As an important branch of nanophotonics, plasmonics has enabled light-matter interactions at a deep subwavelength length scale. Plasmonics, or surface plasmon based photonics, focus on how to exploit the optical property of metals with abundant free electrons and hence negative permittivity. The oscillation of free electrons, when properly driven by electromagnetic waves, would form plasmon-polaritons in the vicinity of metal surfaces and potentially result in extreme light confinement. The objective of this article is to review the progress of subwavelength or deep subwavelength plasmonic waveguides, and fabrication techniques of plasmonic materials.

1. Introduction

Plasmonics, a name coined for surface-plasmon-(SP-) related photonics, has inspired booming research interests since late 1990s. Actually, the history of surface plasmon research dates back to the investigation of surface plasmon resonance (SPR) on metallic thin films [1], or even light scattering from nanoscale metallic particles as early as 1970s [2]. Research focus has then shifted to the integration of plasmonic components into subsystems for optical communications and information exchange, when many novel plasmonic devices have been developed for communications in recent years [3]. Accordingly, plasmonic waveguides, couplers, and modulators become the core topics of the new plasmonics era. Two factors have catalyzed and contributed to this transition. Firstly, along with the advanced numerical tools backed up by computational electromagnetics, powerful computers and computing clusters have been more affordable and accessible. More importantly, with the fast development of nano- and microfabrication technology, researchers have been empowered to fabricate complex structures and manipulate wide selection of materials. In this paper, we will review the development and progress of plasmonic waveguides, especially the applications of metal-insulator-metal waveguides, and various plasmonic materials based on their application spectrum and fabrication techniques.

2. Motivation

Light has emerged as one of the most important carriers for large volume data, as well as a reliable and powerful aide for perception and manipulation of small particles. Compared to its classical form featured with bulky objects and diffraction-limited beams, in recent years the science of optics has utilized much finer elements where the light-matter interactions are strengthened inside a much smaller length scale compared to the lightwave's wavelength. Microoptics and nanophotonics, despite the miniature size of their elements of interest, have shown remarkable impact on all kinds of applications in communications, data storage, sensing, and imaging, and so forth. However, the mode size of a dielectric waveguide is still ruled by the diffraction-limit (close to λ/n, n being the guiding area's refractive index, and λ being the vacuum wavelength of the incident wave), and further shrinking the dimension of dielectric waveguides will inevitably lead to cutoff. This limitation leads to explorations of novel guiding mechanism and materials. Waveguides based on surface plasmons and metals, as found out later, can support propagation mode tightly bounded to the metallic surfaces and possibly confine the guiding wave in deep subwavelength scale. Accordingly, plasmonics has received tremendous attention for its scope of overcoming diffraction limit.

The current trend of technology evolution is marked by the demand of small and compact devices and high-volume integration of multiple modules on the same chip. As Moore's law in Microelectronics enforces more computational power in unit area, the telecommunications has harbored the fiber-to-the-home (FTTH) conception [4] which put high emphasis on reducing the size and cost of individual optical modules. This poses significant challenges for installation of next-generation optical interconnects featuring both compact integration and faster operation, which can be addressed possibly by resorting to plasmonics.

Moreover, light has been anticipated as an indispensable tool to print ultrafine patterns and to manipulate and observe miniscule items. For instance, optical lithography has been pivotal for the prosperity of semiconductor technology [5], but its ability to pace the roadmap of very-large-scale-integration (VLSI) technology has been slowed down because of the diffraction limit of most optical imaging systems. As another example, with complex systems such as DNA sequencing facility [6] designed and developed to incorporate ultrafine optical subsystems, the cost, and quality of optical consumables interfacing with small amount of biological or chemical substances have proved to be decisive. It has also been predicted that plasmonic nanofocusing can revolutionize the traditional magnetic recording by optically heating the media stack in a highly confined fashion, according to the technology called heat-assisted magnetic recording (HAMR) or thermal assisted magnetic recording (TAMR) [7]. Plasmonics, in this sense, shall play a much larger role for optical imaging and sensing subsystem development.

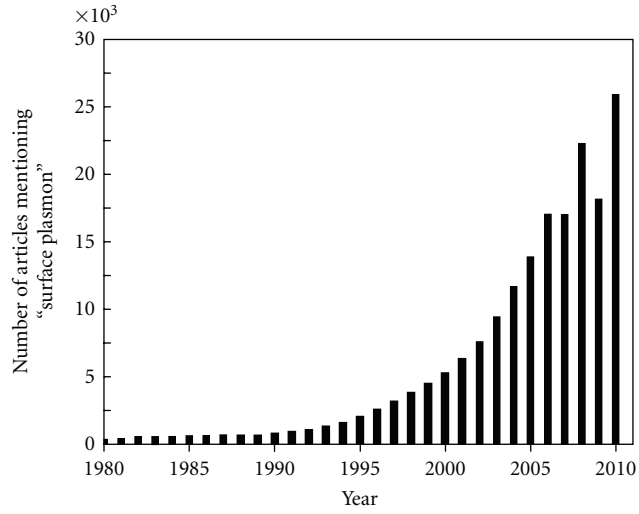

Figure 1: The growth of SP-related research in number of articles from 1980 to 2010, data acquired from Google Scholar (http://scholar.google.com/, accessed on Feb 10, 2012).

Table 1: Plasmonic frequencies and damping factors for Al, Au, Cu, and Al in NIR spectrum [12].

Material	f_p (THz)	γ_τ (THz)
Aluminum	3570	19.79
Gold	2183	6.46
Copper	1914	8.34
Silver	2180	4.353

3. Nanoplasmonic Waveguide

Research in plasmonics or other SP-related topics has gone through very fast progress in the last decade, while significant breakthroughs were reported by the end of last century (Figure 1) [8]. The study of localized SP remains active, which still finds applications from sensing, detecting, lithography, and imaging to optical storage. Since 1990, the study of plasmonic waveguides and plasmonic-enhanced (extraordinary) transmission [9] has greatly boosted the exposure of the subject. In this section, the fundamentals of plasmonics and the theory of plasmonic waveguides will be reviewed in detail.

3.1. Metal Optics with Drude Model. Metallic films are typically regarded as reflectors or cladding layers in guided-wave micro-optics for visible and near-infrared (NIR) spectrum. While metals' role in optics seems limited, the history of plasma optics is surprisingly long, although it in general lacked detailed descriptions from a guided wave perspective. Plasma optics assumes the rationality of effective dielectric constant of conduction electrons or electron gas, which determines the behavior of plasma oscillations in response to external optical driving field [10]. A plasmon is a quantized plasma oscillation, and the motion of the collective oscillation can rightly support electromagnetic (EM) waves at optical frequencies. With a frequency-dependent conductivity being prescribed, a classical Lorentz equation of motion can be used to derive the effective permittivity [11], providing the frequency independent plasma frequency $\omega_p = \sqrt{Ne^2/\varepsilon_0 m}$, while N describes the electron concentration, e the unit electric charge, ε_0 the free space permittivity, and m the electron mass.

The volume plasma has this characteristic plasma frequency ω_p, out of which the Drude model can be used to determine the dielectric constant of metals (ε_0 the free space permittivity):

$$\varepsilon_e(\omega) = \varepsilon_0 + \frac{\sigma_0}{j\omega(1 + j\omega\tau)} \approx \varepsilon_0 - \frac{\sigma_0}{\omega^2\tau} = \varepsilon_0\left(1 - \frac{\omega_p^2}{\omega^2}\right). \quad (1)$$

In this paper, we mostly consider gold and silver for applications engaging NIR and visible light. The plasma frequencies for them are well above 1000 THz, and are in general higher than the frequency of incident optical beams. The plasma frequencies given by $f_p = \omega_p/2\pi$, and the damping factors by $\gamma_\tau = 1/\tau$ for NIR spectrum of aluminium, gold, copper, and silver are shown in Table 1, adapted from [12]. The dielectric constants of these four metals are then plotted in Figure 2 by referring to [13].

By comparing the plasma frequency with the damping factor and considering the optical application regime, we conclude that external driving field from light will in general

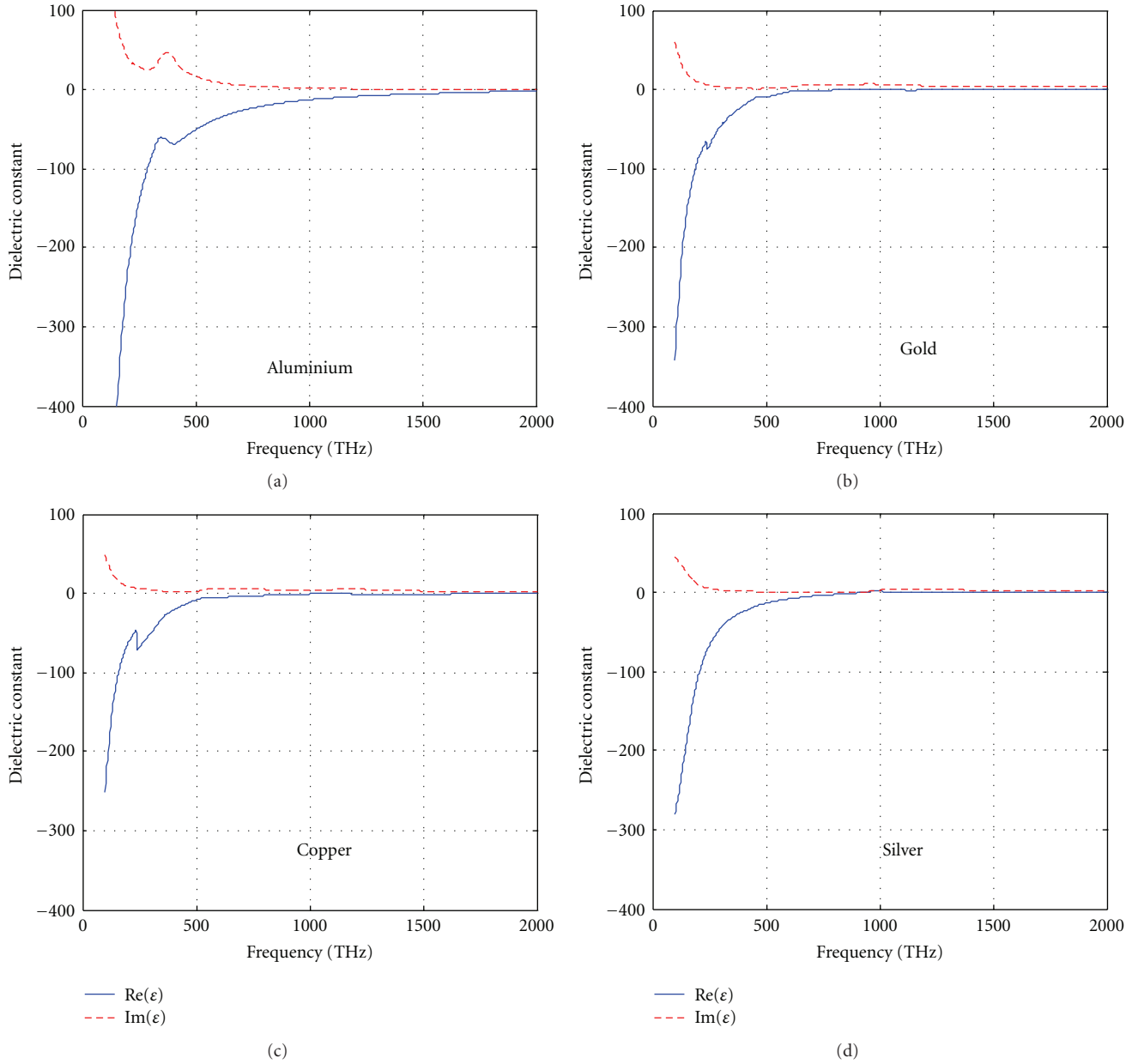

FIGURE 2: Dielectric constants of (a) aluminum, (b) gold, (c) copper, and (d) silver [13].

meet the prerequisite of $\omega \gg 1/\tau$ for the Drude model and the effective permittivity formalism cited above to hold. Therefore, EM waves inside plasmon environment using the effective permittivity formalism (no additional free current or conductivity term) can be characterized by the classical Helmholtz equation derived from Maxwell's equation

$$(\nabla^2 + \varepsilon_e k_0^2)\vec{E} = 0. \tag{2}$$

Note that in the Ampere's law used to derive this equation, there is no free current term. The factor of conductivity can be absorbed to the effective permittivity as below, although the following analysis will generally omit the damping factor γ_τ, assuming the form defined in (1). Therefore

$$\nabla \times \vec{H} = j\omega\tilde{\varepsilon}_e\vec{E} \approx j\omega\,\mathrm{Re}[\tilde{\varepsilon}_e]\vec{E}. \tag{3}$$

3.2. Bulk Plasma and Surface Plasmon. Considering a plane wave solution in the form of $A\exp(-j\vec{k}\cdot\vec{r})$ for (2), a dispersion relation can be obtained as

$$|k|^2 = k_0^2\varepsilon_e(\omega) = \left(\frac{\omega}{c_0}\right)^2\varepsilon_e(\omega). \tag{4}$$

Equation (4) clearly shows that a metal with positive permittivity will support plane waves in the bulk medium. In other words, if the driving frequency goes above the bulk plasma

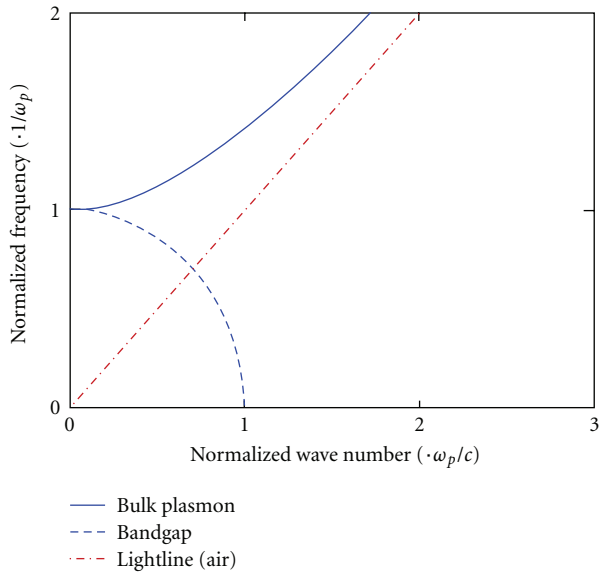

Figure 3: Dispersion relation of free electron gas (solid) compared to that of lightline of dielectric material (dash-dotted).

frequency, the plasma (or metal) becomes transparent to this external EM wave as

$$\beta = \sqrt{\varepsilon_e} k_0 = k_0 \sqrt{1 - \frac{\omega_p^2}{\omega^2}}. \quad (5)$$

This dispersion relation of free-electron gas is shown in the solid blue curve in Figure 3.

On the other hand, a negative dielectric constant is obtained when the driving frequency of the incident optical beam falls below the plasma frequency, which leads to an evanescent wave with an imaginary wave vector, as given by

$$k_{\text{eva}} = \sqrt{\varepsilon_e} k_0 = \pm j k_0 \sqrt{\frac{\omega_p^2}{\omega^2} - 1}. \quad (6)$$

This relation is shown in the dashed curve bearing a lower frequency cutoff related to plasma frequency ω_p in Figure 3. Physically, whatever direction the incident field comes from, the field will impinge into a small thickness known as skin depth, and then be fully shielded by the free electrons. The concept and the term of "skin depth" conveys an implication that only a small fraction of bulk metal could take part in the photon-material interaction, and very limited field-penetration or power-propagation could ever happen. External optical fields can only penetrate into metals for a couple of nanometers range among this spectrum, and are therefore trivial compared to the reflecting power radiated away from the metal surfaces.

The bulk plasma does not support EM waves with negative permittivity. However, it is also known that dispersion with negative permittivity has great potentials to be engineered or incorporated into complex composites for novel applications, as researchers have already done to artificially shaped structures such as photonic crystals [14] or metamaterials [15]. In this sense, the dispersion of plasmons described by the Drude model provides certainly an opportunity to manipulate electromagnetic waves and fields, as will be seen for the case of surface plasmons.

For surface plasmons, the dispersion curve will be more complex. Surface plasmon waves, which reveal the macroscopic motion of surface plasmon-polaritons (SPPs), are a coherent combination of electron gas oscillation (plasmons) and photons. For a simple case of a single metal-insulator interface in 2-dimensional (2D) view, a transverse-magnetic (TM) solution for (2) is available [1, 16]. A matched real propagation constant (β) is required for a maintained wave motion in both materials (ε_m for metal and ε_d for insulator). Therefore, the dispersion relation for SPPs at a single interface is

$$\beta = \frac{\omega}{c_0 \sqrt{\varepsilon_m \varepsilon_d / \varepsilon_m + \varepsilon_d}}. \quad (7)$$

With propagation constant (β), it is feasible to define the skin depths δ as $\delta = 1/2\gamma$ (Figure 4).

With a new term of surface plasmon frequency ($\omega_{\text{sp}} = \omega_p/\sqrt{1+\varepsilon_d}$) being defined, (7) leads to a dispersion plot for SPPs. For the air-metal case, the surface plasmon frequency is 0.707 ω_p.

In Figure 5, there is a bandgap between ω_{sp} and ω_p, when the curve only gives imaginary propagation constant (evanescent waves). When $\omega < \omega_{\text{sp}}$, SPP modes in TM polarization exist. A very large β value can be obtained at ω_{sp}, which denotes a point of resonance at that frequency point, namely the SP resonant oscillation. When $\omega > \omega_p$, $\varepsilon_m > 0$; so metal will exhibit dielectric behaviors with radiation unbounded to insulator since the mode lies above the lightline. The dispersion relation plotted above does not take damping factor into account, which will instead force a finite wave vector Re[β] at ω_{sp} due to the damping of free-electron oscillations. In this case, the right-hand side of (7) becomes a complex value and the dispersion will also slightly differ from the case of ideal conductors [16].

The single-interface case introduced above suggests several important characters related to SPPs. Firstly, a sustained surface wave can be excited along metal surfaces accompanied by ohmic loss, although at the same frequency bulk metal remains "opaque" for EM waves. Secondly, a bounded solution exists even with a half-space metal-cladded insulator, which means the SPP mode is confined to a single interface of metal-insulator with small out-of-plane radiation. Thirdly, the propagation constant of SPP mode is larger than that of a lightline at the same frequency point when the driving field has less-than-ω_{sp} frequency, which indicates a smaller effective wavelength for SPP mode compared to optical mode at same frequency. These three features are the sources of most applications reviewed in this article, and are the fundamentals of many prior efforts.

3.3. Metal-Insulator-Metal (MIM) Waveguides. Although surface plasmons can be confined to the metal-insulator boundary, the mode spread of the SP waves depends on the configuration of the waveguides and also the frequency. The length of the evanescent tail in a waveguide medium can

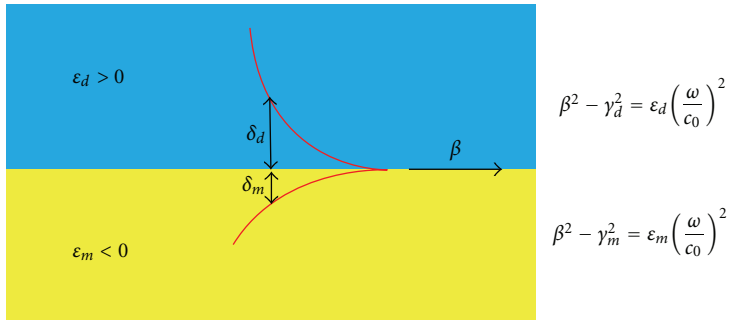

Figure 4: Definition of skin depths and their relation with propagation constant.

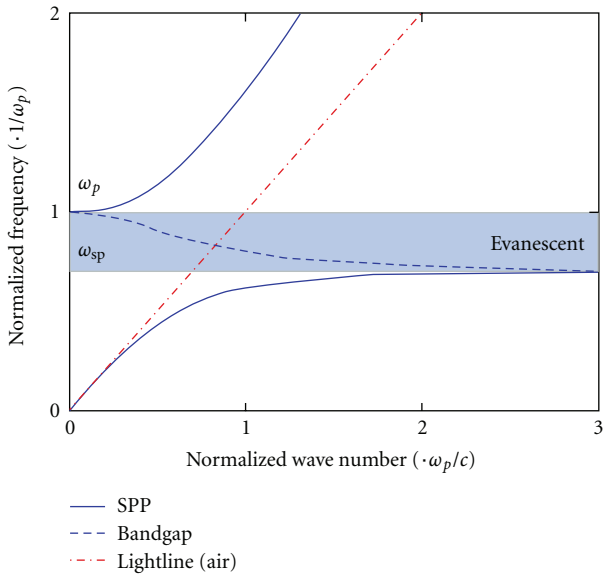

Figure 5: Dispersion relation of SPP (solid) in metal-insulator configuration. The curve for the frequency between 0.707 and 1 denotes imaginary propagation constant.

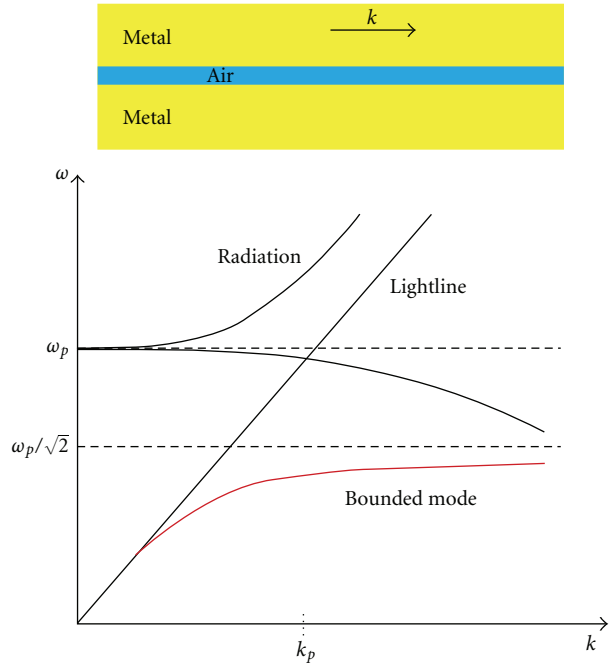

Figure 6: Dispersion plot for the MIM-layered structure adapted from [1].

be approximated by $\delta = 1/2\gamma$, when γ is defined from the conservation of momentum as follows:

$$\beta^2 - \gamma_d^2 = \varepsilon_d \left(\frac{\omega}{c_0}\right)^2 \quad (8)$$

$$\beta^2 - \gamma_m^2 = \varepsilon_m \left(\frac{\omega}{c_0}\right)^2. \quad (9)$$

Table 2 shows that for the metal-insulator (MI) waveguide, the evanescent tails can be very long compared to wavelength. For subwavelength and deep subwavelength mode confinement, it is necessary to explore different waveguide forms. The following section will start from an important plasmonic waveguide, namely metal-insulator-metal (MIM) waveguide.

The idea to incorporate surface plasmons to guided EM waves can be traced back to 1969, in Economou's paper [1] on theoretical study of EM field inside thin-films configuration. Note that it was about 30 years later, with the progress of advanced simulation tools and microscale fabrication technology, that people started to characterize plasmonic waveguides at optical frequencies.

A simple yet important form of plasmonic waveguide is based on a metal-insulator-metal (MIM) configuration (Figure 6). This waveguide, as its name indicates, consists of three layers with a dielectric core of either air or other insulator (usually with low optical loss and comparatively small refractive index), sandwiched by two metal claddings. In Economou's work [1], the dispersion relation for MIM configuration is analytically solved. In recent years, detailed analytical [17, 18] and experimental studies [19] of MIM are still performed and reported.

As verified by extensive numerical analysis, MIM waveguides possess notable tradeoff between acceptable propagation loss and subwavelength mode size. Veronis and Fan [20], along with Feigenbaum and Orenstein [21], have performed 3-dimensional (3D) simulation and mode analysis for MIM (sometimes called MDM for metal-dielectric-metal too)

Table 2: The lengths of evanescent tails at different wavelengths for metal-insulator boundary.

Wavelength (λ)	0.5 μm	1.55 μm	10.5 μm	300 μm
Frequency (c_0/λ)	600 THz	193 THz	28 THz	1 THz
ε_{Al}	$-36.5 + j9.4$	$-252 + j46$	$-8e3 + j5.2e3$	$-6e4 + j9e4$
ε_{Air}	1.0	1.0	1.0	1.0
Decay factor (γ/k_0)	0.1678	0.0631	0.0112	0.0041
Tail length (δ)	0.23 μm	1.95 μm	74.7 μm	5800 μm
Relative tail length (δ/λ)	0.47	1.26	7.12	19.49

Table 3: TM-mode size comparison for dielectric and plasmonic waveguides with λ = 1550 nm light. Data acquired from FDTD Solutions's integrated mode solver (http://www.lumerical.com/).

Waveguide type	Dielectric	MIM	IMI	MI
Materials	Silicon	Silver, air	Silver, air	Silver, air
Core thickness	300 nm	30 nm	30 nm	—
Total cladding thickness	—	300 nm	300 nm	—
n_{eff}	2.5060	1.5788	2.7104	1.0039
Loss (dB/cm)	—	2180.5	846.5	44.0
FWHM (H intensity)	208 nm	46 nm	148 nm	983 nm

structures. They successfully show that while the mode size of MIM can be pushed down to very close to the physical dimension of the guiding core in deep subwavelength regime, the acceptable propagation length keeps MIM waveguides competitive for on-chip signal transmission (Table 3). The 2D to 3D transition is verified by shrinking a 2D nanoslit [1] to a 3D nanospot [20, 22]. This feature brings in the possibility of using MIM structure as a device to guide propagating waves in ultrasmall dimension (Figure 7), and therefore an interesting platform for applications that require extreme field confinement or intensified light-matter interactions. The metal sandwich could possibly contain unwanted scattering loss from rough surfaces, which is another advantage of the MIM configuration.

From a transfer matrix perspective, it has been shown that if the fundamental TM mode is excited inside an MIM gap, the waveguide works well as a transmission line (TL) system, and shows reduced scattering loss from sharp bend [23], unlike traditional optical waveguides. The transmission line (TL) theory, adopted from the microwave realm, has then been applied to cascaded MIM systems [24] to study the reflection and transmission coefficient for complex or multilevel compositions of MIM waveguides. The formalism of TL theory based on eigenmode expansion, is found to be successful especially in calculating the coupling efficiency between SP waves propagated through several MIMs.

Along with the MIM waveguide, the insulator-metal-insulator (IMI) configuration has also found many applications. IMI is formed by burying a thin metal core in dielectric background, and if the symmetry condition is strictly met, a TM mode very similar to a dielectric mode can be supported. Devices incorporating IMI have been demonstrated for both passive [25] and active [26] cases, and because IMI's propagation loss is considerably smaller than MIM, it is frequently used for transmitting NIR optical power in longer distance above 10 μm's mark. The lack of mode confinement, however, hampers its usage in deep subwavelength scale, so does it with metal-insulator (MI) waveguides (Table 3).

Based on the MIM platform highlighted with extreme power confinement, several inventions or discoveries are noteworthy. Atwater and his coworkers have contributed significantly to this topic with their characterization of MIM plasmonic waveguides [27]. Chen [28] from Cornell University evaporated gold onto silicon ribs to form MIM waveguide, which also developed a novel way to effectively excite SP modes from photons. On the field of active plasmonics, nanocavities formed in MIM waveguide are proposed for fast modulation [29, 30], and have exhibited great potentials for development of future small-print modulators.

It is also interesting to look at the MIM waveguide from a different perspective. If an MIM waveguide is chopped for a very small propagation (less than one hundred nanometers, e.g.,), and at the same time a light beam illuminates right into the waveguide from free space, the situation will be very close to transmission through an optical head [31], which can be used to count the power getting through a subwavelength slit or a hole inscribed on a thin film. One important literature published on extra transmission related to SP waves is from Ebbesen et al. [9]. In this paper, the observance of at least 10-folds of transmission enhancement is reported (Figure 8), after facilitated features of surface corrugations are applied. Ironically, such an important literature later is cited by the authors themselves that the reported enhancement is greatly exaggerated because of a problematic measurement. The role of plasmonics in extra transmission is therefore under debate, as [32] and especially [33] have reviewed. One of the authors from the original nature paper, Tineke Thio, converted to be one of the most radical opponents to the role of surface plasmons in enhanced transmission. A diffraction theory [32], from her point of view, is powerful enough to explain most phenomena observed in extratransmission.

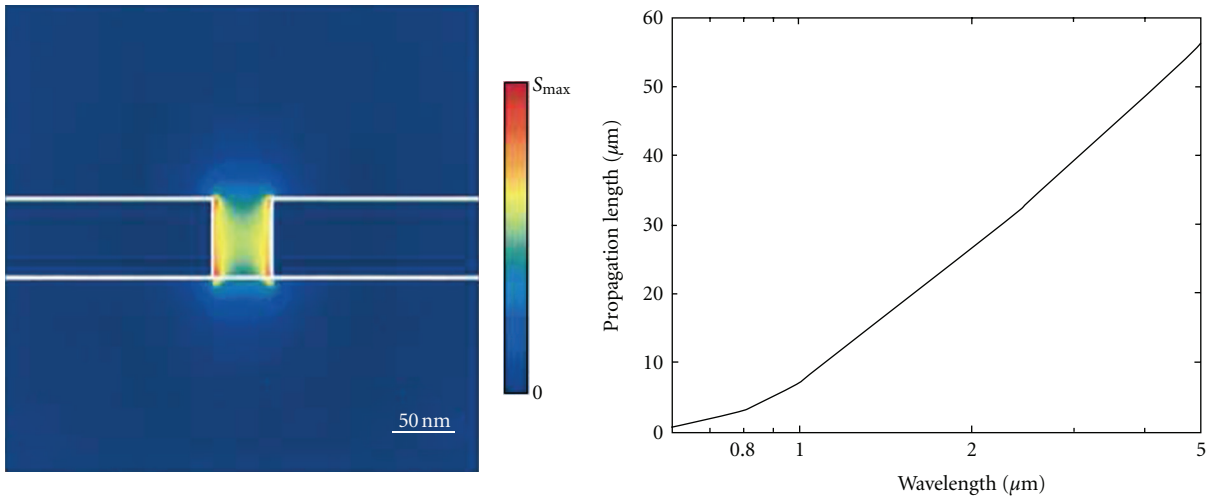

FIGURE 7: (a) A typical MIM-mode profile for 1550 nm light inside a 50 nm-by-50 nm air gap. The substrate and superstrate are silicon dioxide and air, respectively. (b) Propagation distance of the MIM mode for optical to NIR frequency [20].

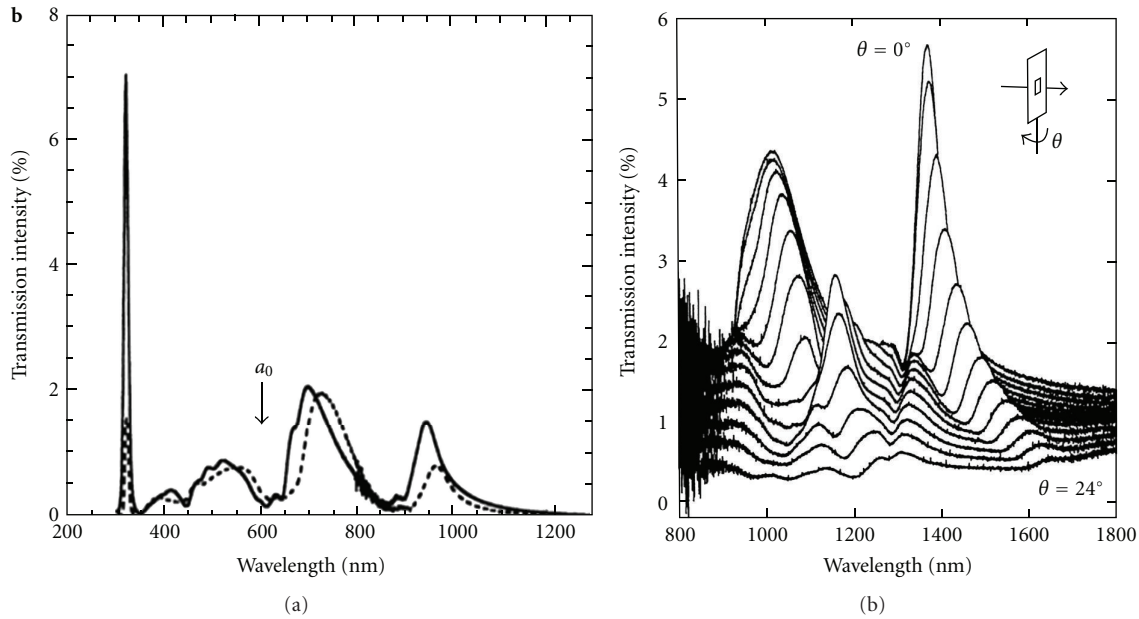

FIGURE 8: Transmission through subwavelength holes patterned in Ag as a function of wavelength (a) and illumination angle (b) [9].

Despite all the debates, it is then impossible to halt the eagerness of researchers on utilizing SP waves to accomplish higher transmission through subwavelength holes or slits. For example, Pacifici et al. [34] have used a near-field detector to characterize the field profile when corrugated surfaces are illuminated by plane waves. They managed to observe subwavelength focusing of light and have given their own physical model to explain it. A carefully designed mask [35] is found to be able to achieve a subwavelength transmission *beyond* near-field with radiationless interference. This discovery might be more interesting than the previous one for far-field applications such as imaging and nanolithography. More and more theoretical calculations on EM waves among periodic surface features or slit diffraction such as [36, 37] or [38] are still being elaborated and published, providing fresh approaches or understandings into this topic.

The extratransmission experiments introduced above are mostly based on incident plane waves from free space or uniform dielectric half space. In 2007, Veronis and Fan published simulation results [39] studying the behavior of NIR light when a dielectric waveguide is butt-connected to an MIM waveguide. They find that although the mode profiles between dielectric and MIM waveguides differ greatly, a transmission of ~70% can be achieved. There are

quite a few previous unknowns mentioned by this theoretical analysis. Firstly, the mode overlap is not found as a key issue for coupling, as the "funneling" effect has been verified by numerical simulation performed recently [40]. Secondly, the direct coupling only works for TM polarization, which is different compared to the classical case of an aperture antenna loaded on an infinite ground plane [41]. Therefore, a different physics unlike the aperture antenna theory must exist. Thirdly, the way that optical modes couple to SP modes are different to TL formalism. A matched propagation constant here does not necessarily guarantee an optimal coupling efficiency, as the eigenmodes in plasmonic waveguides are different in nature regarding the orthonormality compared to conventional rectangular waveguides. As all being said, direct coupling remains an interesting topic to the plasmonics community and has always been appreciated as a practical scheme with plasmonic devices.

3.4. Subwavelength Waveguiding by Periodic Structures. Surface plasmons are grouped oscillations of free electrons near the surface. The coupling of plasmons and photons could happen on the boundary between a metal and an insulator. As the "donor" of plasmons, metals are usually designed to share a flat boundary with insulators to avoid unwanted out-of-plane scattering. Rough boundaries or surface corrugations, on the other hand, are occasionally introduced [16] for excitations or observations of SPPs. Theoretically, surface plasmons exist for middle infrared (MIR) or even far infrared (FIR) regime. We can recall the lengths of evanescent tails in the dielectric side are given by $1/2\gamma_d$, while the term γ_d is given by

$$\gamma_d = \sqrt{\beta^2 - \varepsilon_d \left(\frac{\omega}{c}\right)^2}. \tag{10}$$

For EM waves with frequencies much smaller than optical spectrum, ε_m is a negative term with large absolute value, thus the value of γ_d can be very small. For a metal-insulator case with $|\varepsilon_m| \gg |\varepsilon_d|$, and referring to the dispersion relation in (7), we can see β^2 will approach $\varepsilon_d(\omega/c)^2$, which is the right side of (8). Therefore, γ_d will likely be very small and leads to a very long evanescent tail. This type of surface wave looks close to the so-called Zenneck or Sommerfeld wave [42] and the field confinement will be very poor (Table 3).

Obviously, to achieve tightly bounded surface wave beyond optical spectrum such as terahertz (THz) or even gigahertz (GHz) regime, a flat surface is not enough. On the other hand, the lower frequency (or the longer wavelength) makes it possible to make comparatively small corrugation on metallic surfaces. If the considered corrugation is small enough compared to wavelength, it can be legitimately characterized by using the effective medium formalism. This approach is called "spoof plasmonics" by Pendry et al. [43], in their attempt to achieve arbitrary "spoof" plasma frequency via drilling holes on the perfect electric conductor (PEC).

When the corrugation is uniformly distributed in xy direction (Figure 9(a)), the bulk PEC can be regarded as a uniaxial crystal, a typical anisotropic metamaterial. The dispersion calculation yields an upper cutoff frequency and an extremely slow light towards this cut-off, same as the typical SPP behaves. More importantly, when an effective medium is used for analysis, the theory of conventional plasmonics can be applied to the structured surface. Therefore, the concept of surface plasmon frequency can also be extended to describe the property of this metamaterial. Instead of the canonical value, the new (or effective) surface plasmon frequency is determined by the dimension of surface corrugations. Therefore, the optical property of this metamaterial can be well controlled by tweaking the physical perturbations applied to the bulk material.

The spoof plasmonic approach has inspired many discoveries based on surface corrugations especially in THz region as metals are almost lossless and compact THz waveguides are in high demand. Maier et al. [44] designs a THz waveguide for subwavelength confinement in 2D working at 1 THz. Martin-Cano et al. have designed metal gratings as THz waveguide platform, which can integrate multiple passive devices at the same time [45]. In GHz region, Zhao et al. [46] used designer surface plasmon approach to demonstrate the same concept (Figure 10).

Another platform for spoof plasmonics is based on stratified medium, which finds vast applications in the optical regime. Multilayered composites with periodic layer-unit have been widely implored as negative index materials (NIMs) for superlensing. Treated as an effective medium, its anisotropy is well approximated by straightforward mixing rules [47, 48] if each repeated layer is thin enough compared to wavelength. Along with the superlensing effect [49], multilayered composites have also been designed to support surface-plasmon-like waves [50, 51] and used for nanolithography. Figure 11 shows the schematic electric field diagram of a multilayer structure, when a composition of surface waves is formed [48].

4. Plasmonic Materials and Fabrication Technique

The progress of experimental plasmonics is closely related to the advancement of material research and fabrication technology. Plasmonic phenomena have been observed and investigated for more than 40 years, originally on light scattering from metal particles in early years, gradually including light guiding by particle arrays and layered structures. Without the advanced fabrication methods to process plasmonic materials and integrate plasmonic structures into optical circuitry, it is impossible to expect the vast applications of plasmonic components in sensing, imaging, storage, and communications these days. In this section, the most important plasmonic materials and their processing methods will be reviewed.

In solid-state physics, surface plasmons are treated as grouped oscillation of electron gas. The electron gas model fits materials with a high volume of free electrons, which is inherently more accurate for simple metals (alkali metals). Metals found in semiconductor technology at room temperature have an electron concentration close to the order

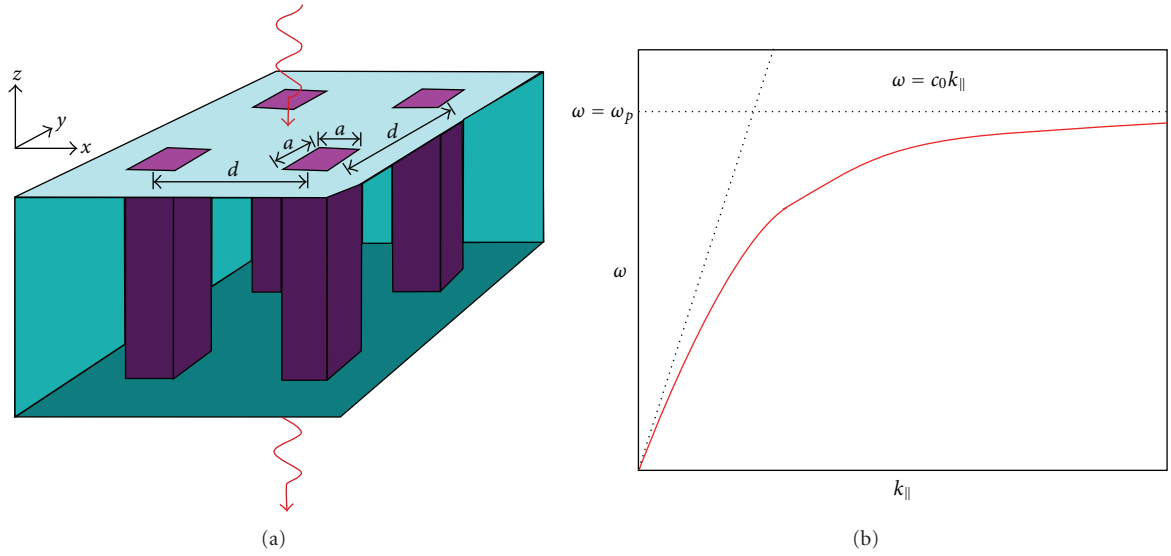

Figure 9: Spoof plasmonics in PEC shown by dimension (a) and dispersion (b) [43].

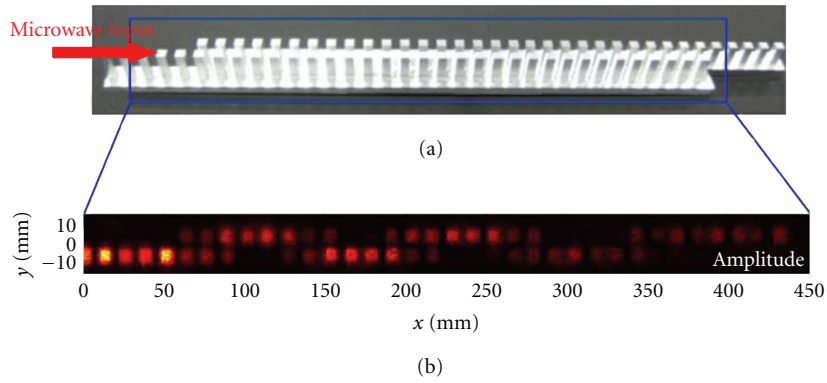

Figure 10: A spoof plasmonic waveguide guiding GHz waves [46], forming a directional coupler.

of 10^{22} per cm^3, while semiconductors or doped materials widely used in this industry have a carrier concentration of less than 10^{17} per cm^3. As a result, most plasmonic structures, especially those for optical spectrum, will involve metals at some level. The overwhelmingly used materials in plasmonics have remained to be those that are stable in room temperature, especially aluminum (Al) and noble metals such as gold (Au), silver (Ag), and copper (Cu) (Table 1). Alternative plasmonic materials known to contain abundant free carriers include metallic alloys, metallic compounds, and graphene.

4.1. Metals. Metals have been studied and understood through the free-electron model, in which the electrons inside metals are regarded as moving almost free from striking with each other. In the Drude formalism for 3D electron gas, the mean relaxation time is described by the damping frequency term γ_τ. For the noble metals frequently used in plasmonics, the total damping comes from not only the interactions between conduction electrons, but also from interband transitions [10, 16]. Wherever the damping of free-electron oscillation actually comes from, the propagation loss in classical electromagnetic problems for plasmonic metals can be evaluated from the imaginary parts of their dielectric constants and the electric field intensity, treated as dissipated or lost in the form of ohmic heat. Therefore, a straightforward figure of merit for choosing plasmonic material is its resistivity. By reading the optical resistivity data or the dielectric constants of various metals [52], it is possible to spot candidates of suitable materials for different frequency ranges. In NIR spectrum, silver has the smallest imaginary part of permittivity and the best conductivity, making it a highly favored material. The easy oxidation somehow limits its applications, and makes gold a popular candidate in this frequency range. For the applications of UV or DUV light such as the 193 nm light for DUV optical lithography, however, aluminum is proved to be the most attractive candidate [12] (Table 1).

Processing metals (especially noble metals) is in general complex, especially compared with semiconductors used in microfabrication. The deposition of plasmonic metals can be achieved in vacuum by sputtering or evaporation. To avoid percolation, and to obtain acceptable uniformity and quality,

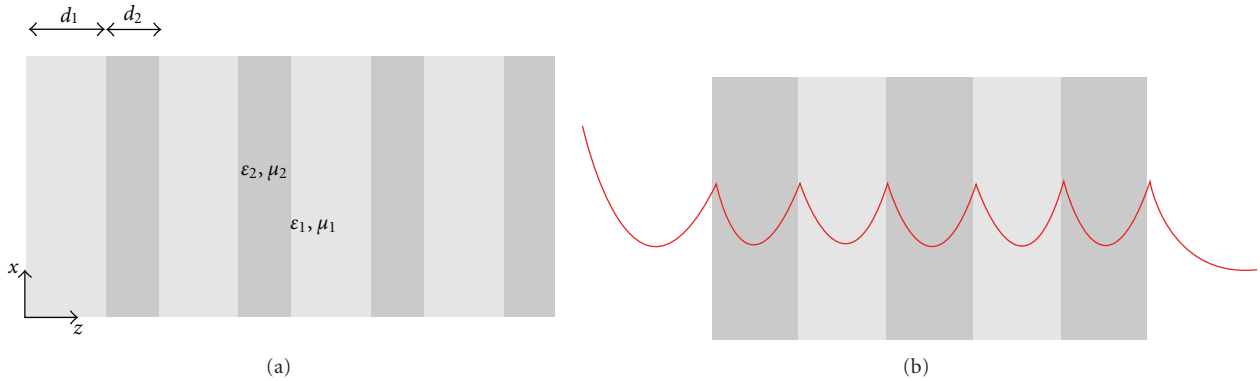

Figure 11: Multilayered, periodic metal-insulator stacks (a) and the schematic *E*-field profile (b) inside [48].

the deposition rate is usually limited to less than 1 nm per second. The small deposition rate is normally not a big issue as in most cases the required thickness for plasmonics is small. Electroplating gives faster metal growth rate but the quality of the surface might not be considered fine enough for plasmon waves.

The pattern transfer from resist to metals is extremely challenging for noble metals, as there are not many effective methods to etch copper, silver, or gold. Plasmonic metals such as aluminum can be etched by plasma etch in Cl_2-based ambient. Other than this, there are generally two approaches to pattern metals. The first one is through image reversal and lift-off process, which requires resist overhang after development. There have been photoresists specifically used for lift-off process such as nLOR from MicroChem [53], while researchers also use bilayer or multilayer compositions to achieve the crucial overhang [54]. When using bilayer resists for liftoff, it is conventionally required to coat a bottom resist layer for at least twice as thick as the lift-off thickness. Therefore, it is not easy to have high aspect ratio, standalone metal features fabricated. A second approach to pattern metal is through ion milling. Focused ion beam can be used to directly mill patterns into gold or silver film, while it usually introduces redepositions from the beam source. Argon ion beam is another option that can work with noble metals, which requires hard masks such as carbon and might greatly increase the number of steps and also the complexity of processing.

4.2. Compounds. Metal silicides are originally used to decrease the contact resistivity in VLSI circuits and especially MOSFET technology. As they have an intermediate conductivity and carrier concentration between metal and semiconductor, silicide compounds have also been investigated for plasmonic applications especially in THz frequency [55]. In the form of compounds consisting of silicon and metals (Ti, Co, W, Ni, Pd, etc.), silicides have a smaller plasmonic frequency compared to noble metals used in the near-infrared regime and in general higher loss. However, as its fabrication and electric property have been extensively studied for large-scale integrated circuit technology, the deposition of very thin layers and accurate patterning is highly reliable.

Transparent conducting oxide (TCO) materials are optically transparent and electrically conductive. As one of the most widely used TCO, Indium tin oxide (ITO) has been widely studied and used in display industry and optoelectronics as an optical coating. The frequency range for ITO to exhibit negative permittivity is also in NIR, in which ITO is reported to have competitively low loss even compared to silver. The deposition of ITO films can be achieved through sputter deposition [56]. The major concern about using ITO is its price, and the instability of its optical property for different growth conditions. Similar materials include aluminum zinc oxide (AZO), gallium zinc oxide (GZO), and so forth [57].

4.3. Graphene and Others. A few rarely-used yet interesting materials exist as potential candidates for plasmonic applications. Among them, graphene and polymer-based plasmonics have attracted more and more attention, because of the distinguished electronic and optical properties. Graphene's plasmonic property has been predicted in [58–60], showing promising tunable optical conductivity. Standard approaches for graphene layer deposition are limited at this time, although depositions based on transfer-printing method [61], CVD [62], and electrostatic method [63] have been reported.

5. Conclusion

Surface plasmon has been studied extensively for optical sensing and imaging, even long before the term "plasmonics" became widely accepted. The transition from SPR in standalone devices to plasmonics, assisted by advanced simulation and fabrication tools, emphasizes the integration of plasmonic features into subsystems for all sorts of optical communications and information exchange. With more and more significant discoveries based on surface plasmon waveguiding in subwavelength or deep subwavelength regime, plasmonics is expected to further impact the research and development of integrated optical communications, data storage, optical sensing, and imaging technology.

Acknowledgment

This paper is based upon work supported in part by the U. S. Army under Award no. W911NF-10-1-0153 and the National Science Foundation under Award no. ECCS-1057381. Acknowledgment is made to the Donors of the American Chemical Society Petroleum Research Fund for partial support of this project.

References

[1] E. N. Economou, "Surface plasmons in thin films," *Physical Review*, vol. 182, no. 2, pp. 539–554, 1969.

[2] R. H. Ritchie, "Surface plasmons in solids," *Surface Science*, vol. 34, no. 1, pp. 1–19, 1973.

[3] M. I. Stockman, "Nanoplasmonics: past, present, and glimpse into future," *Optics Express*, vol. 19, no. 22, pp. 22029–22106, 2011.

[4] K. S. Kim, "On the evolution of PON-based FTTH solutions," *Information Sciences*, vol. 149, no. 1–3, pp. 21–30, 2003.

[5] M. Rothschild, "A roadmap for optical lithography," *Optics and Photonics News*, vol. 21, no. 6, pp. 26–31, 2010.

[6] J. Eid, A. Fehr, J. Gray et al., "Real-time DNA sequencing from single polymerase molecules," *Science*, vol. 323, no. 5910, pp. 133–138, 2009.

[7] W. A. Challener, C. Peng, A. V. Itagi et al., "Heat-assisted magnetic recording by a near-field transducer with efficient optical energy transfer," *Nature Photonics*, vol. 3, no. 4, pp. 220–224, 2009.

[8] M. L. Brongersma and P. G. Kik, *Surface Plasmon Nanophotonics*, Springer, Dordrecht, The Netherlands, 2007.

[9] T. W. Ebbesen, H. J. Lezec, H. F. Ghaemi, T. Thio, and P. A. Wolff, "Extraordinary optical transmission through subwavelenght hole arrays," *Nature*, vol. 391, no. 6668, pp. 667–669, 1998.

[10] C. Kittel, *Introduction to Solid State Physics*, John Wiley & Sons, New York, NY, USA, 1989.

[11] B. E. A. Salen and M. C. Teich, *Fundamentals of Photonics*, Wiley-Interscience, Hoboken, NJ, USA, 2nd edition, 2007.

[12] M. A. Ordal, R. J. Bell, J. Alexander, L. L. Long, and M. R. Querry, "Optical properties of fourteen metals in the infrared and far infrared: Al, Co, Cu, Au, Fe, Pb, Mo, Ni, Pd, Pt, Ag, Ti, V, and W," *Applied Optics*, vol. 24, no. 24, pp. 4493–4499, 1985.

[13] E. D. Palik, *Handbook of Optical Constants of Solids*, Academic Press, Orlando, Fla, USA, 1985.

[14] J. D. Joannopoulos, S. G. Johnson, and J. N. Winn, *Photonic Crystals: Molding the Flow of Light*, Princeton University Press, New Jersey, NJ, USA, 2008.

[15] N. Engheta and R. W. Ziolkowski, *Metamaterials: Physics and Engineering Explorations*, Wiley, 2006.

[16] S. A. Maier, *Plasmonics: Fundamentals and Applications*, Springer, New York, NY, USA, 2007.

[17] R. Gordon, "Light in a subwavelength slit in a metal: propagation and reflection," *Physical Review B*, vol. 73, no. 15, Article ID 153405, 2006.

[18] J. A. Dionne, L. A. Sweatlock, H. A. Atwater, and A. Polman, "Plasmon slot waveguides: towards chip-scale propagation with subwavelength-scale localization," *Physical Review B*, vol. 73, no. 3, Article ID 035407, 9 pages, 2006.

[19] S. I. Bozhevolnyi, V. S. Volkov, E. Devaux, J.-Y. Laluet, and T. W. Ebbesen, "Channel plasmon subwavelength waveguide components including interferometers and ring resonators," *Nature*, vol. 440, no. 7083, pp. 508–511, 2006.

[20] G. Veronis and S. Fan, "Guided subwavelength plasmonic mode supported by a slot in a thin metal film," *Optics Letters*, vol. 30, no. 24, pp. 3359–3361, 2005.

[21] E. Feigenbaum and M. Orenstein, "Modeling of complementary (Void) plasmon waveguiding," *Journal of Lightwave Technology*, vol. 25, no. 9, pp. 2547–2562, 2007.

[22] R. Yang, M. A. G. Abushagur, and Z. Lu, "Efficiently squeezing near infrared light into a 21nm-by-24nm nanospot," *Optics Express*, vol. 16, no. 24, pp. 20142–20148, 2008.

[23] G. Veronis and S. Fan, "Bends and splitters in metal-dielectric-metal subwavelength plasmonic waveguides," *Applied Physics Letters*, vol. 87, no. 13, Article ID 131102, 3 pages, 2005.

[24] Ş. E. Kocabaş, G. Veronis, D. A. B. Miller, and S. Fan, "Modal analysis and coupling in metal-insulator-metal waveguides," *Physical Review B*, vol. 79, no. 3, Article ID 035120, 2009.

[25] R. Charbonneau, C. Scales, I. Breukelaar et al., "Passive integrated optics elements based on long-range surface plasmon polaritons," *Journal of Lightwave Technology*, vol. 24, no. 1, pp. 477–494, 2006.

[26] T. Nikolajsen, K. Leosson, and S. I. Bozhevolnyi, "Surface plasmon polariton based modulators and switches operating at telecom wavelengths," *Applied Physics Letters*, vol. 85, no. 24, pp. 5833–5835, 2004.

[27] J. A. Dionne, H. J. Lezec, and H. A. Atwater, "Highly confined photon transport in subwavelength metallic slot waveguides," *Nano Letters*, vol. 6, no. 9, pp. 1928–1932, 2006.

[28] L. Chen, J. Shakya, and M. Lipson, "Subwavelength confinement in an integrated metal slot waveguide on silicon," *Optics Letters*, vol. 31, no. 14, pp. 2133–2135, 2006.

[29] J. A. Dionne, K. Diest, L. A. Sweatlock, and H. A. Atwater, "PlasMOStor: a metal-oxide-si field effect plasmonic modulator," *Nano Letters*, vol. 9, no. 2, pp. 897–902, 2009.

[30] W. Cai, J. S. White, and M. L. Brongersma, "Compact, high-speed and power-efficient electrooptic plasmonic modulators," *Nano Letters*, vol. 9, no. 12, pp. 4403–4411, 2009.

[31] M. J. Levene, J. Korlach, S. W. Turner, M. Foquet, H. G. Craighead, and W. W. Webb, "Zero-mode waveguides for single-molecule analysis at high concentrations," *Science*, vol. 299, no. 5607, pp. 682–686, 2003.

[32] H. J. Lezec and T. Thio, "Diffracted evanescent wave model for enhanced and suppressed optical transmission through subwavelength hole arrays," *Optics Express*, vol. 12, no. 16, pp. 3629–3651, 2004.

[33] T. Thio, "A bright future for subwavelength light sources," *American Scientist*, vol. 94, no. 1, p. 40, 2006.

[34] D. Pacifici, H. J. Lezec, L. A. Sweatlock, R. J. Walters, and H. A. Atwater, "Universal optical transmission features in periodic and quasiperiodic hole arrays," *Optics Express*, vol. 16, no. 12, pp. 9222–9238, 2008.

[35] R. Merlin, "Radiationless electromagnetic interference: evanescent-field lenses and perfect focusing," *Science*, vol. 317, no. 5840, pp. 927–929, 2007.

[36] F. J. García-Vidal, S. G. Rodrigo, and L. Martín-Moreno, "Foundations of the composite diffracted evanescent wave model," *Nature Physics*, vol. 2, no. 790, pp. 262–267, 2006.

[37] L. Chen, J. T. Robinson, and M. Lipson, "Role of radiation and surface plasmon polaritons in the optical interactions between a nano-slit and a nano-groove on a metal surface," *Optics Express*, vol. 14, no. 26, pp. 12629–12636, 2006.

[38] D. Pacifici, H. J. Lezec, H. A. Atwater, and J. Weiner, "Quantitative determination of optical transmission through subwavelength slit arrays in Ag films: role of surface wave interference

and local coupling between adjacent slits," *Physical Review B*, vol. 77, no. 11, Article ID 115411, 2008.

[39] G. Veronis and S. Fan, "Theoretical investigation of compact couplers between dielectric slab waveguides and two-dimensional metal-dielectric-metal plasmonic waveguides," *Optics Express*, vol. 15, no. 3, pp. 1211–1221, 2007.

[40] R. A. Wahsheh, Z. Lu, and M. A. G. Abushagur, "Nanoplasmonic couplers and splitters," *Optics Express*, vol. 17, no. 21, pp. 19033–19040, 2009.

[41] C. A. Balanis, *Antenna Theory: Analysis and Design*, Wiley, New Jersey, NJ, USA, 2005.

[42] A. Sommerfeld, "Propagation of waves in wireless telegraphy," *Annals of Physics*, vol. 81, pp. 1367–1153, 1926.

[43] J. B. Pendry, L. Martín-Moreno, and F. J. Garcia-Vidal, "Mimicking surface plasmons with structured surfaces," *Science*, vol. 305, no. 5685, pp. 847–848, 2004.

[44] S. A. Maier, S. R. Andrews, L. Martín-Moreno, and F. J. García-Vidal, "Terahertz surface plasmon-polariton propagation and focusing on periodically corrugated metal wires," *Physical Review Letters*, vol. 97, no. 17, Article ID 176805, 4 pages, 2006.

[45] D. Martin-Cano, M. L. Nesterov, A. I. Fernandez-Dominguez, F. J. Garcia-Vidal, L. Martin-Moreno, and E. Moreno, "Domino plasmons for subwavelength terahertz circuitry," *Optics Express*, vol. 18, no. 2, pp. 754–764, 2010.

[46] W. Zhao, O. M. Eldaiki, R. Yang, and Z. Lu, "Deep subwavelength waveguiding and focusing based on designer surface plasmons," *Optics Express*, vol. 18, no. 20, pp. 21498–21503, 2010.

[47] D. J. Bergman, "The dielectric constant of a composite material-a problem in classical physics," *Physics Reports*, vol. 43, no. 9, pp. 377–407, 1978.

[48] B. Wood, J. B. Pendry, and D. P. Tsai, "Directed subwavelength imaging using a layered metal-dielectric system," *Physical Review B*, vol. 74, no. 11, Article ID 115116, 2006.

[49] W. Cai, D. A. Genov, and V. M. Shalaev, "Superlens based on metal-dielectric composites," *Physical Review B*, vol. 72, no. 19, Article ID 193101, 4 pages, 2005.

[50] J. Elser, A. A. Govyadinov, I. Avrutsky, I. Salakhutdinov, and V. A. Podolskiy, "Plasmonic nanolayer composites: coupled plasmon polaritons, effective-medium response, and subdiffraction light manipulation," *Journal of Nanomaterials*, vol. 2007, Article ID 79469, 8 pages, 2007.

[51] R. Yang, X. Huang, and Z. Lu, "Arbitrary super surface modes bounded by multilayered metametal," *Micromachines*, vol. 3, no. 1, pp. 45–54, 2012.

[52] D. R. Lide, *CRC Handbook of Chemistry and Physics*, CRC Press, 2004.

[53] MicroChem Corp, March2012, http://www.microchem.com.

[54] Photolithography Resist Processes and Capabilities (CNF), March 2012, http://www.cnf.cornell.edu/cnf_process_photo_resists.html.

[55] R. A. Soref, S.-Y. Cho, W. Buchwald, and R. E. Peale, "Silicon plasmonic waveguides," in *Silicon Photonics for Telecommunications and Biomedical Applications*, B. Jalali and S. Fathpour, Eds., Taylor & Francis, London, UK, 2010.

[56] "PVD 75 Sputter Deposition from Kurt J. Lesker by CNF," March 2012, http://www.cnf.cornell.edu/cnf5_tool.taf?_function=detail&eq_id=156.

[57] P. R. West, S. Ishii, G. V. Naik, N. K. Emani, V. M. Shalaev, and A. Boltasseva, "Searching for better plasmonic materials," *Laser & Photonics Reviews*, vol. 4, no. 6, pp. 795–808, 2010.

[58] D. R. Andersen, "Graphene-based long-wave infrared TM surface plasmon modulator," *Journal of the Optical Society of America B*, vol. 27, no. 4, pp. 818–823, 2010.

[59] F. H. L. Koppens, D. E. Chang, and F. J. Garciía de Abajo, "Graphene plasmonics: a platform for strong Light-Matter interactions," *Nano Letters*, vol. 11, no. 8, pp. 3370–3377, 2011.

[60] J. T. Kim and S.-Y. Choi, "Graphene-based plasmonic waveguides for photonic integrated circuits," *Optics Express*, vol. 19, no. 24, pp. 24557–24562, 2011.

[61] X. Li, Y. Zhu, W. Cai et al., "Transfer of large-area graphene films for high-performance transparent conductive electrodes," *Nano Letters*, vol. 9, no. 12, pp. 4359–4363, 2009.

[62] A. Reina, X. Jia, J. Ho et al., "Large area, few-layer graphene films on arbitrary substrates by chemical vapor deposition," *Nano Letters*, vol. 9, no. 1, pp. 30–35, 2009.

[63] A. N. Sidorov, M. M. Yazdanpanah, R. Jalilian, P. J. Ouseph, R. W. Cohn, and G. U. Sumanasekera, "Electrostatic deposition of graphene," *Nanotechnology*, vol. 18, no. 13, Article ID 135301, 2007.

Hindawi Publishing Corporation
International Journal of Optics
Volume 2012, Article ID 152937, 7 pages
doi:10.1155/2012/152937

Research Article

Surface Plasmon Singularities

Gabriel Martínez-Niconoff,[1] P. Martinez-Vara,[2] G. Diaz-Gonzalez,[1] J. Silva-Barranco,[1] and A. Carbajal-Domínguez[3]

[1] *Departamento de Óptica, Instituto Nacional de Astrofísica Óptica y Electrónica (INAOE), Apdo. Postal 51 y 216, Tonantzintla, PUE, Mexico*
[2] *Facultad de Ingeniería, Benemérita Universidad Autónoma de Puebla (BUAP), Publa, PUE, Mexico*
[3] *Universidad Juárez Autónoma de Tabasco, (UJAT), Cunduacán, Tab, Mexico*

Correspondence should be addressed to Gabriel Martínez-Niconoff, gmartin@inaoep.mx

Received 5 April 2012; Revised 12 June 2012; Accepted 13 June 2012

Academic Editor: Zhaolin Lu

Copyright © 2012 Gabriel Martínez-Niconoff et al. This is an open access article distributed under the Creative Commons Attribution License, which permits unrestricted use, distribution, and reproduction in any medium, provided the original work is properly cited.

With the purpose to compare the physical features of the electromagnetic field, we describe the synthesis of optical singularities propagating in the free space and on a metal surface. In both cases the electromagnetic field has a slit-shaped curve as a boundary condition, and the singularities correspond to a shock wave that is a consequence of the curvature of the slit curve. As prototypes, we generate singularities that correspond to fold and cusped regions. We show that singularities in free space may generate bifurcation effects while plasmon fields do not generate these kinds of effects. Experimental results for free-space propagation are presented and for surface plasmon fields, computer simulations are shown.

1. Introduction

The contemporary trends in plasmon optics consist of establishing a parallelism with the traditional optical models. The wave nature of the electromagnetic field in both cases implies that the mathematical analysis may present many similarities. However, the physical features may be completely different. An important common behavior is that the electromagnetic field is organized around the singular regions. The simplest singular region is kind fold, and the union of twofold focusing regions generates a cusped focusing region [1]. These are the only focusing regions that can be detected on a plane [1, 2], so that they are the expected singularities for surface plasmon fields. From this fact, some physical features can be analyzed. For optical fields in free space, the inverse process may occur, that is, when a cusped focusing region is split into two folds, vortex and bifurcation effects may occur [3]. For the case of plasmon fields, these features do not appear; however, the focusing region generates charge redistribution [4, 5]. This latter property offers many interesting applications; for example, it can be implemented to polarize particles, allowing the design of plasmonic tweezers.

In the present study, we describe the synthesis of singular regions propagating in free space and they are compared with the singular regions for surface plasmon fields. In both cases, the singularities geometry can be obtained from the phase function [6, 7], and it satisfies the nonlinear partial differential equation [6]

$$\frac{\partial^2 L}{\partial x^2}\frac{\partial^2 L}{\partial y^2} - \left(\frac{\partial^2 L}{\partial x \partial y}\right)^2 = 0, \tag{1}$$

where L is the optical path length. When the boundary condition is a slit-shaped curve, (1) has a simple geometrical interpretation. The singularity is generated by means of the envelope region of a ray set, and each ray must satisfy the Fermat principle [8], and this construction is sketched in Figure 1. According to the transversal condition [9], the rays must emerge perpendicular to the curve slit. In the case of plasmon fields, this geometrical point of view is very important because all the electromagnetic fields propagating

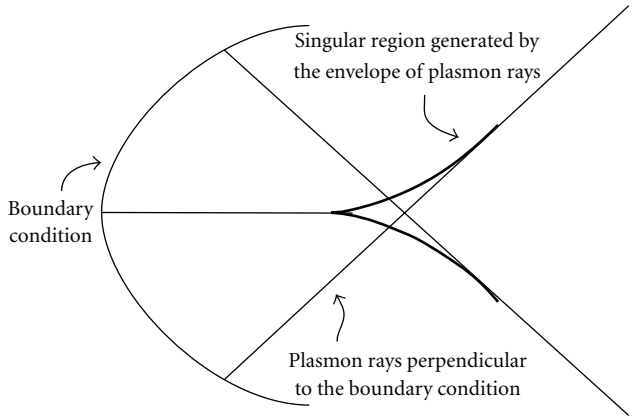

Figure 1: Generation of the singular region by means of a set of plasmon rays. Each ray must satisfy variational principles; this means that the rays must emerge perpendicular to the boundary condition. This construction is valid for waves in free space and surface plasmon fields.

on the metal surface can be considered as a "Geodesic Flow" [10], and in this sense, the singularities are deeply related to the stability of the flow.

2. Long-Range Surface Plasmon Modes

Surface plasmon modes are nonhomogeneous electromagnetic waves propagating on the interface of a dielectric-metal media. For a semi-infinite media, the electric field is

$$E_1(x,z) = \left(\vec{i}a_1 + \vec{k}b_1\right)\exp(-\alpha_1 z)\exp(i\beta x),$$
$$E_2(x,z) = \left(\vec{i}a_2 + \vec{k}b_2\right)\exp(-\alpha_2 z)\exp(i\beta x). \tag{2}$$

Related to this electromagnetic mode is the charge motion of the free electrons, that oscillate longitudinally and transversally to the surface. These oscillations are determined by the trajectory of the electric field, whose geometry can be obtained by establishing an analogy with the classical polarization model. It is easy to show that the trajectory of the electric field on the x-z plane is given by

$$\frac{E_x^2}{a_1^2} + \frac{E_z^2}{\left(\alpha a_1/|\beta|\right)^2} - \frac{2E_xE_z}{a_1^2\alpha/|\beta|}\cos\delta_0 = \exp(-2\alpha z)\sin^2\delta_0, \tag{3}$$

where β is the dispersion relation function that satisfies

$$\beta = \frac{w}{c}\left(\frac{\varepsilon_1\varepsilon_2}{\varepsilon_1+\varepsilon_2}\right)^{1/2}. \tag{4}$$

ε_1 is the permittivity of the dielectric media, ε_2 is the permittivity of the metal, which is a complex number, and consequently, β is a complex function. The imaginary part is responsible for surface plasmon modes propagating at very short distances, about 100 μm. This length of propagation is a serious limitation for the development of plasmon optics. The synthesis of focusing regions implies the generation of long-range surface plasmon modes modifying the dispersion relation function β. This is possible when the surface plasmon is propagating in a metallic thin film of thickness 20–80 nm. The calculus of the new dispersion relation function is described by means of the interaction between two plasmon modes, as shown in Figure 2.

The interaction between the two modes is performed by using the coupling mode theory. This implies to model the surface effects, associating an expression for the refractive index, in the neighborhood of the interface of the dielectric-metal surface, which is given by

$$n = n_1 + a\exp(-pz), \quad z \geq d, \tag{5}$$

where n_1 is the refractive index of the dielectric media, a is a small constant determined by the combination of the materials involved, d is the thickness of the film, and p is a parameter that allows us to model the surface effects. When $z \to \infty$, the proposed refractive index recovers the classical expression for the dielectric media.

For this case, the dispersion relation function acquires the form

$$\beta = \frac{\omega}{c}\left\{\left(\frac{\varepsilon_1\varepsilon_2}{\varepsilon_1+\varepsilon_2}\right)^{1/2} + 2an_1\left(\frac{\varepsilon_1\varepsilon_2}{\varepsilon_1+\varepsilon_2}\right)^{-1/2}\exp(-2\alpha d)\right\}. \tag{6}$$

The calculus details can be found in [4]. When the last expression is substituted in (3), the trajectory geometry of the electrical field on z = constant is an ellipse segment, as shown in Figure 3.

The modulus of the imaginary part given by (6) is minor, when compared with that given by (4). As a consequence the plasmon fields for a thin film propagate large distances. The geometrical interpretation is that the x-component for the electric field is minor, decreasing the amplitude oscillation of the charge along the x-axis.

The parameters implicit in (5) are sketched in Figure 2. The expression for the long-range surface plasmon mode is obtained by replacing the expression for β given by (6) in (2).

To generate the singular regions, it is necessary to describe the long-range plasmon mode on the x-y plane. The corresponding expression is obtained by rotating the z-axis, and the transformation of coordinates is $z \to z$; $x \to x\cos\theta \pm y\sin\theta$. The general expression for the plasmon mode is

$$E(x,y,z) = \left(\vec{i}a + \vec{k}b\cos\theta + \vec{j}b\sin\theta\right) \times \exp(-\alpha_1 z)\exp\left(i\beta\left(x\cos\theta + y\sin\theta\right)\right), \tag{7}$$

with β given as that presented in (6).

3. Singular Regions in Free Space

With the purpose to analyze the singularities, we describe the generation of fold singularities propagating in free space. The transmittance function has a mathematical representation in the frequency space of the form [6]

$$T(u,v) = \delta(u - f(v)), \tag{8}$$

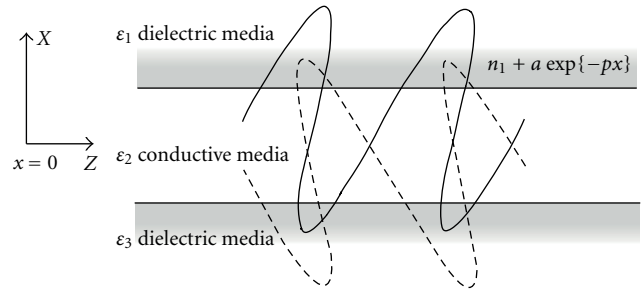

Figure 2: Schematic set up to describe the synthesis of long-range surface plasmon modes. The surface effects are described by assuming an exponential representation for the refractive index. The physical effects are described by assuming two surface plasmon modes propagating on each surface.

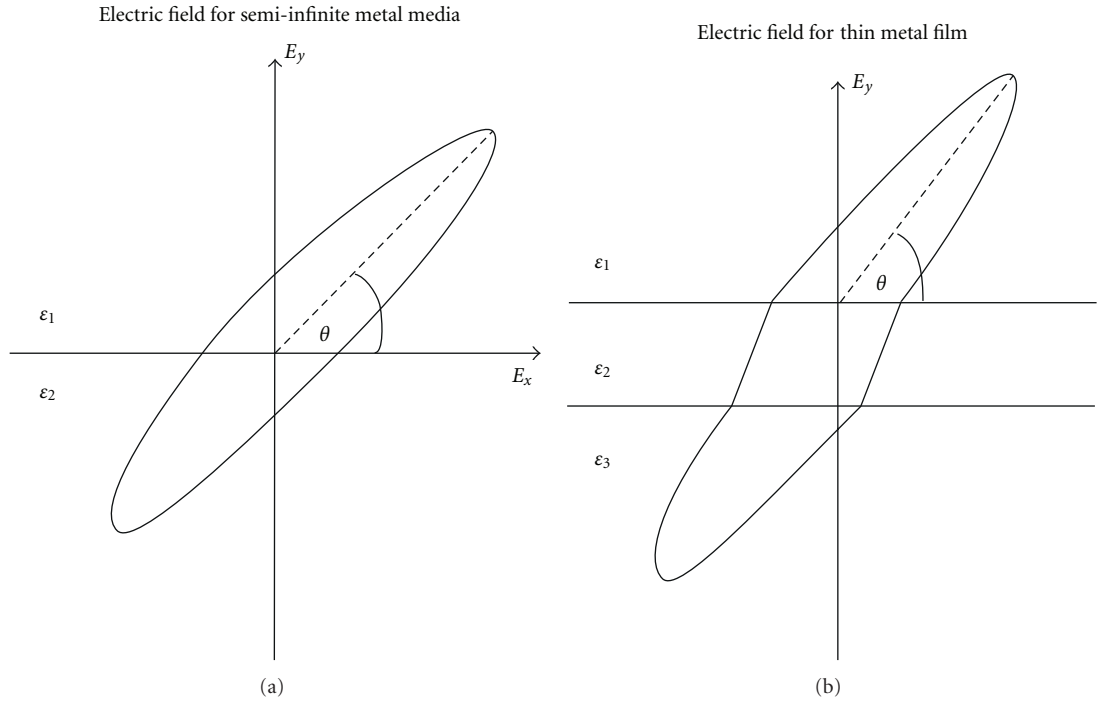

Figure 3: Polarization-like trajectory for surface plasmon modes. (a) Surface plasmon modes propagating in a semi-infinite media. (b) Surface plasmon modes propagating on a thin film.

where δ is the Dirac delta-function. The diffraction field, using the angular spectrum model is given by [11]

$$\varphi(x,y,z) = \iint_{-\infty}^{\infty} \delta(u - f(v)) \times \exp\{i2\pi(xu + yv + zp)\}\,du\,dv, \tag{9}$$

where $u = \cos\alpha/\lambda, v = \cos\beta/\lambda, p = \cos\gamma/\lambda$ are the spatial frequencies that satisfy $u^2 + v^2 + p^2 = 1/\lambda^2$; α, β, and γ are the angles that makes the wave vector with the (x,y,z)-axis; and λ is the wavelength. In Figure 4, the setup to generate the diffraction field associated with slit-shaped curves is shown.

As prototype, we describe the synthesis of two kinds of optical fields. The first one has a transmittance as boundary condition, whose geometry in frequency space is a cubic function given by

$$T(u,v) = \delta(u - v^3). \tag{10}$$

The optical field has the representation

$$\begin{aligned}\varphi(x,y,z) &= \iint_{-\infty}^{\infty} \delta(u - v^3)\exp\{i2\pi(xu + yv + zp)\}\,du\,dv \\ &= \int_{-\infty}^{\infty} \exp\left\{i2\pi\left(xv^3 + yv + z\left(\frac{1}{\lambda^2} - (v^6 + v^2)\right)^{1/2}\right)\right\}dv.\end{aligned} \tag{11}$$

The optical field presents bifurcation effects that are manifested during its propagation. To understand the amplitude

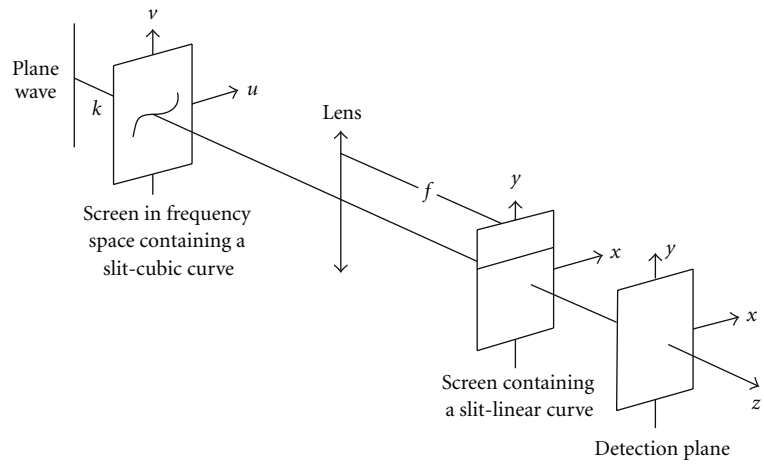

Figure 4: Schematic setup to generate the optical field associated with slit-shape curves.

distribution, we implement a kind of spatial filtering, which is obtained by placing a screen containing a linear slit on $z = 0$, whose representation is $t(y) = \delta(y-1)$. The amplitude distribution is

$$\begin{aligned}\Phi_1(x, y, z = 0) &= \delta(y-1)\int_{-\infty}^{\infty} \exp i2\pi(xv^3 + yv)\,dv \\ &= \delta(y-1)\int_{-\infty}^{\infty} \exp\left(i2\pi(xv^3 + v)\right)dv.\end{aligned} \tag{12}$$

By translating the screen to the position defined by $y = -1$, the mathematical representation for the optical field is given by

$$\begin{aligned}\Phi_2(x, y, z = 0) &= \delta(y+1)\int_{-\infty}^{\infty} \exp\left(i2\pi(xv^3 - yv)\right)dv \\ &= \delta(y+1)\int_{-\infty}^{\infty} \exp\left(i2\pi(xv^3 - v)\right)dv.\end{aligned} \tag{13}$$

The phase function represented by (12) and (13) differs in a sign, being equals along the direction defined by $v = 0$. The bifurcations effects appear when the optical field is propagating to different planes, that is, $z \neq 0$; therefore, each optical field propagates by different paths. In Figure 5(a), the experimental result in $z = 0$ plane is shown, and in Figure 5(b) the experimental result for $z \neq 0$ where the bifurcation effects become evident are presented. From these results, it can be noted that the right branch is shifted to the bottom and the left branch is shifted to the top. The entire optical field unfolds based on the structure of the transmittance function.

4. Singular Surface Plasmon Fields

Singularities for surface plasmon fields can be obtained in a way similar to that employed for the free space case, and the corresponding surface plasmon angular spectrum model is [4, 5]

$$\begin{aligned}E_1(x, y, z) &= \iint_{-\infty}^{\infty} \left(\vec{i}A(u) + \vec{j}B(u) + \vec{k}C(u)\right) \\ &\quad \times \exp(-2\pi\alpha_1 z)\exp\left(i2\pi\beta(xu + yv)\right)du\,dv,\end{aligned} \tag{14}$$

where the term $(\vec{i}A(u) + \vec{j}B(u) + \vec{k}C(u))$ represents the transmittance function in the frequency space. For a slit-shape curve, we have that the transmittance takes the form

$$T(u, v) = \left(\vec{i}a + \vec{j}b + \vec{k}c\right)\delta(u\tau(\lambda, d) - f(v)), \tag{15}$$

where (a,b,c) are the components of a constant vector and are necessary to satisfy the boundary conditions of the electromagnetic field. More details with respect to the value of the constants can be found in [4]. The scale term $\tau(\lambda, d)$ is proposed to describe the coupling between the diffraction field propagating in free space and surface plasmon fields. In Figure 6, the experimental setup to generate surface plasmon singularities is shown.

The singularities are generated by illuminating a slit-shape curve recorded on a thin metal film, whose thickness is in the order of 20–80 nm, and this allows generating long-range surface plasmon modes. The width d of the slit must be smaller than the illumination wavelength λ.

The expression for the surface plasmon diffraction field is given by

$$\begin{aligned}E_1(x, y, z) = \int_{-\infty}^{\infty} &\left(\vec{i}a + \vec{j}b + \vec{k}c\right)\exp(-2\pi\alpha z) \\ &\times \exp\left(i2\pi\beta(x\tau(\lambda, d)f(v) + yv)\right)du.\end{aligned} \tag{16}$$

Let us consider two examples. The first one is when the transmittance function contains a slit-cubic curve, given by

$$T(u, v) = \left(\vec{i}a + \vec{j}b + \vec{k}c\right)\delta\left(u\left(\frac{\lambda}{d} + i\frac{d}{\lambda}\right) - v^3\right), \tag{17}$$

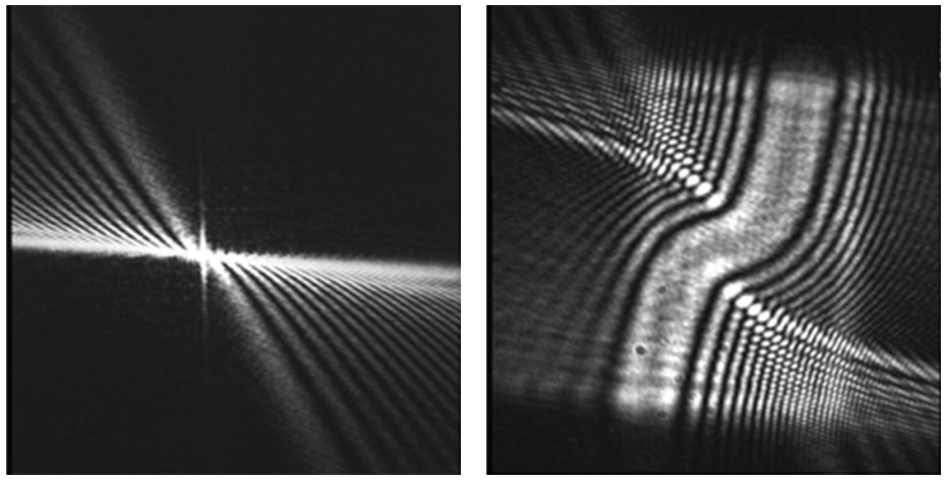

(a) (b)

Figure 5: (a) Optical field on $z = 0$ plane. This optical field is formed by two optical fields, and the spatial evolution of these two fields generates the bifurcation effects. (b) The generation of bifurcation effects. The distance between the two images along z-coordinate is approximately 1 cm; after this distance, the optical field remains practically unchanged.

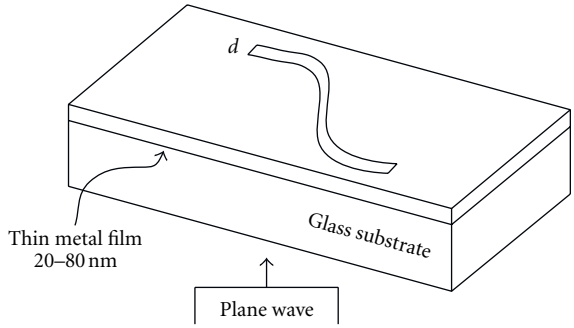

Figure 6: Experimental setup to generate surface plasmon singularities. The thin metal film contains a slit-shaped curve.

The term $\tau(\lambda, d) = (d/\lambda + i(\lambda/d))$ is proposed as an ansatz. When $d >> \lambda$, the imaginary part is very small and the optical field recovers the structure of the optical field propagating in free space. The opposite case $d << \lambda$, means that the imaginary part becomes dominant and the optical field acquires the form of evanescent waves, wich is the condition to generate surface plasmon fields. The surface plasmon diffraction field is

$$E_1(x, y, z) = \int_{-\infty}^{\infty} \left(\vec{i}a + \vec{j}b + \vec{k}c\right) \exp(-2\pi z\alpha) \times \exp\left(i2\pi\beta\left(y\tau(\lambda, d)v + x\tau(\lambda, dv)^3 f(v)^3\right)\right) dv, \tag{18}$$

having a representation of a fold caustic [2] and is similar to an Airy function [12]. The second example is when the transmittance function contains a slit-quadratic curve given by

$$T(u, v) = \left(\vec{i}a + \vec{j}b + \vec{k}c\right)\delta(v\tau(\lambda, d) - u^2), \tag{19}$$

and the surface plasmon diffraction field is

$$E_1(x, y, z) = \int_{-\infty}^{\infty} \left(\vec{i}a + \vec{j}b + \vec{k}c\right)\delta(v\tau(\lambda, d) - u^2) \times \exp(-2\pi\alpha z)\exp\left(i2\pi\beta(yv + xu)\right) du. \tag{20}$$

The amplitude distribution must satisfy the Helmholtz equation, which means that the spatial frequencies must satisfy $\beta^2(u^2 + v^2) - \alpha^2 = 1/\lambda^2$. By substituting this expression in the integral representation and using the paraxial approximation, the amplitude function acquires the form

$$E_1(x, y, z) = \int_{-\infty}^{\infty} \left(\vec{i}a + \vec{j}b + \vec{k}c\right)\delta(v\tau(\lambda, d) - u^2)\exp(-2\pi\alpha z) \times \exp\left(i2\pi\beta\left[y\left(\frac{1}{\lambda\beta} + \frac{\lambda\beta}{2}(\alpha^2 - u^2)\right) + xu\right]\right) du,$$

$$E_1(x, y, z) = \int_{-\infty}^{\infty} \left(\vec{i}a + \vec{j}b + \vec{k}c\right)\exp(-2\pi\alpha z) \times \exp\left(i2\pi\beta\left[y\left(\frac{1}{\lambda\beta} + \frac{\lambda\beta}{2}\left(\alpha^2 - \frac{u^4}{\tau^2}\right)\right) + x\frac{u^2}{\tau}\right]\right) du. \tag{21}$$

In Figure 7, we show the computer simulation. At this point, it is convenient to compare (9) with (16). In both cases, the boundary conditions are described in the x-y plane. However the phase terms in each case are different, having a decreasing exponential function for plasmon fields and a complex dependence for free-space propagation. This means

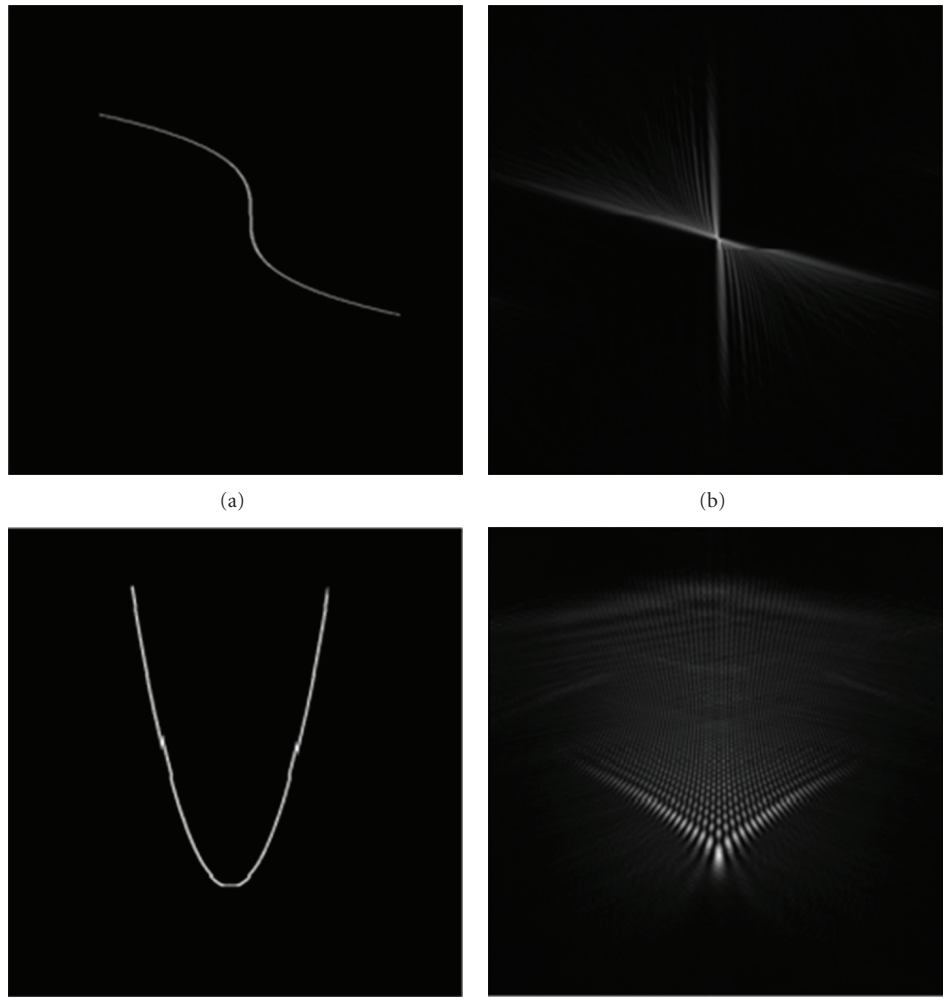

Figure 7: Front view of the metal surface. The illumination is incident from the back of the screen. (a) The screen containing a slit-cubic curve recorded on a thin metal film. (b) The surface plasmon diffraction field and its singular region. (c) Transmittance containing a parabolic curve and (d) singularity associated with this transmittance.

that the bifurcation effects must appear perpendicular to the plane that contains the slit-shaped curve; consequently, the plasmon singularities have a stationary character.

Finally, we remark that the phase function in (18) and (21) has the structure of a catastrophe function [2]. This means that the singularities correspond to the curvature center of the slit curve [6], and has a stationary character, generating charge redistribution given by $\nabla \cdot E_{1,2} = \rho/\varepsilon_{1,2}$, where the electrical field can be represented as

$$\begin{aligned} E(x,y,z) &= \int_{-\infty}^{\infty} \vec{\xi} \exp(-2\pi\alpha z) \\ &\quad \times \exp\big(i2\pi\beta[\text{germ function}(\nu) \\ &\qquad + \text{perturbation function}(\nu,m,n)]d\nu\big), \end{aligned} \tag{22}$$

where m, n are parameters related with the curvature centers. The generic physical properties associated to the singularities of surface plasmon fields can be obtained from this representation.

5. Conclusions

We described the synthesis of surface plasmon singularities by analyzing the spatial evolution of the surface plasmon field emerging from a slit-shaped curve. The singularities can be easily understood by considering that they are generated by an envelope of a set of normal trajectories emerging from each point on the boundary condition. The geometry generated by the envelope of trajectories satisfies a nonlinear partial differential equation, and the surface plasmon singularity generates a charge distribution; for this reason, the singularities offer application as surface plasmon tweezers. This can be implemented by depositing micronano/particles

on the metal surface, illuminating with different frequencies; we can generate a set of plasmon singularities inducing tunable resonance effects. These results and its potential applications will be presented in a forthcoming paper.

References

[1] V. I. Arnold, *Singularities of Caustics and Wave Fronts*, Kluwer Academic, 1990.

[2] M. V. Berry and C. Upstill, "Catastrophe optics: morphologies of caustics and their diffraction patterns," in *Progress in Optics*, E. Wolf, Ed., vol. 18, North-Holland, 1980.

[3] Y. S. Kivshar and E. A. Ostrovskaya, "Optical vortices: folding and twisting waves of light," *Optics and Photonics News*, vol. 12, no. 4, pp. 24–29, 2001.

[4] G. Martínez Niconoff, P. Martínez Vara, J. Munoz-Lopez, J. C. Juárez-Morales, and A. Carbajal-Dominguez, "Partially coherent surface plasmon modes," *Journal of the European Optical Society*, vol. 6, p. 52, 2011.

[5] G. Martinez Niconoff, J. A. Sanchez-Gil, H. H. Sanchez, and A. P. Leija, "Self-imaging and caustics in two-dimensional surface plasmon optics," *Optics Communications*, vol. 281, no. 8, pp. 2316–2320, 2008.

[6] G. Martinez-Niconoff, J. Carranza, and A. Cornejo-Rodriguez, "Caustics of diffraction fields," *Optics Communications*, vol. 114, no. 3-4, pp. 194–198, 1995.

[7] G. Martínez-Niconoff, J. Muñoz-Lopez, and E. Méndez-Martínez, "Description of phase singularities and their application to focusing design," *Journal of the Optical Society of America A*, vol. 18, no. 9, pp. 2089–2094, 2001.

[8] M. S. Sosskin and M. V. Vasnetsov, "Singular Optics," in *Progress in Optics*, E. Wolf, Ed., vol. 42, North-Holland, 2001.

[9] L. Elgoltz, *Differential Equations and Variational Calculus*, Mir, Moscow, Russia, 1977.

[10] F. Papoff and R. Zambrini, "Convective instability induced by nonlocality in nonlinear diffusive systems," *Physical Review Letters*, vol. 94, no. 24, Article ID 243903, 4 pages, 2005.

[11] J. P. Goodman, *Introduction to Fourier Optics*, McGraw-Hill, 2000.

[12] W. Liu, D. N. Neshev, I. V. Shadrivov, A. E. Miroshnichenko, and Y. S. Kivshar, "Plasmonic Airy beam manipulation in linear optical potentials," *Optics Letters*, vol. 36, no. 7, pp. 1164–1166, 2011.

Hindawi Publishing Corporation
International Journal of Optics
Volume 2012, Article ID 146396, 12 pages
doi:10.1155/2012/146396

Research Article

Plasmonic Bandgaps in 1D Arrays of Slits on Metal Layers Excited by Out-of-Plane Sources

Roberto Marani, Marco Grande, Vincenzo Petruzzelli, and Antonella D'Orazio

Dipartimento di Elettrotecnica ed Elettronica, Politecnico di Bari, Via E. Orabona 4, 70125 Bari, Italy

Correspondence should be addressed to Antonella D'Orazio, dorazio@poliba.it

Received 28 March 2012; Accepted 16 May 2012

Academic Editor: Zhaolin Lu

Copyright © 2012 Roberto Marani et al. This is an open access article distributed under the Creative Commons Attribution License, which permits unrestricted use, distribution, and reproduction in any medium, provided the original work is properly cited.

We analyze the effective opening of finite bands of inhibited transmission in realistic systems excited by actual out-of-plane sources. We first observe how the excitation of surface plasmon polaritons in one-dimensional arrays of metal slits depends on the angle of incidence of the source field. Then, the well-known grating-coupling equation is revised in order to find an asymmetric structure with equivalent parameters which, under perfectly normal excitation, is able to exhibit surface plasmon polariton modes at the same wavelengths of the original structure which undergoes a nonorthogonal incidence of the light. In this way we demonstrate through finite-element simulations that a realistic system, probed by a source beam in a finite light-cone, can be effectively decomposed in several equivalent systems with different physical and geometrical parameters, with results in the enlargement of the theoretically expected punctual minimum of transmission.

1. Introduction

In the last years, the excitation of collective oscillations of free electrons over metal interfaces has been deeply investigated in literature since it allows the successful control of light in terms of localization and enhancement of electromagnetic fields. As already known, the free-electron oscillations can assume several forms, ranging from localized surface dielectric oscillations on metal nanoparticles (localized surface plasmons, LSPs) to freely propagating electron density waves on metal surfaces (surface plasmon polaritons, SPPs). Surface plasmons show unique properties when they propagate over metal gratings and interact with free waves in the dielectric surroundings. The results of the fundamental research in the area of plasmonics have demonstrated that SPPs and LSPs can be exploited for many potential applications residing in sensing [1–5], light manipulation [6, 7] and emission [8–10], energy conversion [11–13], and optical nanoantennas [14, 15], just to mention a few.

Many researchers have proved that under particular conditions many effects of enhanced and inhibited transmission emerge. For instance, subwavelength apertures carved on metal layers provide extraordinary optical transmission (EOT) caused by the resonant excitation of SPP modes over the input and the output interfaces between the metal and the dielectric [16, 17]. The in-phase cooperation among modes allows light beams impinging far from the apertures to assist the spectral response with results in normalized-to-area transmissions higher than one. Moreover, a second mechanism of resonance starts arising when the input wavelength is able to excite waveguide modes within the slits which can be exploited to carry energy within the aperture along a direction perpendicular to the grating wavevector, but in the grating plane (gap plasmon, GP) [18]. One-dimensional gratings allow also the existence of minima of transmission, whose properties are directly linked to the geometrical and physical parameters of the whole systems [19]. Moreover, this resonant behavior, due to the formation of propagating SPP modes over the metal-dielectric interface, can be found even in two-dimensional arrays of metal objects [20]. Without loss of generality, the incident electromagnetic field can be decoupled in two components along the grating directions, each one experiencing its own periodicity, so that a two-dimensional array can be simplified in two different one-dimensional gratings, depending on the polarization of the source.

All the considerations made for arrays of slits face with practical problems due to the splitting of surface modes when the system is illuminated by a source with nonorthogonal incidence. As demonstrated with the experimental analysis in [4], whenever a realistic measurement is performed over arrays of metal objects illuminated by white light lamp, the resulting resonance giving inhibited transmission is constituted by a weighted superposition of resonances in a cone of allowed angles of incidence depending on the numerical aperture of the microscope objective used in the optical setup. In other words the expected single resonance broadens since many SPP modes are excited over the metal-dielectric interface, giving rise to an enlargement of the plasmonic bandgap. This feature is useful for applications in thin-film solar cell technology, where such structures are required to act as broadband reflectors for source field impinging with arbitrary incidences.

In this paper we give evidence to the formation of an effective plasmonic bandgap in an array of sub-wavelength slits on a metal layer excited by an out-of-plane actual source. In order to achieve this goal, we start from the analysis of the theoretical effects of the presence of a tilted source on the excitation of SPP modes. Then we define an equivalence of structures able to convert such modes in spatially separated SPP resonances, with the same spectral properties of the original ones, but excited through the application of an orthogonal source. Since the equivalent parameters depend on the angle of incidence of the source field of the original structure, we observe that a practical system, excited by an input beam in a finite light-cone, has a spectral behaviour comparable to the one obtained by a superposition of results coming out by the investigation of several equivalent structures probed by perfectly orthogonal sources. Thus, we demonstrate the effective opening of a finite bandgap in actual systems, although a single minimum of transmission is expected.

The paper is organized as follows: in Section 2 we will show the basis of the analysis of one-dimensional arrays of sub-wavelength slits on metal layers in both symmetric and asymmetric configurations and under different angles of incidence; then, Section 3 will be dedicated to the definition of the parameters of the equivalent structure, together with a comparison of results with those of the original arrangement; conclusions and remarks will be finally reported in Section 4.

2. One-Dimensional Arrays of Slits

A sketch of the structure considered in this paper is reported in Figure 1. It consists of an infinite one-dimensional array of slits carved on a gold thin film. As shown in Figure 1, the geometrical parameters defining the structure are the metal thickness w, the grating period p, and the width of the strips l, whereas a is the extension of the sub-wavelength gaps, easily equal to the difference between the grating period and the strips width. In this first part of analysis, the structure is assumed to be placed in a homogeneous environment made of air.

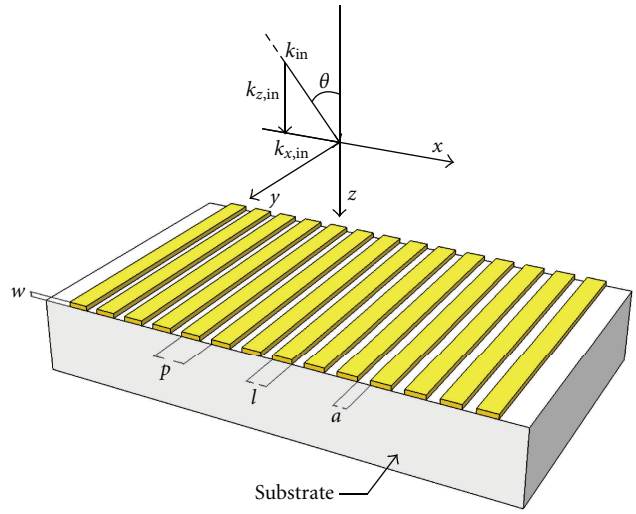

Figure 1: Sketch of an infinite one-dimensional array of metal strips, $(l \times w)$ sized, p is the period of the array, and a is the sub-wavelength extension of the slits.

Maxwell's equations for the propagation of electromagnetic waves have been solved via a finite-element commercial code [21] applied on a computing domain bounded by periodic boundary conditions along the x-direction in Figure 1 and perfectly matched layers in the z-direction. Since Maxwell's equations are rigorously solved depending on the spatial sampling of the window, we impose a maximum size of each subdomain at most equal to the smallest wavelength in each medium divided by a term of 15, whereas the sub-wavelength apertures are sampled with a maximum spatial step of 5 nm to guarantee a sufficient number of elements to model the discontinuities.

Gold regions are then represented through a Drude model assisted by two Lorentz oscillators to fit the experimental data reported in [22]:

$$\varepsilon_m(\omega) = \varepsilon_\infty - \frac{\omega_D^2}{\omega^2 + j\omega\gamma_D} - \sum_{k=1}^{2} \frac{\delta_k \omega_k^2}{\omega^2 - \omega_k^2 + 2j\omega\gamma_k}, \quad (1)$$

where the high-frequency complex dielectric constant of the metal ε_∞ is 5.398, the plasma frequency ω_D and the collision frequency γ_D of the Drude model are $1.398 \cdot 10^{16}$ and $1.033 \cdot 10^{14}$ rad/s, respectively. The parameters describing the contribution of each Lorentz oscillator are the amplitude δ_k, the resonant angular frequency ω_k, and the damping constant γ_k, $k = 1, 2$, which are set according to [23]: $\delta_1 = 0.681$, $\omega_1 = 4.274 \cdot 10^{16}$ rad/s, $\gamma_1 = 4.353 \cdot 10^{14}$ rad/s, $\delta_2 = 1.861$, $\omega_2 = 5.225 \cdot 10^{16}$ rad/s and $\gamma_2 = 6.608 \cdot 10^{14}$ rad/s.

The description of the numerical setup is completed by the definition of the excitation, which is a collection of CW plane waves in the wavelength range between 500 and 1000 nm. This source field emerges from the top boundary of the computing cell with the wavevector $\mathbf{k}_{in}$ depicted in Figure 1, which is tilted of an angle θ with respect to the z-axis. Moreover, the polarization vector is assumed to be parallel to the grating wavevector in order to excite SPPs

over the corrugated interfaces. The resulting fields are then collected on transmission and reflection line monitors placed on the bottom and on the top of the domain, 3 μm far from the array, to compute the integral of the Poynting vector flowing through them.

2.1. Orthogonal Incidence. The exhaustive comprehension of the behavior of the free-standing system depicted in Figure 1 can be easily obtained by giving a first look into the transmission and reflection diagrams. Here the geometrical parameters are $w = 200$ nm, $l = 550$ nm, and $p = 600$ nm. Moreover, the simulation has been performed by considering an input pulse illuminating orthogonally the whole system that is, the input wavevector is perpendicular to the grating plane. Transmission and reflection diagrams are reported in Figure 2(a).

It is important to underline that these spectra result by the application of periodic boundary conditions, that is, considering an infinite array of slits. Although this behavior is merely numerical, it is confirmed by experiments since it has been demonstrated that a number of sub-wavelength slits higher than 6 is enough to get the saturation of transmission to its threshold value [24]. The analysis of Figure 2(a) gives evidence to three distinctive regions of the diagram:

(i) a first region at higher wavelengths (800 nm), or lower frequencies where transmission shows a high maximum,

(ii) a deep of transmission localized around 650 nm corresponding to the center of a dip of transmission,

(iii) a sharp peak of transmission at lower wavelengths, or higher frequencies, around 600 nm.

In other words, the presence of a periodicity seems to induce a dip for the light impinging orthogonally on the metal grating as occurs in photonic bandgap structures. Then, this minimum separates two well-defined states. The first state at lower energies ($\lambda = 800$ nm) presents the character of a first-order Fabry-Pérot (FP) resonance acting in a cavity region bounded by two metal walls, defining the aperture, and two dielectric discontinuities between the homogeneous background and the metal-insulator-metal region [19]. The second resonant state of maximum of transmission at higher energies ($\lambda = 611$ nm) is due to the presence of two SPP modes propagating over both the input and the output interfaces, giving rise to extraordinary optical transmission (EOT) [17]. In this case the input plane wave excites first a SPP mode over the input interface which couples with the symmetric SPP mode over the output interface through the array of slits. Finally SPPs start cooperating to the radiation of an outgoing plane wave with the same momentum, that is, wavelength, of the incident one. It is worth noting that the EOT state suffers the presence of absorption within gold, which already occurs around 600 nm. For this reason this choice of parameters, that is, $w = 200$ nm, $p = 600$ nm, and $l = 550$ nm, does not give evidence to a so-well defined maximum of transmission, which would be clear for an equivalent array of slits made on a silver film. Moreover, although this preliminary study is performed on a one-dimensional array, the same behavior can be found also in 2D arrays of gold rectangular patches [20].

More interesting for our purposes is the state of minimum of transmission at $\lambda = 627.5$ nm. The inspection of Figure 2(b), which maps the absolute value of the total magnetic field at this wavelength, reveals that the electromagnetic energy is totally localized on the input interface, where a SPP mode is excited, so that the field is not transmitted to the output. The coupling mechanism between the incident light and the SPP resonating over the grating originates leaky modes, standing over the interface, which reradiate light to the reflection region with effects in the minimum of inhibited transmission through the aperture. It is of relevance to observe that energy is not flowing along the surface, as clearly shown by the inspection of the Poynting vector in Figure 2(b), thus demonstrating the stationary character of this SPP wave under the illumination of an infinite-extended plane wave.

From an analytical point of view, this minimum state occurs whenever the incident wavelength excites the SPP of the unperturbed air-metal interface, that is, for the first resonant order and under normal incidence:

$$\lambda_{\mathrm{SPP}} = p, \tag{2}$$

where λ_{SPP} is the SPP wavelength given by the dispersion relation of SPPs propagating over a flat interface between the metal and the dielectric. The validity of this formulation is further proven by the initial hypothesis of sub-wavelength apertures, which does not alter significantly the dispersion relation of the SPP propagating on the flat metal layer.

At this stage it is important to point out that each dielectric-metal interface acts independently of the other one since the thickness of the metal layer is much higher than the skin depth of gold at the wavelength of interest. This statement can be proven by the examination of Figure 3(a), which details the spectral behavior of the same array of slits placed over a silica substrate with a refractive index n_{sub} equal to 1.45.

In this case it is clear that the matching condition in (2) is individually verified at the input and the output interfaces which are made of the same metal, but of different dielectrics, namely, air and silica. In particular, the minima occurs at $\lambda = 626.5$ nm, almost equal to the one obtained in the previous symmetric case, and $\lambda = 901.5$ nm, which corresponds to the excitation of a SPP mode on the gold-silica interface. This result is also confirmed by Figures 3(b) and 3(c) which plot the xz-section of the profile of the absolute value of the total magnetic field.

The only difference between the two minima of transmission resides on the presence of electromagnetic energy within the sub-wavelength aperture. With reference to Figure 3(c), the operation wavelength of the input field is no longer able to excite a resonant SPP mode over the air-gold interface. The field penetrates through the apertures and coherently excites a SPP mode over the gold-silica interface. Unlike the case in Figure 3(b), where the excitation of a resonant SPP over the first interface cuts off the waveguide mode within the

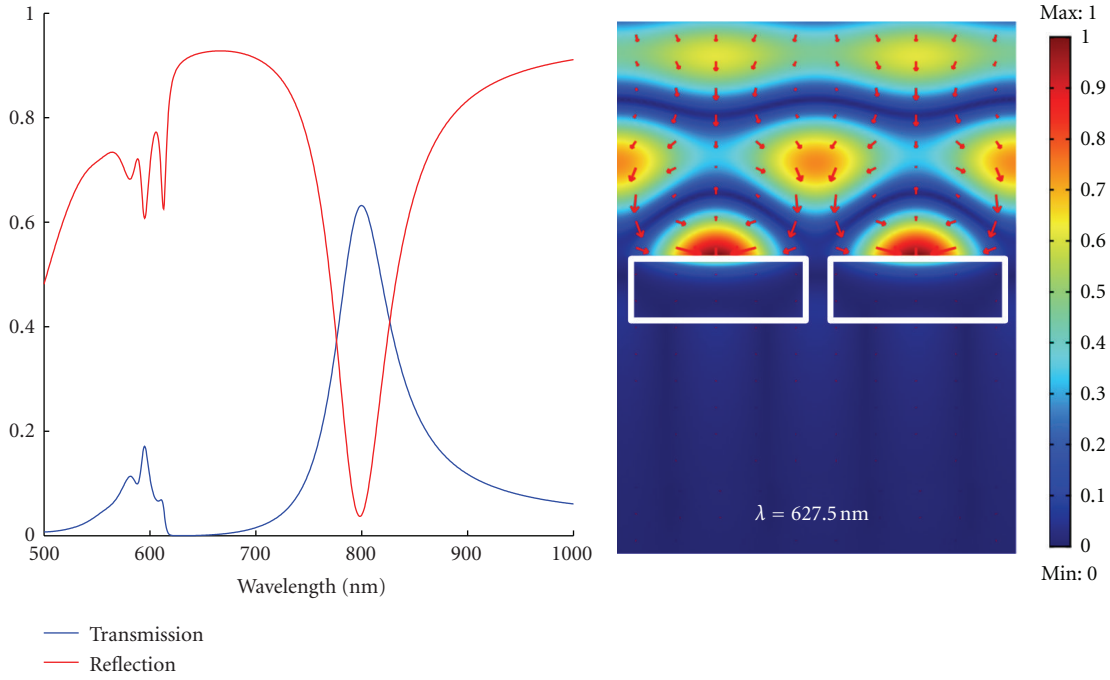

(a) (b)

Figure 2: (a) Transmission and reflection diagrams of the free-standing array of metal stripes with $w = 200$ nm, $p = 600$ nm, $l = 550$ nm. (b) Map of the transversal section of the absolute value of the magnetic field computed at $\lambda = 627.5$ nm; red arrows display the direction of the Poynting vector.

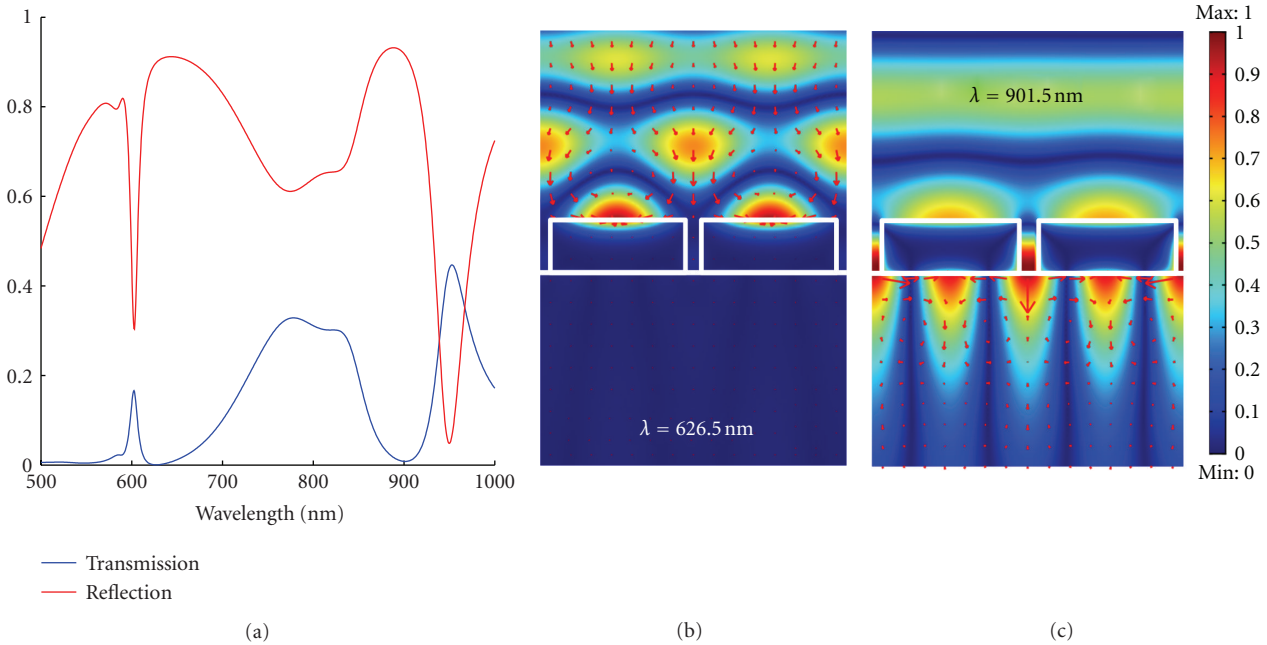

(a) (b) (c)

Figure 3: (a) Spectral response of an array of slits on the gold layer ($w = 200$ nm, $p = 600$ nm, $l = 550$ nm) placed over a silica substrate ($n_{sub} = 1.45$). Profile of the absolute value of the magnetic field computed at (b) $\lambda = 626.5$ nm and (c) $\lambda = 901.5$ nm; red arrows express the direction of the Poynting vector.

aperture, for $\lambda = 901.5$ nm the presence of electromagnetic energy in this region affects the transmission, which does not reach completely zero. This behavior is even more evident by looking at the direction of the Poynting vector in Figure 3(c), where the lengths of the arrows coming out from the apertures are higher than those related to the resonating SPPs over the output interface.

2.2. Nonorthogonal Incidence. The dependence of the angle of incidence θ on the position of the minimum of transmission is of crucial importance in the spectral behavior of the proposed structure. Equation (2) gives the condition for the excitation of SPP via grating coupling only in the case of orthogonal incidence and for a first order of resonance. If the light impinges with an angle θ (see Figure 1), the matching condition between wavevectors gives [25]

$$k_{\mathrm{SPP}} = k_0 \sin\theta \pm \Delta k_x, \tag{3}$$

where $\triangle\ kx = mG = m \cdot 2\pi/p$ gives the contribution of any perturbation to the smooth metal-dielectric interface mediated by the apertures. Equation (3) can be rearranged to highlight the position of the minimum of transmission. In particular $\lambda_{\mathrm{res},m}$, that is, the free-space wavelength at which the external light excites a SPP mode on the metal grating, can be deduced using the following formulation:

$$\lambda_{\mathrm{res},m} = \pm\frac{p}{m}\left(\sqrt{\frac{\varepsilon_d \varepsilon_m(\lambda_{\mathrm{res},m})}{\varepsilon_d + \varepsilon_m(\lambda_{\mathrm{res},m})}} - \sqrt{\varepsilon_d}\sin\theta\right). \tag{4}$$

The most important effect of the presence of a tilted light source resides in the splitting of the minimum of transmission in two different minima, which are very sensitive to the variation of this angle. An example of application of (4) to the case of an infinite array of slits on gold is reported in Figure 4. Here the minimum position is presented for the first two orders. Moreover the periodicity of the array of slits has been chosen equal to 700 nm in order to give clear evidence to the presence of a minimum of transmission for the wavelengths ranging between 500 and 1000 nm. In addition, the structure is placed in a homogeneous medium, namely air, in order to keep the effect of the variation of the angle of incidence apart from the effect of a nonhomogeneous environment due to the presence of a dielectric substrate.

Since two different SPP modes decouple on the input interface of the metal grating, each mode has an effective refractive index, depending on the corresponding wavelength of excitation of the mode, satisfying (4). In particular

$$n^{\pm}_{\mathrm{SPP},m}(\theta) = m\frac{\lambda^{\pm}_{\mathrm{res},m}(\theta)}{p}. \tag{5}$$

Although this representation of the SPP mode is always valid, n_{SPP} can range between well-defined limits. The lowest limit is due to the presence of ohmic losses within gold, since $\lambda^{-}_{\mathrm{res},m}$ often occurs in the bulk-absorption region of the gold itself when θ increases. On the contrary, $n^{+}_{\mathrm{SPP},m}$ can reach asymptotically the condition $n_{\mathrm{SPP}}(\theta = 90\circ) = 2 \cdot n_{\mathrm{SPP}}(\theta = 0)$. This has results in the in-plane excitation of SPP modes which undergoes the well-known theory of the Bragg reflectors, forming the basis of the photonic crystal technology [26, 27].

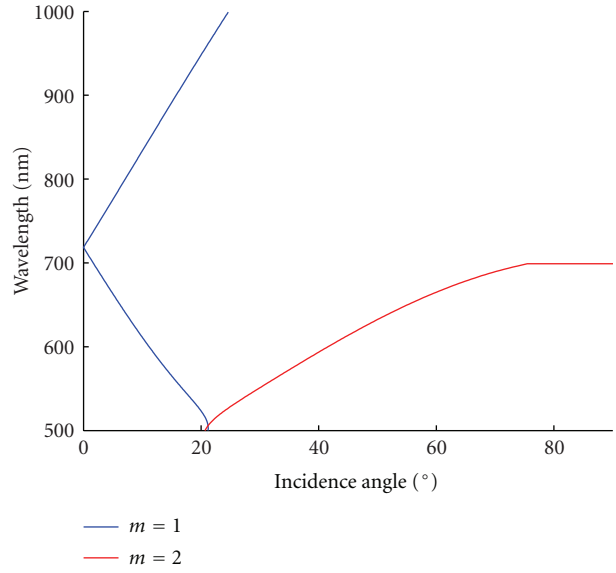

Figure 4: Spectral position of the first two orders of the grating-coupling state as a function of the angle of incidence θ of the source field. The period of the array is now equal to 700 nm.

Transmission and reflection diagrams computed on line monitors parallel to the metal-dielectric interfaces are reported in Figure 5. Here the gold film is 150 nm thick, the array of slits has a period of 700 nm, and the width of the sub-wavelength apertures is 50 nm. Moreover, we assume to probe the structure applying a plane wave with an infinite-extended wavefront, with angles of incidence equal to 0, 5°, 10°, and 15°, respectively.

The excitation of two modes whose spectral positions depend on the incidence angle has effects in the formation of two different dips of transmission along the z-axis. The relative distance between these modes increases with the angle θ, following the behavior displayed in Figure 4, down to the absorption region of gold, which is almost reached for $\theta = 15°$.

The xz-profile of the absolute value of the total magnetic field is shown in Figure 6. In this case we consider the same structure discussed above ($p = 700$ nm, $w = 150$ nm, $l = 650$ nm) with an angle of incidence $\theta = 10°$ (for its definition in the reference system see the inset of Figure 6.

A first look to Figure 6 reveals that these plots are qualitatively comparable with that in Figure 2(b), valid in the case of orthogonal incidence over a free-standing array of slits with period equal to 600 nm. In both cases the absolute value of the magnetic fields resembles a first order of resonance, since only one maximum of the electromagnetic field is always localized in the center of the metal elements.

Different considerations have to be carried out to explain the actual meaning of the direction of the Poynting vectors. Here the two SPP modes, due to the presence of a nonzero

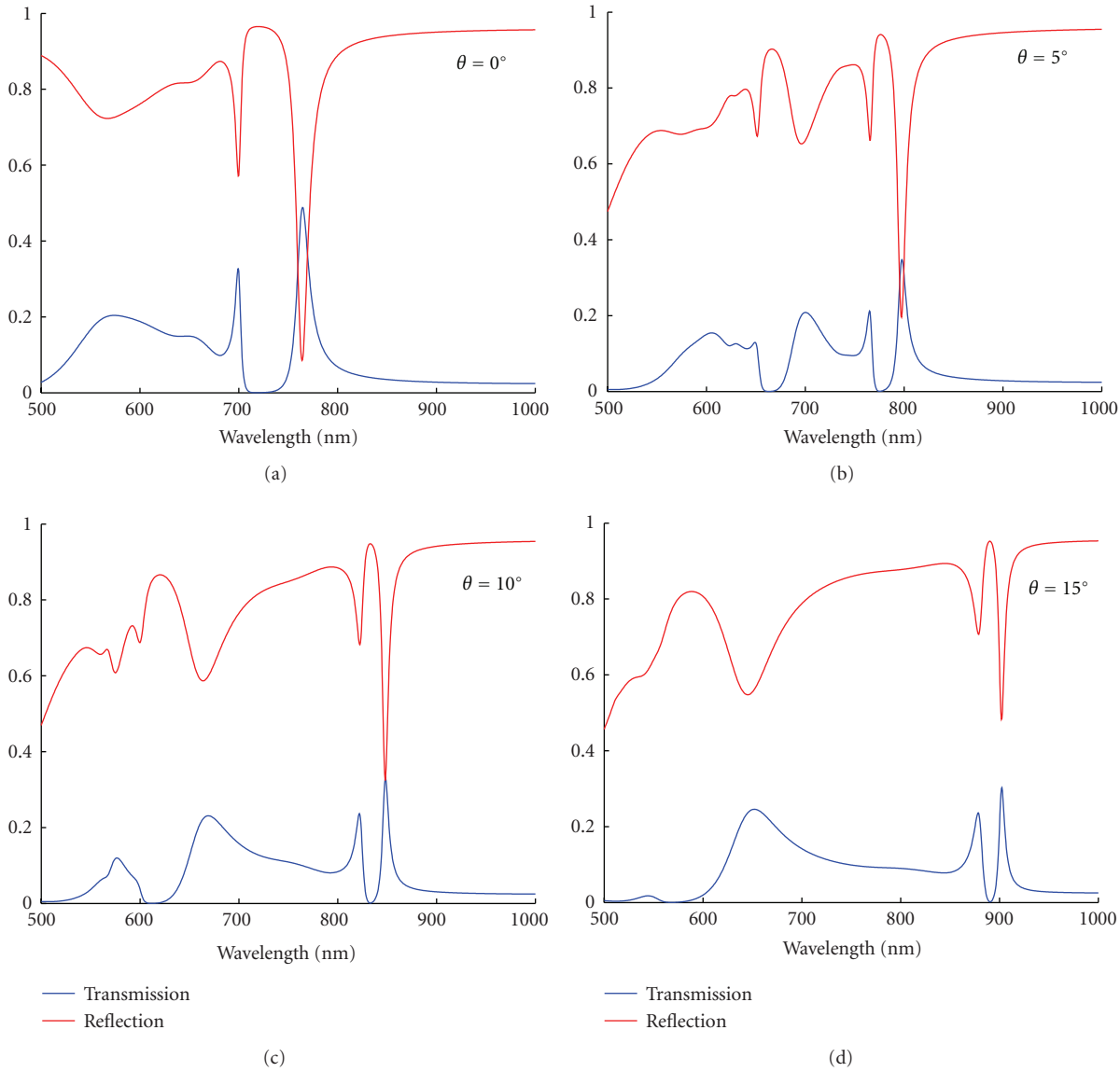

Figure 5: Parametric analysis of the transmission and the reflection diagrams of a free-standing array of gold strips computed for (a) $\theta = 0°$, (b) $\theta = 5°$, (c) $\theta = 10°$, and (d) $\theta = 15°$. The geometrical parameters are $p = 700$ nm, $w = 150$ nm, and $l = 650$ nm.

angle of incidence, are counterpropagating over the metal-dielectric interface. The up mode at $\lambda = 833.61$ nm has an opposite direction with reference to the x-component of the exciting wavevector $\mathbf{k}_{\text{in}}$. Taking this mode to the up edge of the range of existence of $n^{+}_{\text{SPP},1}$, that is, for in-plane excitation ($\theta = 90°$), we will find that the SPP is completely reflected accordingly to Bragg's law. As known in SPP bandgap structures [28], the operation wavelength in the medium has to be substituted by the SPP wavelength coming out by the dispersion equation of the SPP propagating over the smooth metal-dielectric interface. Quantitatively, this condition occurs at $\lambda^{+}_{\text{res},1}(\theta = 90°) = 1403.5$ nm. At the same time, the down mode propagates with the same direction of the x-component of $\mathbf{k}_{\text{in}}$, opposite to that of the up mode. As observed previously, the lowest edge for the propagation of this mode, that is, at $\theta = 90°$, falls down to the absorption region of the metal and thus cannot be estimated with accuracy.

3. Equivalent Structure

Once the physics below the excitation of SPPs over a metal gratin has been explained, we go on with the analysis of realistic systems, invoking an equivalence of structures to better display that the punctual minima of transmission broaden to actually form an effective stop band for light.

With reference to Figure 7, the original structure, illuminated by a nonorthogonal light beam, is studied through an equivalent structure with effective period and substrate,

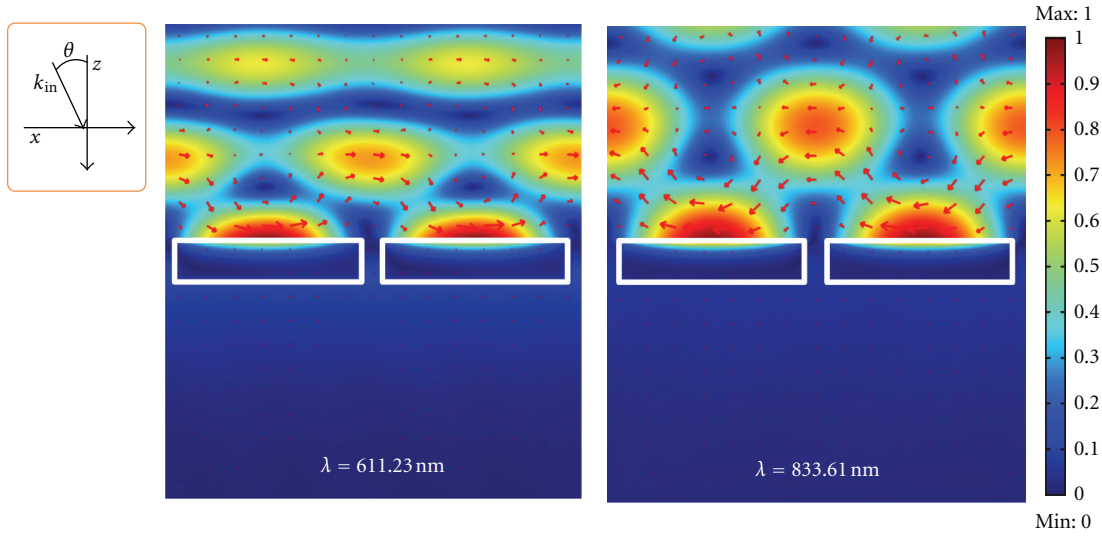

FIGURE 6: Absolute value of the magnetic field for the structure described in Figure 5 with $\theta = 10^\circ$ computed at (a) $\lambda = 611.23$ nm and (b) $\lambda = 833.61$ nm. Red arrows in both plots express the Poynting vector direction.

but orthogonally excited. The choice of the equivalent parameters depends on the couple of values (m,θ) of the original system: the effective period p_{eq} is chosen to reproduce the SPP excitation of the mth down mode at $\lambda^{-}_{res,m}(\theta)$, whereas the effective substrate is found to model the effect of the mth up mode at $\lambda^{+}_{res,m}(\theta)$. In this way the two modes due to the non-zero angle of incidence behave as two SPP modes resonating over the two interfaces of the asymmetric structure: the down mode at $\lambda^{-}_{res,m}(\theta)$ over the metal-cover interface and the up mode at $\lambda^{+}_{res,m}(\theta)$ over the metal-substrate interface. In this hypothesis, it is clear that the validity of the equivalence showed in Figure 7 is guaranteed at the wavelengths where the up and down modes are excited for a particular value of the angle of incidence θ, that is, at $\lambda^{-}_{res,m}(\theta)$ and $\lambda^{-}_{res,m}(\theta)$. For convenience we suppose to cover the equivalent structure with air.

Since the expression of the equivalent period is merely dependent on $\lambda^{-}_{res,m}(\theta)$, we can make (2) more explicit and merge this result to (4), thus obtaining

$$\frac{p_{eq}}{m} = \frac{\lambda^{-}_{min,m}(\theta)}{\sqrt{\varepsilon_m\left(\lambda^{-}_{min,m}(\theta)\right)/\left(1+\varepsilon_m\left(\lambda^{-}_{min,m}(\theta)\right)\right)}}. \quad (6)$$

In a similar way, but referring to the metal-substrate interface of a p_{eq}-periodic grating, we can find the analytical expression of the dielectric function of the equivalent substrate:

$$\varepsilon_{d,eq} = \frac{\varepsilon_m\left(\lambda^{+}_{min,m}(\theta)\right)\left(m\left(\lambda^{+}_{min,m}(\theta)/p_{eq}\right)\right)^2}{\varepsilon_m\left(\lambda^{+}_{min,m}(\theta)\right) - \left(m\left(\lambda^{+}_{min,m}(\theta)/p_{eq}\right)\right)^2}. \quad (7)$$

It is important to underline that this expression can be applied for each wavelength of the range of interest,

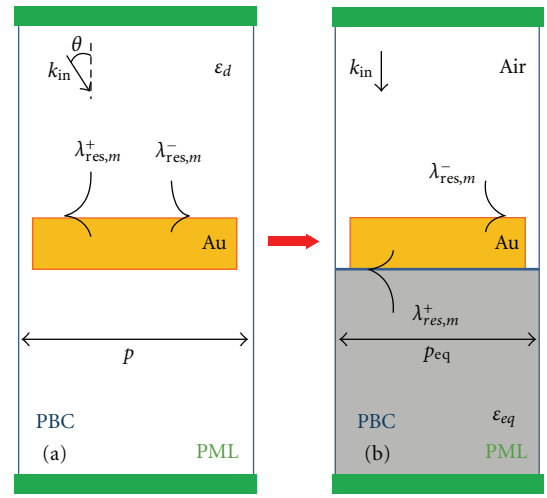

FIGURE 7: Sketch of (a) the original array of slits and (b) the corresponding equivalent structure with orthogonal excitation. SPP modes are also reported on the proper metal-dielectric interfaces.

since it does not interact with the equivalent down mode resonating over the metal-cover interface (see Paragraph 2.1). Nevertheless, it only has a physical meaning for values of λ close to that one assumed by $\lambda^{-}_{res,m}(\theta)$ for a particular θ value. Moreover, the formulations (6) and (7) do not include the metal thickness, since it does not alter considerably the SPP resonance over the grating when the thickness itself is much larger than the skin depth of metal, that is, as in the presented cases.

The analytical formulation of the parameters involved in the model of the equivalent system allows the detailed extraction of the actual values to be implemented. Table 1

Table 1: Resonant wavelengths corresponding to the excitation of the SPP modes over the air-metal interface of the array of gold stripes with $p = 700$ nm and corresponding parameters for the equivalent structures.

θ	$\lambda^{+}_{\mathrm{res},1}$ (nm)	$\lambda^{-}_{\mathrm{res},1}$ (nm)	p_{eq} (nm)	$\varepsilon_{\mathrm{eq}}(\theta)$
0°	718.49	718.49	700	1
5°	775.72	663.08	641.02	1.3814
10°	833.61	611.23	583.88	1.9071
15°	891.29	565.12	530.07	2.6169

reports the resonant wavelengths of the SPP modes of the first order for the cases already presented in Figure 5 and the equivalent parameters obtained by the application of (6) and (7).

The application of these parameters to the equivalent structure allows the comparison of spectra with those already exposed in Figure 5. In particular Figure 8 reports this result in terms of transmission profile for the case in which the original structure is illuminated by a light beam with an angle of incidence equal to 5°, 10°, and 15°.

Before going through the inspection of Figure 8, it is of relevance to notice that the equivalence described by (6) and (7) is suitable only in a wavelength range close to the SPP resonances, so that the comparison of diagrams is expected to show significant differences far from the resonant wavelengths of the two SPP modes. As a result, the diagrams in Figures 8(a) and 8(b) show a good agreement between SPP resonances found by the equivalent structure on those of the original one. Table 2 reports the comparison of the resonant wavelengths resulting from the analysis of the original structure and the equivalent ones with angles of incidence of the source field equal to 5°, 10° and 15°.

In particular, it is evident a good matching between the resonant wavelengths of the systems corresponding to the cases of $\theta = 5°$ and $\theta = 10°$, with a relative error smaller than 0.7%. On the other hand, Figure 8(c) gives evidence to an overestimation of the resonant wavelengths with respect to the one obtained with the original structure. The nature of this phenomenon can be found in the presence of losses induced by the metal on the down mode which raises close to the absorption band of gold. This mode only affects the expression of the equivalent period, according to (6), thus inducing an error in its model. Then, the measurement uncertainty due to high absorption interferes with the definition of the higher resonance, which depends itself on the down mode. These considerations allow us to confirm that the range of validity of θ for the proposed equivalence of structures is determined by the relative position of the down mode with respect to the absorption band of the metal, in a similar way to what noticed in the previous paragraph with reference to (5). This implies that, if perfect metals are considered, that is, any ohmic-loss mechanism is taken into account, the equivalence is always verified. Further simulations prove the equivalence of results under this hypothesis with negligible relative errors (lower than 0.06 %) for each angle of incidence.

Moreover, although this is not of interest for this paper, which is mostly focused on the excitation of SPP modes, it is important to show that the peaks of resonance of high transmission at the lowest edges of the up modes disappear in all the proposed cases. This occurrence has a physical meaning ascribable to the character of this kind of resonance. In other words, since this peak of high transmission is due to the presence of coupled SPPs propagating on both input and output interfaces with the same phase laws, it can be only found in symmetric systems [17]. The presence of an equivalent substrate cuts off this resonant mode with results in the transmission profiles.

Figure 9 maps the absolute value of the resonant magnetic field obtained by the analysis of the equivalent structure related to the case of $\theta = 10°$.

The analysis of Figure 9 highlights the different behaviors of the two resonating modes. As expected, the down mode at $\lambda^{-}_{\mathrm{res},1} = 611.23$ nm resonates as a SPP mode over the air-gold interface, inducing an efficient stop condition for the energy impinging on the grating, in a manner similar to that in Figure 6(a), valid for the original system with $\theta = 10°$. For this reason all the down modes have a depth comparable to the ones obtained by the response of the original structures, within a numerical tolerance. Conversely, the up mode changes its nature becoming a SPP mode resonating over the gold-substrate interface. As already observed in Paragraph 2.1, the excitation of a SPP mode over the output interface does not switch off the resonance within the sub-wavelength aperture, thus allowing light to reach the transmission. This aspect does not allow the achievement of the zero-transmission condition for the up mode, as comes out from Figure 8.

Another important aspect regards the direction of the Poynting vector related to the resonant modes over the two interfaces. As shown previously, the presence of a non-zero angle of incidence induces the excitation of two counterpropagating modes at different wavelengths in the original system. By looking at the red arrows in Figure 9, the energy of the SPP modes stands over the grating without a dominant flow direction. This is the result of the orthogonal excitation of the slit array which produces a stationary mode reradiating to the reflection. Nevertheless, it is important to underline that this is only due to the kind of excitation used in our numerical measurements, that is, an infinite-extended plane wave. When the source is spatially bounded, assuming, for instance, a Gaussian shape, each mode at $\lambda^{-}_{\mathrm{res},m}$ and $\lambda^{-}_{\mathrm{res},m}$ stationary resonates with the profile in Figure 9 only in the bound region effectively covered by the incidence of the input beam. Figure 10 shows the magnetic field response of the structure in Figure 9 under the application of a Gaussian-shaped input pulse able to excite the down mode at $\lambda = 611.23$ nm.

The analysis of the Poynting vector directions in Figure 10 proves that, since each of these modes is the superposition of the two counterpropagating modes, these components decouple propagating in opposite direction through the side regions. Moreover, the propagation length of such modes has been found the same of the original structure, since the main loss mechanism suffered by SPPs

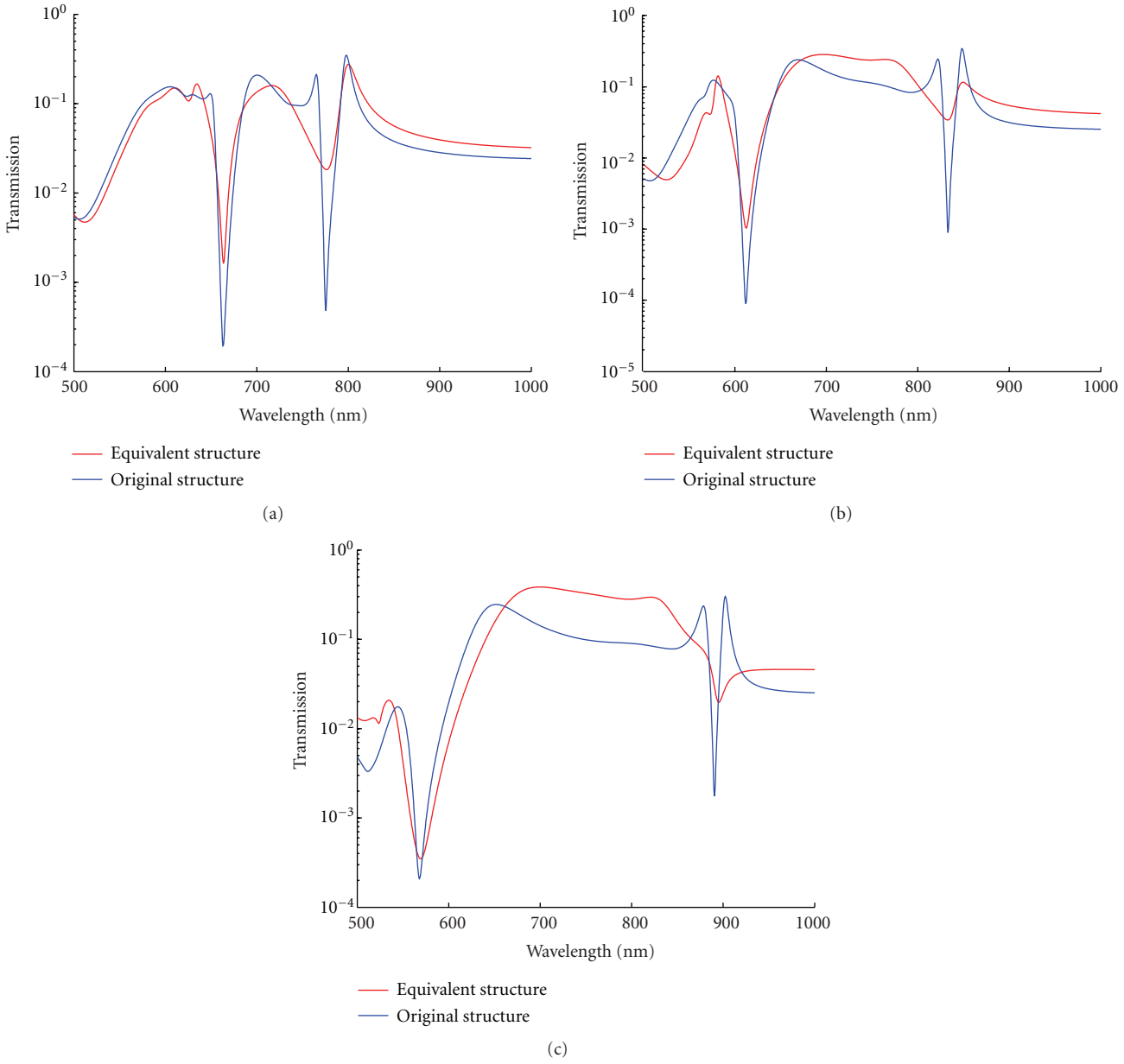

Figure 8: Blue lines report the transmission diagrams already presented in Figure 5 in logarithmic scale, whereas red lines display on the same scale the results obtained by the equivalent structures with the parameters listed in Table 1. The angles of incidence of the input light for the original arrays are (a) $\theta = 5^\circ$, (b) $\theta = 10^\circ$, and (c) $\theta = 15^\circ$.

Table 2: Comparison of the resonant wavelengths obtained by the analysis of the original structure with different angles of incidence and its equivalent counterparts.

	Original structure		Equivalent structure	
θ	$\lambda^{+}_{res,1}$ (nm)	$\lambda^{-}_{res,1}$ (nm)	$\lambda^{+}_{res,1}$ (nm)	$\lambda^{-}_{res,1}$ (nm)
5°	775.72	663.08	776.15	663.51
10°	833.61	611.23	832.78	612.36
15°	891.29	565.12	895.42	569.08

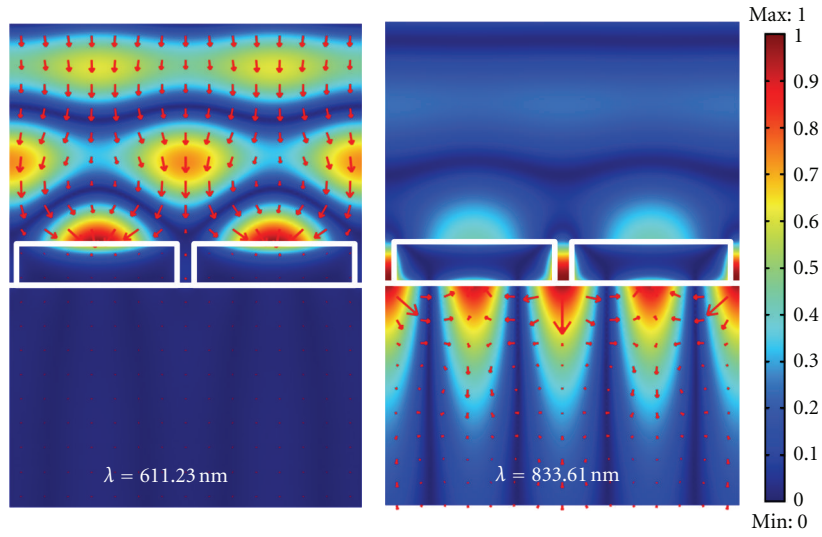

FIGURE 9: Absolute value of the magnetic field for the equivalent system applied to the case of $\theta = 10^\circ$ ($p_{eq} = 583.88$ nm and $\varepsilon_{eq} = 1.9071$). Computations are performed at (a) $\lambda = 611.23$ nm and (b) $\lambda = 833.61$ nm. Red arrows indicate the Poynting vector direction.

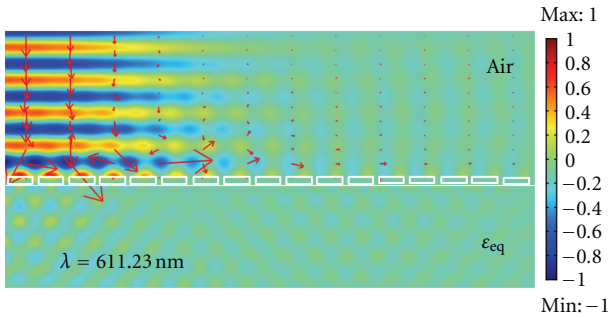

FIGURE 10: Magnetic field component H_z at $\lambda = 611.23$ nm of the equivalent system with the parameters in Figure 9 applied to the case of $\theta = 10^\circ$. Exploiting the even symmetry of the structure, the left side of the magnetic field is the mirrored replica of this plot. Red arrows indicate the direction of the Poynting vector. In this case the source has a Gaussian-shaped spatial profile.

is due to radiation phenomena owing to the presence of the sub-wavelength apertures.

The equivalence of structures allows an easy comprehension of the actual bandgap formation in slit arrays subjected to an out-of-plane excitation, although the effective incidence of a source field over a metal grating would only generate a dip of transmission following the momentum conservation in (3).

With reference to the experimental demonstration in [4], a measurement setup able to excite SPP modes over periodic arrangements of metal elements for sensing purposes makes use of microscope objectives to focus a white light over the grating. As a consequence, the impinging light is in a cone more than 10° wide. This produces a measured effect of an enlargement of the complete-reflection band. Since the proposed equivalence of structures is still valid for two-dimensional arrays of metal square elements, as the two polarizations act independently, experiencing the same periodicity, the simple original structure can be seen as a weighted superposition of results coming out by the analysis of several equivalent systems. Exploiting the mathematical formalism given by (6) and (7), we find that the equivalent structures for the air-metal interface have periods ranging in an interval of about 100 nm, with a maximum shift of the dielectric constant equal to 0.87. It means that the original system with practical normal excitation can be seen as made of many different structures with a perfectly orthogonal excitation. In this way the broadening of the stop band for input light becomes clear, although the physical meaning resides in the excitation of several SPP up and down modes over the grating. Thus, we can consider the effective opening of a finite bandgap for light impinging orthogonally on actual systems.

Moreover, this equivalence is also helpful to understand the capability of these arrangements of metal elements in solar cells designed to improve the energy absorption. In fact, a single system excited by sunlight with random incident angles behaves as a set of structures, each one with its equivalent period and substrate, with effects in the broadening of the bandgap of transmitted energy, very suitable for back reflectors.

4. Conclusions

In this paper we have demonstrated through numerical experiments that a non-zero angle of incidence induces the formation of an effective finite bandgap in practical systems. From a physical point of view, out-of-plane incidences over metal gratings made of periodic arrangements of slits on metal layers generate two SPP modes whenever the

momentum conservation is fulfilled. Such modes propagate over the metal grating in opposite directions and degenerate in a standing wave if light impinges orthogonally with an infinite wavefront. By exploiting the independence of surface modes over the two interfaces of the metal film, we define an equivalence of structures able to convert the counter-propagating SPP modes, due to the non-zero incident angle of the source field, in two spatially separated SPP modes, generated by an orthogonal source field and propagating at the same wavelength of those of the original system, but on different interfaces. The equivalence of structures has been applied to the case of a realistic measurement setup, where the input light is in a cone at least 10° wide. In this case the behaviour of the actual structure can be described by a set of equivalent systems ideally illuminated by a perfectly orthogonal excitation with effective periods ranging in an interval of about 100 nm, with a maximum shift of the dielectric constant of the equivalent substrate equal to 0.87. In this way we prove that realistic systems show effective bandgaps owing to the excitation of several SPP modes.

Acknowledgments

The authors acknowledge the CINECA Award for the proposed project *SPMAPS—Surface Plasmon Management in Active and Passive Systems—2011* and for the availability of high-performance computing resources and support.

References

[1] R. Ameling, L. Langguth, M. Hentschel, M. Mesch, P. V. Braun, and H. Giessen, "Cavity-enhanced localized plasmon resonance sensing," *Applied Physics Letters*, vol. 97, no. 25, Article ID 253116, 2010.

[2] Y. T. Chang, Y. C. Lai, C. T. Li, C. K. Chen, and T. J. Yen, "A multi-functional plasmonic biosensor," *Optics Express*, vol. 18, no. 9, pp. 9561–9569, 2010.

[3] M. Grande, R. Marani, F. Portincasa et al., "Asymmetric plasmonic grating for optical sensing of thin layers of organic materials," *Sensors and Actuators, B*, vol. 160, no. 1, pp. 1056–1062, 2011.

[4] M. Grande, M. A. Vincenti, T. Stomeo et al., "Experimental demonstration of a novel bio-sensing platform via plasmonic band gap formation in gold nano-patch arrays," *Optics Express*, vol. 19, no. 22, pp. 21385–21395, 2011.

[5] M. Grande, M. A. Vincenti, T. Stomeo et al., "Two-dimensional plasmonic nano-structures for linear and non-linear regimes," in *Proceedings of the Micro- and nano-photonic materials and devices (MINAP '12)*, pp. 73–76, Trento, Italy, January 2012.

[6] J. Bravo-Abad, F. J. García-Vidal, and L. Martín-Moreno, "Wavelength de-multiplexing properties of a single aperture flanked by periodic arrays of indentations," *Photonics and Nanostructures—Fundamentals and Applications*, vol. 1, no. 1, pp. 55–62, 2003.

[7] R. Marani, V. Marrocco, M. Grande, G. Morea, A. D'Orazio, and V. Petruzzelli, "Enhancement of extraordinary optical transmission in a double heterostructure plasmonic bandgap cavity," *Plasmonics*, vol. 6, no. 3, pp. 469–476, 2011.

[8] D. J. Bergman and M. I. Stockman, "Surface plasmon amplification by stimulated emission of radiation: quantum generation of coherent surface plasmons in nanosystems," *Physical Review Letters*, vol. 90, no. 2, Article ID 027402, 4 pages, 2003.

[9] M. A. Noginov, G. Zhu, A. M. Belgrave et al., "Demonstration of a spaser-based nanolaser," *Nature*, vol. 460, no. 7259, pp. 1110–1112, 2009.

[10] R. Marani, A. D'Orazio, V. Petruzzelli et al., "Gain-assisted extraordinary optical transmission through periodic arrays of subwavelength apertures," *New Journal of Physics*, vol. 14, Article ID 013020, 2012.

[11] K. R. Catchpole and A. Polman, "Plasmonic solar cells," *Optics Express*, vol. 16, no. 26, pp. 21793–21800, 2008.

[12] M. Losurdo, M. M. Giangregorio, G. V. Bianco, A. Sacchetti, P. Capezzuto, and G. Bruno, "Enhanced absorption in Au nanoparticles/a-Si:H/c-Si heterojunction solar cells exploiting Au surface plasmon resonance," *Solar Energy Materials and Solar Cells*, vol. 93, no. 10, pp. 1749–1754, 2009.

[13] V. Marrocco, R. Marani, M. Grande et al., "Modification of the scattering of silver nanoparticles induced by Fabry-Pérot resonances rising from a finite Si layer," *Journal of Optics*, vol. 13, no. 1, Article ID 015004, 2011.

[14] D. Dregely, R. Taubert, J. Dorfmüller, R. Vogelgesang, K. Kern, and H. Giessen, "3D optical Yagi-Uda nanoantenna array," *Nature Communications*, vol. 2, no. 1, article 267, 2011.

[15] T. Dattoma, M. Grande, R. Marani, G. Morea, V. Marrocco, and A. D'Orazio, "Resonancewavelength dependence and mode formation in gold nanorod optical antennas with finite thickness," *Progress In Electromagnetics Research B*, no. 30, pp. 337–353, 2011.

[16] T. W. Ebbesen, H. J. Lezec, H. F. Ghaemi, T. Thio, and P. A. Wolff, "Extraordinary optical transmission through sub-wavelenght hole arrays," *Nature*, vol. 391, no. 6668, pp. 667–669, 1998.

[17] J. A. Porto, F. J. García-Vidal, and J. B. Pendry, "Transmission resonances on metallic gratings with very narrow slits," *Physical Review Letters*, vol. 83, no. 14, pp. 2845–2848, 1999.

[18] D. F. P. Pile, T. Ogawa, D. K. Gramotnev et al., "Two-dimensionally localized modes of a nanoscale gap plasmon waveguide," *Applied Physics Letters*, vol. 87, no. 26, Article ID 261114, pp. 1–3, 2005.

[19] D. De Ceglia, M. A. Vincenti, M. Scalora, N. Akozbek, and M. J. Bloemer, "Plasmonic band edge effects on the transmission properties of metal gratings," *AIP Advances*, vol. 1, no. 3, Article ID 032151, 2011.

[20] R. Marani, M. Grande, V. Marrocco et al., "Plasmonic bandgap formation in two-dimensional periodic arrangements of gold patches with subwavelength gaps," *Optics Letters*, vol. 36, no. 6, pp. 903–905, 2011.

[21] COMSOL Multiphysics, http://www.comsol.com.

[22] E. D. Palik, *Handbook of Optical Constants of Solids*, Academic Press, San Diego, Calif, USA, 1998.

[23] J. M. McMahon, J. Henzie, T. W. Odom, G. C. Schatz, and S. K. Gray, "Tailoring the sensing capabilities of nanohole arrays in gold films with Rayleigh anomaly-surface plasmon polaritons," *Optics Express*, vol. 15, no. 26, pp. 18119–18129, 2007.

[24] Y. S. Jung, J. Wuenschell, H. K. Kim, P. Kaur, and D. H. Waldeck, "Blue-shift of surface plasmon resonance in a metal nanoslit array structure," *Optics Express*, vol. 17, no. 18, pp. 16081–16091, 2009.

[25] H. Raether, *Surface Plasmons on Smooth and Rough Surfaces and on Gratings*, Springer, Berlin, Germnay, 1986.

[26] K. Sakoda, *Optical Properties of Photonic Crystals*, Springer, Berlin, Germany, 2005.

[27] J. D. Joannopoulos, S. G. Johnson, J. N. Winn, and R. D. Meade, *Photonic Crystals—Molding the Flow of*, Princeton University Press, Princeton, NJ, USA, 2008.

[28] S. I. Bozhevolnyi, J. Erland, K. Leosson, P. M. W. Skovgaard, and J. M. Hvan, "Waveguiding in surface plasmon polariton band gap structures," *Physical Review Letters*, vol. 86, no. 14, pp. 3008–3011, 2001.

Hindawi Publishing Corporation
International Journal of Optics
Volume 2012, Article ID 148985, 12 pages
doi:10.1155/2012/148985

Review Article

Coupling Schemes in Terahertz Planar Metamaterials

Dibakar Roy Chowdhury,[1] Ranjan Singh,[1] Antoinette J. Taylor,[1] Hou-Tong Chen,[1] Weili Zhang,[2] and Abul K. Azad[1]

[1] *Center for Integrated Nanotechnologies, Materials Physics and Applications Division, Los Alamos National Laboratory, Los Alamos, NM 87545, USA*
[2] *School of Electrical and Computer Engineering, Oklahoma State University, Stillwater, OK 74078, USA*

Correspondence should be addressed to Dibakar Roy Chowdhury, dibakar@lanl.gov and Ranjan Singh, ranjan@lanl.gov

Received 2 October 2011; Accepted 2 December 2011

Academic Editor: Zhaolin Lu

Copyright © 2012 Dibakar Roy Chowdhury et al. This is an open access article distributed under the Creative Commons Attribution License, which permits unrestricted use, distribution, and reproduction in any medium, provided the original work is properly cited.

We present a review of the different coupling schemes in a planar array of terahertz metamaterials. The gap-to-gap near-field capacitive coupling between split-ring resonators in a unit cell leads to either blue shift or red shift of the fundamental inductive-capacitive (*LC*) resonance, depending on the position of the split gap. The inductive coupling is enhanced by decreasing the inter resonator distance resulting in strong blue shifts of the *LC* resonance. We observe the *LC* resonance tuning only when the split-ring resonators are in close proximity of each other; otherwise, they appear to be uncoupled. Conversely, the higher-order resonances are sensitive to the smallest change in the inter particle distance or split-ring resonator orientation and undergo tremendous resonance line reshaping giving rise to a sharp subradiant resonance mode which produces hot spots useful for sensing applications. Most of the coupling schemes in a metamaterial are based on a near-field effect, though there also exists a mechanism to couple the resonators through the excitation of lowest-order lattice mode which facilitates the long-range radiative or diffractive coupling in the split-ring resonator plane leading to resonance line narrowing of the fundamental as well as the higher order resonance modes.

1. Introduction

The interaction of electromagnetic waves with unstructured bulk matter is mainly governed by the inherent chemistry of material, and its properties are usually described in terms of permittivity and permeability. Recently developed electromagnetic metamaterials allow engineered material at the unit cell level, which has enabled novel methods to manipulate the electromagnetic properties [1]. Metamaterials have attracted a tremendous amount of interest because of their exotic properties such as negative refractive index [2], perfect focusing [3], cloaking [4, 5], and resonance modulation in the active and passive modes [6–29]. The electromagnetic responses offered by metamaterials are unique and are not found in naturally occurring materials. The fundamental building blocks of metamaterials are mainly comprised of a metallic split-ring resonators (SRRs) fabricated on a die-lectric/semiconducting substrate. The operation of most metamaterial devices depends on the designs employed to control the fundamental resonances of SRRs, since the major tuning of material permittivity and permeability is enabled by these resonances [6–29]. Apart from the single-SRR approach, several research groups have explored lateral coupling between nearest neighbor SRRs and its effects on the resonances [30–42]. It turns out that one of the prominent schemes to passively tune the metamaterial resonances is achieved by changing either the intercell distance or the relative orientation of SRRs with respect to each other. These studies revealed that the laterally coupled mechanisms provide an extra degree of freedom for the manipulation of metamaterial responses. Moreover, the terahertz frequency range offers a convenient platform for these studies, since sample fabrication is straightforward, and terahertz time-domain spectroscopy (THz-TDS) provides a phase-coherent characterization technique.

2. Coupling Mechanisms in Planar Metamaterials

The short-range coupling in metamaterials occurs via the electric and magnetic fields due to the close proximity of

the nearest neighbor resonators. The electric field couples through the gaps of the SRRs, while the magnetic field couples through the circumference, producing a red shift or blue shift of the resonance, depending on the nature of near-field coupling. We employed two different SRR design schemes to experimentally probe the effect of such coupling. In the first scheme, the density of the resonators is kept fixed, while the nearest neighbor interaction between two SRRs in the unit cell is probed as a function of their separation and mutual orientation. In the second type of experimental design, the effect of packing density is also taken into account. In this case, the number of SRRs excited by the incident beam varies from one sample to another as the resonators are collectively brought closer to each other. Thus, these results highlight the coupling behavior in metamaterials with low-, medium-, and high-density SRR arrays.

Recently, it has been demonstrated that near-field electric and magnetic coupling is not the only mechanism by which the SRRs in a planar arrangement remains coupled to each other [38–40]. In addition, there is also long-range radiative coupling as demonstrated with inductive-capacitive (*LC*) resonances by Singh et al. [39] and for higher-order resonance by Bitzer et al. [38]. This long-range diffractive coupling occurs when the lattice periodicity of the SRR array matches the wavelength of incident light at the fundamental *LC* or higher-order resonances, leading to a tremendous reduction in radiation damping that enhances the quality factor of the coupled resonances.

2.1. Capacitive Coupling between SRR Pairs in a Planar Array. In this section, we discuss the effect of different gap-to-gap coupling schemes on the fundamental *LC* resonances. The metamaterial samples studied were fabricated on semi-insulating GaAs substrates by photolithography methods, electron beam deposition 200 nm thick Au using 10 nm thick Ti as adhesion layer, and followed by a lift-off process. In the fabricated samples, each of the metamaterial unit cells contains two SRRs oriented with their gaps facing toward each other, as shown in Figures 1(a)–1(d) [29]. The samples were characterized in transmission using THz-TDS in a confocal geometry [43], using a bare GaAs substrate as the reference. The incident THz beam was linearly polarized with the electric field oriented parallel to the gap-bearing side, as shown in Figure 1(d).

In Figures 1(a) and 1(b), the two SRRs are individually identical, and their mutual coupling is controlled by varying their separation. As the separation between the resonators decreases from MM1 to MM2, a blue shift of metamaterial resonance is observed (Figure 2(a)). The coupling can also be controlled by asymmetry through displacing one of the gaps but keeping the other gap at the center of the gap-bearing arm (MM3 in Figure 1(c)), or by displacing both the gaps but in the opposite directions (MM4 in Figure 1(d)).

While displacing the gaps in MM3 and MM4 from their original position in MM2, the separation between SRRs within the unit cell is kept fixed at 2 μm. We observe a red shift accompanied by a reduction in the strength of the *LC* resonance for MM3 as compared to MM2 due to the asymmetry and a further red shift and strength reduction in MM4 (Figure 2(b)).

The fundamental *LC* resonance mode arises because of the electric currents oscillating around the full circumference of the SRR loop. The electric currents are excited along the SRR arms by the incident electric field due to the asymmetric arm length of the individual elements of SRR unit cells. The position of the anticipated *LC* resonance frequency can usually be described by a simple expression, $\omega_{LC} = 1/\sqrt{LC}$, where L and C are the effective inductance and capacitance of the individual SRR. In order to have better understanding of the physical mechanisms related to the resonant frequency shift from MM1 to MM4, we simulated the electric and magnetic field distributions using the numerical solver CST Microwave Studio [44]. Simulation results reveal that the magnetic field distributions for the coupled resonators remain almost similar to the uncoupled SRRs, and therefore, do not contribute to the resonance frequency shift significantly. However, the electric fields within the SRR pairs, as shown in Figure 3, clearly go through significant changes for the various coupled resonators. When the SRRs are far apart and SRR gaps are aligned, as in the case of MM1, fringing fields around the gap-bearing side contribute significantly to the overall capacitance of the individual resonators, as seen from the electric field distribution in Figure 3(a). As the separation between SRRs is reduced, these fringing fields increasingly couple the individual responses of the rings. Coulomb repulsion occurs through the fringing fields between like charges in the paired rings, thereby opposing charge accumulation near the gap resulting in a reduction of the fringing capacitance in both rings, as shown in Figure 3(b). This is responsible for the observed blue shift of the resonance frequency in MM2 as compared to MM1. When one gap is displaced completely towards the corner, as in the case of MM3, the Coulomb interaction between charges in one of the arms of the paired rings becomes attractive, thereby increasing the net electric flux density, as shown in Figure 3(c). This produces additional capacitance between the rings causing a red shift in the resonance.

For the sample MM4, both the gaps are displaced towards the corner, therefore, enhancing the Coulomb attraction between the opposite charges between the paired rings by maximum extent. This effect gives rise to a larger value of the coupling capacitance, resulting in maximum red shift of the *LC* resonance. The red shift in MM3 and MM4 is accompanied by a weakening of the resonance, as revealed by the increased resonant transmission minimum. This is because of the weak excitation of SRRs with displaced gaps by the external electric field. Therefore, two apparently independent and simultaneous effects are observed: strong capacitive coupling between SRRs causing resonance frequency shifts and symmetry breaking in the individual rings causing variation of the resonance strength. The larger the capacitive coupling between the paired rings, the larger the resonance frequency shift. Similarly, the larger the asymmetry of the rings, the weaker the *LC* resonance strength due to the weak coupling of the incident THz radiation with the SRRs.

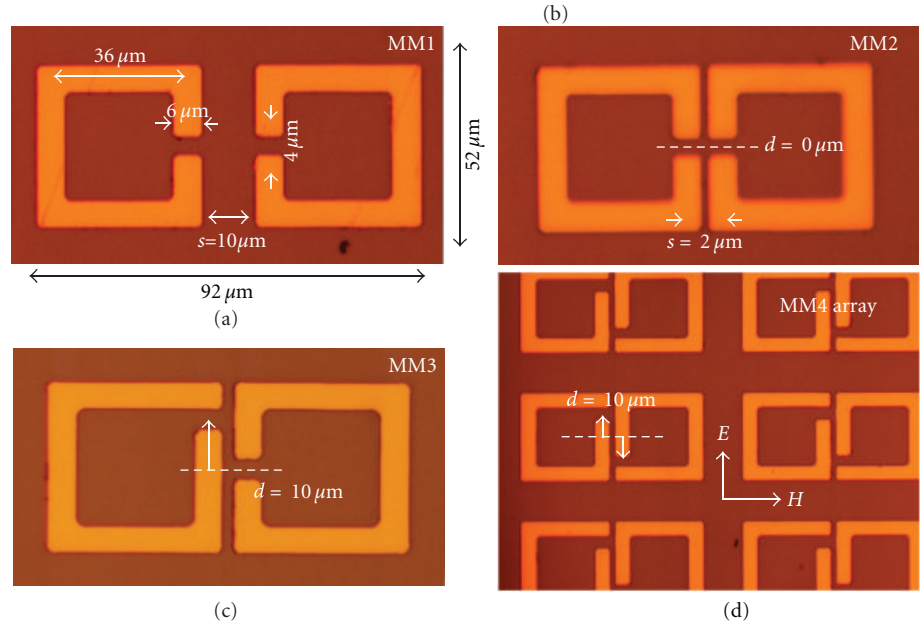

Figure 1: Optical microscope images of the fabricated metamaterial samples. (a) In the unit cell with symmetric gap-to-gap coupled SRRs, the separation is either (a) 10 μm (MM1) or (b) 2 μm (MM2). (c) The asymmetric SRRs with one gap displaced from the center (MM3) and (d) the SRR array where both gaps are displaced in the opposite direction from the center (MM4). The dimensions of the unit cells and their features are indicated in the figure. The unit cell periodicity for all the metamaterial samples is identical.

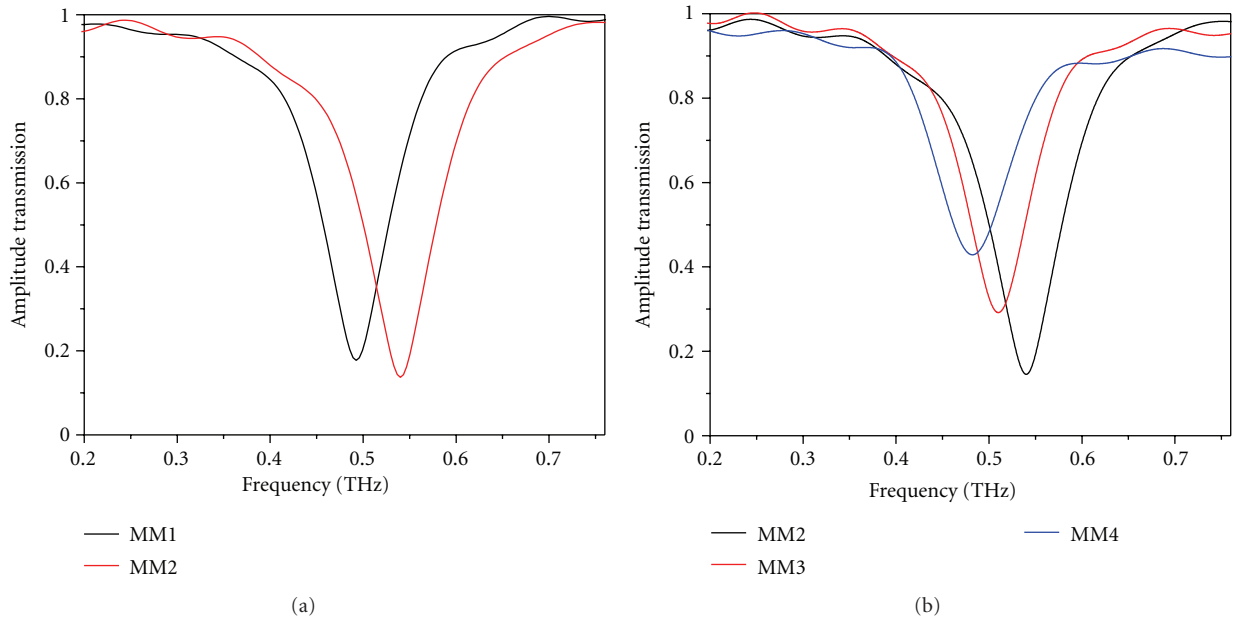

Figure 2: Measured THz electric field amplitude spectra when transmitting through the metamaterial samples for (a) MM1 and MM2 (b) and MM2, MM3, and MM4.

2.2. Inductive Coupling in the Metamaterial Array. The effect of strong inductive coupling was probed in terahertz SRRs by maintaining a fixed orientation and the capacitive gaps facing upwards in all samples, which minimizes the effect of the capacitive coupling [39]. Thus, the metamaterials are designed to have different periodicity from one sample to another. Nine sets of samples were prepared with periodicity of $P = 200, 150, 100, 60, 50, 40, 35, 30$, and $25\ \mu$m, keeping the geometrical dimensions of the SRR fixed. Figure 4(a) shows the metamaterial sample with $P = 25\ \mu$m. The dimensions of SRR were chosen such that its LC resonance wavelength is $\lambda \sim 200\ \mu$m (i.e., 1.5 THz) on the silicon substrate. Different periodicities in samples were designed so that the resonance wavelength to lattice constant ratio λ/P varies from a value

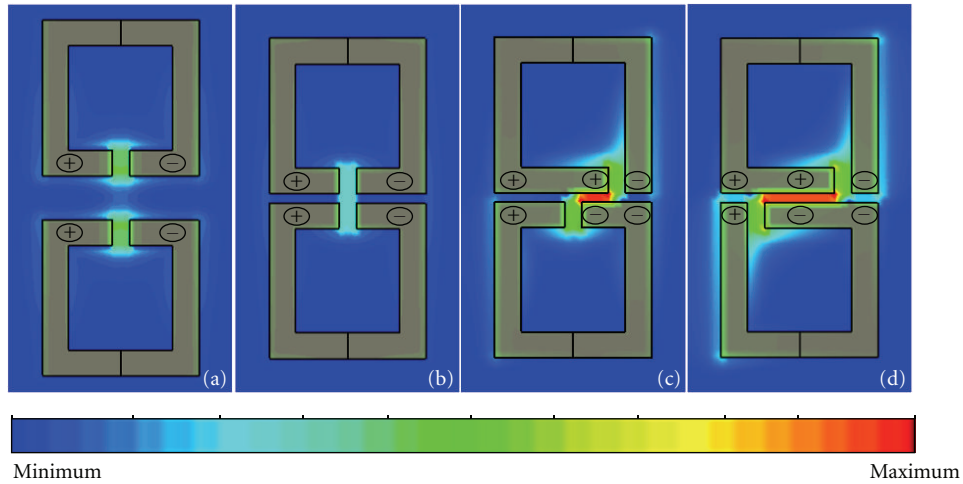

Figure 3: The numerically simulated electric field strength distributions for the coupled SRRs: (a) MM1 (b), MM2 (c), MM3 (d), and MM4. The electric field strength is indicated by the color map at the bottom. The polarity of the induced electronic charges on the SRR arms is indicated in the figure.

of $\lambda/P = 1$ for $P = 200\,\mu$m to $\lambda/P = 8$ for $P = 25\,\mu$m. Each metamaterial sample is excited by an incident terahertz beam with the focal diameter of 3.5 mm, with which the number of excited SRRs is gradually increased from 960 for $P = 200\,\mu$m to 61,500 for $P = 25\,\mu$m. This enables the study of the inter-SRR packing-dependent coupling and its impact on the overall collective resonant response in THz transmission.

The measured resonant transmission spectra are plotted in Figure 4(b). The evolution of the *LC* resonance was observed at around 1.5 THz. The resonance was fairly weak for the 200, 150, and 100 μm periodicities. A strong resonance feature is observed for the metamaterial sample with period of 60 μm, and then a gradual broadening of the resonance was seen for smaller periodicities or higher packing densities.

The dominant coupling mechanism among SRRs at the *LC* resonance with increasing packing density is mainly magnetic/inductive in nature. The increase in the packing density leads to spatially closer magnetic loops strongly coupled to each other. When this happens, the mutual inductance between SRRs tends to reduce the self-inductance of the SRR loop leading to a reduced effective inductance and thus an increase or blue shifting of the *LC* resonance frequency. Thus, the stronger is the inductive coupling between the SRRs, the higher the resonance frequency will be, since each SRR due to mutual coupling reduces the magnetic flux of its neighbors. The experimental data shows that stronger (high density) or weaker (low density) magnetic coupling leads to lowering of *Q* factor of SRRs as shown in Figure 4(c). Further, there seems to be an optimal packing density with periodicity of 60 μm where the SRRs are coupled to yield the sharpest *LC* resonance due to diffractive coupling. This coupling mechanism is explained in detail in the next section.

2.3. Long-Range Diffractive Coupling in Metamaterial Array. In this section, we describe the long-range radiative coupling encountered in the experiment described in the previous section. We highlight that the inter-SRR distance and its number density or periodicity can control the *Q* factor and the strength of the *LC* resonance of SRRs. The measured amplitude transmission in Figure 4(b) shows that the *LC* resonance at 60 μm periodicity yields the narrowest resonance linewidth. Coincidentally, it also corresponds to a λ/P ratio of 3.33 which is the refractive index of the silicon substrate on which the SRRs are fabricated. Thus, we observe a strong suppression of radiative losses and thus a sharp enhancement of the *Q* factor at a certain critical periodicity, P_c, that exactly matches the SRR resonant wavelength in the silicon substrate, that is, $P_c = \lambda_{LC}/n$, where λ_{LC} is the *LC* resonance wavelength in vacuum, and n is the refractive index of the substrate material. The sharpening of *LC* resonance is mainly due to Wood's anomaly or the diffractive lattice mode corresponding to the critical periodicity, the resonant wavelength, and the substrate index [38–40, 45]. When the periodicity is further reduced, a gradual decline in *Q* factor of the fundamental SRR resonance is observed in Figure 4(c).

The narrowest resonance occurs when the incident light field corresponds to diffractive grating order (i, j) change from evanescent to radiative, $P_c = \sqrt{(i^2 + j^2)}\lambda/n$; here n is the refractive index of the substrate in use, (i, j) are the diffraction grating orders, and λ is the resonance wavelength. In the experiment, $P_c = 60$ um corresponds to the lowest-order $(1, 0)$ diffractive lattice mode. Every time the lowest-order lattice mode matches either the lower-order fundamental *LC* resonance or higher-order resonances, a sudden sharpening of the resonance will occur. The narrowing of the resonance in an optimally packed metamaterial can also be best understood by the suppression of radiation damping due to the confinement or trapping of electromagnetic fields in the metamaterial plane. This mechanism is based on diffractive coupling during which the diffracted fields are trapped in the metamaterial lattice, and each SRR radiatively couples to the neighboring SRR. The lower *Q* factor for larger

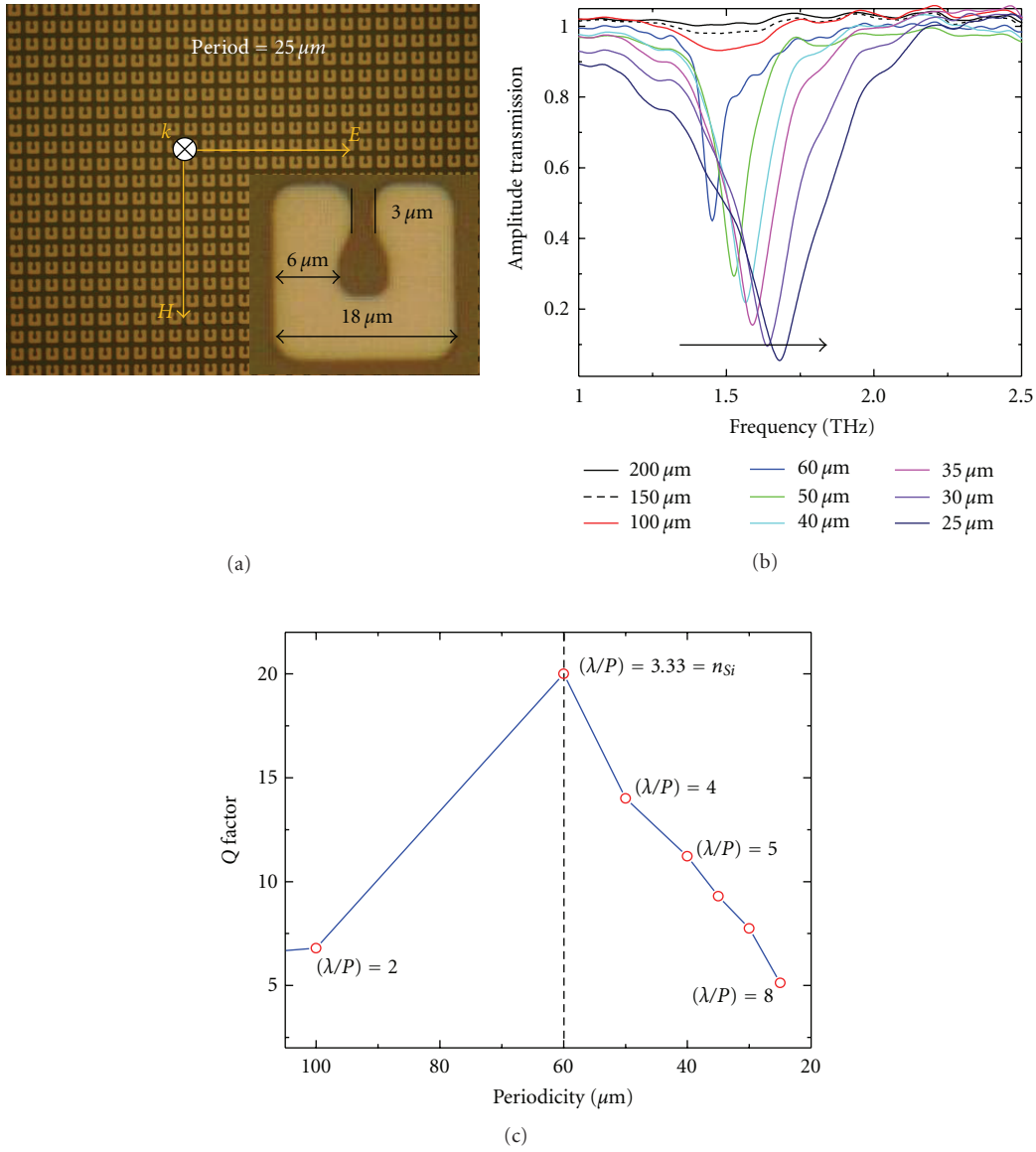

FIGURE 4: (a) Microscopic image of the highest-density metamaterial sample. The SRRs are comprised of 200 nm thick Al on 640 μm thick n-type silicon substrates. (b) Measured transmission spectra of metamaterials with different periodicities. (c) Quality factor extracted from the measured transmission for different period metamaterials.

periods is associated to an enhanced radiation damping. The lower Q factor for smaller periods is mainly due to the mismatch with the lattice mode during which the radiated fields of the coherently coupled SRRs interfere destructively in the plane of the metamaterial, leading to higher radiative losses and increase of nonradiative losses due to a capacitive and inductive coupling.

Tailoring the periodicity of metamaterials will allow the design of frequency-selective surfaces with an adjustable Q factor for metamaterials across the entire electromagnetic spectrum optimized for various applications. This finding is important for the development of metamolecule density and substrate-refractive-index-tuned THz devices and components.

2.4. Capacitive and Inductive Coupling for Different Orientation and Separation in Nearest-Neighbor SRRs. In this section, we probe scenarios where neighboring split rings have their gap either on the same or on opposite sides with the change in periodicity [37]. The lowest-order odd eigenmode and the lowest-order even eigenmodes for two different excitations are marginally affected, whereas the higher-order eigenmode experiences a significant spectral reshaping [37, 46] due to a coherent interaction.

We designed metamaterials composed of three different supercells each containing four SRRs. The geometrical arrangement of the SRRs in each supercell is shown in Figure 5. In the first sample, all SRRs have their gap on the same side. In a second sample, the SRRs are arranged

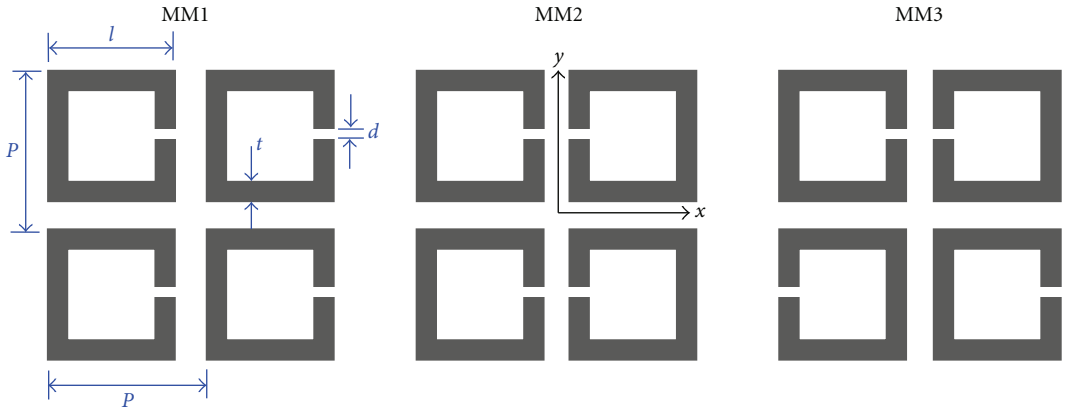

Figure 5: Unit cell of the three types of differently oriented split-ring resonators. The dimensions of all SRRs are $t = 6\,\mu$m, $l = 36\,\mu$m, and $d = 2\,\mu$m. In the design, the period P is varied.

with vertical mirror symmetry. In a third sample, the SRRs have the same orientation of their gaps along the diagonal directions of the supercell. In this work, the effects of the orientation on the spectral position and the width of each resonance are investigated. It was observed that control over the orientation of the SRRs and the periodicity enables extremely sharp features in the spectrum that are promising candidates for various practical applications such as sensing devices.

Simulations were done with the Fourier modal method [47] using the structure parameters shown in Figure 6 where only the periodicity parameter "P" was swept from $P = 50\,\mu$m to $P = 39\,\mu$m. Figure 6 shows the transmission for the three configurations as a function of period and frequency. In all cases, the incident E-field is polarized along the gap-bearing arms in the y-axis direction as shown in MM2. The main effects observed in the simulations are the impact of each configuration, the impact of the periodicity for each configuration on the spectral positions and the widths of the resonance, and the occurrence of coherent phenomena once SRRs are closely spaced. It can be clearly seen that the fundamental mode LC resonance at 0.5 THz does not undergo significant change in resonance position or resonance linewidth, but the higher-order dipole resonance undergoes a huge spectral change at about 1.5 THz.

Between MM1 and MM2, as the periodicity is reduced, the resonance at 1.5 THz broadens in MM2, and the same resonance in MM3 splits and exhibits a very sharp spectral feature, shown by a white-dotted ellipse. Such large spectral reshaping prompted us to carry out the experiment in all of these configurations.

Six samples of planar SRRs (denoted in the following section as MM1–MM6) were fabricated. As shown in Figure 5 above, MM1–MM3 are single SRRs with lattice constant $P = 50\,\mu$m. MM4–MM6 are single SRRs with the same symmetry as MM1–MM3 but with reduced periodicity of $P = 39\,\mu$m. The measured amplitude transmission spectra of MM1–MM3 are shown in Figure 7(a). The two significant dips in transmission are traces from the two lowest-order

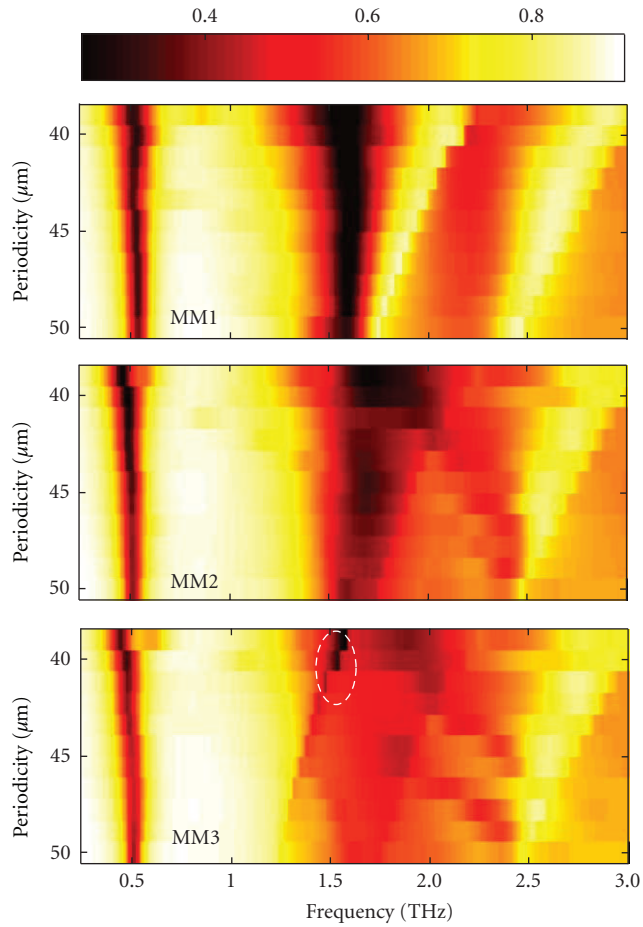

Figure 6: Simulated transmission spectra of the three differently oriented metamaterials with period, P, swept from $P = 50\,\mu$m to $P = 39\,\mu$m.

odd eigenmodes. Significant differences in the spectra are observed, depending on the orientation of the gap of neighboring SRRs. When comparing the resonances of MM2 with those of MM1, it can be seen that the LC resonance at 0.5 THz

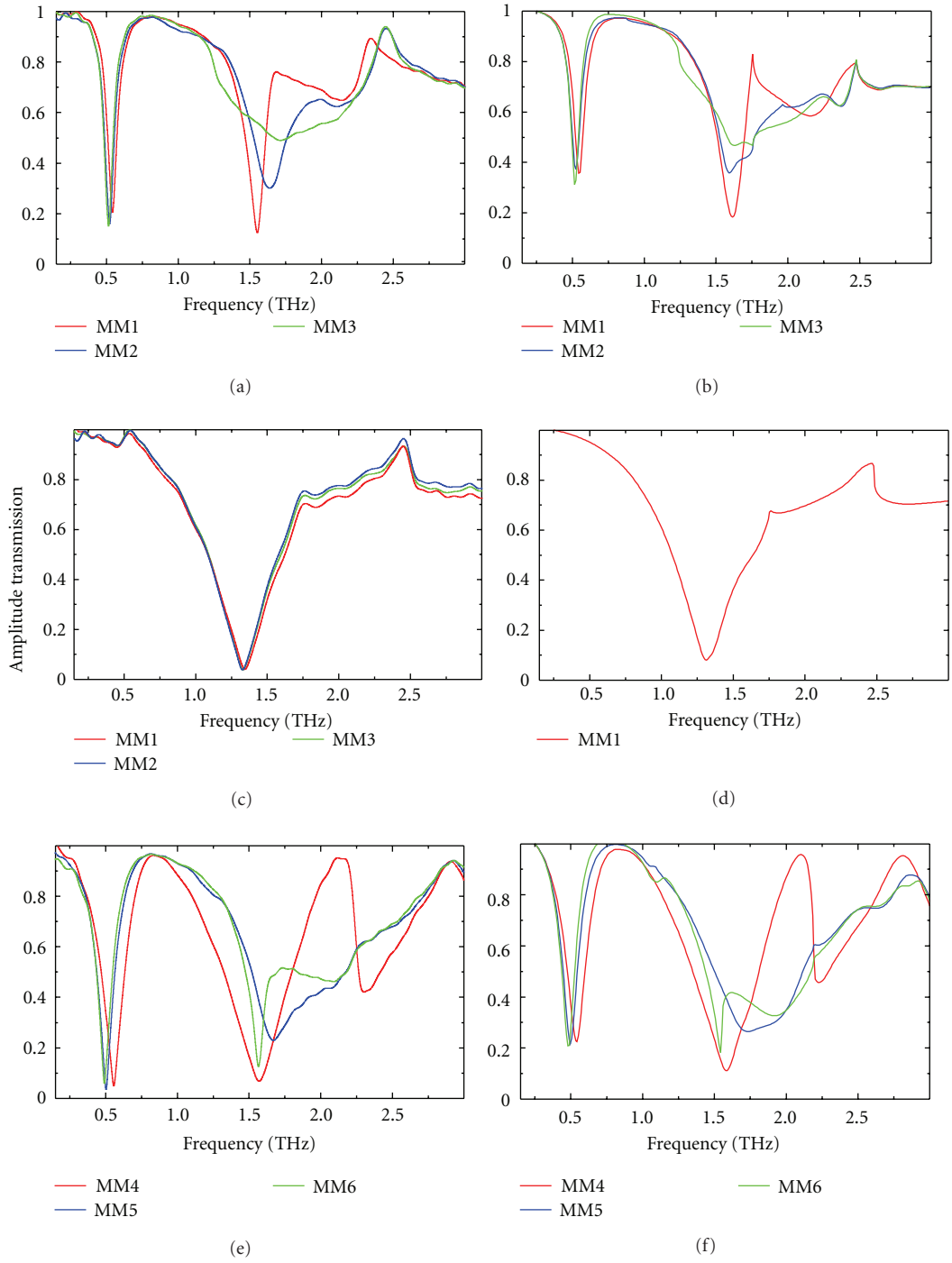

FIGURE 7: (a), (b) are measurement and simulations of differently oriented metamaterials, MM1, MM2, and MM3, for $P = 50\,\mu$m for excitation in x direction, (c), (d) are the same but excitation in y direction, and (e), (f) are measurement and simulations for three differently oriented unit cells with period $P = 39\,\mu$m.

is red shifted slightly. In contrast, the next higher-order odd resonance at 1.5 THz broadens, blue-shifts by 84 GHz, and the transmission increases significantly in MM2. Furthermore, the orientation of the SRRs in the supercell for MM3 causes only a marginal additional red shift of the lowest-order eigenmode by 8 GHz and nearly no change on transmission. The next higher-order resonances suffer from a severe broadening and a significant increase in transmission up to 49%. The simulated spectra in Figure 7(b) are in good agreement with the measurements except the amplitude transmission depth at the *LC* resonance due to the limited resolution of our numerical code. For an incident *E*-field perpendicular to the gap-bearing arms, the response of MM1–MM3 is shown in Figure 7(c). Independent of the

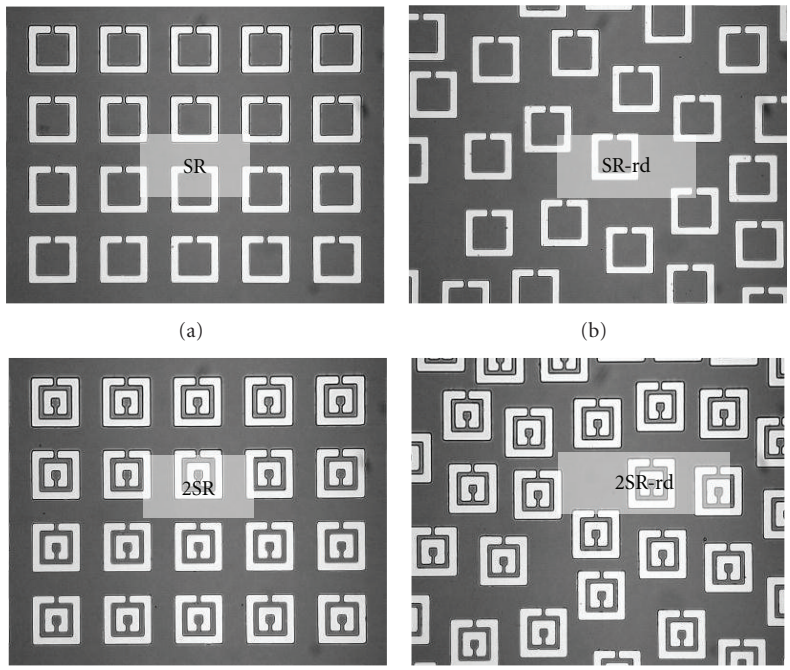

Figure 8: Microscopic images of the (a) periodic and (b) random single SRR array, (c) periodic and (d) random double SRR array. The dimensions of the outer ring are the same as in Figure 5 and of the inner smaller ring are the same as in Figure 4(a).

arrangement, all spectra show a strong resonance at 1.33 THz and have nearly the same spectral dependence. Exactly the same observation is made in the simulation. This resonance is the lowest-order even eigenmode.

The experimentally measured transmission spectra for MM4–MM6 are shown in Figure 7(e). The incident *E*-field is polarized along *y*-axis. Due to reduced periodicity and high density of SRRs, we observe a different spectral behavior in comparison with the samples MM1–MM3. In MM4, there are three distinct resonances, the *LC* resonance at 0.556 THz, the next higher-order odd eigenmode at 1.57 THz, and a third strong resonance at 2.3 THz. This third resonance, however, is a Wood's anomaly in the substrate. In MM5, the lowest-order odd eigenmode appears red-shifted and has a reduced linewidth when compared to MM4. The next higher-order odd eigenmodes are broadened and blue-shifted. In MM6, the lowest-order odd eigenmode is again marginally further red-shifted. Finally, and potentially most interesting, the next higher-order odd eigenmode appears as an extremely sharp feature with a linewidth of only 69.5 GHz, resonating approximately at the same frequency as the higher-order odd eigenmode of MM4. The resonance has a high *Q*-factor of 18.5. This high *Q*-factor is an essential property for the achievement of high sensitivity in planar THz MM sensors, as sensitivity increases with the sharpness of the spectral resonance feature. In Figure 7(f), the simulation agrees well with the measurements.

To explain the influence of the arrangement on the spectral properties of the lowest-order LC resonance mode, one may evoke analogies to transmission line theory. Placing SRRs like in MM2 and MM3 will cause an increase of the effective capacitance as the next neighbor in such situation provides a parasitic or mutual capacitance in parallel that would add up with the gap capacitance. The increase in effective capacitance causes the red shift of the *LC* resonance.

For the lowest-order even eigenmode when the excitation field is along *x* direction, placing the gap on either side of the SRR has no effect, as this mode is dominantly characterized by oscillating currents in the side arms of the SRR that have no gap. Therefore, modification of the resonance conditions for the SRR is neither observed nor expected.

For the third resonance which is the second-order odd eigenmode, the resonance shape and position depends on the chossen period and consequently on the absolute inter-SRR distance between the neighbors. By taking into account the fact that the resonance wavelength is comparable to the chosen interparticle separation, the coherent superposition of the scattered field by neighboring SRRs causes the strong modification of the transmission in this spectral domain. The formation of a *subradiant* and a *superradiant* type mode, depending on the interparticle distance and the gap orientation, causes a blue shift or a red shift of the resonance [43]. The superradiant (subradiant) mode also increases (decreases) the radiation losses of the excited eigenmode which leads to a broadening (narrowing) of the spectral resonance.

2.5. Coupling in the Randomly Distributed Metamaterial Array. In this section, we review the outcome of the introduction of positional disorder of SRRs in metamaterials on the quality factor of the fundamental *LC* and higher-order dipole resonances. Several existing metamaterials are

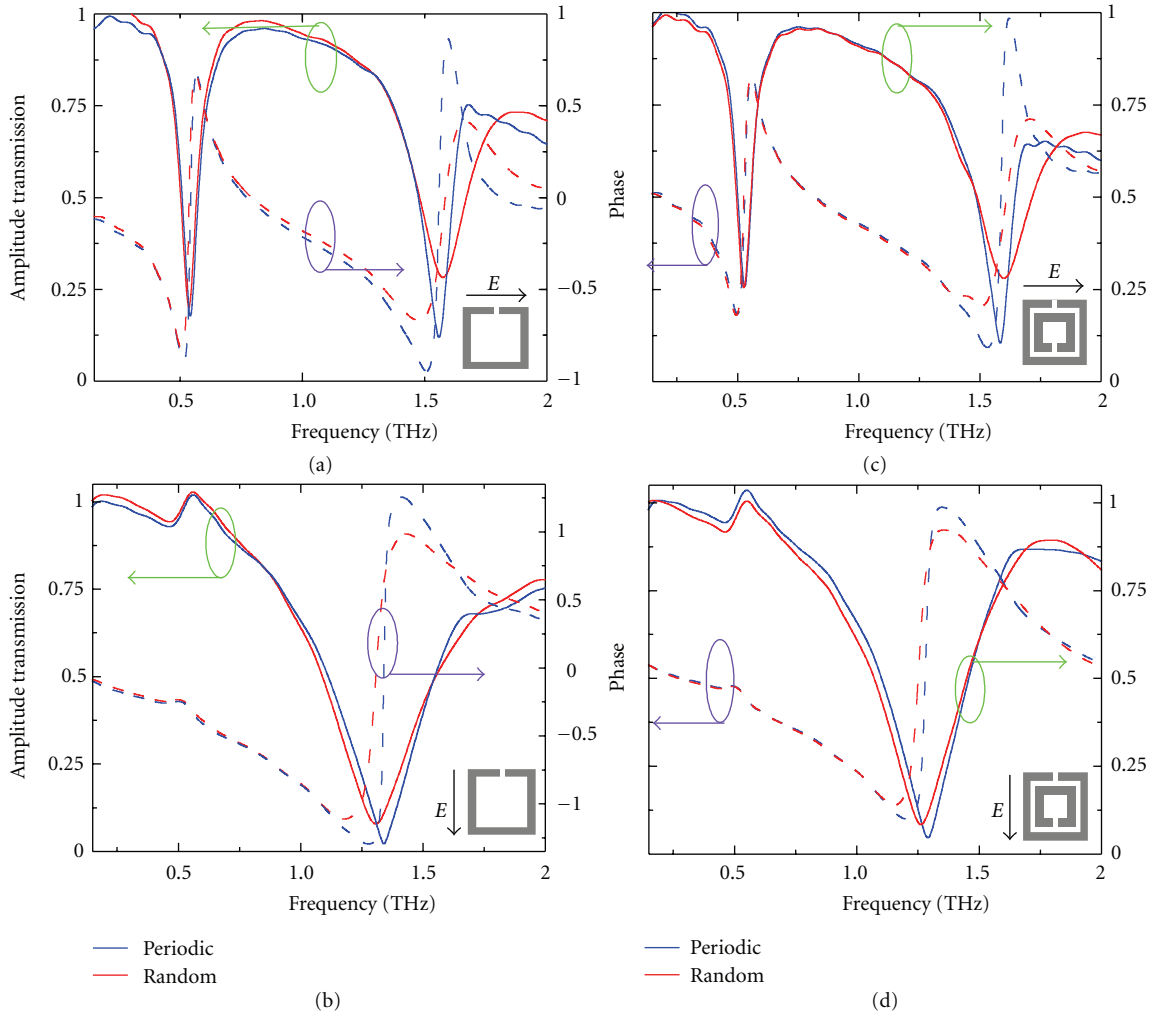

FIGURE 9: Measured (a) parallel and (b) perpendicular excitation of single-ring periodic and random resonators; (c), (d) are the same for double-ring resonators. The dash curves are the corresponding phase changes.

anisotropic in nature. However, for most practical applications across the entire electromagnetic spectrum, isotropic materials are required, and isotropic medium is sometimes based on randomly distributed cells in the volume of the host structure. Much of the previous work on metamaterials was focused on investigating the unique properties of wave propagation through periodic structures. There has been a tremendous desire to explore the collective behavior of SRRs when disorder is present in either their geometrical dimensions or periodic positioning on the host media [48–52].

The disorder has been studied in the single and the double split-ring resonators [50]. For single SRRs, only the outer ring with the same dimensions is retained. The disorder in arrangement was introduced by manually changing the lattice points of SRRs in a random fashion during the mask design. Each of the periodic SRRs was initially at a lattice position, $\vec{r}_n$, where $\vec{r} = x\vec{i} + y\vec{j}$, and individual SRRs were then displaced by $\pm\vec{\delta x}$ and $\pm\vec{\delta y}$ to introduce positioning disorder as shown in Figure 8. Thus, $\delta r = \delta x\vec{i} + \delta y\vec{j}$ is used to define the degree of randomness. In our case, $|\vec{\delta x}| \leq 32\,\mu$m and $|\vec{\delta y}| \leq 32\,\mu$m, leading to a maximum disorder $|\vec{\delta r}| \leq 45.25\,\mu$m, which is equivalent to 85% of the periodicity, $P = 53\,\mu$m. The random SRRs retain the same number density as that of the counterpart periodic SRRs, giving the same metal volume filling fraction, $f = 0.25$ for the single SRRs, *SR* (periodic), and *SR-rd* (random), $f = 0.33$ for the double SRRs, *2SR* (periodic), and *2SR-rd* (random).

For the random sample *SR-rd* in the parallel orientation, as shown in Figure 9(a), no change in the *LC* resonance feature is observed compared to that of *SR*. The next higher resonance, however, blue-shifts by 16 GHz with a linewidth broadening by 80 GHz and a significant transmission modification from 12% to 28%. In the perpendicular orientation, the lowest-order eigenmode of the random structure, *SR-rd*, red-shifts by 34 GHz and broadens by 106 GHz, as shown in Figure 9(b). This behavior indicates that the dipole resonance is clearly affected by the positional disorder of SRRs.

Figures 9(c) and 9(d) illustrate the frequency-dependent amplitude transmission of the double SRR samples, *2SR* and *2SR-rd*. Similar effects are observed in the periodic and aperiodic double SRRs, as seen for the single SRRs. The *LC* resonance of *2SR* and *2SR-rd* was found identical in all

respects. The second-order odd eigenresonance at 1.58 THz blue-shifted by 16 GHz and broadened by 99 GHz, and the resonance minimum decreased by 17.5%. The lowest even eigenmode red-shifts by 28.5 GHz and broadens by 49 GHz. The corresponding phase change spectra are shown in all the figures.

The character of the *LC* resonance is independent of randomness in the positioning of SRRs as its peak frequency and resonance strength remain unaffected. The response of the random SRRs at the *LC* resonance is identical to that of their periodic counterpart as long as their number density remains constant by maintaining equal volume metal filling fraction. The inter-SRR interaction between the individual elemental SRR is negligible since the collective behavior of the periodic and the random metamaterials is just a direct addition of individual SRR contributions.

Unlike the *LC* resonance, the dipole resonances in the random structures undergo a change compared to that of the periodic SRRs. This can be expected due to the different current profiles for the SRRs at *LC* and dipole resonance frequencies. The second odd and lowest even eigenmode resonances in the transmission spectra of all the SRRs are due to linear currents in the SRR side arms and have similar current density distributions. Therefore, those resonances undergo similar spectral modification when disorder is introduced in the SRRs. The incident terahertz electric field excites plasmon oscillations of conduction electrons at the surface of individual metallic SRR arms that are parallel to the illuminating field, producing a collection of oscillating dipoles with a dipole moment. The dipole resonance is due to the dipole-dipole interaction between the SRR arms along the direction of the incident electric field. The plasmon energy and the resonance linewidth strongly depend on the interparticle distance. The dipole resonance wavelength in the metamaterial structures becomes comparable to the interparticle spacing, and as the distance between the dipoles is varied, there is formation of a coupled plasmon mode which alternates between superradiative and subradiative behavior modifying the resonance spectral width and causing frequency shifts. The dipole coupling among the randomized split ring resonators is highly complicated due to their random positioning with respect to each other and is influenced by a number of other factors, hence rendering a straightforward explanation impossible. In the periodic structures, the coupling between the dipoles is stronger compared to the randomly distributed SRRs since the interaction between the oscillating particles is partially cancelled by the disorder, which leads to weaker coupling among the dipoles and higher radiative damping. As a result, broadened and weaker plasmon resonances in the randomly scattered SRR metamaterials are observed. This is also due to inhomogeneous broadening that is caused due to the randomly scattered dipoles.

3. Conclusion

In conclusion, in-plane coupling of terahertz SRRs can manipulate and tailor the fundamental as well as higher-order resonances. The near-field coupling via the SRRs electric and magnetic field causes the fundamental mode resonance to red-shift and blue-shift, respectively. The mutual orientation and the separation plays dominant roles in tuning the higher-order dipolar resonance, leading to excitation of sharp subradiant resonances that can act like hotspots for sensing applications. The effect of packing density in SRRs can be very strong, enabling the design of tunable transmission and quality factor metamaterials. Long range radiative coupling also leads to resonance sharpening and electromagnetic energy trapping in the metamaterial lattice, and these long-range interactions are mediated by the fundamental-order diffractive mode of the periodic grating. Thus, the different coupling mechanisms in planar matamaterials could be exploited for the development of terahertz devices with various functionalities.

Acknowledgments

The authors thank C. Rockstuhl, J. F. O' Hara, M. Walther, and X. Lu for their outstanding contribution and fruitful discussions in this work. Some of the work was partially supported by the U.S. National Science Foundation (NSF). This work was performed, in part, at the Center for Integrated Nanotechnologies, a U.S. Department of Energy, Office of Basic Energy Sciences user facility. Los Alamos National Laboratory, an affirmative action equal opportunity employer, is operated by Los Alamos National Security, LLC, for the National Nuclear Security Administration of the U.S. Department of Energy under Contract no. DE-AC52-06NA25396.

References

[1] J. B. Pendry, A. J. Holden, D. J. Robbins, and W. J. Stewart, "Magnetism from conductors and enhanced nonlinear phenomena," *IEEE Transactions on Microwave Theory and Techniques*, vol. 47, no. 11, pp. 2075–2084, 1999.

[2] R. A. Shelby, D. R. Smith, and S. Schultz, "Experimental verification of a negative index of refraction," *Science*, vol. 292, no. 5514, pp. 77–79, 2001.

[3] N. Fang, H. Lee, C. Sun, and X. Zhang, "Sub-diffraction-limited optical imaging with a silver superlens," *Science*, vol. 308, no. 5721, pp. 534–537, 2005.

[4] J. B. Pendry, D. Schurig, and D. R. Smith, "Controlling electromagnetic fields," *Science*, vol. 312, no. 5781, pp. 1780–1782, 2006.

[5] D. Schurig, J. J. Mock, B. J. Justice et al., "Metamaterial electromagnetic cloak at microwave frequencies," *Science*, vol. 314, no. 5801, pp. 977–980, 2006.

[6] W. J. Padilla, A. J. Taylor, C. Highstrete, M. Lee, and R. D. Averitt, "Dynamical electric and magnetic metamaterial response at terahertz frequencies," *Physical Review Letters*, vol. 96, no. 10, Article ID 107401, pp. 1–4, 2006.

[7] H. T. Chen, W. J. Padilla, J. M. O. Zide, A. C. Gossard, A. J. Taylor, and R. D. Averitt, "Active terahertz metamaterial devices," *Nature*, vol. 444, no. 7119, pp. 597–600, 2006.

[8] H. T. Chen, J. F. O'Hara, A. K. Azad et al., "Experimental demonstration of frequency-agile terahertz metamaterials," *Nature Photonics*, vol. 2, no. 5, pp. 295–298, 2008.

[9] H. Tao, A. C. Strikwerda, K. Fan, W. J. Padilla, X. Zhang, and R. D. Averitt, "Reconfigurable terahertz metamaterials," *Physical Review Letters*, vol. 103, no. 14, Article ID 147401, 2009.

[10] Z. Tian, R. Singh, J. Han et al., "Terahertz superconducting plasmonic hole array," *Optics Letters*, vol. 35, no. 21, pp. 3586–3588, 2010.

[11] T. Driscoll, H. T. Kim, B. G. Chae et al., "Memory metamaterials," *Science*, vol. 325, no. 5947, pp. 1518–1521, 2009.

[12] R. Singh, E. Plum, W. Zhang, and N. I. Zheludev, "Highly tunable optical activity in planar achiral terahertz metamaterials," *Optics Express*, vol. 18, no. 13, pp. 13425–13430, 2010.

[13] J. Gu, R. Singh, Z. Tian et al., "Terahertz superconductor metamaterial," *Applied Physics Letters*, vol. 97, no. 7, Article ID 071102, 2010.

[14] B. Jin, C. Zhang, S. Engelbrecht et al., "Low loss and magnetic field-tunable superconducting terahertz metamaterial," *Optics Express*, vol. 18, no. 16, pp. 17504–17509, 2010.

[15] H. T. Chen, H. Yang, R. Singh et al., "Tuning the resonance in high-temperature superconducting terahertz metamaterials," *Physical Review Letters*, vol. 105, no. 24, Article ID 247402, 2010.

[16] R. Singh, A. K. Azad, Q. X. Jia, A. J. Taylor, and H. -T. Chen, "Thermal tunability in terahertz metamaterials fabricated on strontium titanate single-crystal substrates," *Optics Letters*, vol. 36, no. 7, pp. 1230–1232, 2011.

[17] R. Singh, J. Xiong, A. K. Azad et al., "Optical tuning and ultrafast dynamics of high-temperature superconducting terahertz metamaterials," *Nanophotonics*. In press, http://arxiv.org/abs/1111.3917.

[18] S. Y. Chiam, R. Singh, W. Zhang, and A. A. Bettiol, "Controlling metamaterial resonances via dielectric and aspect ratio effects," *Applied Physics Letters*, vol. 97, no. 19, Article ID 191906, 2010.

[19] N.-H. Shen, M. Massaouti, M. Gokkavas et al., "Optically implemented broadband blueshift switch in the terahertz regime," *Physical Review Letters*, vol. 106, no. 3, Article ID 037403, 2011.

[20] D. Roy Chowdhury, R. Singh, J. F. O'Hara, H.-T. Chen, A. J. Taylor, and A. K. Azad, "Dynamically reconfigurable terahertz metamaterial through photo-doped semiconductor," *Applied Physics Letters*, vol. 99, no. 23, Article ID 231101, 2011.

[21] J. Gu, R. Singh, A. K. Azad et al., "An active hybrid plasmonic metamaterial," *Optical Materials Express*, vol. 2, Article ID 1617, 2011, http://www.opticsinfobase.org/ome/abstract.cfm?uri=ome-2-1-31.

[22] H.-T. Chen, J. F. O'Hara, A. K. Azad, and A. J. Taylor, "Manipulation of terahertz radiation using metamaterials," *Laser & Photonics Reviews*, vol. 5, no. 4, pp. 513–533, 2011.

[23] R. Singh, A. K. Azad, J. F. O'Hara, A. J. Taylor, and W. Zhang, "Effect of metal permittivity on resonant properties of terahertz metamaterials," *Optics Letters*, vol. 33, no. 13, pp. 1506–1508, 2008.

[24] D. R. Chowdhury, R. Singh, M. Reiten et al., "A broadband planar terahertz metamaterial with nested structure," *Optics Express*, vol. 19, no. 17, pp. 15817–15823, 2011.

[25] J. F. O'Hara, R. Singh, I. Brener et al., "Thin-film sensing with planar terahertz metamaterials: sensitivity and limitations," *Optics Express*, vol. 16, no. 3, pp. 1786–1795, 2008.

[26] I. A.I. Al-Naib, C. Jansen, and M. Koch, "Thin-film sensing with planar asymmetric metamaterial resonators," *Applied Physics Letters*, vol. 93, no. 8, Article ID 083507, 2008.

[27] R. Singh, E. Smirnova, A. J. Taylor, J. F. O'Hara, and W. Zhang, "Optically thin terahertz metamaterials," *Optics Express*, vol. 16, no. 9, pp. 6537–6543, 2008.

[28] W. Withayachumnankul and D. Abbott, "Metamaterials in the Terahertz Regime," *IEEE Photonics Journal*, vol. 1, p. 99, 2009, http://ieeexplore.ieee.org/xpls/abs_all.jsp?arnumber=5130235.

[29] D. R. Chowdhury, R. Singh, M. Reiten, J. Zhou, A. J. Taylor, and J. F. O'Hara, "Tailored resonator coupling for modifying the terahertz metamaterial response," *Optics Express*, vol. 19, no. 11, pp. 10679–10685, 2011.

[30] F. Hesmer, E. Tatartschuk, O. Zhuromskyy et al., "Coupling mechanisms for split ring resonators: theory and experiment," *Physica Status Solidi B*, vol. 244, no. 4, pp. 1170–1175, 2007.

[31] R. S. Penciu, K. Aydin, M. Kafesaki et al., "Multi-gap individual and coupled split-ring resonator structures," *Optics Express*, vol. 16, no. 22, pp. 18131–18144, 2008.

[32] I. Sersic, M. Frimmer, E. Verhagen, and A. F. Koenderink, "Electric and magnetic dipole coupling in near-infrared split-ring metamaterial arrays," *Physical Review Letters*, vol. 103, no. 21, Article ID 213902, 2009.

[33] R. Singh, I. A.I. Al-Naib, Y. Yang et al., "Observing metamaterial induced transparency in individual Fano resonators with broken symmetry," *Applied Physics Letters*, vol. 99, no. 20, Article ID 201107, 2011.

[34] N. Liu, S. Kaiser, and H. Giessen, "Magnetoinductive and electroinductive coupling in plasmonic metamaterial molecules," *Advanced Materials*, vol. 20, no. 23, pp. 4521–4525, 2008.

[35] R. Singh, C. Rockstuhl, F. Lederer, and W. Zhang, "Coupling between a dark and a bright eigenmode in a terahertz metamaterial," *Physical Review B*, vol. 79, no. 8, Article ID 085111, 2009.

[36] N. Feth, M. König, M. Husnik et al., "Electromagnetic interaction of split-ring resonators: the role of separation and relative orientation," *Optics Express*, vol. 18, no. 7, pp. 6545–6554, 2010.

[37] R. Singh, C. Rockstuhl, F. Lederer, and W. Zhang, "The impact of nearest neighbor interaction on the resonances in terahertz metamaterials," *Applied Physics Letters*, vol. 94, no. 2, Article ID 021116, 2009.

[38] A. Bitzer, J. Wallauer, H. Helm, H. Merbold, T. Feurer, and M. Walther, "Lattice modes mediate radiative coupling in metamaterial arrays," *Optics Express*, vol. 17, no. 24, pp. 22108–22113, 2009.

[39] R. Singh, C. Rockstuhl, and W. Zhang, "Strong influence of packing density in terahertz metamaterials," *Applied Physics Letters*, vol. 97, no. 24, Article ID 241108, 2010.

[40] J. Wallauer, A. Bitzer, S. Waselikowski, and M. Walther, "Near-field signature of electromagnetic coupling in metamaterial arrays: a terahertz microscopy study," *Optics Express*, vol. 19, no. 18, pp. 17283–17292, 2011.

[41] D. A. Powell, M. Lapine, M. V. Gorkunov, I. V. Shadrivov, and Y. S. Kivshar, "Metamaterial tuning by manipulation of near-field interaction," *Physical Review B*, vol. 82, no. 15, Article ID 155128, 2010.

[42] R. Singh, I. A.I. Al-Naib, M. Koch, and W. Zhang, "Sharp Fano resonances in THz metamaterials," *Optics Express*, vol. 19, no. 7, pp. 6312–6319, 2011.

[43] D. Grischkowsky, S. Keiding, M. van Exter, and C. Fattinger, "Far-infrared time-domain spectroscopy with terahertz beams of dielectrics and semiconductors," *Journal of the Optical Society of America B*, vol. 7, p. 2006, 1990, http://www.opticsinfobase.org/josab/abstract.cfm?URI=josab-7-10-2006.

[44] *Computer Simulation Technology (CST)*, Darmstadt, Germany.

[45] V. G. Kravets, F. Schedin, and A. N. Grigorenko, "Extremely narrow plasmon resonances based on diffraction coupling

of localized plasmons in arrays of metallic nanoparticles," *Physical Review Letters*, vol. 101, no. 8, Article ID 087403, 2008.

[46] C. Rockstuhl, T. Zentgraf, C. Etrich, J. Kuhl, F. Lederer, and H. Giessen, "On the reinterpretation of resonances in split-ring-resonators at normal incidence," *Optics Express*, vol. 14, no. 19, pp. 8827–8836, 2006.

[47] L. Li, "New formulation of the Fourier modal method for crossed surface-relief gratings," *Journal of the Optical Society of America A*, vol. 14, no. 10, pp. 2758–2767, 1997.

[48] N. Papasimakis, V. A. Fedotov, Y. H. Fu, D. P. Tsai, and N. I. Zheludev, "Coherent and incoherent metamaterials and order-disorder transitions," *Physical Review B*, vol. 80, no. 4, Article ID 041102, 2009.

[49] C. Helgert, C. Rockstuhl, C. Etrich et al., "Effective properties of amorphous metamaterials," *Physical Review B*, vol. 79, Article ID 233107, 4 pages, 2009.

[50] R. Singh, X. Lu, J. Gu, Z. Tian, and W. Zhang, "Random terahertz metamaterials," *Journal of Optics A*, vol. 12, no. 1, Article ID 015101, 2010.

[51] G. Acuna, S. F. Heucke, F. Kuchler, H. T. Chen, A. J. Taylor, and R. Kersting, "Surface plasmons in terahertz metamaterials," *Optics Express*, vol. 16, no. 23, pp. 18745–18751, 2008.

[52] A. K. Azad, J. Dai, and W. Zhang, "Transmission properties of terahertz pulses through subwavelength double split-ring resonators," *Optics Letters*, vol. 31, no. 5, pp. 634–636, 2006.